Trinity College Dublin
Coláiste na Tríonóide, Baile Átha Cliath
The University of Dublin

Department of Electronic and Electrical Engineering

Design of a High Performance Low-Power ECG Amplifier for Textile Based Un-gelled Electrodes

Soumyajyoti Maji
12329165

October 22, 2021

A thesis submitted in partial fulfilment
of the requirements for the degree of
Ph.D. in Electronic and Electrical Engineering

Declaration

I hereby declare that this project is entirely my own work and that it has not been submitted as an exercise for a degree at this or any other university.

I agree that the Library may lend or copy this thesis upon request.

I have read and I understand the plagiarism provisions in the General Regulations of the University Calendar for the current year, found at `http://www.tcd.ie/calendar`.

I have also completed the Online Tutorial on avoiding plagiarism 'Ready Steady Write', located at `http://tcd-ie.libguides.com/plagiarism/ready-steady-write`.

Signed:  Date: October 22, 2021

Dedication

A man's heart deviseth his way: but the Lord directeth his steps. [Proverbs 16:9, KJV]

But seek ye first the kingdom of God, and his righteousness; and all these things shall be added unto you. [Matthew 6:33, KJV]

For Christ sent me not to baptize, but to preach the gospel: not with wisdom of words, lest the cross of Christ should be made of none effect. [1 Corinthians 1:17, KJV]

Abstract

This thesis presents analytical studies and bench experiments which highlight how electrocardiographic recording equipment which adheres to current international standards can still introduce distortion and affect the recorded signal. Most performance specifications are applicable to standard adhesive electrodes and therefore will not be met in recordings scenarios using un-gelled electrodes. This work was carried out in the light of the current international performance standards IEC 60601 pertaining to electrocardiographic equipment and has led to the identification of shortcomings in this standard. The design criteria for the amplifier input impedance needed for recording diagnostic quality of ECG signals with dry un-gelled electrodes are established and suggestions are made for revision of the standards. However, this would require a knowledge of the electrophysiological properties of the electrodes.

The electrical properties of equivalent models for several conductive, textile based electrodes in addition to one conductive rubber electrode and a standard self-adhesive electrode is presented in this work. In ECG recording the skin-electrode-amplifier interface can be modelled as an equivalent electrical circuit having one or two parallel C-R networks and series resistance. The electrical components of these models have been established using a time domain methodology. For the single C-R electrode model values of resistance ranged from 10 kΩ to 28 MΩ while values of capacitance ranged from 0.03 nF to 15 μF. The associated time-constant ranged from 0.1 ms to 5 s. In the case of the double C-R model values of resistance ranged from 1 kΩ to 25 MΩ while values of capacitance ranged from 9 pF to 872 μF. The associated time-constants ranged from 0.05 ms to 10 s. Measurements of noise generated were made using very low noise operational amplifiers and with mains power supply interference eliminated from the recorded signals so that they reflected only genuine noise. Curves of the form y = K/f + C were fitted to the recorded noise spectral density functions. Coefficients obtained for the white noise spectral density ranged from 1.1 to 5.6 nV/Hz and for the flicker (1/f) noise spectral density ranged from 8 to 80 nV$\sqrt{Hz}$.

The work presents a low-power, low-noise ECG amplifier that attains a minimum common-mode input impedance of 10 GΩ within a frequency range of 0.1-150Hz. This boosted input impedance is maintained by reducing input amplifier capacitance through power supply bootstrapping. The amplifier attains a differential gain of 41dB, CMRR was 90dB at 50Hz frequency with the inclusion of right leg drive and the semiconductor noise was measured at 32μV at a frequency of 250Hz.

In-vivo measurements were undertaken on two subjects at rest, arm waving and doing the Harvard step test. There was semiconductor noise superimposed on the ECG waveforms but no noticeable distortion was seen.

Acknowledgements

First and foremost, I would like to thank the Lord for giving me the strength, determination and the courage in all these years to complete this thesis. I would like to express my sincere gratitude to my supervisor Dr. Martin J. Burke for all his help and guidance throughout the course of this project. His sense of humour in some of the darkest moments have made me realise to always look at challenging problems in a grand way. The depth of his analytical skills, the technical knowledge in this niche area and the bench debug skills have always inspired me and is something I would always look upto.

I would like to extend my sincere thanks to Shane, Eugene, James and other technical officers in Trinity College for helping me with component ordering and bench debugging. I would particularly like to thank Shane for helping me with the PCB design and soldering those surface mount components. A big shout out goes to Teresa and Michael for looking after the postgraduate student welfares in the department. I would also like to thank Sarah for helping me designing the vest and stitching the electrodes into it.

I wouldn't have been able to make it this far if not for the sacrifices made by my parents. I am forever indebted to all their unconditional love, support and blessings that they have showered on me in all these years. I would like to thank my brother Subhra, for helping me with all those challenging mathematical concepts that I found difficult to grasp. I have missed sharing dinners with you for the last three years!

I would like to take this opportunity to acknowledge my long-term girlfriend, Joshi, for tolerating me over the last few years, especially during this COVID-19 pandemic. She has emotionally supported me for the last four years and has also participated in many measurements of this project and rightfully deserves my sincere gratitude.

I would like to extend my appreciation to my wonderful friends in Trinity. I would particularly like to thank Parth for helping me with all the administrative work during my time as a research student representative in college. I would also credit my colleague at Intel Ireland, Gourav, for always motivating me at work to keep pursuing my research interests in analog electronics.

Finally, I would like to thank the funding agencies for supporting this work and presenting my contribution to a wider international audience. In particular, I would like to acknowledge the IEEE Instrumentation & Measurement Society to award me with a student travel grant to present a conference paper at the 2018 IEEE International Symposium on Medical Measurements and Applications (MeMeA), Rome, Italy.

Contents

List of Figures

List of Tables

List of Abbreviations

ECG	Electrocardiogram
SA	Sino-Atrial
AV	Atrioventricular Valve
CMRR	Common-Mode Rejection Ratio
RLD	Right Leg Drive
AFE	Analog Front End
pk	peak
ptp	Peak-to-Peak
dc	direct current
ac	alternating current
IEC	International Electrotechnical Commission
AHA	American Heart Association
AAMI	Associationfor the Advancement of Medical Instrumentation

1 Introduction

Since its original recording by Einthoven [35] in 1904, the human electrocardiogram or ECG has become one of the most valuable diagnostic tools used in modern medicine. The familiar chest and limb electrodes used in hospital clinics allow signals to be recorded from the surface of a patient's body, which when amplified and conditioned appropriately, provide indispensable information on the condition and operation of the heart and cardiovascular system. The time profile of the recorded ECG facilitates the diagnosis and treatment of many heart diseases and adverse clinical conditions. The various electrodes record signals associated with different activities during the cardiac cycle observed from different aspects and therefore give comprehensive insight into the state of health and functioning of the heart and cardiovascular system.

1.1 Need for Ambulatory ECG Monitoring

The introduction of the portable Holter monitor [36–38] in the 1960s allowed recording of the ECG in ambulatory scenarios on hospital outpatients [38–41]. Extended recording of the ECG became possible over 24 – 48 hour periods and proved a valuable tool in the treatment of outpatients such as those undergoing post-surgery cardiac rehabilitation. Today, ECG monitoring has extended into areas outside of the conventional hospital environment such as the general practitioner's surgery [42–44], physiotherapy clinics [45, 46], sports physiology centres [47, 48] and even to the factory floor and the homes of new-born babies at risk of Sudden Infant Death Syndrome (cot death) [49–52]. Miniaturisation and large-scale integration of components and low-power electronic circuitry has provided the portable battery-operated instrumentation needed in these scenarios [53–56]. This has also been facilitated by the de-

velopment and increased use in recent years of 'dry' recording electrodes which do not require the use of a coupling gel as an electrical interface between the electrode and the patient's skin [52, 57–61].

1.2 Problems associated with conventional ambulatory ECG recording

Modern electrodes used in both hospital wards and clinics and in ambulatory recording are made of flexible foam with adhesive edges and a sponge centre soaked in a conductive electrolyte and are stuck to the patient's chest. In recent years, improvements have been made in the quality and performance of disposable or adhesive electrodes. Nevertheless, several problems remain unsolved with conventional methods of ECG recording. These electrodes generally need a degree of skin preparation before use [62, 63]. When used for a period of a few days these electrodes tend to dry out and give a poor quality of signal or to fall off the patient's chest altogether. When used over extended periods, they very often cause skin irritation or allergic reactions, particularly in the elderly [64].

1.3 Opportunities offered by un-gelled electrodes

Dry electrodes are made up of conductive rubber composite materials and are mounted on a belt or vest worn by the patient. Such electrodes do-not need the preparation of the skin before application, apart from disinfecting and they can be re-used almost indefinitely. Furthermore, the use of dry electrodes also eliminates allergic reaction or skin irritation commonly associated with electrolytic gels [65–68]. The removability and replicability of dry electrodes over gelled electrodes considerably increases the length of the time for which they can be worn, allowing patients to bath or shower. This results in the improvement of patient comfort and compliance, allowing the recording technique to cater for a wider range of users such as elderly, the long-term ill, cardiac rehabilitation patients and paediatrics [67, 69].

1.4 Signal quality

Currently, gel-less electrodes are primarily employed in heart-rate monitors used largely in the field of sports and athletics. These devices only measure and display the value of the wearer's heart-rate on a beat-to-beat basis. This information is largely used in an athletic training capacity rather than any clinical role. While these devices detect the ECG signal they do not preserve the morphology or time profile of the signal which carries the clinical information. An ambulatory ECG recording system using gel-free electrodes but which can provide clinical diagnostic signal quality would therefore be of huge benefit. If the recorded ECG signal is to be used for diagnostic purposes, it is of the utmost importance that the profile and the quality of signal is as faithfully preserved as possible from the surface of the skin and in its passage through the conditioning amplifier [6, 70].

1.5 Project Aim

The project reported in this thesis aims to develop a system of recording of the ambulatory human electrocardiogram (ECG) using dry, non-gelled electrodes mounted in a body-fit elasticated vest with the associated precision, high-performance, low-power, battery-operated portable instrumentation amplifier and signal conditioning circuitry. While the project involves a substantial amount of design and technology development, a considerable amount of analytical work has also been undertaken to obtain the knowledge and understanding of the mechanisms involved in the signal detection, processing and preservation. International standards have been used to design an optimised interfacing amplifier that ensures accurate ECG signal reproduction. In particular, standards and recommendations published by the International Electrotechnical Commission (IEC), the American National Standards Institute (ANSI) and the American Heart Association (AHA) have been used to establish and evaluate the requirements of the amplifier stages. The amount of published work in the field of instrumentation applied to dry-electrode ECG recording is quite limited due to the difficulty of acquiring an ECG signal of diagnostic quality without a conductive gel and the much more

stringent demands placed on the recording amplifier. The amplifier has been designed to have very high input impedance needed with dry electrodes and very low power consumption, operating ideally from a 3V supply. It provides the full ECG signal bandwidth with a frequency response characteristic that preserves the signal without distortion. It has high common-mode rejection ratio to suppress mains hum and other extraneous sources of interference. It is intended to cater for ECG signals having amplitudes in the range 0.1mV-10mV. The dissertation addresses novel circuit design solutions to incorporate active means of CMRR improvement, input impedance boosting techniques and of reducing the long initialisation and overload recovery times currently associated with such amplifiers. The ultimate goal of the project was to implement the measurement circuitry in low-power technology using surface mounted components. This involves pushing the performance of current commercially available components and devices to the limit.

1.6 Thesis Outline

The dissertation addresses the following four primary aspects associated with ambulatory monitoring of the human electrocardiogram using dry electrodes:

1. electrical characterization, including noise properties, of conductive fabric-based ECG recording electrodes and amplifier front-end input impedance requirements.

2. avoiding signal distortion due to the skin-electrode-amplifier interface.

3. interference suppression and boosting common mode amplifier input impedance.

4. minimization of amplifier initialisation time.

A brief outline of each chapter is given below:

Chapter 2: Background and Literature Review

This chapter outlines the ECG profile, recording and its diagnostic usage in modern medicine. The chapter discusses the performance requirements of the recording amplifier in the light of the ANSI, AHA and IEC-60601 standards pertaining to electrocardiography. It assesses the

work of previous research carried out in the area.

Chapter 3: Electrical Characterisation of Fabric-Based Dry Electrodes

A brief introduction on electrical modelling of the skin-electrode-amplifier interface is outlined in this chapter. It presents the values of the electrical elements of equivalent models for several conductive textile-based electrodes. This allowed the effective source impedance of the electrodes to be established when used as surface electrodes in un-gelled or dry electrode recording of the ECG signal on ambulatory patients. The chapter also outlines the noise generation characteristics of these textile-based electrodes. Noise measurements are necessary to determine the best performing textile-based electrode that can be used in a vest to record diagnostic quality ECG's.

Chapter 4: Transient Performance and Skin-Electrode Interface

This chapter outlines a substantial amount of analytical and experimental work which involved modelling of the skin-electrode-amplifier interface and its electrical behaviour. This was done in the light of the current international performance standards, IEC 60601, pertaining to electrocardiographic equipment. The work has allowed design criteria for the amplifier input impedance needed for recording diagnostic quality of ECG signals with dry un-gelled electrodes to be established and suggestions to be made for revision of the standards.

Chapter 5: Design Overview

This chapter presents a design overview of the ECG recording amplifier and outline a proposed multi-stage architecture. The chapter also provides an appraisal of the previous ECG amplifiers that have been designed and developed in the Department of Electronics & Electrical Engineering, Trinity College Dublin. A brief summary of the performance characteristics considered in selecting suitable commercially available op-amps is outlined.

Chapter 6: Design of High Impedance Input Stage

A brief literature review of some of the existing techniques to boost the amplifier input impedance is presented in this chapter. The chapter then outlines a novel method using low power op-amps to extend the bandwidth over which very high amplifier input impedance can

be maintained by reducing amplifier input capacitance via power supply bootstrapping.

Chapter 7: Boosting Amplifier Common-Mode Rejection Ratio

This chapter discusses different designs that have been used over the years to boost the CMRR performance of ECG recording amplifiers. However, most of these designs are associated with high power consumption or limited CMRR bandwidth. This chapter explores a novel methods to boost the CMRR performance of the recording amplifier.

Chapter 8: Construction and Testing of Prototype ECG Amplifiers

This chapter outlines the construction and testing of a low-power low-noise, battery-operated amplifier to be used with dry electrodes. This chapter presents comprehensive bench tests to assess the performance parameters of two prototype recording amplifiers. The design was first implemented on a strip-board and subsequently on professional PCB. Actual in-vivo ECG measurements on dry and wet electrodes are also presented.

Chapter 9: Conclusion & Future Work

The work summarises the novel contributions in the field of dry electrode ECG recording. The limitations of the work are highlighted and problems that needs to be addressed as a part of future research are also discussed.

1.7 Publications

The following publications are associated with this Thesis:

S. Maji and M.J. Burke, "Effect of Electrode Impedance on the Transient Response of ECG Recording Amplifiers," *13th Annual IEEE International Symposium on Medical Measurements and Applications (MeMeA)*, Rome, Italy, June, pp. 1-6, 2018. **[Best Graduate Paper Award]**

S. Maji and M.J. Burke, "The Skin-Electrode Interface Impedance and the Transient Performance of ECG Recording Amplifiers," *17th IEEE SENSORS*, New Delhi, 2018, pp. 1-4.

S. Maji and M.J. Burke, "Establishing the Input Impedance Requirements of ECG Recording Amplifiers," *IEEE Transactions on Instrumentation & Measurement*, vol. 69, no. 3, pp. 825-835, March 2020.

S. Maji and M.J. Burke, "Determining the Input Impedance of ECG Amplifiers Using Accurate Electrode Modelling," *Biomedical Physics & Engineering Express*, vol. 6, no. 1, pp. 1-15, 2020.

S. Maji and M.J. Burke, "Electrical characterization of conductive textile based ECG recording electrodes", *Measurement:Sensors*, vol. 15, pp. 100044, 2021.

S. Maji and M.J. Burke, "Noise performance of textile-based dry ECG recording electrodes," *Electronics Letters*, vol. 57, no. 2, pp. 45-48 , 2021.

S. Maji and M.J. Burke, "A low-noise, low-noise micro-powered dry ECG recording amplifier," *IEEE Transactions on Biomedical Circuits & Systems*, 2021 (In-Preparation).

2 Background & Literature Review

2.1 Physiological & Measurement Background

2.1.1 Structure and Anatomy of the Heart

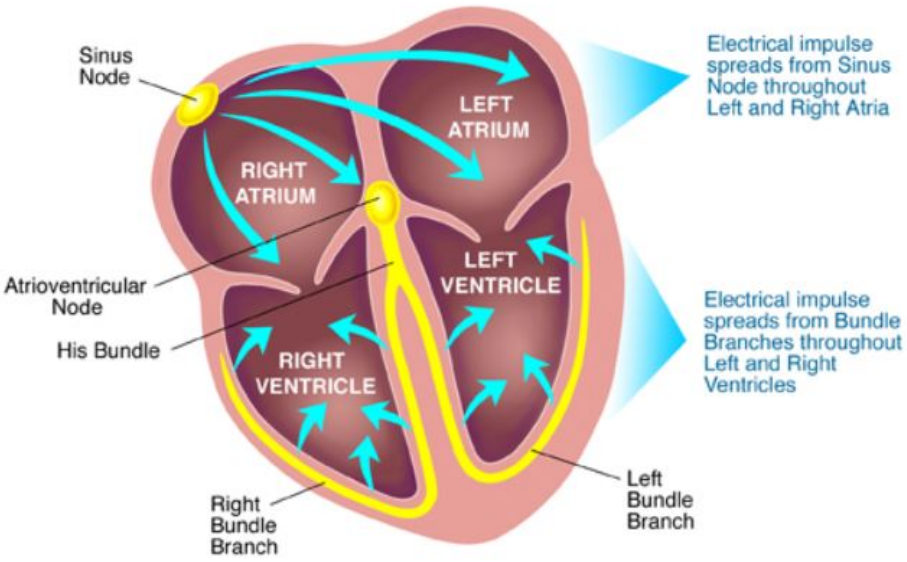

Figure 2.1: Electrical conduction system of the heart [1]

The human heart shown in simplified form in Fig. 2.1 consists of four chambers: two upper chambers (the atria) and two lower ones (the ventricles). The atria are the chambers that store blood when the ventricles are pumping. The filling state of the heart cycle is popularly known as the diastole and the pumping phase is referred to as the systole. The atrioventricular (AV) valves connect the atria and the ventricles. The right ventricle is separated from the pulmonary artery by the pulmonary semilunar valve. The aortic valve separates the left ventricle from the aorta.

2.1.2 Electrical Conduction in the Heart

Periodic electrical pulses in the heart, or heart-beat, control the contraction of the heart muscles and the regular flow of electrical current through its muscles. The electrical conduction system of the human heart can also be seen in Fig. 2.1. The sinoatrial (SA) node located in the top of the right atrium produces electrical impulses spontaneously that stimulate the atria to contract. Therefore, the SA node is essentially a pacemaker and determines the heart-rate. The atrio-ventricular (AV) node then delays the impulse before it is transmitted to the ventricles and causes the ventricles to contract and pump blood throughout the circulatory system. The primary steps associated with the electrical cycle of the human heart can be summarised as follows [5, 8]:

1. Atrial depolarisation occurs due to the excitation of the SA node. The electrical impulse then propagates from the right atrium to the left atrium, stimulating the myocardium of the atria to contract. The electrical activity subsequently travels from the SA node to the AV node through internodal tracts.

2. AV node then conducts the impulse slowly, forcing a delay between the excitation of the atria and the ventricles. The absence of this delay would otherwise force the atria and the ventricles contract at the same time. The atria pumps the blood into the ventricles towards the end of this delay period.

3. Ventricular depolarisation occurs due to the excitation of the His Bundle, Purkinje fibres & ventricular muscles [71, 72]. The interventricular septum is first activated, forcing the electrical impulse to flow from the left to the right ventricle. Then, the endocardial surface and the ventricular free walls forming the muscles of the ventricles gets stimulated and finally is the activation of the epicardial surface.

4. The final event of the cycle is the ventricular repolarisation. Ventricular repolarisation is essentially the restoration of the resting state. Following ventricular repolarisation, the ventricles start to relax and the pressure within the ventricles drops.

2.1.3 Clinical Measurement

The ECG signal is associated with underlying electrical activity that can be detected on the surface of the chest. This electrical activity is associated with the depolarisation and repolarisation of the muscles of the heart chambers. Corresponding electrical signals can then be detected on the skin using suitable electrodes connected to a recording amplifier as shown in Fig. 2.2.

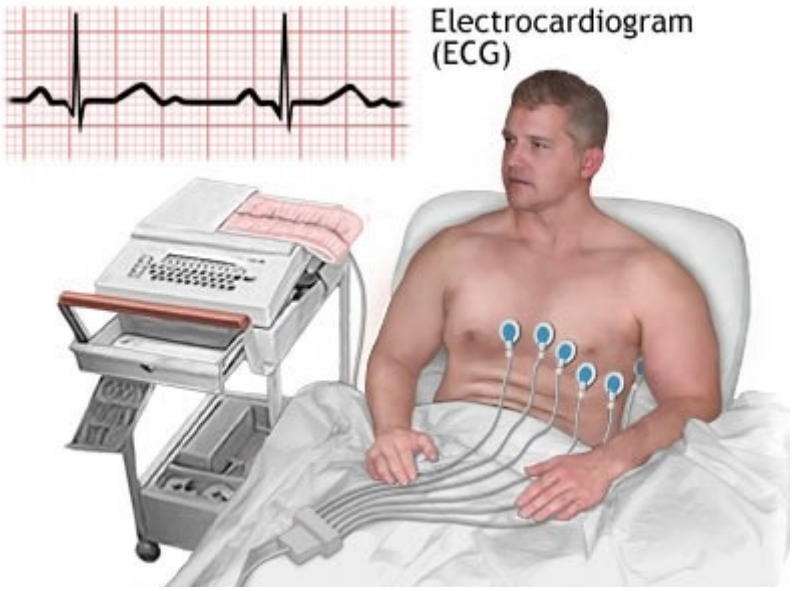

Figure 2.2: Measurement of the Electrocardiogram

2.1.4 A Typical ECG Profile

The standard 12 lead placement shown in Fig. 2.3 is commonly used to accurately record a complete electrocardiogram. Six chest electrodes, V_1 to V_6, as well as four limb electrodes are used for the measurement. The limb leads are made up of the three electrode placements. These electrodes shown in Fig. 2.3 form the Einthoven triangle when placed on the left arm (LA), right arm (RA) and the left leg (LL). There are also augmented versions of these leads.

The Einthoven triangle has three leads [5]. Lead I goes from the RA to LA, lead II is oriented from RA to LL and lead III is assigned to the direction LA to LL as in 2.3. The electrode that is placed on the right leg is a ground lead but is sometimes connected to a circuit which is

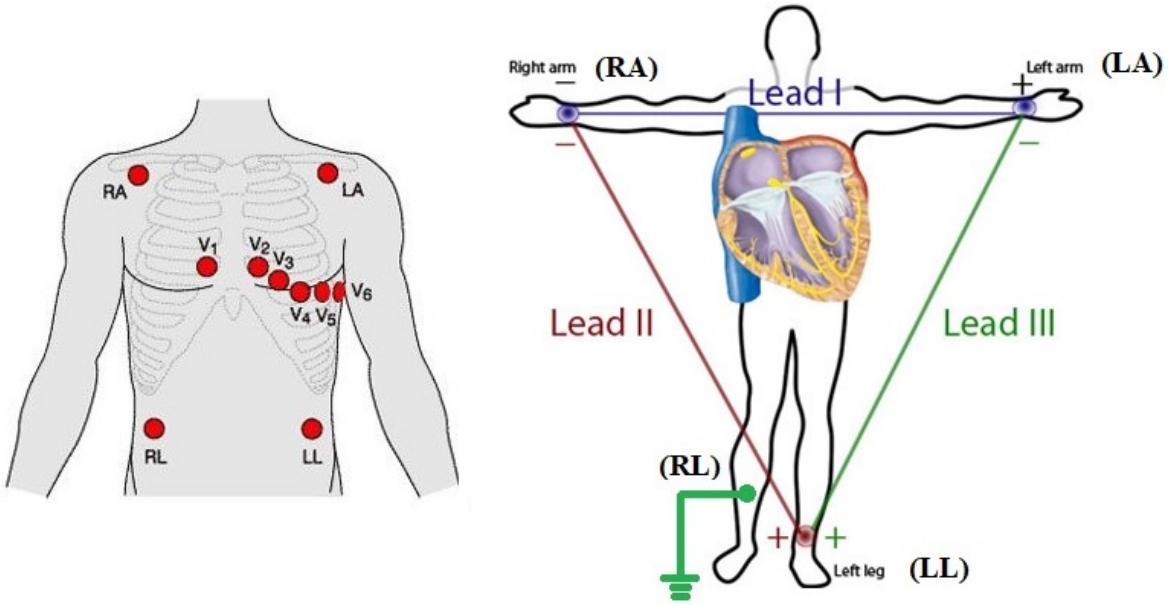

Figure 2.3: Three Leads forming an Einthoven triangle [2]

known as the right-leg-drive circuit, used to suppress common mode interference. Therefore, we can mathematically express the three leads [73] as follows:

$$V_I = \phi_{LA} - \phi_{RA} \tag{2.1.1}$$

$$V_{II} = \phi_{LL} - \phi_{RA} \tag{2.1.2}$$

$$V_{III} = \phi_{LL} - \phi_{LA} \tag{2.1.3}$$

where V_I, V_{II}, V_{III} are denoted as limb voltages in Lead I, Lead II and Lead III and ϕ indicates the surface potential relative to ground at the node of an electrode. The potential difference between these two pairs of limb voltages is essentially known as lead configuration in ECG measurement.

By Kirchhoff's voltage law (KVL), we know that the net potential drop around any closed loop is zero. Therefore, we can write:

$$(\phi_{LA} - \phi_{RA}) + (\phi_{LL} - \phi_{RA}) + (\phi_{LL} - \phi_{LA}) = 0 \tag{2.1.4}$$

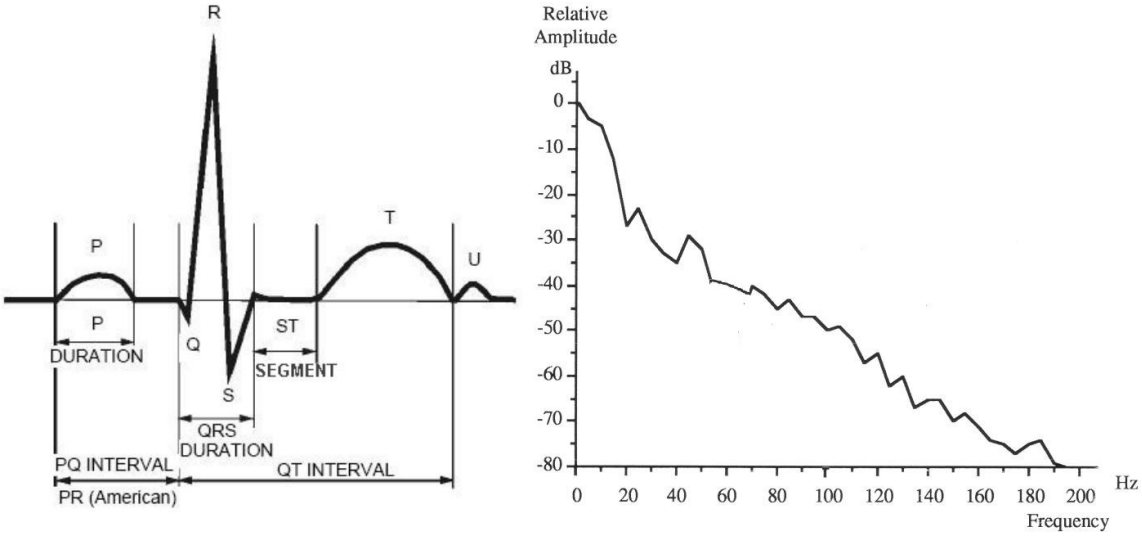

Figure 2.4: A typical ECG profile and the frequency spectrum of a lead II ECG signal [3, 4]

which gives:

$$V_I + V_{III} = V_{II} \tag{2.1.5}$$

This shows that all limb measurements are inter-dependent. A typical ECG signal profile and the frequency spectrum of a lead II ECG recording are shown in Fig. 2.4.The three successive waves in the ECG signal namely "P", "QRS" and "T" [71, 74] are associated with different events in the cardiac cycle as follows:

• The P wave is associated with left and right atrial depolarisation and the contraction of the atria. The wave duration is typically 90 ms and the amplitude is limited to 0.2 mV.

• The QRS complex is associated with left and right ventricular depolarisation. The first deflection is the negative Q wave which goes down from the basline. This is followed by a positive deflection which is the R wave and then is trailed by a negative deflected S wave. The QRS complex wave typically lasts between 85 ms and 120 ms. The QRS complex also masks the reploralisation of the ventricles.

• The T wave represents ventricular repolarisation. Its amplitude is lower than the QRS complex, as is the spectral content.

• Following the T wave, there is also a U wave which is sometimes detected. Several hy-

potheses have been proposed to explain the origin of the U wave [75–77] but none of them has received universal acceptance [78, 79].

The P-R and the S-T segments are normally at the baseline potential. The conduction delay in the atrioventricular (AV) node is primarily responsible for the P-R interval. The S-T segment represents the interval between ventricular depolarization and repolarization.

2.1.5 The significance of the ECG

Essential physiological and clinical information can be extracted from the ECG signal. Changes in either one of the PR or ST segments have clinical implications and are described as follows:

• Heart injuries can be observed in the ECG signal as an alteration in the ST segment profile [6, 70, 80]. For example, a downward excursion of the ST segment represents significant damage to the cardiac wall muscles. Similarly, an elevated ST segment can be indicative of heart attack.

• The amplitude and the duration of the P, QRS and T waves in the ECG signal indicate the position, size and the shape of the heart [9]. For example right atrial enlargement is diagnosed when the P wave is recorded with an amplitude exceeding 2.5 mm in Lead II and Lead III . Similarly, left atrial enlargement occurs when there is a prolonged P wave duration in Lead I and Lead II.

• Irregularities of the heart rhythms are associated with significant changes in the number and duration of ECG cycles per minute.

• The presence of drugs may alter segments and interval durations, as well as wave morphology [81].

Normal & Abnormal Heart Rhythms

A normal resting heart rate is approximately 70 beats-per-minute (bpm). The rate is accelerated during exercise, fever, or emotional stimuli (tachycardia) and is slowed during sleep (bradycardia). Abnormal cardiac rhythms occur when the sinoatrius (SA) node is suppressed,

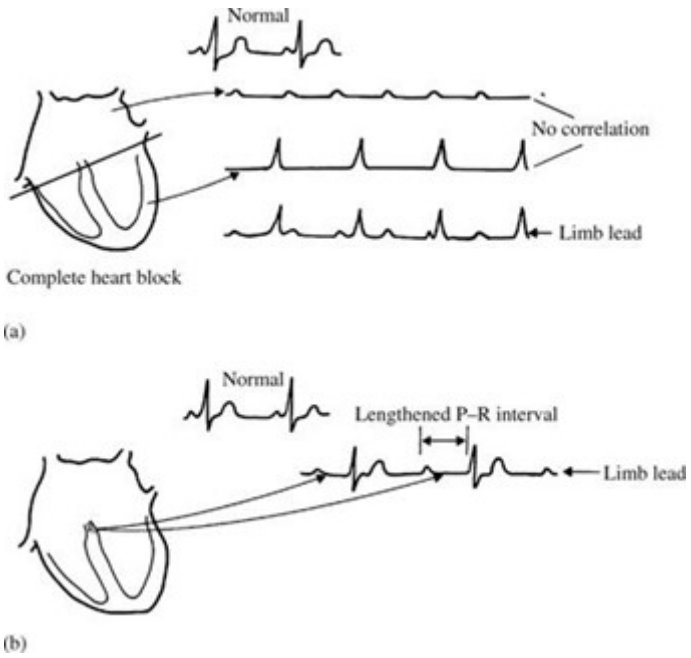

Figure 2.5: Atrioventricular block (a) Complete heart block (b) First-degree block [5]

the His bundle is damaged, or when the ventricles discharge at a faster rate than the SA node response [5]. A common type of abnormal heart rhythm, or atrioventricular block, shown in Fig. 2.5 occurs in the AV node when the electrical impulse to the ventricles is delayed or blocked in its passage from the atria [5]. First-degree heart block shown in 2.5(b) occurs when all atrial impulses reach the ventricles but the P-R interval is abnormally prolonged [5]. In Type I AV block, the length of the P-R interval progressively increases until a subsequent beat is dropped. It can occur in a variety of pathological settings, especially in damaged blood vessels in the walls of ventricles. In complete heart block shown in Fig. 2.5(a) most of the electrical impulses originating in the AV node fail to reach the ventricles.

Arrhythmia

Figure 2.6: Normal ECG followed by an extra beat or PVC

Irregular heart-rate or arrhythmia occurs when the heart beats too quickly or too slowly or with an irregular rhythm. Often arrhythmias are caused by ectopic focus. This is when abnormal

sites outside the SA node begin to create false impulses. The cardiac rhythm is transiently interrupted when the focus discharges only once, thereby causing a second beat to occur before the next expected normal beat [5]. This extra beat is often known as extrasystole or premature ventricular contraction (PVC), an example of which is shown in Fig. 2.6. Tachycardia, or fast heart-rate occurs when the focus discharges repetitively at a rate exceeding that of the SA node [5]. This can result in paroxymal tachycardia or atrial flutter as shown in Fig. 2.7.

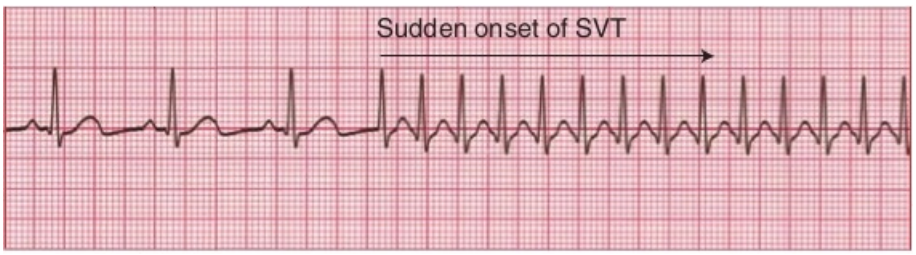

(a) Supraventricular tachycardia (SVT)

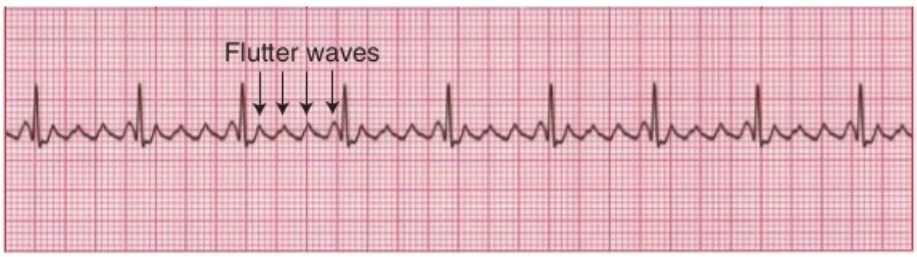

(b) Atrial Flutter

Figure 2.7: Paroxysmal tachycardia

A much more irregular or rapid discharging ectopic focus in the atria or ventricles may cause atrial or ventricular fibrillation. This rapid uncoordinated flutter causes the atria or the ventricles to stop their regular beat, and as a result, low amplitude irregular waves appear in the ECG signal, as illustrated in Fig. 2.8

Myocardial Infarction & Myocardial Ischemia

A depression in the ST segment of an ECG wave is considered indicative of the onset of myocardial infarction or heart attack [5, 82]. An augmented S wave in an ECG signal can be clinically interpreted as an early sign of myocardial ischemia, which occurs when the blood supply to the heart muscles drops significantly [5]. This can cause partial or complete blockage of coronary arteries.

The above summary shows that much clinical diagnosis depends heavily on an interpretation

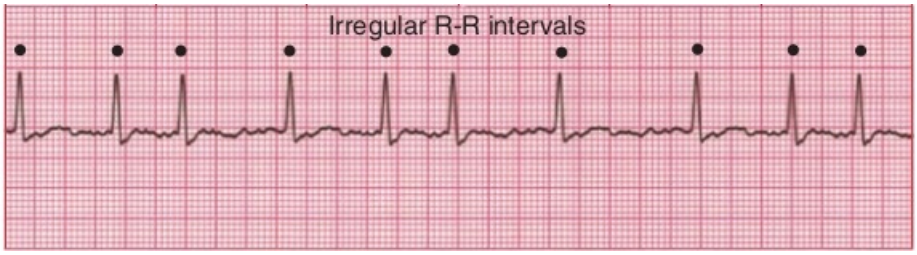

(a) Atrial Fibrillation

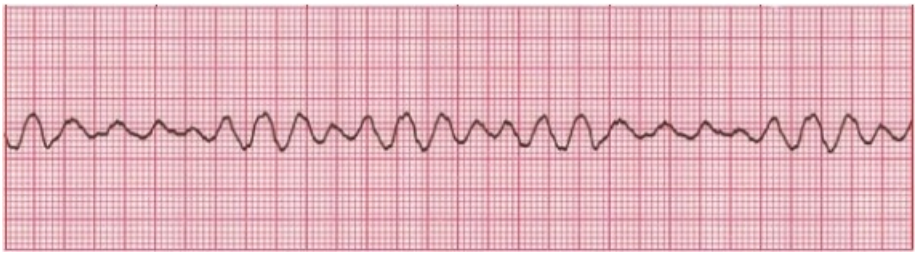

(b) Ventricular Fibrillation

Figure 2.8: Atrial and Ventricular Fibrillation

of the time profile of the ECG signal. It is therefore essential that the signal profile is faithfully preserved during ECG recording.

ECG Signal Distortion

Berson and Pipberger have shown that an ECG amplifier implementing an inadequate response high-pass-filter can cause distortion in the ST segment and T wave of the ECG [6].

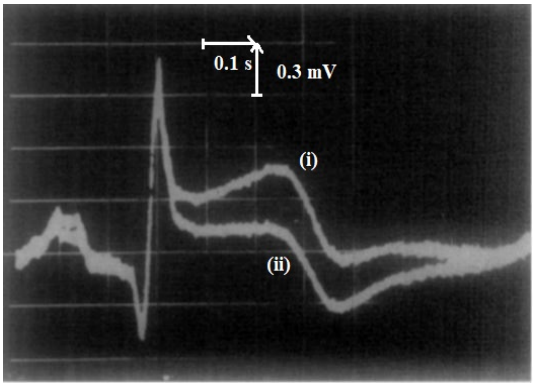

(a)

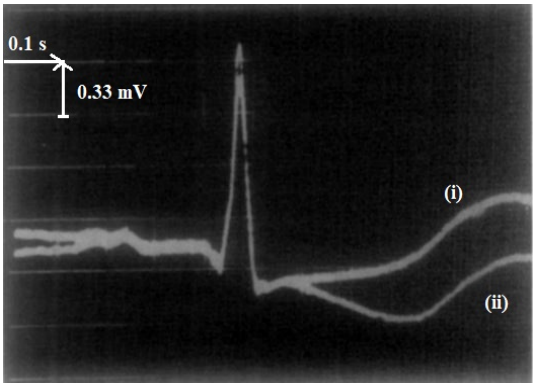

(b)

Figure 2.9: Oscilloscope photographs of patients suffering from (a) acute myocardial infarction and (b) an old infarct [6]. The upper record labelled as (i) is the output of a simulated dc amplifier system. The lower record shown as (ii) represents the output of high-pass filter having 0.5 Hz cut-off frequency.

This source of error and distortion in ECG recording may cause clinical misdiagnosis. For example, inadequate filter response as shown in Fig 2.9(a) can significantly distort the ST segment by reducing the elevation and producing inversion of the terminal part of T wave. In addition, it was also demonstrated as shown in 2.9(b) that a downward sloping ST segment in a ECG waveform has been altered into an elevated ST segment.

Taylor and Vincent demonstrated that phase non-linearity can exacerbate recording error and misdiagnosis [70]. Erroneous ST segment shifts as shown in Fig.2.10 are mainly due to a nonlinear phase response at low frequency. The phase non-linearity and the resulting ST segment distortion introduced at the amplifier input stage can not be corrected in a subsequent stage without detriment to other portions of the ECG waveform [70]. Early AHA specifications recommended that the phase shift introduced by the amplifier should not exceed that of a single-pole high-pass filter having a cut-off frequency of 0.05 Hz [7]. This is discussed in more detail in Section 2.2.

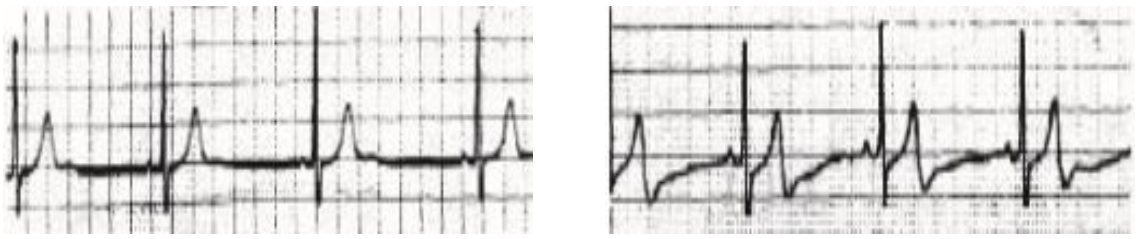

(a) ECG

(b) ECG distortion due to non-linear phase response

Figure 2.10: Effect of non-linear phase distortion on a ECG waveform [7]

2.2 ECG Measurement Setup

A typical ECG recording system with identical electrodes on each side of a differential amplifier is shown in Fig. 2.11. The effective skin-electrode impedance is modelled as Z_E. Current limiting resistors R_S are introduced in series with Z_E to prevent transient current spikes reaching the patient. The equivalent common-mode input resistance on each sides of the differential amplifier with respect to ground is denoted as R_C. Similarly, the equivalent differential input resistance between the two inputs of the amplifier is indicated as R_D. The elements R_C and

R_D are considered to be purely resistive. A dc blocking capacitor C_C on both inputs of the differential amplifier is introduced in series with the electrodes. This is done to remove the dc offset polarisation voltage, which is much higher in dry electrodes than is the case with conventional wet electrodes. An ideal bio-potential amplifier should amplify the differential input voltage signal sensed by the two similar electrodes. However, in practice, the electrodes sense interfering signals at the front end of the amplifier and also introduce noise into the ECG signal.

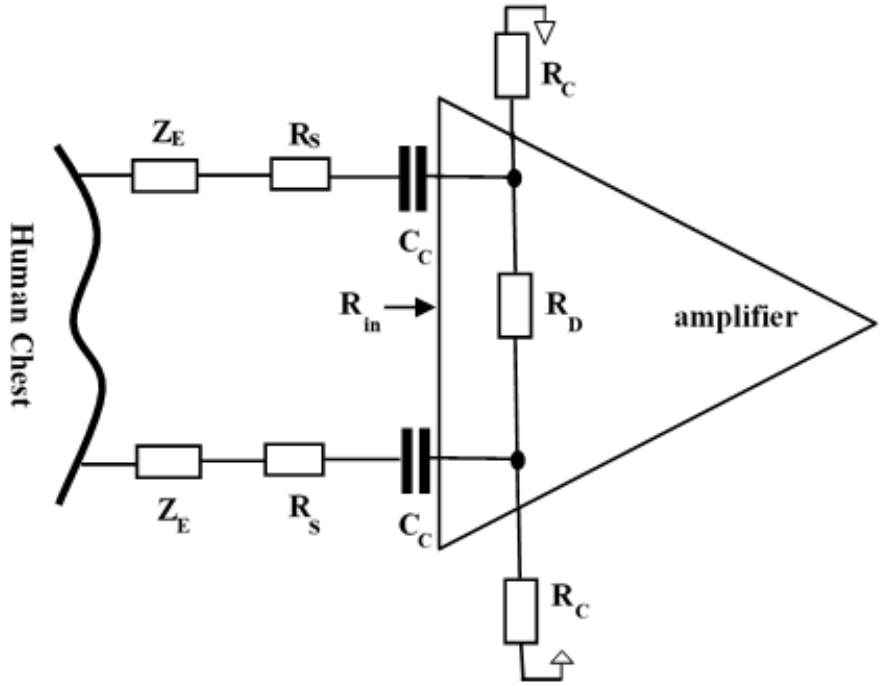

Figure 2.11: ECG Measurement Setup with a pair of identical electrodes

2.3 Recording Amplifier Requirements

Performance specifications for electrocardiographs have been developed over the past decades and today are issued by the American National Standard Institute (ANSI), The Association for the Advancement of Medical Instrumentation (AAMI) in the USA and by the International Electrotechnical Commission (IEC) in Europe and internationally [3, 22, 83]. Despite the fact that standards in place in the USA are closely based on IEC documents, American standards generally consider the recommendations of the American Heart Association (AHA) for their final texts [84, 85]. Minor differences appear between criteria endorsed by ANSI and those of

the IEC.

There are many problems that are frequently encountered by healthcare professionals and instrumentation engineers when recording electrocardiograms. These factors have to be taken into consideration in the design and development of bio-potential amplifiers. Some of these factors are:

- preservation of the frequency spectrum bandwidth
- conservation of the waveform profile in the time domain
- elimination of dc-offset voltages
- minimisation of motion artefacts
- preservation of signal-to-noise ratio
- discrimination between the wanted ECG signal and unwanted interfering signals
- fast initialisation time and overload recovery
- maintenance of patient safety
- meeting international performance standards pertaining to electrocardiograph equipment.

These general issues associated with the recording of ECG signals are considered in more detail below from the point of view of the design of the recording amplifier.

2.3.1 Frequency Domain Requirements

The frequency performance specification has been developed by the American Heart Association (AHA) and the Institute of Electrical and Electronic Engineers (IEEE) in the USA. Early performance specifications for ECG recording amplifiers recommended that the variation in magnitude of the frequency response should be kept within $\pm 0.5dB$ (6 %) of the mid-band gain down to a frequency of 0.67 Hz. This frequency corresponds to a minimum beat-to-beat heart rate of 40 bpm. The gain can overshoot this limit at frequencies below 0.67 Hz but it is wiser not to allow this as it may lead to amplification of low frequency artefact components and baseline drift. They also recommend that the phase shift introduced by the amplifier

should not exceed that of a single-pole high-pass filter having a cut-off frequency of 0.05 Hz. This is shown in Fig. 2.12.

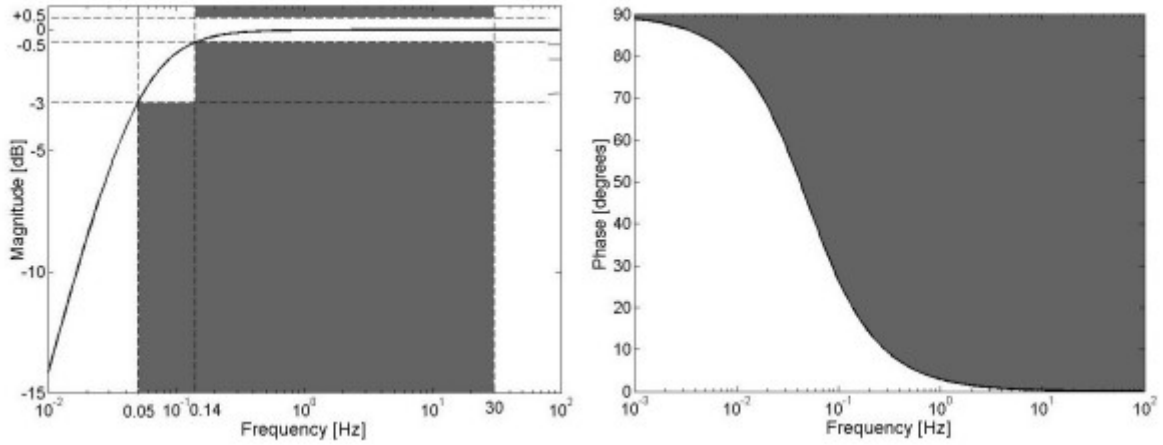

Figure 2.12: Magnitude and Phase Requirements

2.3.2 Time Domain Requirements

Following continuous difficulty in identifying the precise nature of the distortion caused in the recorded ECG signal when the phase specification was violated, attention turned towards the transient response of the amplifier in the time domain. The IEC 60601 has introduced a rectangular pulse, time-domain, method of testing the performance of ECG recorders intended for clinical diagnostic measurements. This is shown in Fig. 2.13.

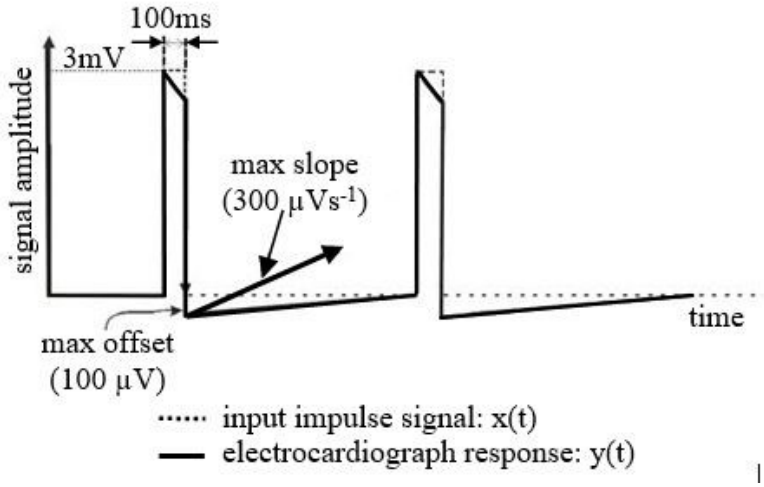

Figure 2.13: Time Domain Requirements

In this method, the response to a 3mV amplitude, 100ms duration, narrow rectangular pulse

must show no more than 100 μV undershoot from the baseline at the end of the pulse, when normalised for gain. The maximum recovery slope following the undershoot, must also be less than 300 μVs^{-1}. Signal distortion in the form of false S-wave creation or exaggeration and depression of the S-T segment has been observed when the recommended IEC 60601 time domain specifications are violated [86][87]. This distortion can lead to clinical misdiagnosis of events such as myocardial ischemia or the onset of myocardial infarction [88].

2.3.3 DC Saturation

A high offset voltage produced at the electrodes of the ECG measurement system can cause saturation of the amplifier that can clip the profile of the ECG signal. This can cut-off the peaks of the QRS complex at the output of the amplifier which exceed the supply voltage [4, 8]. The S wave can also be cut-off if the amplifier undergoes negative saturation [4, 8]. Therefore, a dc blocking capacitor must be introduced at the front end of the ECG amplifier to eliminate any offset voltages. This has implications for the amplifier frequency response.

2.3.4 Minimisation of Motion Artefacts

Motion artefacts are introduced into the amplifier input signal due to the movement of subjects during exercise [89, 90]. Triboelectric effects result from electrode and skin friction [91, 92]. An artefact is also generated due to changes in the skin-electrode interface impedance and the polarisation potential [92, 93]. Tan and Webster [91] have shown that motion artefacts can be greatly reduced by skin abrasion with sandpaper. However, occasional bleeding and skin irritation were observed after abrasion. Slow changes in the skin-electrode polarisation potential do not cause noticeable variation of the ECG base line provided they are suppressed by the use of ac coupling. However, high-rate changes in offset potential produce artefacts within the ECG bandwidth that cannot be removed by filtering. Motion artefact is therefore best minimised when electrode movement is prevented by the use of an elasticated belt or vest that holds the electrodes in place on the skin [9, 94]. Skin potential variation (SPV) insensitive dry electrodes have been developed in recent years to compensate motion artefacts [95]. The skin potential is not coupled into the electrode and this in turn prevents its influence

on the bio-potential recording in the dynamic state. However, these electrodes are specialised and very expensive.

2.3.5 Electrical Interference

One of the major problems in any biopotential recording system is interference from the main power supply, which is commonly referred as hum [96]. This electrical interference from the power supply can be introduced into the ECG signal by two means, namely electromagnetic induction and electrostatic induction. The magnetic field associated with the mains current flowing through any nearby electrical equipment cuts the loop enclosed by the subject, the electrode leads and the amplifier. This in turn induces an electromotive force and a resulting current flow in the leads proportional to the area of the loop, as shown in Fig. 2.14. The emf, which is induced, can be reduced by twisting the leads or using coaxial cables to eliminate the loop. In the author's work, it is intended that the electrodes and the preamplifier would be mounted in a body tight vest and hence there will be little or no loop area present and therefore electromagnetically induced interference will be negligible.

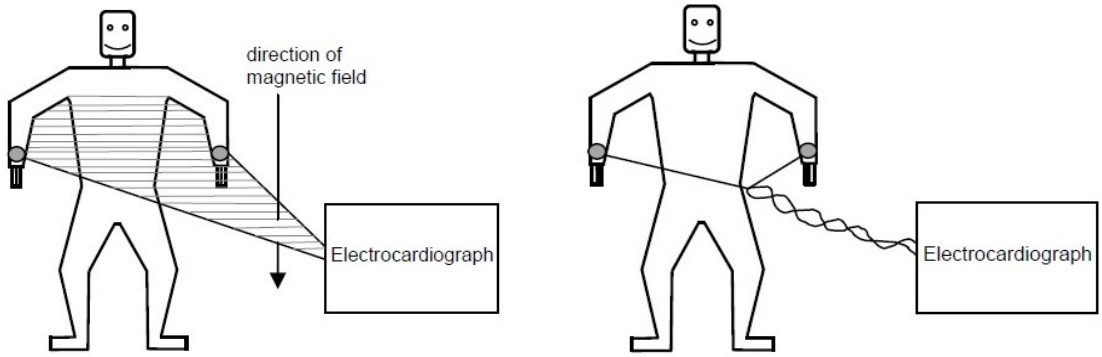

Figure 2.14: Diagram showing (a) the principle of electromagnetic induction and (b) its minimisation in ECG measurement [8]

In electrostatic induction, the electric field associated with the mains power supply is capacitively coupled to the subject who is also coupled to the ground via their body capacitance [97, 98] as shown in Fig. 2.15. An interfering signal is generated at the input of the amplifier due to a displacement current which flows from the mains supply through the subject

to ground. The interference is normally common-mode when the electrodes are mounted close together on the subject. In the past a displacement current of the order of 0.5μA has generated an interfering signal level in the region of 40mV [20, 99]. This common-mode interference is a significant problem in recording the ECG signal and the common-mode rejection capability of the amplifier is relied upon to supress it [20, 99, 100].

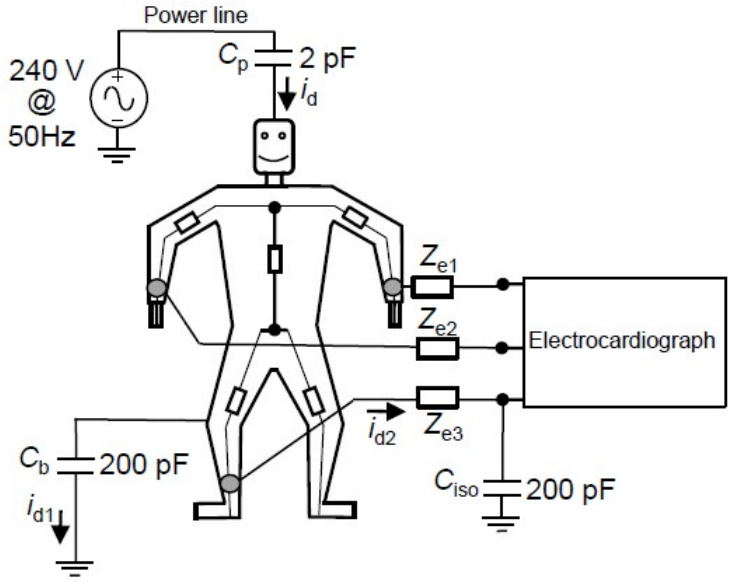

Figure 2.15: The electric field from the power line supply is coupled to the subject's body. Z_{e1}, Z_{e2} and Z_{e3} represent the electrode impedances [8, 9]

2.3.6 The Skin-Electrode-Amplifier Interface

Recent studies [86, 88, 101] have suggested that it is important to accurately model the skin-electrode-amplifier interface in order to prevent unnecessary attenuation and distortion of the ECG signal. The electrical properties of the skin-electrode-amplifier interface determine the amplifier input impedance necessary to prevent distortion of the ECG signal. The skin-electrode interface can be modelled by a single time-constant or a much more accurate double time-constant network.

Single Time Constant Model

A simple single time-constant network is shown in Fig. 2.16 as a skin-electrode impedance model was first proposed by Swanson and Webster [10]. This model is a combination of a

resistor in series with a parallelled resistor and capacitor. It is applicable mainly for wet electrodes because E_{hc} describes the voltage between the skin and the electrolytes. The electrical charge double layer between the skin and the electrode is represented by the capacitance C_p. The resistance R_p represents the conductive charge transfer between the skin and the electrode. The underlying skin tissue is represented by R_s. The IEC 60601 standard is primarily intended to apply to wet electrodes for ECG measurement equipment. This standard uses a 51kΩ resistor in parallel with a 47nF capacitor to model the skin-electrode interface impedance in some performance measurements.

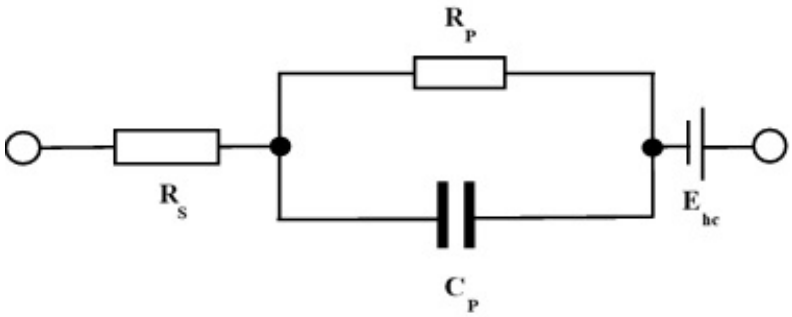

Figure 2.16: Single Time Constant Skin-Electrode Impedance Equivalent Model [10]

Double Time Constant Model

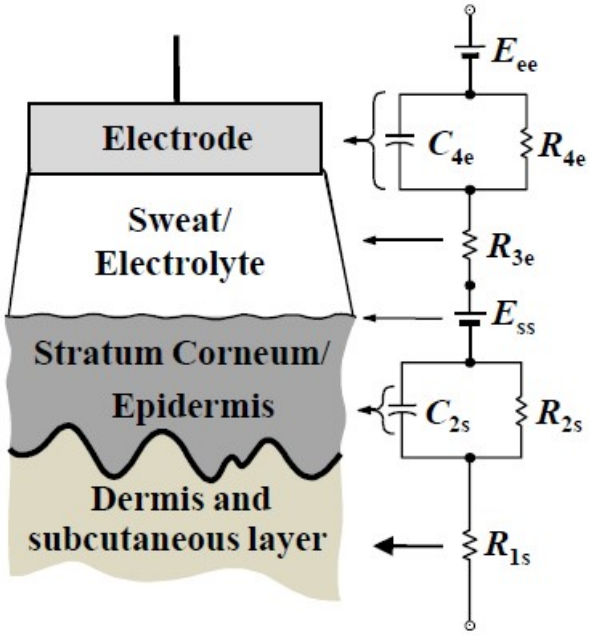

Figure 2.17: Double Time Constant Skin-Electrode Impedance Equivalent Model [11].

The double time-constant electrode model shown in Fig. 2.17 was first proposed by Neuman

[11, 102]. This double time-constant model combines two single-time constant networks. The first one represents the electrode-electrolyte boundary and the second one represents the boundary of electrolyte and the epidermal layer of the skin. The half-cell potential of the electrode is labelled E_{ee}, R_{4e} and C_{4e} constitute the impedance associated with the interface between electrode and electrolyte. The series resistance R_{3e} is the effective resistance due to electrolyte between the electrode and the skin (largely perspiration in the case of dry electrodes). E_{ss} represents the ionic potential difference across the membrane of the stratum corneum, and R_{2s} and C_{2s} make up the impedance of the epidermal layer. The dermis, subcutaneous layer and deeper tissues are largely conductive and modelled by a lumped resistance R_{1s}. Considering the models it can be concluded that the double time-constant electrical model is applicable for both wet and dry electrodes [103, 104]. Baba and Burke [104, 105] studied both of these models and showed that the double time constant model exhibits more accurate results in terms of ECG measurements and frequency response effects.

2.3.7 Large Electric Transients

Large electric transient voltages can cause the amplifier to saturate and it requires a finite amount of time to bring the ECG amplifier back into its active region of operation, which depends on the overload recovery time of the system [8]. This recovery time period is governed by large time constants in the circuit structure of the amplifier. The effect of a large transient and the subsequent slow recovery of an amplifier is shown in Fig. 2.18.

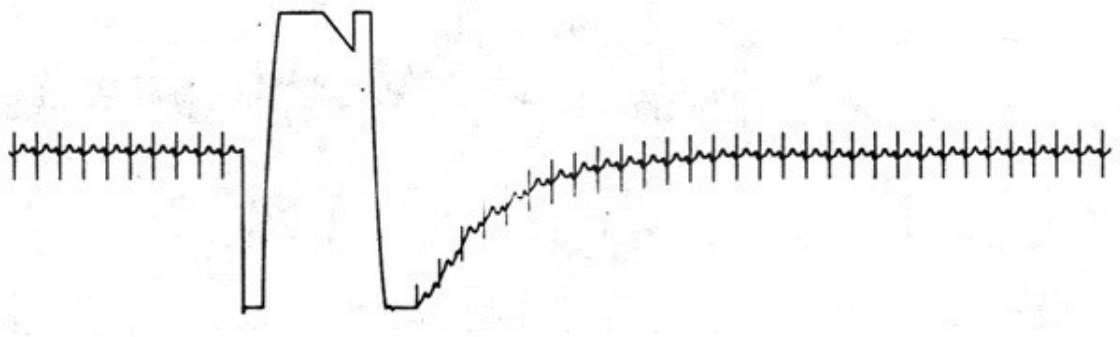

Figure 2.18: The effect of a large voltage transient on a recorded ECG signal [5]

Large time constants would also increase the power-up initialisation time of the amplifier. Electric transients can be produced by extensive motion artefacts generating potentials greater

than that of the ECG signal. Artefacts caused by static electric charge on a patient can be greatly reduced through the use of conductive clothing, shoes and flooring [5, 8].

2.3.8 Patient Safety

The bio-potential amplifier must also provide protection to patients from electrical shocks. Defective input stages of the pre-amplifier can expose patients to unwanted levels of current. Therefore, current limiting components are normally connected between the recording electrodes and the amplifier to limit the current flowing into the patients body. To maintain the safety of an electrocardiograph during its operational life, a number of stipulations are made with regard to this current. The permitted levels of current through a patient's body are shown in Table 2.1 . The IEC 60601-1 specifies that the maximum leakage current that can flow through patient-connected leads under normal conditions is 10 μA rms from dc to 1 kHz [22, 83, 106]. Under single-fault conditions, the maximum current allowed is 50μA rms over the same frequency range. However, the more relaxed limit under single-fault conditions is not supported by the AHA which recommends that the "ECG apparatus shall be designed so that no more than 10μA rms, from direct current to the tenth harmonic of power line frequency, shall flow through any patient-connected lead under either normal or single-fault conditions" [107]. The presence of dc blocking capacitors in series with the sensing electrodes prevents continuous dc current from flowing through the patient's body. In addition, current-limiting resistor, can be included so that no more than 10μA rms, or 28μA pp, occurs in a worst-case fault scenario.

Table 2.1: Safe limits of current through a patient's body

Current Flow Condition	Ambulatory & Non Ambulatory ECG	
	AHA	ANSI & IEC
Max. current under normal condition	10μA rms	10μA rms
Max. current through a single-fault condition	10μA rms	50μA rms

2.3.9 ECG Input Signal Dynamic Range

The ECG pre-amplifier can overload when the differential or the common-mode input signal increases beyond a certain level. Conversely, with a decrease in the input signal level, the output voltage can be predominantly contaminated with noise [4]. Therefore, a prior knowledge of the range of the ECG input dynamic signal is crucial for the appropriate design of the amplification stages of an electrocardiograph. The differential input signal range, its dc offset voltage level and the maximum slew rate specifications as outlined in the performance standards are summarised in Table 2.2.

Table 2.2: Input Dynamic Voltage Range and Offset Voltage Requirements

	Ambulatory ECG	Non-ambulatory ECG
	ANSI & IEC	ANSI & IEC
Input Range	$\pm$3 mV	$\pm$5 mV
Min. Feature size	50 μV p-p @ 10 Hz	NA
Slew Rate	125 mV/s	315 mV/s
Dc Offset Voltage	$\pm$300 mV	$\pm$300 mV

For non-ambulatory clinical monitoring of the human electrocardiogram, the ECG pre-amplifier in the presence of dc offset voltage of $\pm$300mV must be capable of recording differential input signal levels of $\pm$5mV, varying at a maximum rate of 320mV/s. The ECG pre-amplifier for ambulatory monitoring of the electrocardiogram, must be capable of recording differential input signal levels of $\pm$3mV, varying at a maximum rate of 125mV/s. A minimum feature size of 50μV p-p at 10 Hz is required in ambulatory electrocardiography to ensure that low amplitude P waves are faithfully preserved. However, the recent revision of standards for non-ambulatory ECG monitoring do not include this requirement [3, 22].

The voltage gain in the required frequency bandwidth is between 40dB and 46dB if the pre-amplifier is to provide a 1V p-p output signal to subsequent amplifier stages. The slew rate performance of operational amplifiers must also be ensured to cater for the maximum input rate of variation.

2.4 Dry electrode ECG amplifier design

Most of the research on dry electrodes has centered on the design and development of the electrode itself. Only a few research groups in recent years have contributed to the development of amplifier recording systems using dry electrodes. These groups have worked on problems associated with dry ECG recording, such as the amplifier CMRR [108–110], input-referred noise [8, 20, 99],input impedance [8, 15, 20], parasitic capacitance [111], dc offset voltage [112] and others [113, 114]. The bio-amplifier requirements in obtaining a diagnostic signal quality using dry electrodes are much more stringent than in the case of conventional conductive gelled electrodes.

2.4.1 System Interference

One of the major hindrances in recording a diagnostic quality ECG signal is the presence of interference contaminating the wanted ECG signal. This is generated within the recording system and prevents the observation of detail in small signals. Therefore, it is of the utmost importance that biopotential amplifiers be insensitive to interference and reject the unwanted external voltages which appear simultaneously at both inputs. However, this ability to supress interference is hindered by the finite value of common-mode impedance seen at the amplifier's input and imbalance in the electrode source impedances, allowing the conversion of common mode input signals into differential signals [8, 20]. The CMRR requirements of the performance standards are summarised in Table 2.3.

The IEC 60601 electrode model is that of a 51kΩ resistor with a 47nF capacitor in parallel. For this model, it is also stated that the noise should not exceed 30μV ptp referred to the amplifier input. The skin-electrode interface is responsible for much of the noise produced by dry electrode bioelectric amplifiers [115, 116]. The figures presented in Table 2.3 do not consider the additional noise generated by dry electrodes. The noise generated by the electrodes is investigated in much more in detail in Chapter 3.

Pallas Areny and Webster [31] recommended avoiding the use of preamplified electrodes due

Table 2.3: System Interference Requirements

	Ambulatory ECG	Non-ambulatory ECG	
	ANSI & IEC	ANSI	IEC
Max. noise (input refereed)	50μV ptp	30μV ptp	30μV ptp
Min. CMRR (mains frequency)	60 dB	95 dB	89 dB

to component tolerance mismatch leading to reduced CMRR. Pallas Areny and Fernandez [117] further used active electrodes in electrocardiography to reduce noise and common mode interference by about 20dB. Degen and JÄckel [118] later proposed adapting the gain of the difference amplifier to cancel the effects of resistor tolerances and therefore maximize the CMRR of the total system. The gain of the difference amplifier was controlled using an optimal value for a variable resistor.

A high degree of source impedance mismatch can have a pronounced effect on the CMRR. Degen and JÄckel [119] proposed a new method to continuously monitor skin-electrode impedance without reducing the CMRR of the amplifier. Continuous real-time monitoring of the skin-electrode impedance mismatch can be used to provide user feedback on pairing of electrodes. This impedance mismatch can also be further used as an error signal for an adaptive filter to reduce motion artefacts [120]. Spinelli et.al. [121] used a simple circuit to establish the skin-electrode impedance mismatch at power line frequency.

Richard and Chan [122] have used a two electrode technique to monitor the heart rate and the ECG using textile electrodes in a wearable garment. Reducing the number of electrodes minimises electrode costs and also improves patient safety by removing the patient ground electrode. However, the noise performance of the two electrode system using dry electrodes was not assessed by any of these authors. Spinelli et. al. [30] used a similar technique to boost the CMRR above 100dB at 50Hz with a 1.2MΩ source impedance imbalance. However, it is well known that some dry electrodes exhibit very high impedance values and in turn can degrade the CMRR performance. The noise performance of their ECG bioamplifier was measured at 71μVptp. Ali and Rasoul in 2019 [123] proposed a wearable dry electrode bioamplifier using a two wire current modulated active electrode (CMAE). The CMAE is in

effect an operational transconductance amplifier, modulating the supply current with the input voltage signal through its two supply rails. An adaptive canceller is used to improve the CMRR to 120 dB. The total input referred noise was measured to be 3.9μVrms. The prototype is reported to operate with a current consumption of 60μA. The high power consumption of this prototype (0.2mW/channel) remains one of its main limitations.

2.4.2 Input Impedance Requirements

In order to preserve the morphology of the ECG signal, the common mode input impedance must be high enough to compensate for mismatches in the skin-electrode interface impedance over the desired signal bandwidth. The international standards reviewed so far recommend an input impedance at the front end of the amplifier of magnitude greater than 2.5MΩ for non-ambulatory ECG and 10MΩ for ambulatory ECG. A 6% signal attenuation is accepted for non-ambulatory monitoring while 20% is tolerated for ambulatory electrocardiography. This is summarised in Table 2.4.

Table 2.4: Input impedance requirements.

	Ambulatory ECG ANSI & IEC	Non-ambulatory ECG ANSI & IEC
max. attenuation @ 10 Hz	20%	6%
min. single-ended input impedance	10MΩ	2.5MΩ

Negative Impedance Converters (NICs) can be utilised in integrated designs, allowing for stable, tunable, negative capacitance generators to be built [124]. This small negative capacitance can be obtained using a feedback mechanism to neutralise positive input capacitance to preserve bandwidth and also eliminate any instability. However, this method is not feasible in discrete form due to the difficulty in generating reliable small values of negative capacitance. Y.M. Chi et. al [125] and Z. Zhou et. al [126] used bootstapping techniques in integrated form to reduce parasitic capacitance.

Power supply boostrapping has been used over the years to reduce input capacitance. Kootsey and Johnson [127] first proposed this technique using emitter follower buffers, opamps and

diodes to provide DC shifts. The idea was later on improved by Lányi et.al. [26] and Hribik et.al [128]. However, all of the circuits proposed require a separate regulated supply for the unity gain amplifier. Ultra high input impedance has also been achieved using input guarding [129], bootstrapping [27–29, 130] and neutralising [15, 131, 132] techniques. Capacitance neutralisation using discrete components has been successfully implemented by Chi et. al. [131] and Spinelli et. al. [132]. However, the circuits used require adjustment and are difficult to implement in discrete form. Spinelli in 2018 [30] further proposed a novel discrete two-wire active electrode that provides high input impedance using power supply bootstrapping. The implemented prototype reduced the input capacitance of the op-amp from 4pF to 71fF. However, no boosted impedance value is given, even though it claims to have boosted the input impedance within the 1kHz target bandwidth. The power consumption was measured at 25mW and is one of the main drawbacks of their proposed idea.

2.5 TCD Based Research & State of the Art

For more than two decades, the Bioinstrumentation & Measurement research group in the Department of Electronic & Electrical Engineering, Trinity College Dublin, Ireland has been designing and developing low-power, dry-electrode ECG recording amplifiers fulfilling IEC and other international standards pertaining to electrocardiography. The research group has stressed the importance of considering several factors that affect the quality of the recorded ECG signal. These parameters are: the skin-electrode-amplifier interface, amplifier frequency response, electrical interference, amplifier CMRR and the semiconductor noise generated in the amplifier [20, 24, 24, 25]. Burke in 1994 [24] designed the first micro-power instrumentation amplifier using three CMOS op-amps TLC27L4CN(Texas Instruments Inc.). Burke and Gleeson [20] later modified and extended the design using six MAX400 series (Maxim Inc.) op-amps. The prototype was reported to have a measured input impedance of 75MΩ, CMRR of 88dB (with right leg drive), input-referred noise voltage of 50μV peak-to-peak and a power consumption of 30μW. The preamplifier was then later improved by Burke and Assambo [100] to provide an input impedance of 280MΩ at 0.05 Hz, CMRR was above 80dB and

the power consumption decreased to 20μW. Later the common-mode input impedance was further boosted to 2GΩ, the CMRR was greater than 95dB at 50 Hz and power consumption increased to 45μW [25]. However, the input-referred noise was very high and was measured at 200μV ptp. Reducing the semiconductor noise generally requires the use of op-amps with higher supply current, and consequently higher power consumption.

Table 2.5: Commercially available ECG Front End Integrated Circuits

Key Features	**ADS129X**	**ADS119X**	**ADAS1000-1**	**AD8233**	**MAX30003**
Input Impedance	1GΩ	1GΩ	1GΩ	5GΩ	45GΩ
Input Capacitance	20pF	20pF	10pF	15pF	10pF
Input Noise ptp	4 μV	12 μV	16 μV	10 μV	4.6μV
Bias Current	200pA	200pA	1nA	50pA	1μA
CMRR	115dB	105dB	110dB	86dB	77dB
Power Consumption	0.75mW	0.55mW	11mW	50μA supply	85μW
Resolution	24 bits	16 bits	24 bits	N/A	18 bits

The performance specifications of a number of commercially available bio-amplifier integrated circuits are listed in Table 2.5. It can be seen that most of these integrated devices have digital output, high power consumption, high bias current and in some cases relatively low amplifier input impedance. The amplifier input impedance required is governed by the electrical properties of the electrodes. The skin-electrode-amplifier interface is analysed in detail in Chapter 4 and it is shown that the amplifier must have a minimum 10GΩ input impedance for use with most dry electrodes. The AD8233 (Analog Devices Inc.) reports to have a CMRR of 86dB from DC to 60 Hz. The CMRR drops to 75dB in extending the bandwidth to 250 Hz. Considering the input impedance to be 10GΩ and the source impedance to be 1MΩ, the target is to boost the CMRR to above 80dB within the ECG bandwidth of 250 Hz. The voltage noise spectral density is also very high and is measured at 150 nV/$\sqrt{Hz}$. It is noteworthy that even though the MAX30003 (Maxim Semiconductor) in Table 2.5 looks promising, it also has some shortcomings. The measured CMRR value is reported as 77dB with the IEC electrode model (47nF||51kΩ). Similarly, ADAS1000-1 (Analog Devices Inc.) has reported the CMRR to be 110dB with 51kΩ source imbalance. The IEC model is primarily intended to apply

to wet electrodes for ECG measurement equipment. Dry electrodes exhibiting higher source impedance mismatch will have a pronounced detrimental effect on the CMRR attained. The resistor value reported in the IEC model is quite low and is not realistic. Therefore, electrical characterisation on a number of electrodes and subjects has been carried out and is reported in Chapter 3.

2.6 Practical Design & Target Specification

Table 2.6: Target performance specification for ECG Preamplifier

Input signal amplitude:	0.05 mV - 10 mV ptp
Slew rate:	320mVs^{-1}
dc offset voltage:	$\pm$300 mV
Output signal amplitude:	1 V ptp
System noise:	30 μV ptp max. (referred to input)
CMRR:	95 dB min. in 0.5 - 100 Hz bandwidth
Input impedance:	10GΩ in the 3-dB bandwidth
Frequency response:	3-dB bandwidth 0.05 - 250Hz
Differential gain:	40dB-46dB
Gain Variation:	$\pm$0.5 dB over the range 0.14 to 30 Hz
Phase Response:	$\leq$0.05 Hz single-pole high-pass filter
Impulse Undershoot:	0.1 mV max. undershoot after 3 mV-100ms impulse
Recovery Slope	0.3 mVs^{-1} max.
Power supply:	Supply voltage: 3V-5V
	Supply current: 150 μV max.
Power consumption:	$\leq$1mW

The skin-electrode-amplifier interface impedance remains one of the main limitations in recording clinical quality ECG signals using dry electrodes. This requires boosting the input impedance of the amplifier to mitigate against the effects of electrode impedance. A elasticated vest needs to be constructed using a highly elasticated material so that it will be body tight and correctly shaped to provide sufficient tension to hold the electrodes in place and give adequate skin contact. This will significantly reduce the effect of baseline wander and motion artefact. The

cables and the electrodes need to be properly shielded to reduce electrical interference. Most bio-amplifiers are connected to ground through the power line, or in some cases, through a separate local ground point in the room. Ground loops appear when two instruments have electrodes attached to the patient and are connected to ground using two or more different ground points [5]. A current can flow through the patient from the higher potential ground to the lower potential ground point. A large potential difference between two ground points can cause unsafe levels of current to flow through the patient. This poses serious safety concerns and in addition also elevates the patient's body potential above the lowest ground point. This results in common-mode voltages occurring on the electrocardiogram that, if it has poor CMRR, can increase the amount of interference present. In the case of the ambulatory ECG recording the situation is further complicated by the absence of a true ground point.

New versions of the IEC standards for ambulatory and non-ambulatory electrocardiographic equipment are due very shortly. Drafts, made available in advance for public review do not, however, address issues specific to dry electrodes and minimum requirements for input impedance and rejection of common-mode signals are not expected to change. The author [86, 87] has already shown that the that the minimum 10MΩ amplifier input impedance recommended in IEC 60601 is insufficient for gelled or un-gelled electrodes which can only be accurately modelled by an appropriate two-time constant model. The standards-compliant equipment can still introduce distortion of over 100μV undershoot from the baseline of the pulse and of over 300μV/s recovery slope in response to a standard IEC 60601 test pulse as indicated in section 2.3.2. The IEC 60601 standard primarily deals with the performance of the recording amplifier but have neglected the effects of the skin-electrode interface impedance. Therefore, the current performance specification for the transient response of electrocardiographs is inadequate and needs to be revised to take account of the impedance of the skin-electrode impedance network in the relevant tests. It is important to establish a sound theoretical and practical foundation for design constraints which can be used to establish the input impedance required in the recording amplifier based on the electrical properties of the electrode, once these are known or can be measured. The effective input impedance of the amplifier must also be chosen such that the transient time-domain specifications of the IEC

60601 standard are fulfilled. The most stringent requirements must be used from among all the known standards in an effort to design a universal low power, dry-electrode ECG recording amplifier. The target specifications for the intended ECG preamplifier design undertaken by the author are summarised in Table 2.6.

The following chapters will present the underlying analytical work as well as the practical design and verification of a low-power amplifier intended to meet the requirements outlined above for un-gelled ECG recording.

3 Electrical Characterisation of Textile-Based Dry Electrodes

It is essential to model the electrical behaviour of ECG electrodes in order to design the input stage of the recording amplifier correctly. A number of conductive electrodes have been introduced commercially and these have mainly been of a conductive rubber or polymer type. Previous work has been carried out to characterise these electrodes [8, 13, 20, 104, 133]. Since the intention in this project is to mount the electrodes in an elasticated vest, textile-based electrodes will be used.

Studies have been reported on methods of determining the values of the equivalent electrical components of these models in both the frequency and the time domains [104, 134]. Efforts to determine the properties of un-gelled ECG electrodes have shown that the component values of skin-electrode-interface impedance models and the associated time-constants are too large to be measured accurately in the frequency domain [134]. Measurements made in the time domain on conductive rubber electrodes have yielded more reliable values of the model components [104, 135]. Another issue of concern is the magnitude of the active current used in measuring the electrical properties of electrodes which are used passively in recording the ECG. Currents ranging from 0.5 μA - 100 μA have been reported in the literature [136–139] with varying values of components obtained for electrodes of similar type depending on the current used for the measurement. The fear is that the magnitude of the current used has influenced the component values obtained.

This chapter reports the measurement of the electrical properties of four textile-based elec-

trodes and the extraction of the values of the electrical model components using a time-domain, current-source based method. These values are also compared with the equivalent values for a conductive rubber electrode and a standard self-adhesive electrode. A preliminary study was carried out to establish the effect of the active measurement current on the component values obtained for a number of electrodes. Once a suitable value of active current was established, this was then used to determine the component values for both single C-R and double C-R based models as shown in Figs. 3.1(a) and 3.1(b) respectively, for all of the electrodes. This chapter also reports the measurement of the noise voltages generated by the skin-electrode interface for four fabric based electrodes and their comparison with those of a conductive rubber electrode and a standard self-adhesive electrode. Evaluation of the coefficients of a spectral noise density model for these electrodes was undertaken.

3.1 Background

The electrical properties of the skin-electrode-amplifier interface as described in Chapter 2 can be represented using a simple single time-constant C-R model or a more accurate double-time C-R model. Polarization potentials are omitted from the models of Fig. 3.1 as these will not be measured in the tests carried out, and the electrodes will be ac coupled to the input of the amplifier in practice.

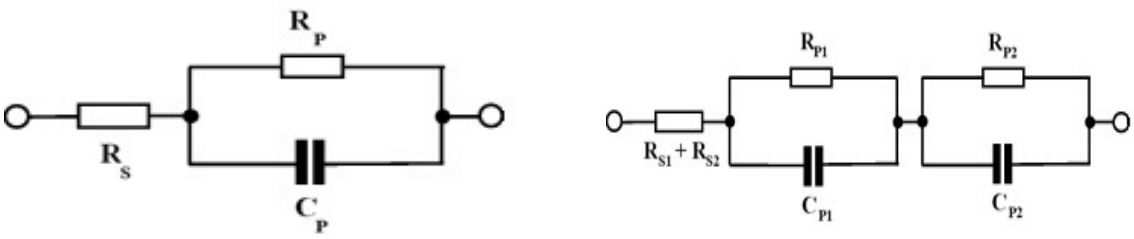

(a) Single C-R time-constant skin-electrode interface model

(b) Double C-R time-constant skin-electrode-interface model

Figure 3.1: Electrical models of the skin-electrode-amplifier interface [12]

Time domain measurements involve using a dc current source which can be switched on and off or modulated with a sinusoidal source as shown in the simplified block diagram of Fig. 3.2. This allows dc, ac or long duration pulse based measurements to be made through two identical

electrodes placed on the skin. The resulting voltage across the pair of electrodes is measured at the electrical connection to the upper electrode while the second electrode is connected to ground. The output voltage is then recorded for digitization and processing.

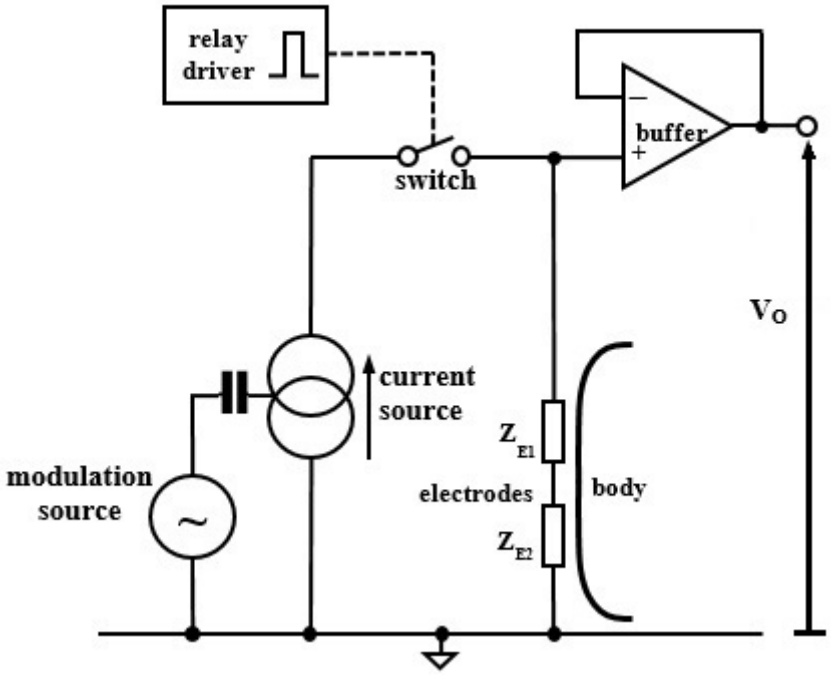

Figure 3.2: Principle of time-domain measurement

A more comprehensive circuit diagram of the current source and measurement system is shown in Fig. 3.3. The current is controlled by the op-amp A_1 (OPA192, Texas Instruments Inc.) and the p-type MOS transistor, T_1 (BSP220, Vishay Inc.). A reference voltage obtained at the wiper of potentiometer R_{V2} is used to vary the value of the dc current, with potentiometer R_{V1} providing fine tuning within the potential divider formed by R_1, R_{V1} and R_{V2}, operating from a 30V supply. A small negative supply voltage of -3V (not shown) is also used with the op-amps to ensure that their common mode input voltage range includes ground. The switch SW_1 and resistors R_5 and R_6 allows one of two ranges of current to be selected, namely, 0.1 – 10 μA or 1 – 100 μA.

The resistors R_3 and R_4 aid in controlling very low levels of current conduction in the MOS transistor that are close to its leakage current, which was measured at 40nA. The reference voltage can be modulated with a sinusoidal signal applied via the dc blocking capacitor C_1 and the protection resistor R_2. The switch SW_2 allows the load to be selected as either the fixed

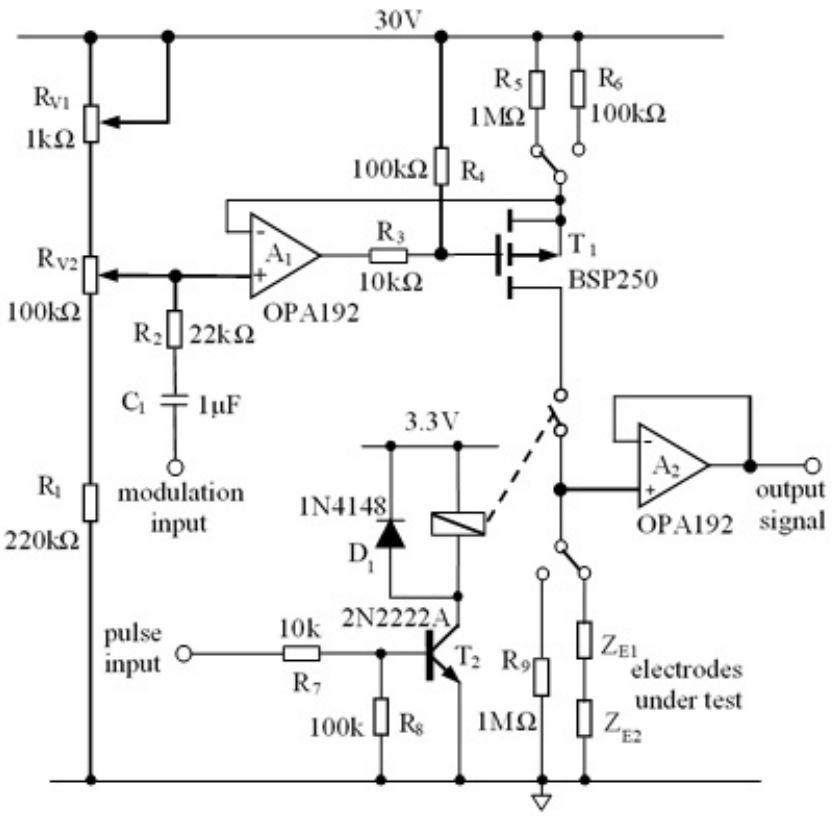

Figure 3.3: Schematic diagram of the current source.

resistor R_9 of 1 MΩ, which is used to set up the dc current accurately, or the impedance of the electrodes under test. The output voltage developed across the load impedance is measured by the buffer op-amp A_2 which provides a very high input impedance of $\geq 10^{12}\Omega$ and a low output impedance to feed monitoring equipment. A relay, R_{L1} (CRR03, Meder Ltd.) is used to allow the load to be connected or disconnected from the current source so that the fall phase of measurement depends only on charge stored in the electrode capacitance and not on any leakage current flowing in the transistor. This relay is miniature and operates from a 3 V supply with negligible contact bounce. The relay is driven by a simple buffer circuit consisting of the bipolar transistor T_2 (2N2222A, NTE Electronics Inc.), resistors R_7, R_8 and diode D_1 (1N4148, Vishay Inc.) which accepts a TTL level input pulse to activate the relay.

3.2 Methodology

3.2.1 Electrode Details and Ethical Issues

The skin-electrode-interface impedance values vary from individual to individual. For each individual, the measured impedance also varies depending on the electrode type, placement location, and dimensions of the electrode used in the measurement. Measurements were carried out on four conductive textile/fabric electrodes, one conductive rubber electrode and one adhesive pre-gelled electrode. Details of the model, construction and dimensions of the electrodes examined are presented in Table 3.1. Measurements were undertaken on 20 volunteering subjects aged between 22 and 64 years. There were two male and two female volunteers in each of five national/ethnic groups namely: European (Irish), Chinese, Indian, African and Latin American. These groups covered the five internationally recognized skin types classified according to melanin content [140]. The nature and procedures of the measurements were explained to each subject in detail verbally, as well as providing them with the same information in a pamphlet and each subject was asked to sign a consent form. The study was approved in advance by the appropriate ethics committee in Trinity College Dublin and ensured to be fully compliant with all regulations governing procedures involving human subjects as well as with current data protection and GDPR legislation.

3.2.2 Measurement Procedure

The electrical measurements were conducted using a current-based time-domain approach. Two identical electrodes were placed together at one of two locations on the subject's body. One site was the lower abdomen and the second was the forearm of the subject. The skin was not prepared in any manner so that there was no cleansing, abrasion or hair removal. The electrodes were placed 3 cm apart at the measurement site. A flexible cotton bandage with an elastic clip fastener was wrapped around the electrodes and limb or torso to hold the electrodes in place at the site. A flexible cotton bandage was wrapped around the electrodes and the limb or torso to and hold the electrodes in place and secured with elastic clip fasteners. The

Table 3.1: Physical Details of Electrodes and Supplier

Elec. No. & Model	Material Type and Construction	Dimensions (cm)	Manufacturer/Supplier
1. Red Dot 50-2237	Self-adhesive, solid gel center (17mm)	4 diam.	3M Health Care Ltd., Ontario, Canada.
2. Self constructed	Silver woven fabric on 1.5mm polyester fibre cloth backed with 1.2mm polyester	5 x 5	Robot Shop, Hethersett, Norfolk, UK.
3. Round conductive electrode 50	Silver fibre fabric with sponge backing	5 diam.	Current Pleasures Inc., California, USA
4. YD-C106	Silver fibre fabric with sponge backing	3 diam.	YD Strong Technology, Shenzhen, China.
5. CGP83294	Silver woven fabric with thick sponge backing and outer cotton fabric.	2.5 x 6.5	Medi-Stim Inc., Minnesota, USA
6. WA45	Conductive silicone rubber	4.5 x 4.5	Wandy Rubber Industrial Co. Ltd., Taipei, Taiwan.

bandage was wrapped to fit snugly but without significant stretching. It proved impossible to measure the degree of stretching in the bandage but every effort was made to ensure consistent tension in the elastic fasteners. This ensured that the electrodes had the same degree of contact against the skin as would be the case when mounted in an elasticated vest. The electrodes were left to stabilize for 2 or 3 minutes during which time the subject sat comfortably in a chair while resting the forearm on a table. During the experiments, subjects were asked to sit as still as possible and to breathe normally to avoid movement artefact in the recorded signals. The fixed resistor, R_9, in Fig. 3 was used to set up the required level of dc current. The injected current was initially set to a fixed value and modulated to a depth of 50% of the dc value by a sinusoidal signal at a frequency of 10 kHz, obtained from a signal generator (Le Croy, Wave-Station 2012). At this high frequency the impedances of the parallel C-R networks in the electrical models are negligible and the output signal level is determined entirely by the value of the series resistance either R_S or $R_{S1} + R_{S2}$, depending on the model. This allowed the values of these components to be measured directly and recorded.

During time-domain tests the dc current was activated using the relay R_{L1} and allowed to flow through the pair of electrodes for a duration of 30 s. This period was chosen to be longer than any of the time constants of the electrodes, but short enough to prevent inaccuracy due to drift or temperature changes. Current was then deactivated by opening the relay contacts for a period of 30 s. Several cycles of this rise-and-fall application of current were allowed so that a single cycle having the lowest attainable degree of noise could be obtained at the output of op-amp A_2. A typical waveform of a recorded cycle of output voltage is shown in Fig. 3.4. A digital oscilloscope (Keysight, DSOX3024A) was used to digitalize and store the rise and the fall output voltage waveforms on a memory stick.

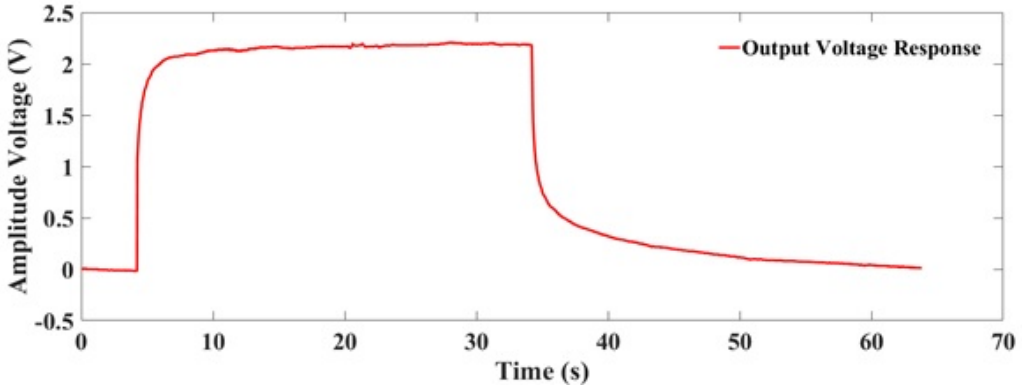

Figure 3.4: A typical cycle of recorded output voltage.

3.2.3 Single Time-Constant Model Characterisation

The input test signal can be considered effectively as a single current pulse characterised as two steps of magnitude I_{REF} and opposite sense separated by a duration T. This can be described in the time domain as:

$$i(t) = I_{REF}\left[u\left(t\right) - u\left(t - T\right)\right] \tag{3.2.1}$$

The skin-electrode-interface impedance measurement is carried out using two identical electrodes, Z_{E1} and Z_{E2}, placed on the skin as illustrated in Fig. 3.2 and taken to have the same impedance. The impedance of the pair of electrodes, when each is modeled as a single

time-constant C-R network, can be described in the Laplace domain as:

$$Z_E = 2\left[R_s + \frac{R_p}{1 + sR_pC_p}\right] \tag{3.2.2}$$

where, $Z_E(s)$=$Z_{E1}(s)$+$Z_{E2}(s)$.

The transient voltage at the output of the buffer amplifier A_2 in response to a current pulse characterised by (3.2.1) is given in the time domain as:

$$V_E = I_{REF}\left[2R_s + 2R_p\left(1 - e^{-\frac{t}{C_PR_P}}\right)\right]u(t) - I_{REF}\left[2R_s + 2R_p\left(1 - e^{-\frac{(t-T)}{C_PR_P}}\right)\right]u(t-T) \tag{3.2.3}$$

Following activation of the relay, during the rise phase the output voltage of the buffer amplifier is described as:

$$V_E = 2I_{REF}\left[R_s + R_p\left(1 - e^{-\frac{t}{C_PR_P}}\right)\right] \tag{3.2.4}$$

At the end of the duration T of the pulse, just prior to the falling edge, the output voltage of the amplifier A_2 is described as:

$$V_E = 2I_{REF}\left[R_s + R_p\left(1 - e^{-\frac{T}{C_PR_P}}\right)\right] \tag{3.2.5}$$

For a sufficiently long pulse duration $T >> C_pR_p$ the final value of the rise phase of this voltage is given as:

$$V_E = 2I_{REF}\left(R_s + R_p\right)] \tag{3.2.6}$$

Immediately following the trailing edge of the pulse at t = T on deactivation of the relay, the output voltage is given as:

$$V_E = 2I_{REF}R_p\left(1 - e^{-\frac{T}{C_PR_P}}\right) \tag{3.2.7}$$

In the case of a pulse of long duration so that $T >> C_pR_p$ this can be taken and $R_p >> R_s$:

$$V_E = 2I_{REF}R_p \tag{3.2.8}$$

The output voltage during its fall phase, once the relay has been deactivated, can be then be closely approximated in the time domain as:

$$V_E(t) = 2I_{REF}R_p e^{-\frac{(t-T)}{C_pR_p}} \tag{3.2.9}$$

This voltage will eventually return to the zero value base-line.

The Curve Fitting Tool in MATLAB was used to fit curves separately to the rise and fall phases of the most noise-free cycle of the voltage waveform recorded at the output of the buffer amplifier A_2. Initially, a fixed dc value of current I_{REF} allowed the value of R_S+R_P to be determined and the ac measurement made at 10 kHz provided the value of R_S. These values were substituted as initial parameters into the curve fitting procedure in MATLAB. The curves described by (3.2.4) and (3.2.9) were then fitted to the rise and fall phases of the voltage waveforms, respectively. This allowed the time constant $\tau = C_pR_p$ and the individual values of R_P and C_P to be extracted separately for the rise and fall phases. The accuracy of the curve fitting was optimized by running a range of error determining constraint algorithms available in the toolbox such as Trust Region or Levenberg-Marquardt and selecting the one which gave the minimum least mean square error in the curve fit.

3.2.4 Double Time-Constant Model Characterisation

The skin-electrode impedance when modelled as a double time-constant network can be expressed in the Laplace domain as:

$$Z_E = 2\left[R_{S1} + \frac{R_{P1}}{1 + sC_{P1}R_{P1}} + R_{S2} + \frac{R_{P2}}{1 + sC_{P2}R_{P2}}\right] \tag{3.2.10}$$

The resulting voltage at the output of the buffer amplifier A_2 in response to the input current described by (3.2.10) is given in the time domain as:

$$\begin{aligned} V_E = 2I_{REF}\left[R_S + R_{P1}\left(1 - e^{-\frac{t}{C_{P1}R_{P1}}}\right) + R_{P2}\left(1 - e^{-\frac{t}{C_{P2}R_{P2}}}\right)\right]u(t) \\ -2I_{REF}\left[R_S + R_{P1}\left(1 - e^{-\frac{(t-T)}{C_{P1}R_{P1}}}\right) + R_{P2}\left(1 - e^{-\frac{(t-T)}{C_{P2}R_{P2}}}\right)\right]u(t-T) \end{aligned} \tag{3.2.11}$$

where, the series resistance, $R_S = R_{S1} + R_{S2}$. The output voltage during the rise phase of the current is given in the time domain as:

$$V_E(t) = 2I_{REF}\left[R_S + R_{P1}\left(1 - e^{-\frac{t}{C_{P1}R_{P1}}}\right) + R_{P2}\left(1 - e^{-\frac{t}{C_{P2}R_{P2}}}\right)\right] \tag{3.2.12}$$

If the duration of the pulse is sufficiently long so that, $T >> C_{p1}R_{p1}$ and $C_{p2}R_{p2}$, then the exponential terms at t = T in (3.2.12) become negligible and the final value of the rise phase voltage is then:

$$V_E(t) = 2I_{REF}\left[(R_S + R_{P1} + R_{P2})\right] \tag{3.2.13}$$

The output voltage immediately following the end of the pulse at t=T, when the input current is abruptly deactivated is described in the time domain as:

$$V_E(t) = 2I_{REF}\left[R_{P1}\left(1 - e^{-\frac{T}{C_{P1}R_{P1}}}\right) + R_{P2}\left(1 - e^{-\frac{T}{C_{P2}R_{P2}}}\right)\right] \tag{3.2.14}$$

The output voltage in (3.2.14) with $T >> C_{p1}R_{p1}$, $C_{p2}R_{p2}$ can be rewritten as:

$$V_E = 2I_{REF}(R_{P1} + R_{P2}) \tag{3.2.15}$$

The output voltage given by (3.2.14) has an initial negative step of -$2I_{REF}(R_{S1}+R_{S2})$ from the end value of the rise phase given by (3.2.13). This is the essential point of the start of the fall phase. However, results revealed that the magnitude of $R_{P1}+R_{P2} >> R_{S1}+R_{S2}$ by some orders of magnitude and the resulting negative step was insignificant. Therefore, the final value of the rise phase given by (3.2.13) could be taken as the initial value of the fall

phase. Therefore, the output voltage during the fall phase can be closely approximated in the time domain as:

$$V_E(t) = 2I_{REF}\left(R_{P1}e^{-\frac{(t-T)}{C_{P1}R_{P1}}} + R_{P2}{}^{-\frac{(t-T)}{C_{P2}R_{P2}}}\right) \tag{3.2.16}$$

The same curve fitting procedure was used in MATLAB to fit the double time-constant equations of (3.2.12) and (3.2.16) to the cleanest cycle of recorded data for the rise and fall phases of the voltage waveform, respectively. Steady state dc measurement with a fixed current allowed the value of $R_{S1}+R_{S2}+R_{P1}+R_{P2}$ to be determined and the ac measurements at 10 kHz provided the value of $R_{S1}+R_{S2}$. These values were entered into the curve fitting procedure in MATLAB as initial parameters. Values for the components C_{P1}, R_{P1}, C_{P2}, and R_{P2}, as well as the time-constants $\tau_1 = C_{P1}R_{P1}$ and $\tau_2 = C_{P2}R_{P2}$ were extracted separately for the rise and fall phases from the curve fitting procedure.

3.2.5 Measurement Current

The first issue examined was the magnitude of the current, I_{REF} that should be used in measuring the electrical properties of the electrodes. The electrodes of interest were intended for use in an ECG recording environment, where the only current flowing through them in practice is that induced by the ECG signal itself. Consequently, it is of the utmost importance that electrical properties measured are not influenced by the current used to measure them, since the values obtained determine the design requirements of the associated recording amplifier [82, 86, 87, 101].

The effect of the current level on the value of overall skin-electrode interface model components was measured on four subjects and four different electrodes (nos. 1, 4, 5, 6 in Table 3.1). The current I_{REF} was set at values of 0.3, 0.5, 1, 2, 5, 10, and 20μA. It proved impossible to control the current reliably at values below 0.3 μA because of leakage currents in the BSP220 transistor. The current was activated for 30 s and deactivated for 30 s for several cycles as outlined in Section 3.2.2 above and the output voltage of the buffer amplifier A_2 was recorded for each value of current. The component values R_P and C_P were then extracted using the

curve fitting procedure for the single time-constant model outlined in Section 3.2.3.

The values of the components obtained are shown plotted in Fig. 3.5 for the conductive fabric electrode no. 5 of Table 3.1, placed on the arm of the four subjects. It can clearly be seen that the values of the model components R_P and C_P vary significantly across the range of current. In all cases the variation is greater than 2:1 across the range rising to 11:1 in the highest case. The resistance R_P ranges from 320 kΩ to 11 MΩ while the capacitance ranges from 5.6 nF to 716 nF. The curves of Fig. 3.5 show without doubt that the level of current used has a major influence of the values of the components measured. Much higher values of both components are measured at very low levels of current and the trend suggests that some values would be higher at currents lower than the minimum of 0.3 μA used.

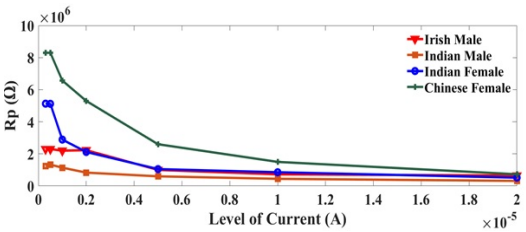

(a) R_P Measured in fall phase for electrode no. 5 placed on the arm

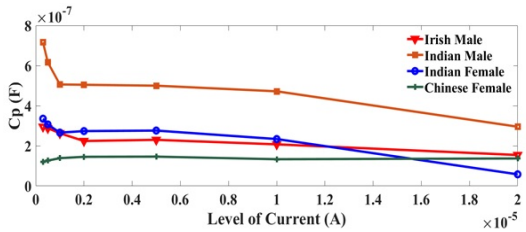

(b) C_P Measured in fall phase for electrode no.5 placed on the arm

Figure 3.5: Variation in single time-constant model components vs. current, I_{REF}

The trend is the same for both R_P and C_P so that there is a pronounced effect on the values of the time-constant $C_P R_P$ which ranged from 4 ms to 1.7 s. The ranges of the extracted component values, as well as the range the time-constant τ for paired values of C_P and R_P are given in Table 3.2. The trend of the curves of Fig. 3.5 was broadly repeated for all electrodes in all subjects studied for both arm and abdomen locations and both rise and fall phases of current. It is therefore clearly evident that if an accurate model of an in–vivo electrode is to be established, these properties must be measured using a current of less 1μA. This throws doubt on the values of components of electrode models cited in many studies reported in the literature [104, 136–139, 141]. The authors consequently decided to use a current of 0.5 μA so that accurate control of the current as well as a reasonable signal-to-noise ratio could be maintained, while at the same time having the lowest possible current.

Table 3.2: Range of variation of electrode properties with varying current levels (R_P MΩ, C_P nF, τ s)

Elec. No.	Parameters	Subject 1				Subject 2				Subject 3				Subject 4			
		Abdomen		Arm		Abdomen		Arm		Abdomen		Arm		Abdomen		Arm	
		Rise	Fall	Rise	Fall	Rise	Fall	Rise	Fall	Rise	Fall	Rise	Fall	Rise	Fall	Rise	Fall
1	R_{Pmin}	0.07	0.07	0.07	0.07	0.09	0.09	0.15	0.15	0.13	0.13	0.14	0.14	0.08	0.09	0.06	0.06
	R_{Pmax}	0.12	0.12	0.1	0.1	1.29	1.29	2.3	2.3	0.36	0.36	0.6	0.6	0.22	0.22	0.63	0.63
	C_{Pmin}	26.5	468	171	268	76	113	65	163	205	231	72.5	175	145	518	352	311
	C_{Pmax}	713	2380	2020	606	237	338	201	406	444	382	1910	365	2630	850	1130	1510
	τ_{min}	0.01	0.04	0.01	0.01	0.01	0.03	0.03	0.04	0.04	0.03	0.01	0.04	0.03	0.04	0.07	0.11
	τ_{max}	0.02	0.28	0.21	0.03	0.27	0.28	0.42	0.42	0.15	0.14	0.16	0.2	0.07	0.19	0.22	0.33
4	R_{Pmin}	0.73	0.73	0.58	0.58	0.4	0.4	0.24	0.24	0.72	0.72	0.57	0.57	0.15	0.15	0.44	0.44
	R_{Pmax}	11	11	7.73	7.73	1.2	1.2	1.85	1.85	11.3	11.3	7.3	7.3	0.6	0.6	2.34	2.34
	C_{Pmin}	9.4	262	32.6	94	131	68.6	92.3	249	10.5	139	38.7	79	403	615	51	87.3
	C_{Pmax}	36.4	880	120	179	1020	961	540	467	44.8	334	87	239	730	904	269	299
	τ_{min}	0.03	0.06	0.02	0.07	0.06	0.03	0.04	0.06	0.07	0.01	0.05	0.06	0.01	0.12	0.04	0.04
	τ_{max}	0.14	0.48	0.43	0.89	0.83	0.78	0.55	0.5	0.17	0.36	0.45	1.2	0.4	0.5	0.63	0.7
5	R_{Pmin}	0.73	0.73	0.65	0.65	0.73	0.73	0.32	0.32	0.72	0.72	0.52	0.53	0.7	0.8	0.73	0.73
	R_{Pmax}	10.6	10.6	2.3	2.3	5.62	5.62	1.25	1.25	13	13	5.13	5.13	6.8	6.8	8.3	8.3
	C_{Pmin}	5.6	14	40	154	198	57	140	295	20	103	42.5	58	15.2	103	16	121
	C_{Pmax}	32	90	410	295	96	165	700	716	100	332	102	335	138	164	72	146
	τ_{min}	0	0.07	0.02	0.11	0.14	0.12	0.05	0.09	0.07	0.24	0.04	0.03	0.01	0.1	0.6	0.1
	τ_{max}	0.34	0.47	0.7	0.68	0.54	0.61	0.83	0.89	0.33	1.38	0.87	1.7	0.93	1	0.01	1
6	R_{Pmin}	0.14	0.14	0.67	0.67	0.11	0.11	0.09	0.09	0.16	0.16	0.17	0.17	0.21	0.22	0.17	0.17
	R_{Pmax}	2	2	0.06	0.06	3	3	2.6	2.6	2.83	2.83	2.8	2.8	2.8	2.8	4.22	4.22
	C_{Pmin}	287	556	4880	25800	110	700	400	1180	124	840	170	968	195	615	103	528
	C_{Pmax}	730	2900	12800	14000	270	2000	80	3600	257	2720	511	2440	401	1890	214	664
	τ_{min}	0.04	0.08	0.33	1.3	0.03	0.1	0.03	0.28	0.03	0.2	0.04	0.17	0.06	0.13	0.03	0.12
	τ_{max}	1.49	5.9	8.9	5.6	0.32	5.9	0.2	2.9	0.64	7.7	0.5	3.7	0.7	2.48	0.43	2.21

3.3 Electrode Properties

The values of the components in the equivalent electrical models of all 6 electrodes were extracted from the measured voltage responses to activation and deactivation of the current, I_{REF}, via the relay, R_{L1}, in Fig. 3.3. The values of R_P and C_P obtained for the single time-constant model are shown in Fig. 3.6 for electrodes placed on subject's abdomen in (a) for the rise phase of the current when activated and in (b) for the fall phase of the current when deactivated. Values of R_P are given on the left-hand ordinate axis of all figures while values of C_P are given on the right-hand ordinate axis. Parameter values are shown for all subjects and all electrodes. Fig. 3.7 shows the same parameters for electrodes when placed on the subject's arm.

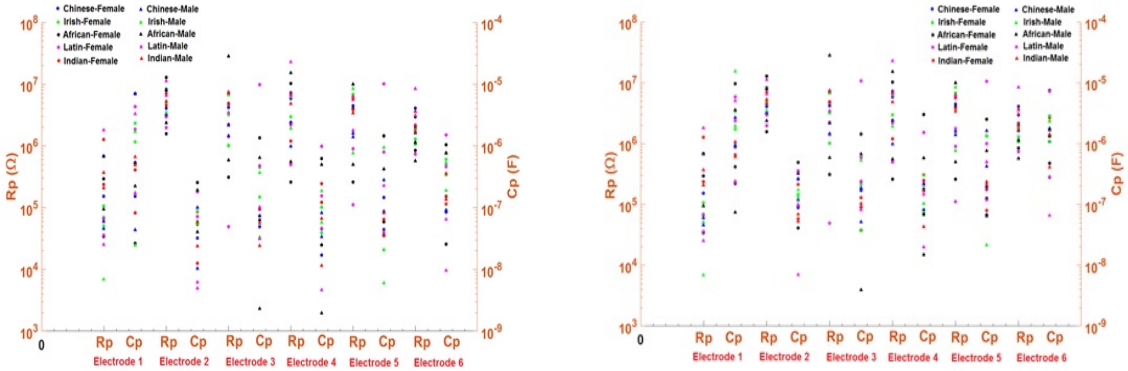

(a) Current rise phase

(b) Current fall phase

Figure 3.6: Parameter values for the single time-constant model with electrodes placed on the subject's abdomen.

The parameters R_{P1}, C_{P1}, R_{P2} and C_{P2} are shown in Fig. 3.8 and Fig. 3.9 for the corresponding conditions for a double time constant model of the electrodes. Table 3.3 presents the minimum and maximum values of the parameters obtained as well as the minimum and maximum values of the single time-constant $C_P R_P$ classified according to ethnicity and hence skin type. Table 3.4 presents the corresponding values of the parameters for the double time-constant model as well as the range of values for the time constants $\tau_1 = C_{P1}R_{P1}$ and $\tau_2 = C_{P2}R_{P2}$.

Table 3.3: Summary of single time C-R model component values across all electrodes

			Abdomen				Arm			
			Rise Phase		Fall Phase		Rise Phase		Fall Phase	
Ethnicity	Sex		R_P (MΩ)	C_P (nF)	R_P (MΩ)	C_P (nF)	R_P (MΩ)	C_P (nF)	R_P (MΩ)	C_P (nF)
Chinese	Male	Min	0.04	10	0.04	51	0.1	0.5	0.1	12
		Max	3.2	7000	3.2	2854	14	233	14	604
	Female	Min	0.15	17	0.15	67	0.1	12	0.1	60
		Max	8.3	541	8.3	1072	12	162	12	331
Irish	Male	Min	0.01	6	0.01	21	0.03	0.03	0.03	0.1
		Max	8.36	1687	8.36	15327	8460	6956	8460	8010
	Female	Min	0.01	21	0.01	74	0.1	18	0.1	46
		Max	6.7	2317	6.7	3411	7.7	2634	7.7	3571
African	Male	Min	0.1	2	0.1	4	0.4	3	0.4	13.5
		Max	28	777	28	3581	23	510	23	1117
	Female	Min	0.03	25	0.03	38	0.2	5	0.2	17
		Max	12.9	7000	12.9	9639	19	1334	20	1469
Latin American	Male	Min	1.8	5	1.8	7	0.05	13	0.05	1.8
		Max	23	3319	23	5037	13	3650	13	8983
	Female	Min	0.1	72	0.1	221	0.1	0.003	0.1	4.1
		Max	3	9980	3	10000	28	1000	28	2960
Indian	Male	Min	0.2	12	0.2	43	0.1	80	0.1	252
		Max	7.3	662	7.3	1420	5.3	643	5.3	2378
	Female	Min	0.2	13	0.2	58	0.1	19	0.1	77
		Max	7.9	409	7.9	2688	6	995	6	2978

Table 3.4: Summary of double time C-R model component values across all electrodes

Ethnicity	Sex		Rise Phase								Fall Phase							
			Abdomen				Arm				Abdomen				Arm			
			R_{P1} (MΩ)	C_{P1} (nF)	R_{P2} (MΩ)	C_{P2} (μF)	R_{P1} (MΩ)	C_{P1} (nF)	R_{P2} (MΩ)	C_{P2} (μF)	R_{P1} (MΩ)	C_{P1} (nF)	R_{P2} (MΩ)	C_{P2} (μF)	R_{P1} (MΩ)	C_{P1} (nF)	R_{P2} (MΩ)	C_{P2} (μF)
Chinese	M	Min	0.02	1.4	0.03	0.02	0.04	57	1E-3	4E-3	0.06	0.4	0.03	2E-4	0.1	9	0.01	0.03
		Max	2.9	2E4	1.9	169	2.8	3E4	1.7	872	11	370	4	38	12	3E3	9	8
	F	Min	0.1	0.17	0.01	0.01	0.05	40	0.1	0.01	0.06	0.33	0.01	9E-4	0.05	5.8	0.05	0.01
		Max	4.4	4.1E3	7.2	529	5.7	3E4	6.3	5.7	10	933	8	12	7	1E4	10	297
Irish	M	Min	7E4	3E3	0.01	3E-4	7E-4	53	2E-3	0.03	0.02	0.04	0.01	0.01	0.01	1.9	0.04	4E-3
		Max	6.6	17	4.3	17	6.7	1E5	5.2	235	20	6E5	4.6	12	6.4	1E4	4.3	14
	F	Min	0.03	0.01	6.7	0.05	5E-4	45	0.06	1.4	0.01	8	0.01	0.02	0.01	19	0.04	0.04
		Max	4.5	9E3	0.01	1E3	5.7	2E5	1.1	84	6.3	2E5	3.1	5.4	4.33	6E4	4.33	15
African	M	Min	0.1	1	0.01	0.01	0.1	1.3	4E-3	1E3	0.04	0.8	0.4	9E-5	0.01	8	0.4	5E-3
		Max	21	722	7.7	435	24	5E3	5.4	0.03	12	6E4	12	4.6	19	2E4	17	600
	F	Min	0.01	18	0.01	0.01	0.02	15	0.01	356	0.1	2.8	0.1	0.1	0.02	0.01	0.06	9E4
		Max	9.7	3E5	3.2	145	10.3	2E4	2.7	0.4	12	1E4	7	12	18	152	2.5	200
Lat. Amer.	M	Min	0.01	1.7	0.01	2E-4	0.01	4	0.01	0.01	6E-4	0.33	0.05	1E-4	0.01	6E4	0.04	0.04
		Max	19	4E3	5.1	17	19	5E3	5.3	28	8.2	2E5	7.5	3.4	19	19	7.7	15
	F	Min	1.6	125	0.01	0.04	0.01	181	0.02	0.1	0.01	0.7	0.03	3E-5	0.01	1.9	0.02	4E-3
		Max	5E-2	3E5	2.1	280	1.8	6E5	2.1	326	28	8E3	22	32	25	1.4E4	25	14
Indian	M	Min	0.1	15.3	0.1	3E-4	0.05	29	0.01	0.03	0.1	0.8	0.02	0.1	0.05	39	0.07	0.1
		Max	6.3	2E3	4.4	6.6	6.1	2E4	4.3	294	3.8	812	2.7	229	4	1E3	3.6	57
	F	Min	0.2	0.1	0.01	0.05	0.2	31	0.1	0.03	0.1	1.3	0.01	4E-3	0.1	125	0.03	0.15
		Max	5.5	2E4	3.6	316	5	5E4	7	17	3.9	665	4.2	405	5	1E4	1.5	19

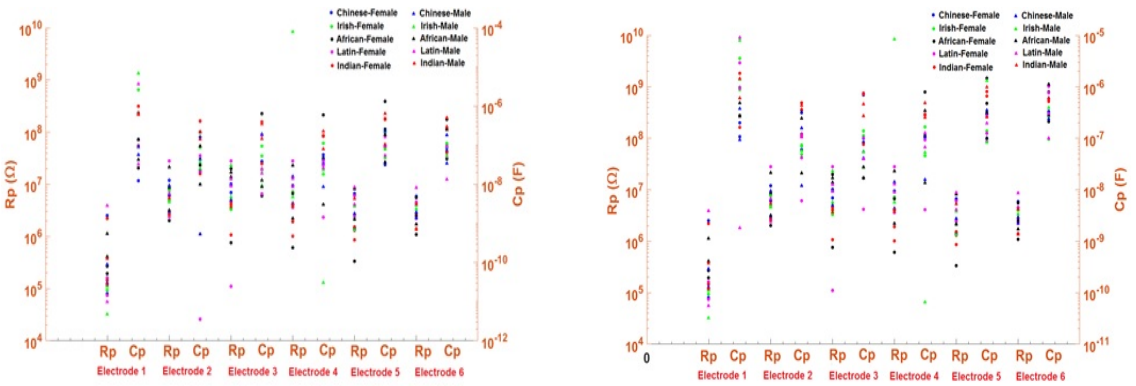

(a) Current rise phase

(b) Current fall phase

Figure 3.7: Parameter values for the single time-constant model with electrodes placed on the subject's arm.

3.4 Discussion

A limited number of 20 subjects with only 4 in each category of melanin skin type, 2 male and 2 female, were involved in this study and only 4 conductive fabric based electrodes were examined. It must therefore be accepted that no statistically reliable inferences can be drawn from the results. Nevertheless, given that there are 2 male and 2 female subjects in each ethnic skin type group likely differences can be recognized between ethnic groups or skin types and sexes. Examining Figs. 3.6 – 3.9 it can be seen that the trends in the variation in parameter values across the range of electrodes is consistent for both single and double time-constant models and for both abdomen and arm locations. There is slightly wider variation in the parameter values obtained for the rise phase compared with the fall phase of current, though this is more noticeable in the case of the double time-constant model. This is thought to be due to the fact that in the rise phase, current is actively injected through the tissue cell membranes while in the fall phase the charge present is passively returning to its norm. There are undoubtedly associated changes in the permeability of the cell membranes to ions present in the inter- and intra-cellular fluids that are different in each case giving different electrical behaviours. This is also reflected in the differences in time-constants for the rise and fall phases as evidenced in Tables 3.3 and 3.4.

A comparison of the results also reveals that the electrode with the highest contact area

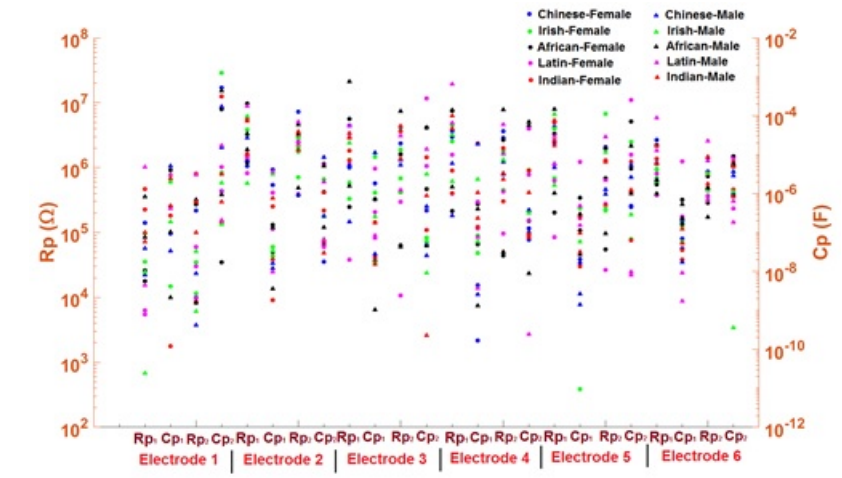

(a) Current rise phase

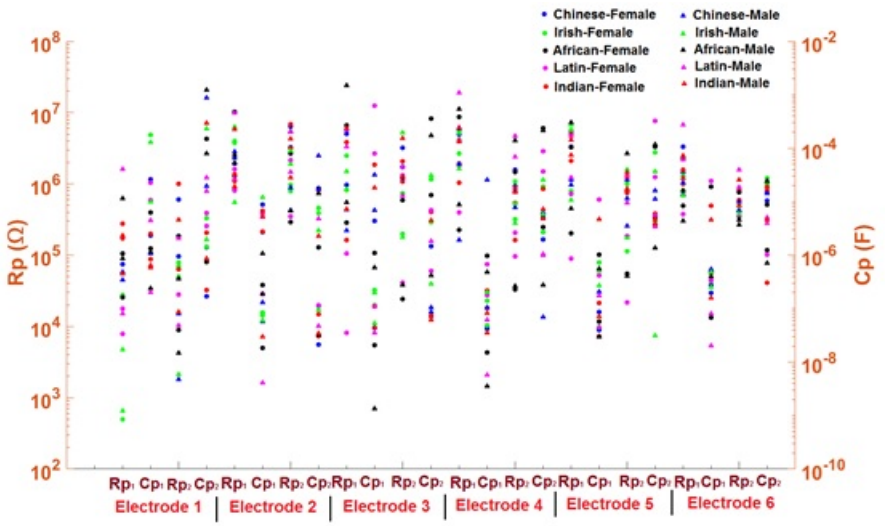

(b) Current fall phase

Figure 3.8: Parameter values for the single time-constant model with electrodes placed on the subject's abdomen.

results in the lowest interface impedance. This is true for all of the subjects whether the electrode was placed on the abdomen or the arm. This is not surprising as for a conductive material, the resistance is inversely proportional to the cross-sectional area and the capacitance is proportional to the effective contact area between the electrode and the skin. Electrode 2 having the largest area can be seen to exhibit the lowest values of resistance and highest values of capacitance, and consequently the lowest impedance.

Comparing ethnic groups, it can be seen that, broadly speaking, subjects with darker skin types having higher melanin content exhibit higher resistance and lower capacitance values. This appears consistent across African, Indian and Latin American subjects, while Irish and

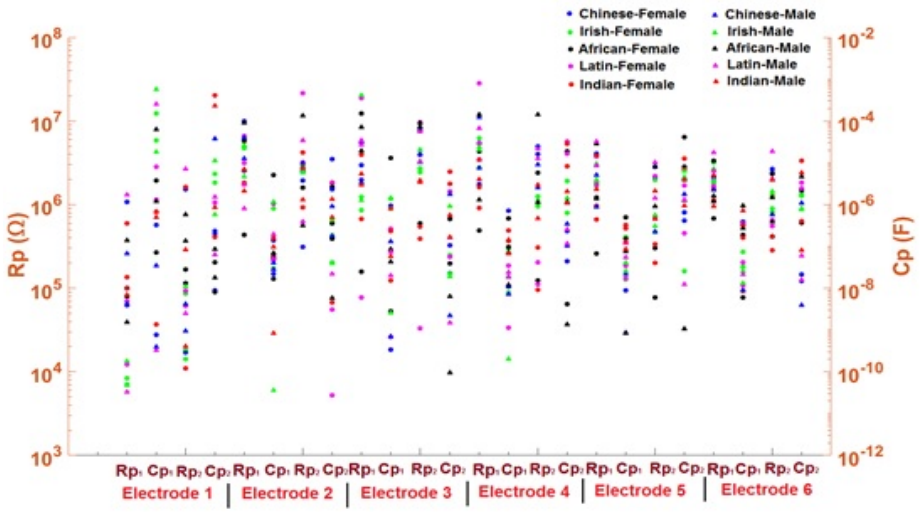

(a) Current rise phase

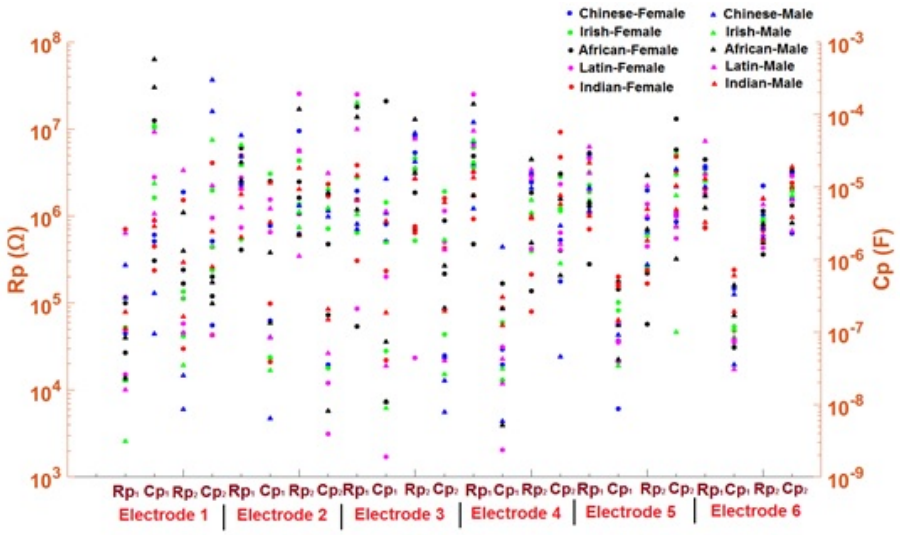

(b) Current fall phase

Figure 3.9: Parameter values for the single time-constant model with electrodes placed on the subject's arm.

Chinese subjects exhibit lower resistance and higher capacitance values, irrespective of electrode location on the body. It can also be seen that for similar measurement scenarios, female subjects often, but not always, exhibit higher values of resistance and lower values of capacitance than male subjects in the same ethnic group. In general, the same electrodes when located on the arm yield higher resistance and lower capacitance values than when placed on the abdomen. This is thought to be due to higher degree of toughness of the more exposed skin on the arm.

3.5 Noise Performance of Electrodes

The skin-electrode interface noise performance is a crucial factor in high resolution surface bio-potential measurements. Recorded ECG signals have very low amplitudes of 50 μV-10 mV in the bandwidth of 0.05-250 Hz and are highly susceptible to contamination from unwanted interference and noise [117, 142, 143]. Dry, un-gelled electrodes have consistently been reported in the literature to be noisier than the standard gelled, self-adhesive electrodes used in the hospital clinics [62, 144]. The origin of the noise in surface electrodes has been investigated over the years by several researchers [117, 145–149]. However, there is yet limited information available when it comes to the source of noise in dry electrodes and in particular textile-based electrodes.

3.5.1 Noise Measurement Circuit & Experimental Setup

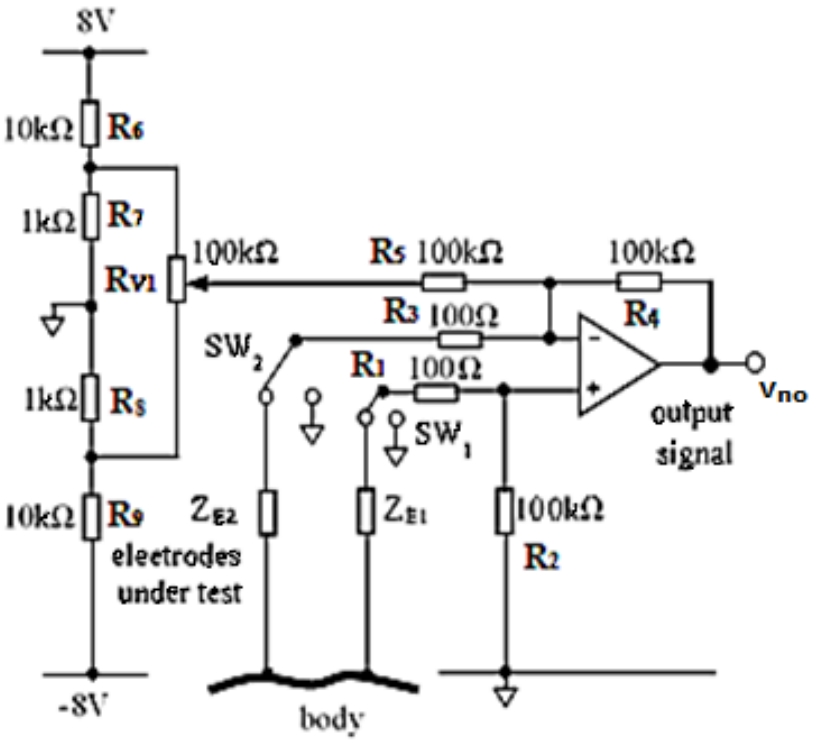

Figure 3.10: Schematic Diagram of Electrode Noise Measurement System.

A schematic diagram of the circuit used for noise measurement is shown in Fig. 3.10. A low-noise, battery-operated op-amp (LTC2058, Analog Devices Inc.) structure implementing

a differential gain of 1000 provides the output voltage noise V_{no}. The white voltage noise and current noise spectral densities for this op-amp are extremely low and are quoted by the manufacturer as 9nV/$\sqrt{Hz}$ and 1pA/$\sqrt{Hz}$ respectively. The op-amp exhibits practically no 1/f noise component and its input referred noise is considered purely white. A resistive potential divider arrangement allows cancellation of electrode polarisation potentials and amplifier offset voltages within the range +800 to -800 mV without recourse to ac coupling. A battery-operated, high-resolution digital oscilloscope (PicoScope 4262) was used in conjunction with a laptop computer to digitize the output noise voltage obtained from the amplifier. This instrument featured a slow recording time-base combined with high sampling rate and 16 bit resolution and internal noise of < 0.25 LSB which was not available in conventional laboratory digital oscilloscopes. The use of battery operated instrumentation inside a Faraday cage and deactivation of the mains power supply in the measurement environment ensured an extremely low level of 50 Hz pick-up without the need for grounding the subject through a third electrode. Two identical electrodes were placed at a 3cm separation on the subject's forearm without any manner of skin preparation. A flexible cotton bandage with an elastic clip fastener was wrapped snugly around the electrodes and arm to hold the electrodes in place, which were then left to stabilize for 5 minutes. During the measurements, subjects were asked to sit as still as possible to avoid movement artefact in the recorded signals. The output data was recorded for 100s at a sampling rate of 1Msample/s. Files were saved in .mat format for further processing in MATLAB (MathWorks 2019b).

3.5.2 Circuit Noise Analysis

The amplifier noise voltage was measured by grounding the 100Ω resistors using switches SW_1 and SW_2 shown in Fig. 3.10. The effective resistance seen at each input terminal of the op-amp is therefore 100Ω. The rms thermal noise voltage produced by this resistance is given as:

$$V_{nR_g^-} = V_{nR_g^+} = V_{nR_g} = \sqrt{4kTBR_g} \tag{3.5.1}$$

where k = 1.23 $\times 10^{-23}$ J/K is Boltzmann's constant, T = 300 K is the ambient room temperature in Kelvins, B = 250 Hz is the signal bandwidth and R_g is the effective noise resistance seen at either input pin of the op-amp. The thermal noise voltage given by (1) is V_{nRg} = 20.34 nVrms. Including the semiconductor sources of noise in the op-amp, the total output noise is given as:

$$V_{no,rms} = \left(1 + \frac{R_4}{R_3}\right) \times \sqrt{V_{na}^2 + 2V_{nR_g}^2 + 2i_{na}^2 R_g^2} \tag{3.5.2}$$

where V_{na} represents the op-amp noise voltage and i_{na} the op-amp current noise within the bandwidth of interest. Substituting the values of V_{na} = 142.3 nV and i_{na} = 15.8 pA obtained for the bandwidth of interest gives $V_{no,rms}$ = 0.145 mVrms. Applying a single-pole, low-pass filter correction factor, the peak-to-peak output noise voltage is finally given as:

$$V_{no,ptp} = 1.57 \times 6.6 V_{no,rms} = 1.5 m V_{ptp} \tag{3.5.3}$$

The continuous noise voltage recorded from a practical bench test is shown in Fig. 3.11 and verifies the theoretical calculations at $1.66 m V_{ptp}$.

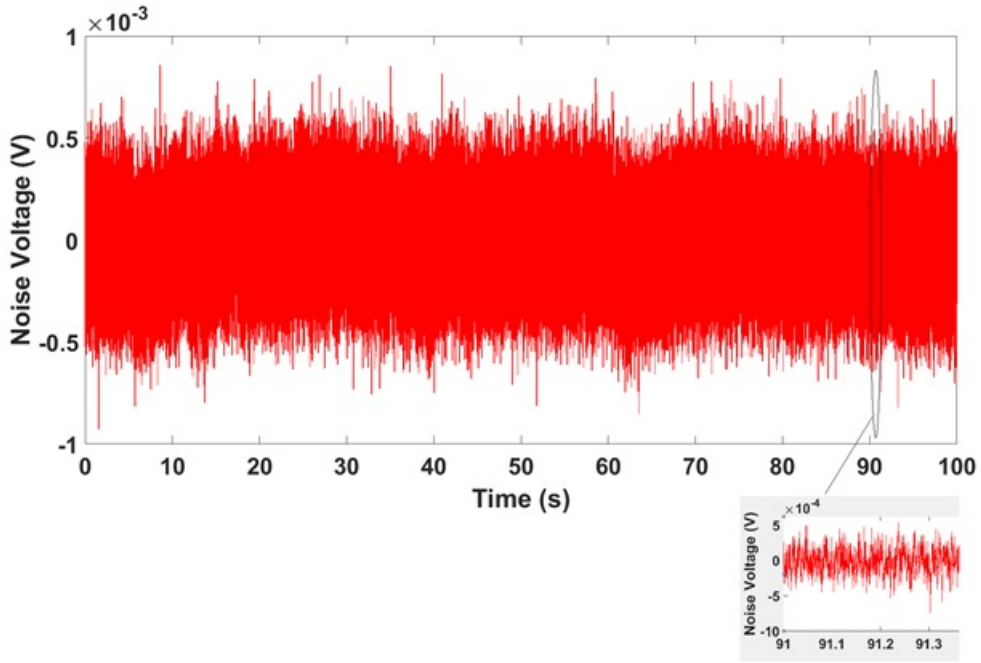

Figure 3.11: Peak-to-Peak Noise Voltage recorded from the Amplifier.

The noise voltage measurements were then conducted on six volunteers using all the electrodes

listed in Table 3.1. Allowing for the two electrodes present in each test, the electrode noise power can be evaluated by subtracting the squared noise voltage measured with the amplifier inputs grounded from the squared noise voltage obtained with the electrodes placed on a subject's arm so the noise voltage for a single electrode is given as:

$$V_{ne,rms} = \sqrt{0.5\,(V_{nt}^2 - V_{ni}^2)} \tag{3.5.4}$$

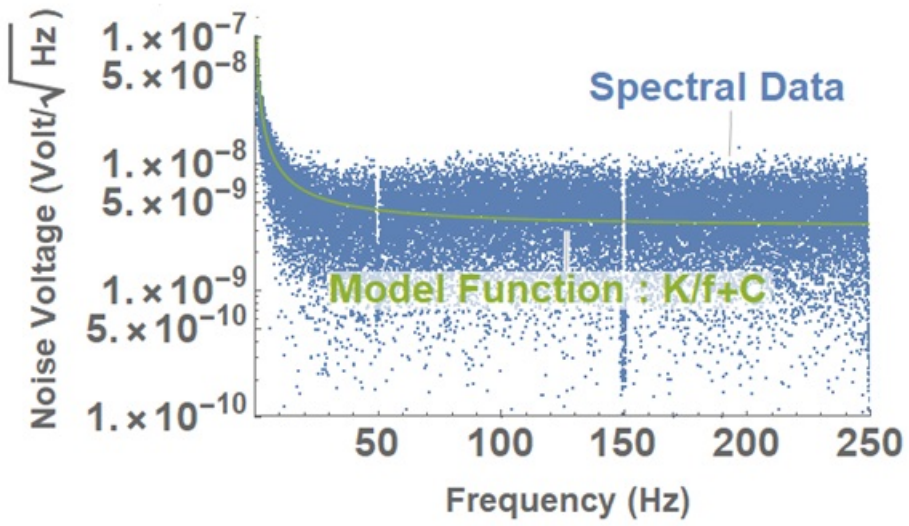

Figure 3.12: Input referred noise voltage spectrum and model function for Male 1, Electrode No. 1.

where $V_{ne,rms}$ is the electrode noise voltage, V_{nt} represents the amplifier total output noise voltage recorded with electrodes in place and V_{ni} denotes the noise voltage with the amplifier inputs grounded. The resulting electrode noise voltage is referred to the input by dividing by the amplifier gain.

This gave a noise spectral density across the bandwidth of interest for each electrode used on each subject. The noise spectral densities recorded were filtered with narrow-band IIR filters in MATLAB in order to remove any residual 50 Hz mains interference and its third harmonic at 150 Hz. The curve fitting function 'NonlinearFit' in Mathematica (Wolfram Research) was used as shown in Fig. 3.12 to fit a curve of the form of y = K/f + C to each of the noise spectra recorded . This gave a noise model having a white component, C and a flicker or

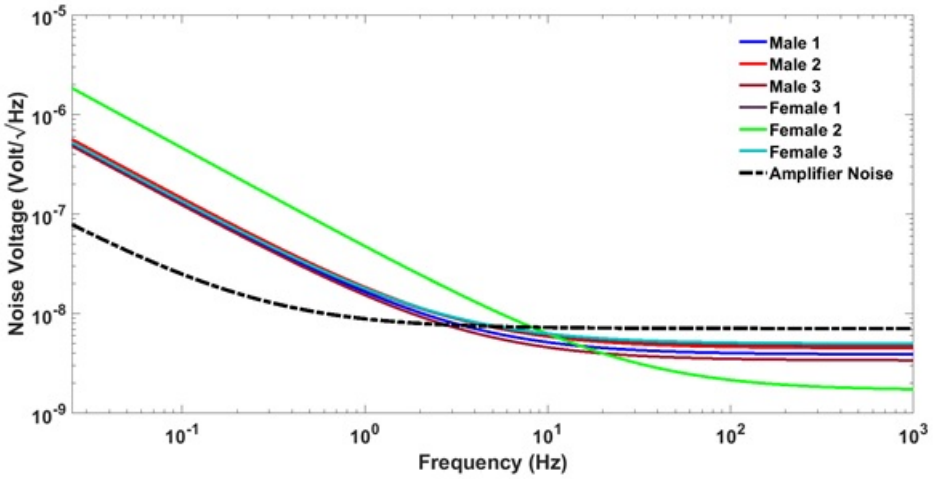

Figure 3.13: Noise Spectral Density Function for Electrode 2 across all subjects.

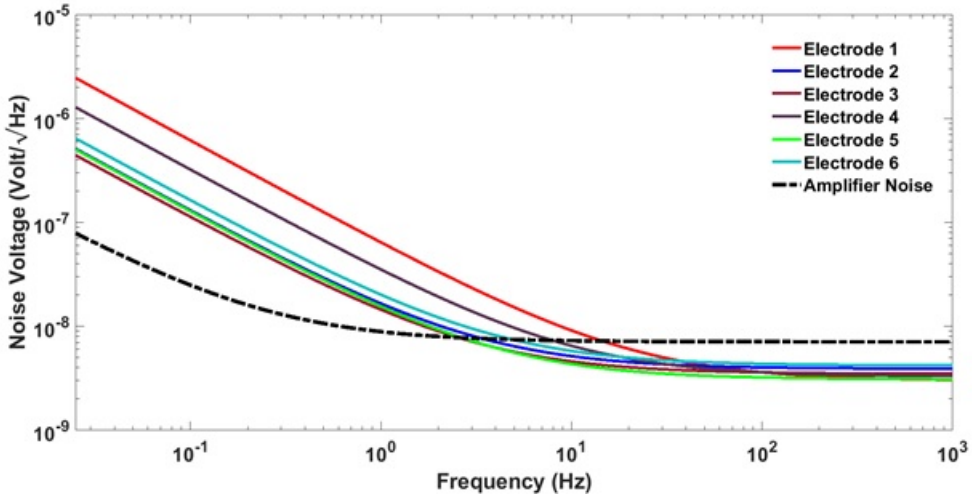

Figure 3.14: . Noise Spectrum Density Function for Male 1 across all electrodes.

1/f component of coefficient K. This was done for the noise spectrum obtained from each subject for each electrode studied. The input-referred noise spectral density function is shown plotted in Fig. 3.13 for Electrode 2 in all subjects and in Fig. 3.14 for Male Subject 1 across all electrodes. In both cases the spectral density function is also shown for the amplifier with the inputs grounded. It can be seen that the corner frequency of the amplifier noise is in the region of 0.2 Hz and is white above this frequency rather than from dc as stated by the manufacturer. The plots also show that the amplifier noise voltage is higher above about 10 Hz than that of the electrode. The coefficients of the noise spectral density functions as well as the corner frequencies are listed in Table 3.5 for all electrodes and subjects.

Examining Table 3.5, it can be seen that the gelled adhesive electrode (Electrode No. 1)

has lower levels of white noise. This is to be expected as this type of electrode provides more reliable skin contact and lower skin interface impedance. It can also be seen that there is considerable intra-individual variation as the white noise voltage ranges from 1.1 - 4.6 $nV/\sqrt{Hz}$. Electrode 4, having the smallest area exhibits the highest values of white noise. This is not surprising, as for a conductive electrode the noise generated is inversely proportional to the square root of the cross-sectional contact area of the electrode [145].

Table 3.5: Electrode voltage noise variations across all subjects

	Elec. No.	1	2	3	4	5	6
Male 1	f_{cv} (Hz)	17	8	6.9	13.2	8.8	14
	C ($nV/\sqrt{Hz}$)	3	3.9	3.5	3.3	3.1	4.2
	K ($nV\sqrt{Hz}$)	61.4	12.7	11	32	12.5	16
Male 2	f_{cv} (Hz)	13	5.9	8	9	10	12
	C ($nV/\sqrt{Hz}$)	1.4	4.5	3.4	3.1	3.3	2.9
	K ($nV\sqrt{Hz}$)	21	14	12	13	12.5	12
Male 3	f_{cv} (Hz)	7	9	10	6	9.5	11
	C ($nV/\sqrt{Hz}$)	4.6	3.4	4.6	4.8	4.3	3.3
	K ($nV\sqrt{Hz}$)	14	12	13	11	14	12
Female 1	f_{cv} (Hz)	9	9.3	16	10	7.8	7.8
	C ($nV/\sqrt{Hz}$)	4.2	4.8	4.3	4.9	4.5	4.3
	K ($nV\sqrt{Hz}$)	24.3	13	44.1	13	12.5	12
Female 2	f_{cv} (Hz)	28	21	17	24	20	19
	C ($nV/\sqrt{Hz}$)	1.8	1.7	1.9	2.3	2.1	2.6
	K ($nV\sqrt{Hz}$)	80	46	45	47	50	44
Female 3	f_{cv} (Hz)	30	8.3	8.5	7	9	12
	C ($nV/\sqrt{Hz}$)	1.1	5	4.4	5.6	4.5	3.2
	K ($nV\sqrt{Hz}$)	55	13	15	8	13	15

It is also noteworthy that the flicker K/f noise contribution from the gelled adhesive electrode is higher than for most of the dry electrodes investigated in this study. This is particularly the case for the Male 1, Female 2 and Female 3 subjects and may be due to the fact that these subjects had either body hair on the arm or dry skin. It can also be seen that for similar measurement circumstances, female subjects often, but not always, exhibit higher values of white noise than male subjects. This is thought to be due to the fact that female subjects tend to exhibit higher values of skin-electrode impedance [104] and consequently higher values

of intrinsic noise. However, the relationship between electrode noise and source impedance is still not clear and requires further investigation. The input noise currents of the op-amps used for bio-potential measurements are generally considered to generate significant noise voltages when flowing through the impedance of the electrodes. The noise voltages can be significantly higher for the dry fabric-based electrodes than for traditional gelled electrodes due to their higher impedance [104]. Therefore, while more noise may be present when using dry electrodes, the noise may not be generated intrinsically by the electrode itself, but by the input noise current of the amplifier flowing through the electrode. However, many of the commercially available very low-power op-amps popular in bio-amplifiers used in portable ambulatory recording applications have high input noise currents as well as significant white noise voltages within the signal bandwidth.

3.6 Concluding Remarks

The noise voltage generated by the electrodes themselves is found to be lower than that introduced by the amplifier. The high source impedance of the fabric electrodes is seen to contribute to the noise generated at the amplifier due to input noise current of the latter. However, when an amplifier with low input noise current is used the evidence does not suggest that un-gelled fabric based electrodes are intrinsically more noisy than others. Consequently, they should be suitable for use in an elasticated vest.

4 Establishing the Input Impedance Requirement of ECG Amplifier

This chapter establishes design criteria for amplifier input impedance requirements based on the equivalent electrical properties of the recording electrodes. Both single-time constant and an more accurate double-time constant electrode models are considered. The input impedance of the amplifier when considered in relation to that of the source electrodes has a profound effect on both the time and frequency domain responses of the amplifier as well as on its ability to reject common-mode interfering signals. Recommendations are established for the input impedance needed in the amplifier in terms of the electrode characteristics to meet the transient response requirements of the IEC 60601 performance specification. The effect of input impedance on CMRR is also considered.

4.1 Benchmark Single-Pole High-Pass Filter

A single-pole unity-gain high-pass filter is cited in the IEC 60601 specification as a benchmark circuit for assessing the transient performance of ECG recording amplifiers. A simple schematic of such a circuit is shown in Fig. 4.1.

The input resistance is denoted as R_i and the coupling capacitor as C_c. The transfer function of this unity-gain stage can be described in the Laplace domain as:

$$\frac{V_o(s)}{V_i(s)} = \frac{sC_cR_i}{1+sC_cR_i} = \frac{s}{s+\frac{1}{C_cR_i}} = \frac{s}{s+\frac{1}{\tau_c}} = \frac{s}{s+p} \tag{4.1.1}$$

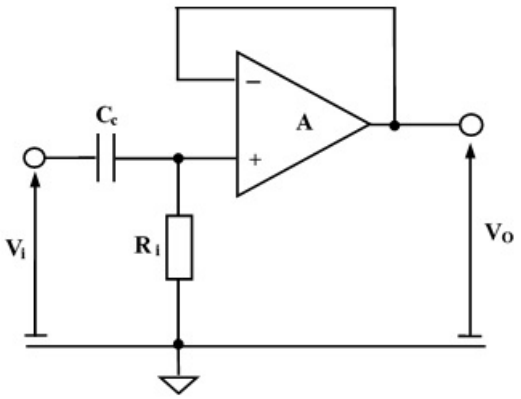

Figure 4.1: Single-Pole High-Pass Filter.

where the pole is located at $s = -p = -\frac{1}{\tau_c} = -\frac{1}{C_c R_i}$.

In order to determine the transient response, the input pulse is modelled as two step functions of amplitude V_m separated by a duration T as shown in Fig. 4.2. The pulse is described in the Laplace domain as:

$$V_i(s) = \frac{V_m}{s} - \frac{V_m}{s} e^{-sT} \tag{4.1.2}$$

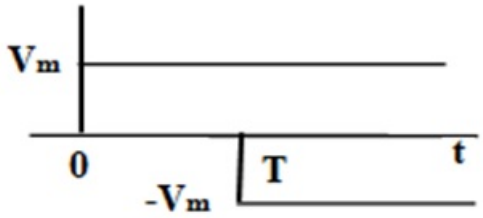

Figure 4.2: Narrow Test Pulse.

Combining this source pulse with the transfer function of the filter, the output voltage is given as:

$$V_o(s) = \frac{s}{s+p} V_i(s) = \frac{s}{s+p} \frac{V_m}{s} \left(1 - e^{-sT}\right) \tag{4.1.3}$$

Which reduces to:

$$V_o(s) = \frac{V_m}{s+p} \left(1 - e^{-sT}\right) \tag{4.1.4}$$

Then taking the inverse Laplace Transform of (4.1.4) we have the output voltage in the time domain as:

$$V_o(t) = V_m e^{-pt} u(t) - V_m e^{-p(t-T)} u(t-T) \tag{4.1.5}$$

At the end of the pulse, following the falling edge at t = T the output voltage is described as:

$$V_o(t = T) = V_m e^{-pT} - V_m = -V_m \left(1 - e^{-pT}\right) \tag{4.1.6}$$

This is the value of the undershoot below the baseline on the falling edge of the pulse. During the recovery phase following undershoot with t > T, the output voltage is described as:

$$V_o(t) = -V_m \left(1 - e^{-pT}\right) e^{-p(t-T)} \tag{4.1.7}$$

The slope of the profile at t = T at the beginning of the recovery phase following undershoot is given as:

$$\frac{dV_o}{dt}|_{t=T} = pV_m \left(1 - e^{-pT}\right) \tag{4.1.8}$$

Imposing the undershoot constraint of 100 μV and T = 100 ms on (4.1.6) as given in the IEC 60601 specification gives:

$$p \leq 0.34 \tag{4.1.9}$$

This gives $C_c R_i \geq 2.94s$ so that $f_c \leq 0.054$ Hz, which shows that a single-pole high-pass filter with a rounded cut-off frequency of $f_c = 0.05$ Hz is guaranteed to meet the undershoot requirement. The precise value of the undershoot in this case is 93μV.

The recovery slope constraint when applied to (4.1.8) requires:

$$pV_m\left(1-e^{-pT}\right) \leq 300 \times 10^{-6} \tag{4.1.10}$$

Using a Newton-Raphson iterative method of solution in Matlab with the values $V_m = 3$ mV and T = 100 ms gives:

$$p \leq 0.125 \tag{4.1.11}$$

so that $C_c R_i \geq 1.025s$. This corresponds to a cut-off frequency of $f_c \leq 0.155$ Hz which is considerably higher than is required to meet the undershoot constraint. The recovery slope is measured to be only $28\mu Vs^{-1}$ with $f_c = 0.05$.

4.2 DC Coupled Single Time-Constant Skin-Electrode Model

A simple electrical model of the interface of two contact electrodes in use with a differential recording amplifier is shown in Fig. 4.3. This model is used in the IEC 60601 specification when measuring CMRR. It represents the skin-electrode interface, where each electrode is modelled by a single parallel $C_P - R_P$ network with a small series resistance R_S.

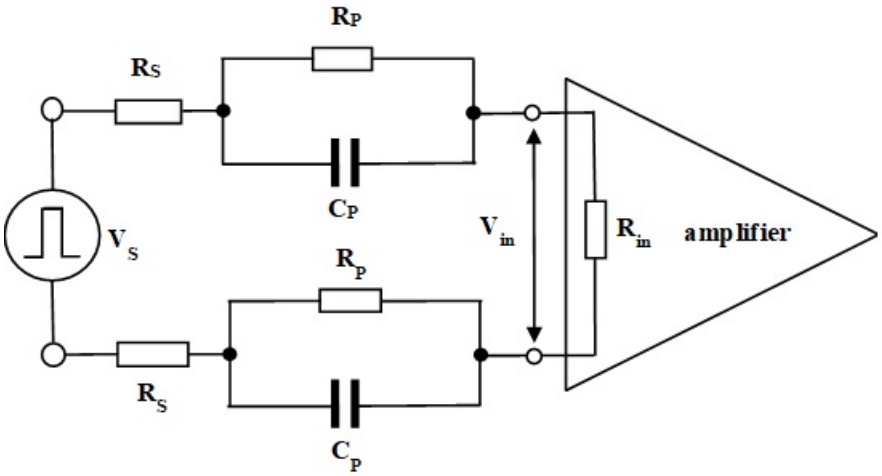

Figure 4.3: Single Time Constant Skin-Electrode-Amplifier Model.

The electrodes are taken as matched and considered initially as dc coupled to a differential recording amplifier as shown. The input impedance of the amplifier is taken to be purely resistive and is designated as R_{in}, although the effective input impedance may have differential and common-mode components in practice. The amplifier is otherwise considered ideal. A source signal of a narrow rectangular pulse V_s is applied from an ideal voltage source to the electrodes and the signal appearing at the input of the amplifier is designated as V_{in}. The resistance R_S generally represents electrical contact and lead wire resistance but may sometimes include some small tissue resistance. It is, however, very small compared with the other resistances present and can be omitted from analysis.

The transfer function of the skin-electrode-amplifier interface with $R_{in} >> R_s$ is expressed in the Laplace domain as:

$$\frac{V_{in}(s)}{V_s(s)} = \frac{\left(s + \frac{1}{C_p R_p}\right)}{\left(s + \frac{\frac{R_{in}}{2} + R_p}{C_p \frac{R_{in}}{2} R_p}\right)} = \frac{(s+z)}{(s+p)} \tag{4.2.1}$$

where the value of the pole is given by $p = \frac{\frac{R_{in}}{2} + R_p}{C_p \frac{R_{in}}{2} R_p}$ and the 1/2 factor is generated by the presence of two electrodes.

The resulting voltage at the input of the amplifier due to the narrow rectangular input pulse of Fig. 4.2 can be expressed in the Laplace domain as:

$$V_{in}(s) = \frac{V_m}{s}\left(1 - e^{-sT}\right)\frac{(s+z)}{(s+p)} \tag{4.2.2}$$

This can then be expressed in the time domain as:

$$V_{in}(t) = \frac{V_m}{\left(\frac{R_{in}}{2} + R_p\right)}\left[\begin{array}{l}\left(\frac{R_{in}}{2} + R_p e^{-pt}\right)u(t) - \\ \left(\frac{R_{in}}{2} + R_p e^{-p(t-T)}\right)u(t-T)\end{array}\right] \tag{4.2.3}$$

Imposing the undershoot constraint required by the IEC 60601 standard when t = T at the

end of the pulse expressed as a fraction of the pulse amplitude gives:

$$\frac{V_{in}(t=T)}{V_m} = \frac{R_p}{\left(\frac{R_{in}}{2}+R_p\right)}\left(1-e^{-pT}\right) \leq 0.033 \tag{4.2.4}$$

Substituting values of T = 100 ms, R_p = 51 kΩ and C_p = 47 nF as given for the model used in the IEC 60601 standard requires $R_{in} > 2.98$ MΩ. This is satisfied using the minimum value of 10 MΩ recommended in IEC 60601. During the recovery phase, following the undershoot at the trailing edge of the pulse, the slope of the output voltage at t=T is described by:

$$\frac{dV_{in}(t)}{dt}|_{t=T} = V_m \frac{R_p}{\left(\frac{R_{in}}{2}+R_p\right)} p\left(1-e^{-pT}\right) \tag{4.2.5}$$

When the value of the pole p is substituted from (4.2.1) above it is established that to meet the IEC 60601 maximum recovery slope requirements:

$$\frac{V_m}{C_p \frac{R_{in}}{2}}\left(1-e^{-pT}\right) \leq 3\times 10^{-4} \tag{4.2.6}$$

which gives $R_{in} > 426$ MΩ. These results clearly suggest that if the electrode model suggested for other measurements in IEC 60601 is used in the transient analysis also, the input impedance of the amplifier must be greater than 426 MΩ and the value of 10 MΩ recommended in the specification is much too low. The electrode model given in the IEC 60601 standard has very low impedance values compared with other models cited in the literature [13–21].

At this stage it was decided to carry out simulations of several electrode models that use a single time-constant where authors have given component values in the literature [13–21], in addition to that of the IEC 60601 standard used above. Table 4.1 shows the values of the components in the parallel network for the selected electrodes as well as the values of associated time-constant C_pR_p.

The models given in the Table 4.1 are a selection of electrodes which include gelled wet Ag-AgCl electrodes and conductive dry types of electrodes. Details of the materials used in the latter type are given where known. Each of the electrode models was simulated as in the

circuit of Fig. 4.3 in MultiSim with the 3 mV- 100 ms rectangular pulse defined in Fig. 2.13 as the source signal.

Table 4.1: Model component values for the range of electrodes used in analysis and simulations

Ref	Electrode No.	Electrode Type	R_p (kΩ)	C_p (nF)	C_pR_p (ms)
IEC	1	Wet Ag-AgCl	51	47	2.4
[150]	2	Cond. Textile	987	16	15.6
[14]	3	Textile	100	47	4.7
[151]	4	Wet Ag-AgCl	350	25	8.8
[16]	5	Wet Ag-AgCl	650	36	23.4
[17]	6	Wet Ag-AgCl	56	42	2.3
[18]	7	Wet Ag-AgCl	929	20	18.6
[19]	8	Gold-plated	980	14.4	14.1
[20]	9	Cond. Rubber	1400	20	28
[21]	10	Cotton Fabric	4000	7	28

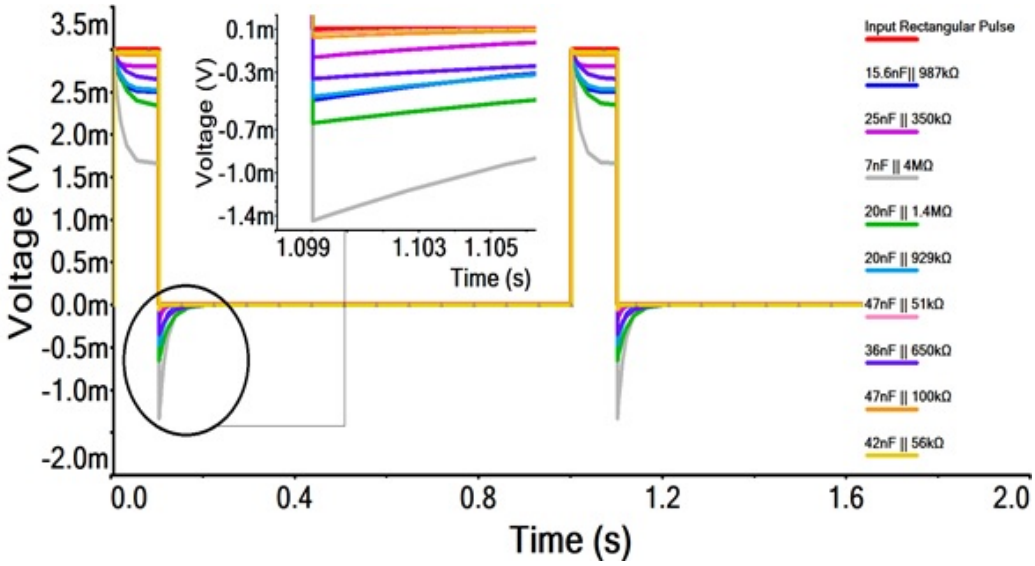

Figure 4.4: Transient Response to the 3 mV- 100 ms Narrow Pulse for the Range of Electrodes.

The amplifier input resistance was maintained at 10 MΩ. The undershoot and recovery slope values obtained from these simulations are given in Table 4.2 and waveforms of the responses of each electrode model to the narrow pulse are shown in Fig. 4.4. It can be seen that in seven cases the undershoot constraint is violated and the recovery slope is exceeded by more

Table 4.2: Undershoot and Recovery Slope values obtained for the range of electrodes[13–21] when $R_{in} = 10$ MΩ

Electrode No.	R_p (kΩ)	C_p (nF)	Undershoot (μV)	Recovery Slope (μV/s)
1	51	47	30	12710
2	987	16	494	37910
3	100	47	59	12730
4	350	25	196	23970
5	650	36	348	14210
6	56	42	34	14222
7	929	20	470	29798
8	980	14.4	492	41560
9	1400	20	654	29905
10	4000	7	1335	85771

than an order of magnitude in all cases.

Following this a synthesised test ECG signal was used in Matlab [152, 153]. The waveform has a heart-rate of 120 bpm, a flat isoelectric baseline and omits any negative going excursion of the signal at the end of the QRS complex, as seen in Fig. 4.5. This allows the degree of undershoot introduced into the waveforms by the skin-electrode interface to be observed in its own right.

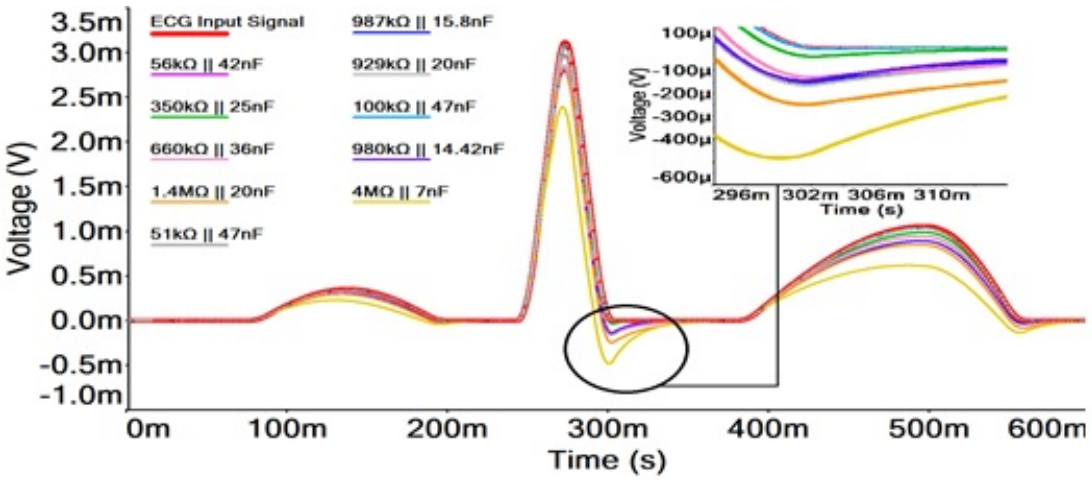

Figure 4.5: Waveforms of Interface Response to a Synthesized ECG Signal without S-Wave and Heart Rate of 120 bpm for Electrode Models [13–21].

Simulations were carried out using the synthesized signal for the same electrode models as above, dc coupled to an amplifier having an input resistance of 10 MΩ. The undershoot and recovery slope values were measured at the end of the QRS complex downslope and are given in Table 4.3. It can be seen from Fig. 4.5 that for all electrode models a pseudo S-wave with an associated recovery is created following the down-slope of the QRS complex as distortion introduced into the waveform when the amplifier input resistance is limited to 10 MΩ. Table 4.3 confirms that some of the undershoot introduced and all of the recovery slope values are outside of the limits allowed. Inspection of the waveforms in Fig. 4.5 also shows that there is a depression of the S-T segment from the baseline following the QRS complex in some cases. This has been introduced entirely by the response of the skin-electrode-amplifier interface.

Table 4.3: Undershoot and Recovery Slope values for the range of electrodes in response to a synthetic ECG signal without S-wave, HR = 120 BPM

Electrode No.	R_p (kΩ)	C_p (nF)	Undershoot (μV)	Recovery Slope (μV/s)
1	51	47	1	315
2	987	16	55	9400
3	100	47	5	1210
4	350	25	39	2380
5	650	36	131	3420
6	56	42	1	334
7	929	20	161	6592
8	980	14.4	144	9633
9	1400	20	248	6626
10	4000	7	482	14370

Following this a real recorded ECG signal was obtained from the MIT-PhysioNet database [154]. This signal has a heart rate of 120 bpm and was used as the source signal to carry out bench tests of the interface with all of the electrode models. Waveforms showing the ECG signals obtained at the input of the amplifier are presented in Fig. 4.6. In this case it can be seen that the negative going S-wave at the end of the QRS complex has been exaggerated

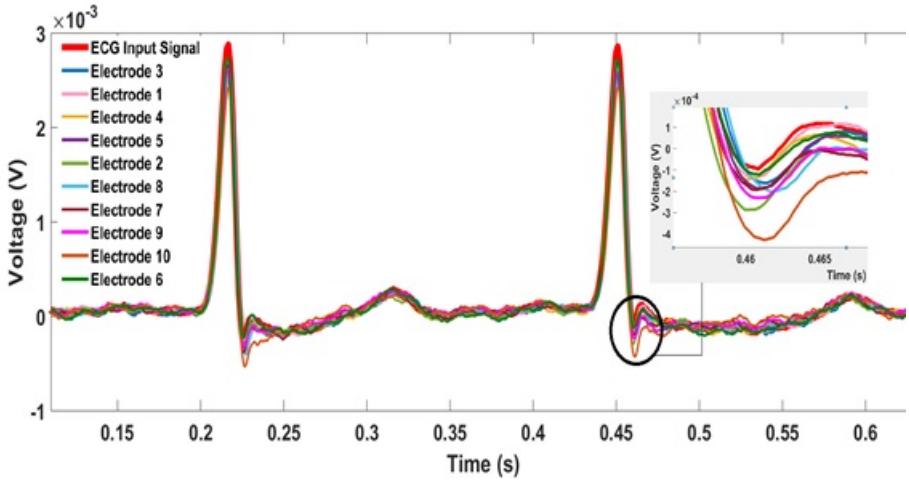

Figure 4.6: Waveforms of Interface Response to a ECG Signal with S-Wave and Heart Rate of 120 bpm for Electrode Models [13–21].

at the input of the amplifier. Table 4.4 gives the difference between the magnitude of the S-wave in the test waveform and that in the amplifier input signal specified as an increased undershoot for each electrode model. This has been caused by the response of the skin-electrode-amplifier interface. It can also be observed that the profile of the signal waveform immediately following the S-wave as it returns to the baseline has been distorted. It has been prolonged and its slope at the beginning of its recovery phase has been increased. The extent of this increase in slope is listed in Table 4.4 for all electrode models and is also attributable to the response of the skin-electrode interface. The distortions introduced into the waveforms are significant enough to visibly alter the profile of the signals. This could make the difference in a diagnosis where a feature of the ECG signal is close to a critical assessment limit when undistorted.

The aim of the above work has been to show conclusively the degree of signal distortion which takes place at the input of an ECG recording amplifier due to insufficiently high input resistance. It is clear from the simulations and bench tests carried out that the value of 10 MΩ input impedance recommended in the IEC 60601 standard is far too low, even for many wet electrodes. The IEC 60601 constraints given in (4.2.4) and (4.2.6) for undershoot and recovery slope, respectively, can be normalized with respect to the pulse amplitude by dividing by V_m. They can then be re-written to give constraints on the minimum value of

Table 4.4: Undershoot and Recovery Slope values for the range of electrodes in response to a realistic ECG signal including S-wave, HR = 120 BPM

Electrode No.	R_p (kΩ)	C_p (nF)	Increased Undershoot (μV)	Increased Recovery Slope (μV/s)
1	51	47	14	1760
2	987	16	173	15600
3	100	47	25	2380
4	350	25	141	7030
5	650	36	93	11000
6	56	42	27	2530
7	929	20	104	11900
8	980	14.4	110	14900
9	1400	20	138	15100
10	4000	7	335	33000

input resistance R_{in}. This gives for the undershoot requirement:

$$R_{in} > 58.60R_p - \frac{2R_p e^{-pT}}{0.033} \tag{4.2.7}$$

and for the recovery slope:

$$R_{in} > \frac{20}{C_P}\left(1 - e^{-pT}\right) \tag{4.2.8}$$

If, as is necessarily the case, $R_{in} >> R_p$, then the value of the pole approaches that of the zero and can be closely approximated as p = $1/C_P R_P$. Table 4.5 below shows the value of the exponential term e^{-pT}, which can be seen to be insignificant for all of the electrode models considered.

In this case (4.2.7) and (4.2.8) above can be simplified and rounded to be used as design criteria for the amplifier input resistance as:

$$R_{in} > 60R_p \tag{4.2.9}$$

Table 4.5: Value of the exponential term of (4.2.7) and (4.2.8) for the range of electrodes considered

Electrode No.	R_p (kΩ)	C_p (nF)	$1/C_pR_p$ (1/s)	e^{-pT}
1	51	47	417	7.6×10^{-19}
2	987	16	64	1.6×10^{-3}
3	100	47	213	5.75×10^{-10}
4	350	25	114	1.08×10^{-5}
5	650	36	43	1.3×10^{-2}
6	56	42	426	3.15×10^{-19}
7	929	20	54	4.51×10^{-3}
8	980	14.4	71	8.36×10^{-3}
9	1400	20	36	2.81×10^{-2}
10	4000	7	36	2.81×10^{-2}

or

$$R_{in} > \frac{20\,\text{sec}}{C_P} \tag{4.2.10}$$

whichever yields the greater value.

This value of resistance R_{in} given by (4.2.9) and (4.2.10) was then calculated for all of the electrode models considered in simulations. These values are listed in Table 4.6 for both the undershoot and the recovery slope requirements. Simulations were then re-run with the same electrode models dc coupled to the recording amplifier of Fig. 4.3 and driven by the narrow 3 mV – 100 ms pulse of Fig. 2.13 to establish the input resistance required to meet the IEC 60601 specification. With each given electrode the input resistance was varied and the minimum value required to meet the IEC 60601 constraints was recorded. This was done for the undershoot and the recovery slope criteria separately. The results given in Table 4.7 show that an input resistance considerably greater than 10 MΩ is required in most cases to meet the undershoot limit and much higher values are required to meet the recovery slope limit, with values in excess of 2.5 GΩ being obtained. The corresponding values in Table 4.6 and 4.7 prove to be extremely close and verify that the simplified design constraints of (4.2.9)

Table 4.6: Values of input resistance given by (4.2.7) and (4.2.8) for the range of electrodes considered

Electrode No.	R_p (kΩ)	C_p (nF)	Undershoot R_{in} ($M\Omega$)	Recovery Slope R_{in} ($M\Omega$)
1	51	47	3	426
2	987	16	58	1266
3	100	47	59	426
4	350	25	21	800
5	650	36	38	556
6	56	42	3.3	476
7	929	20	55	1000
8	980	14.4	58	1400
9	1400	20	82	1000
10	4000	7	235	2857

and (4.2.10) can be used to determine a suitable minimum value of input resistance for the recording amplifier that will ensure the IEC 60601 specification for the transient response to the narrow pulse of Fig. 4.2 is met. This, however, requires a knowledge of the equivalent electrical electrode properties.

4.3 AC Coupled Single Time-Constant Skin-Electrode Model

Much of today's electrocardiographic equipment is portable and battery operated. With decreasing supply voltages, the front-end amplifiers of ECG recorders cannot handle large dc offsets or the polarization voltages generated at the skin-electrode interface. In this case the electrodes must be ac coupled to the amplifier as shown in Fig. 4.7. This circuit shows the addition of a coupling capacitor C_C at the input terminals of the amplifier compared with the dc coupled circuit of Fig.4.3 and therefore combines the effects of the skin-electrode impedance with a high-pass filter response. The transfer function of this ac coupled skin-

Table 4.7: Values of input resistance determined by simulation for the range of electrodes to meet IEC 60601

Electrode No.	R_p (kΩ)	C_p (nF)	Undershoot R_{in} ($M\Omega$)	Recovery Slope R_{in} ($M\Omega$)
1	51	47	3	426
2	987	16	58	1270
3	100	47	59	426
4	350	25	21	800
5	650	36	38	547
6	56	42	3.1	475
7	929	20	55	1000
8	980	14.4	57	1390
9	1400	20	81	984
10	4000	7	230	2830

electrode-amplifier interface with $R_{in} >> R_S$ is expressed in the Laplace domain as:

$$\frac{V_{in}(s)}{V_s(s)} = \frac{s\left(s + \frac{1}{C_p R_p}\right)}{\left[s^2 + s\frac{\left[C_c\left(\frac{R_{in}}{2}+R_p\right)+C_p R_p\right]}{C_c C_p R_p \frac{R_{in}}{2}} + \frac{1}{C_c C_p R_p \frac{R_{in}}{2}}\right]} \tag{4.3.1}$$

where the 1/2 factor is present because there are two electrodes.

The zero of this transfer function is expressed as:

$$z_1 = \frac{1}{C_p R_p} \tag{4.3.2}$$

The poles of this transfer function are given as the roots of the denominator quadratic as:

$$p_1, p_2 = \frac{-\left[C_c\left(\frac{R_{in}}{2} + R_p\right) + C_p R_p\right] \pm \sqrt{\left[C_c\left(\frac{R_{in}}{2} + R_p\right) + C_p R_p\right]^2 - 4 C_c C_p R_p \frac{R_{in}}{2}}}{2 C_c C_p R_p \frac{R_{in}}{2}} \tag{4.3.3}$$

On combining the input pulse described by (4.1.2) with the transfer function of (4.3.1), the

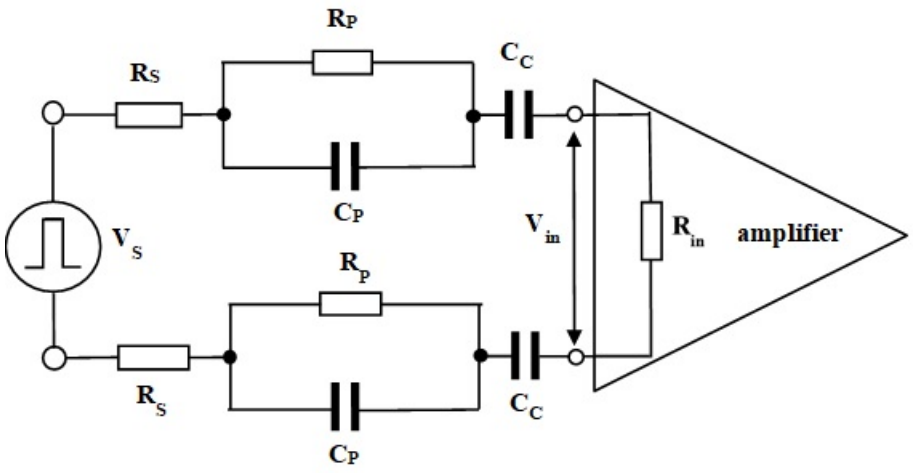

Figure 4.7: AC Coupled Single C-R Electrode Model.

voltage at the input of the amplifier can be expressed in the time domain as:

$$\begin{aligned} V_{in}(t) &= \tfrac{V_m}{(p_2-p_1)}\left[(z_1-p_1)\,e^{-p_1 t}-(z_1-p_2)\,e^{-p_2 t}\right]u(t) \\ &-\tfrac{V_m}{(p_2-p_1)}\left[(z_1-p_1)\,e^{-p_1(t-T)}-(z_1-p_2)\,e^{-p_2(t-T)}\right]u(t-T) \end{aligned} \tag{4.3.4}$$

At the end of the pulse following the falling edge at t = T this voltage is given as:

$$V_{in}(t) = -\frac{V_m}{(p_2-p_1)}\left[(z_1-p_2)\left(e^{-p_2 T}-1\right)-(z_1-p_1)\left(e^{-p_1 T}-1\right)\right] \tag{4.3.5}$$

This is the value of the undershoot from the baseline at the end of the pulse. During the recovery phase, following the trailing edge of the pulse, the slope of the output voltage at the beginning of the recovery phase is given at time t = T as:

$$\frac{dV_{in}(t)}{dt}\Big|_{t=T} = \frac{V_m}{(p_2-p_1)}\left[(z_1-p_2)\left(e^{-p_2 T}-1\right)p_2-(z_1-p_1)\left(e^{-p_1 T}-1\right)p_1\right] \tag{4.3.6}$$

Equations (4.3.5) and (4.3.6) do not yield convenient expressions that allow the undershoot and recovery slope constraints to be applied to establish design requirements for either the input resistance R_{in} or the high-pass cut-off frequency, f_C, of the ac coupled amplifier. Consequently, this task was approached in an different manner. Simulations were run in Matlab

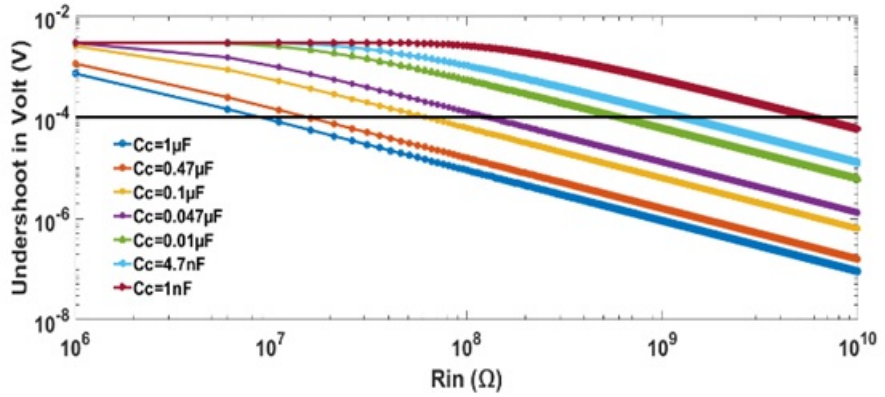

(a) Undershoot

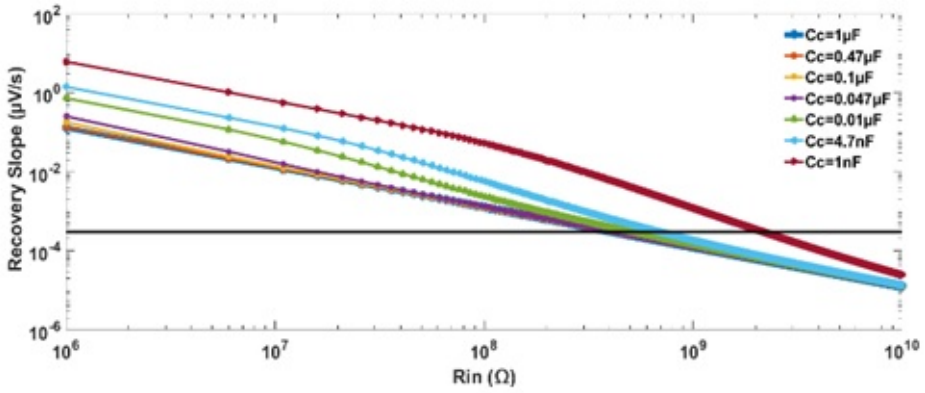

(b) Recovery Slope

Figure 4.8: Curves showing the Undershoot and Recovery Slope Obtained for the AC Coupled IEC 60601 Electrode Model [3, 22]

for the electrode models considered previously under dc coupled conditions. The value of the coupling capacitance C_c was varied in steps from 100 pF to 100 μF. For each value of capacitance, the resistance was varied from 1 MΩ to 100 GΩ. This allowed the corresponding values of the undershoot and the recovery slope present in the signal at the input of the amplifier to be established over these wide ranges of component values, for each of the electrode models. Fig. 4.8 provides plots of (a) undershoot and (b) recovery slope obtained in response to the narrow rectangular pulse of Fig. 1 for the IEC 60601 electrode model [3, 22, 82] which has R_P = 51 kΩ and C_P = 47 nF. Note that both vertical and horizontal scales are logarithmic.

A similar set of curves was obtained for each of the other electrode models [13–21]. From the curves in Fig. 4.8(a), it can be seen that the undershoot tends to level out at lower values of input resistance R_{in} and this occurs at a higher resistance for very low values of coupling

capacitance C_C. At low values of coupling capacitance the impedance of C_C is the more dominant in the series combination of an electrode and coupling capacitor and becomes the deciding factor in determining the undershoot.The recovery slope curves of Fig. 4.8(b) can be seen to converge asymptotically to a straight line on the logarithmic scale of the plot at very high values of input resistance R_{in}. This corresponds to a constant value of product $C_C R_{in}$. At very high values of R_{in} the impedance of the electrode becomes negligible compared with the input resistance and the recovery slope is dominated by the time-constant $C_C R_{in}$.

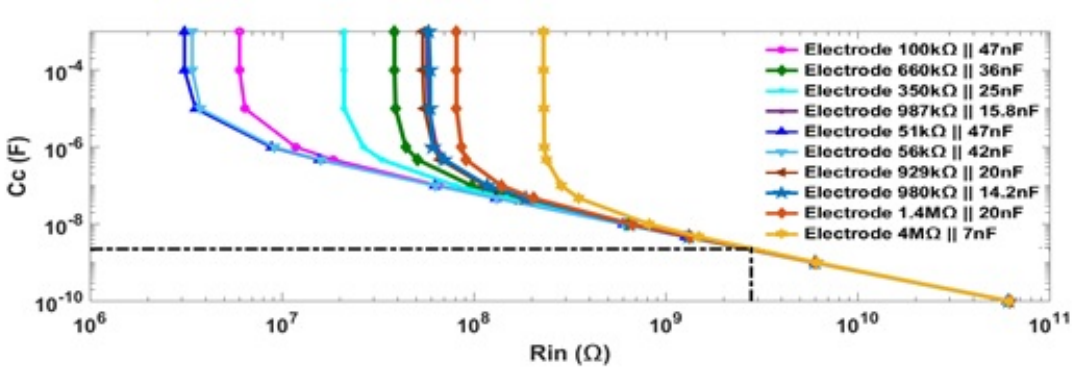

(a) Undershoot Limit for Different Electrodes

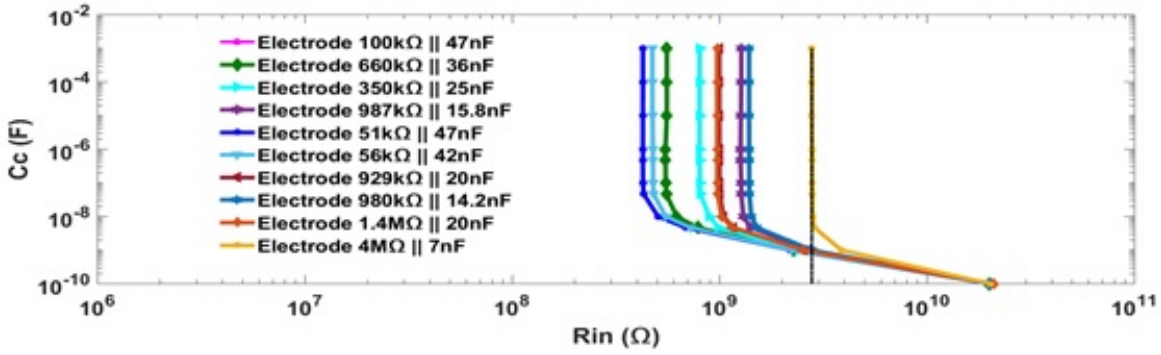

(b) Recovery Slope Limit for Different Electrodes

Figure 4.9: Undershoot and Recovery Slope $C_C R_{in}$ Coordinates for the Electrode Models.

On each plot a horizontal line is drawn representing the IEC 60601 specification limit, 100μV undershoot in Fig. 9(a) and 300μV/s recovery slope in Fig. 4.8(b). This allows the minimum value of R_{in} required with each value of Cc in order to meet the IEC 60601 specification to be determined. The points where each curve crosses the horizontal limit identify the coordinates of the time constant $C_C R_{in}$ which just satisfies the IEC 60601 requirement. A set of these coordinates was obtained for each electrode. The set of coordinates was then plotted on a

plane with C_C as the vertical axis and R_{in} as the horizontal axis as shown in Fig. 4.9. These curves show the loci of the $C_C - R_{in}$ coordinates for (a) undershoot limit and (b) recovery slope limit for each of the electrode models.

Examining the curves in Fig. 4.9(a) for the undershoot limit, it can be seen that for high values of coupling capacitor C_C, of typically greater than 1μF, the value of input resistance R_{in} needed to meet the IEC 60601 performance standard becomes independent of C_C. In this case there is a minimum value of R_{in} required which is directly aligned with the value of resistance of the electrode. For very high values of input resistance R_{in}, in excess of approximately 500 MΩ, the curves for all electrodes merge to a straight line which represents a constant value of time-constant $C_C R_{in}$ that is independent of the properties of the electrodes. The asymptotic value of this time-constant is very close to 6 s, corresponding to a high-pass cut-off frequency $f_C = 0.05$ Hz.

Examining the curves in Fig. 4.9(b) for the recovery slope, similar patterns can be found at very high values of coupling capacitance and input resistance. In this case, however, at high values of $C_C > 1\mu$F the limiting conditions are dictated by the capacitance of the electrode, C_P and this is why the curves for the pairs of electrodes having $C_P = 47$ nF and $C_P = 20$ nF almost merge. The minimum input resistance R_{in} required ranges from 5 MΩ to 2.86 GΩ in this case. At very high values of R_{in} the curves again merge asymptotically to a constant value of $C_C R_{in} = 2$ s which represents a -3 dB cut-off frequency of $f_C = 0.07$ Hz.

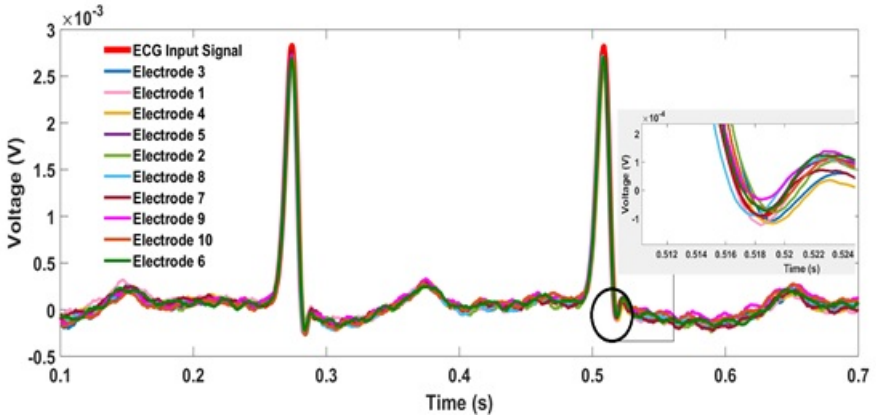

Figure 4.10: Response to ECG Signal of 120 bpm for Electrode Models [13–21] when $R_{in} = 3$ GΩ and $C_C = 2.2$ nF.

To establish design requirements for the recording amplifier, both sets of curves of Fig. 4.9

must be considered together. It can be seen that the minimum value of R_{in} is set by the recovery slope limit and is taken as the highest value of R_{in} with $C_C > 1\mu$F for the right most curve in Fig. 9(b) as indicated by the vertical dotted line on this curve, which gives $R_{in} =$ 2.87 GΩ. The curves of Fig. 4.9(a) for the undershoot limit dictate the minimum $C_C R_{in}$ time constant. This is established by projecting the dotted line of Fig. 4.9(b) upwards onto the asymptotic time constant $C_C R_{in} = 6$ s in Fig. 4.9(a) which, when projected onto the y-axis, gives the value of $C_C = 2.1$ nF. It is possible to use a higher value of C_C for convenience but this increases the time constant at the input of the recording amplifier and consequently the initialisation time. Finally, Fig. 4.10 shows the waveforms obtained from bench tests of the same electrode models when values of $R_{in} = 3$ GΩ and $C_C = 2.2$ nF are used at the amplifier input. All waveforms can be seen to follow the input PhysioNet database ECG signal without distortion.

When $R_{in} >> R_P$ the poles of the transfer function given by (4.3.1) can be closely approximated as:

$$p_1 = \frac{1}{C_c \frac{R_{in}}{2}}; \qquad p_2 = \frac{\left(\frac{R_{in}}{2} + R_p\right)}{C_p R_p \frac{R_{in}}{2}} \tag{4.3.7}$$

One of these poles is essentially that of the high-pass response of the ac coupled amplifier while the other characterizes the electrode-amplifier interface. The undershoot given by (4.3.5) can be normalized with respect to the pulse amplitude, V_m and, when set equal to the limiting value of 3.3% of the IEC60601 standard, gives:

$$\frac{1}{(p_2 - p_1)}\left[(z_1 - p_2)\left(e^{-p_2 T} - 1\right) - (z_1 - p_1)\left(e^{-p_1 T} - 1\right)\right] = 0.033 \tag{4.3.8}$$

For high values of coupling capacitor, C_C, the pole $p_1 \to 0$ and p_2 is as given in (4.3.7) above then this becomes:

$$\frac{(z_1 - p_2)}{p_2}\left(e^{-p_2 T} - 1\right) = 0.033 \tag{4.3.9}$$

It can be observed that the pole p_2 in the ac coupled circuit of Fig. 4.7 is identical to the pole

p in the dc coupled circuit of Fig. 4.3 Therefore, for the electrodes considered, the exponential term is given as in Table 4.4 and it can be taken that $e^{-p_2 T} \rightarrow 0$ so that after manipulation the limiting value of R_{in} is given as:

$$R_{in} = 60 R_p \tag{4.3.10}$$

This is, in fact, the value which describes the vertical asymptote of the curves for the undershoot in Fig. 4.9(a) with C_C very large. The recovery slope defined by (4.3.6) can be simplified in the same manner to give:

$$\frac{(z_1 - p_2)}{(p_2 - p_1)} \left(e^{-p_2 T} - 1\right) p_2 = 0.1 \tag{4.3.11}$$

which gives a final limiting value when $C_C >> C_P$ of:

$$R_{in} = \frac{20}{C_P} \tag{4.3.12}$$

This defines the vertical asymptote of the curves of Fig. 4.9(b). The asymptotic values of the curves of Fig. 4.9 can also be found for high values of input resistance R_{in}. When $R_{in} >> R_P$ the pole p_2 merges with the zero z_1 and they cancel each other out. In this case the transfer function reduces to that of a single-pole high-pass response with the pole $p_1 = 1/[C_C(R_{in}/2)]$ which behaves in the same manner as the circuit of Fig. 2.13. The normalized undershoot and recovery slope expressed by (4.3.5) and (4.3.6) when these conditions are applied then become:

$$V_{in}(t) = \frac{(z_1 - p_1)}{(z_1 - p_1)} \left(e^{-p_1 T} - 1\right) \tag{4.3.13}$$

and

$$\frac{d V_{in}(t)}{dt}\Big|_{t=T} = -\frac{(z_1 - p_1)}{(p_2 - p_1)} (z_1 - p_1) \left(e^{-p_1 T} - 1\right) p_1 \tag{4.3.14}$$

When the values of the pole p_1 and the zero z_1 are substituted and the IEC 60601 constraints

for undershoot and recovery slope are imposed, the limiting values of the time constant and the corresponding -3dB cut-off frequency of the equivalent high-pass filter can be determined as follows. For undershoot:

$$C_c R_{in} = 5.88s \tag{4.3.15}$$

and for recovery slope:

$$C_c R_{in} = 2.05s \tag{4.3.16}$$

These constraints correspond to the right-hand constant-slope asymptotes of Figs. 4.9 (a) and (b), respectively, to which the curves for all electrodes converge. As a means of examining all constraints simultaneously, the undershoot and recovery slope curves can be superimposed as shown in Fig. 4.11 for the electrode model which results in the highest demands on amplifier input resistance [82].

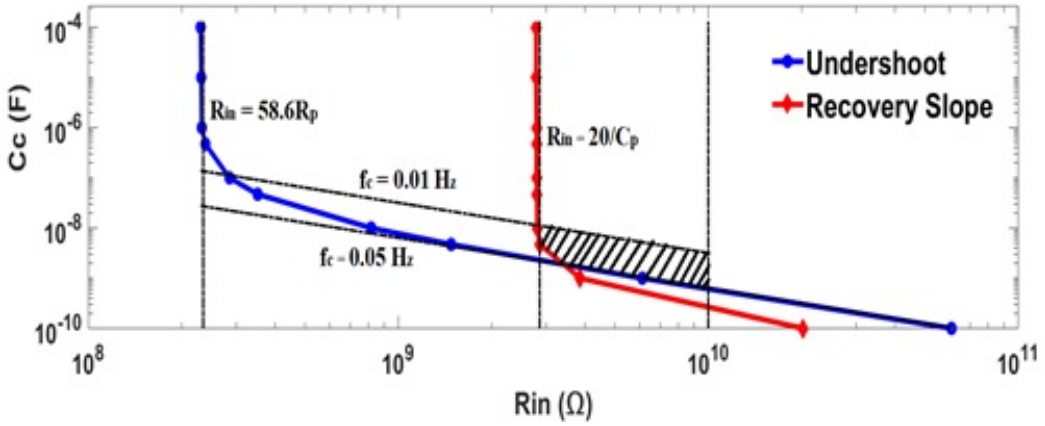

Figure 4.11: Solution Space for the ECG Recording Amplifier Input Impedance

The values of input resistance, R_{in}, and coupling capacitor, C_C, chosen must provide a co-ordinate which lies above and to the right-hand side of both curves of Fig. 4.11 in order to satisfy the IEC 60601 performance criteria. In practice there will be some maximum value of input resistance which can be practically realized in any particular circuit configuration and some minimum acceptable value for the high-pass cut-off frequency. These have been shown arbitrarily as dotted lines $R_{in,\,MAX} = 10\text{G}\Omega$ and $f_{C,\,MIN} = 0.01\text{Hz}$ in Fig. 4.11. This then

creates a solution space indicated by the shaded area in this figure. Clearly, the most desirable outcome is to work in the lower left-hand region of the shaded area so that the values of both R_{in} and C_C are minimized. A curious point in this region must therefore be the coordinate at which the two curves cross each other. This represents a value of R_{in} and of C_C which satisfies both the undershoot and the recovery slope criteria simultaneously, but that also maintains the lowest acceptable input resistance and the highest acceptable cut-off frequency in the amplifier. If (4.3.5) and (4.3.6) are normalized with respect to the pulse amplitude V_m and made equal to the limiting values of the IEC standard, and if (4.3.5) is multiplied by the pole p_1 so that both equations are matched dimensionally, then a pair of simultaneous equations is obtained as:

$$\frac{1}{(p_2 - p_1)}\left[(z_1 - p_1)\left(e^{-p_1 T} - 1\right) p_1 - (z_1 - p_2)\left(e^{-p_2 T} - 1\right) p_1\right] = 0.033 p_1 \qquad (4.3.17)$$

$$\frac{1}{(p_2 - p_1)}\left[(z_1 - p_2)\left(e^{-p_2 T} - 1\right) p_2 - (z_1 - p_1)\left(e^{-p_1 T} - 1\right) p_1\right] = 0.1 \qquad (4.3.18)$$

This gives:

$$(z_1 - p_2)\left(e^{-p_2 T} - 1\right) = 0.1 - 0.033 p_1 \qquad (4.3.19)$$

It can be seen from Fig. 4.11 that the curve for the undershoot has essentially reached its asymptotic value of time constant at the point of cross-over of the two curves. This means that a time constant corresponding to a high-pass cut-off frequency f_C = 0.05 Hz or $C_C R_{in}$ = 6.37 s can be substituted into 4.3.19) to give:

$$-(z_1 - p_2) = 0.089 \qquad (4.3.20)$$

When values of the poles and zeros as given by (4.3.7) with p_1 = 6.37 s are substituted into

(4.3.17) this gives:

$$R_{in} = \frac{22.47}{C_P} \tag{4.3.21}$$

For the electrode represented by the curve in Fig. 4.11 this is a value of input resistance of $R_{in} = 3.21$ GΩ which is a little higher than the asymptotic value of 2.86 GΩ. Table 4.8 gives the value of R_{in} required for each of the electrode models as calculated from (4.3.21) as well as the nearest values of commercially available components.

Table 4.8: Amplifier input resistance as calculated from (4.3.21) and nearest available values for the range of electrodes

Electrode No.	R_p (kΩ)	C_p (nF)	R_{in} (MΩ)	C_c (nF)	$R_{in,near}$ (MΩ)	$C_{c,near}$ (nF)
1	51	47	478	13	500	12
2	987	16	1422	4	1500	3.9
3	100	47	478	13	500	12
4	350	25	899	7	1000	8
5	650	36	624	10	660	10
6	56	42	535	12	600	12
7	929	20	1124	5.6	1500	6
8	980	14.4	1560	4	2000	3.9
9	1400	20	1124	5.7	1500	6
10	4000	7	3210	2	4000	2

In order to validate the results of the simulations of the various electrode models, practical bench tests were carried out. A standard unity-gain 3 op-amp instrumentation amplifier was constructed using the OPA602BP op-amp from Texas Instruments Inc. This was then used to implement the circuit of Fig. 4.7 with models of each of the electrodes [3, 13–21] and the associated minimum value of input resistance as given in Table 4.8, where the nearest available commercial values of components were used. The input pulse outlined in Fig. 2.13 was generated using a signal generator (Le Croy 2012) and applied to the constructed circuit. A pulse of 300mV was used because of the high level of noise produced by the signal generator and the output signal of the amplifier was then attenuated by a factor of 100 to restore the

relative levels. The signals at the output of amplifier were recorded and stored in a digital oscilloscope (Keysight DSOX3024A). The values of undershoot and recovery slope were then established for each model from the recorded signals and are presented in Table 4.9. The values obtained can all be seen to be within the limits specified by the IEC 60601 standard. This validates the findings of simulations.

Table 4.9: Undershoot and Recovery Slope values measured for the range of electrodes in the constructed circuit

Electrode No.	R_p (kΩ)	C_p (nF)	Undershoot (μV)	Recovery Slope (μV/s)
1	51	47	94	270
2	987	16	99	293
3	100	47	94	293
4	350	25	98	275
5	650	36	84	275
6	56	42	78	270
7	929	20	72	225
8	980	14.4	75	240
9	1400	20	70	220
10	4000	7	78	230

4.4 DC Coupled Two Time-Constant Skin Electrode Amplifier Model

The representative schematic diagram of a differential recording amplifier dc coupled to a signal source via two electrodes is given in Fig. 4.12. Electrodes are modelled by two parallel C-R networks combined with series resistors and are considered as matched. The input impedance of the amplifier, R_{in}, is treated as purely resistive. The input signal is a narrow pulse, V_S, obtained from an ideal source to drive the electrodes and the voltage present at the input of the amplifier is designated V_{in}. The amplifier is otherwise considered ideal. The series resistances R_{S1} and R_{S2} are universally very small compared with R_{P1} and R_{P2} and in particular considered in relation to the resistance at the amplifier input so that $R_{in} >> (R_{S1} + R_{S2})$.

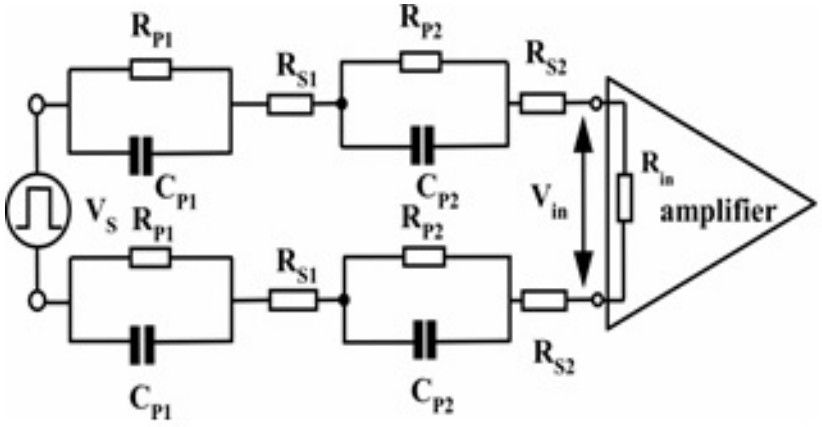

Figure 4.12: DC Coupled Electrical Model of Two Time-Constant Skin-Electrode-Amplifier Interface.

The transfer function of the skin-electrode-amplifier interface is then given as:

$$\frac{V_{in}(s)}{V_s(s)} = \frac{\left(s+\frac{1}{C_{p1}R_{p1}}\right)\left(s+\frac{1}{C_{p2}R_{p2}}\right)}{\left(s+\frac{\frac{R_{in}}{2}+R_{p1}}{C_{p1}R_{p1}\frac{R_{in}}{2}}\right)\left(s+\frac{\frac{R_{in}}{2}+R_{p2}}{C_{p2}R_{p2}\frac{R_{in}}{2}}\right)} = \frac{(s+z_1)(s+z_2)}{(s+p_1)(s+p_2)} \tag{4.4.1}$$

where p_1, p_2, z_1 and z_2 denote the poles and the zeros of the response as determined by the relevant time-constants. The voltage present at the input of the amplifier, $V_{in}(s)$, in response to the pulse given in Fig. 4.2 can be described in Laplace terms as:

$$V_{in}(s) = \frac{V_m}{s}\left(1-e^{-sT}\right)\frac{(s+z_1)(s+z_2)}{(s+p_1)(s+p_2)} \tag{4.4.2}$$

This voltage is given in the time domain as:

$$V_{in}(t) = V_m\left[\begin{array}{l}\left(\frac{z_1z_2}{p_1p_2} - \frac{(z_1-p_1)(z_2-p_1)}{p_1(p_2-p_1)}e^{-p_1t} + \frac{(z_1-p_2)(z_2-p_2)}{p_2(p_2-p_1)}e^{-p_2t}\right)u(t) - \\ \left(\frac{z_1z_2}{p_1p_2} - \frac{(z_1-p_1)(z_2-p_1)}{p_1(p_2-p_1)}e^{-p_1(t-T)} + \frac{(z_1-p_2)(z_2-p_2)}{p_2(p_2-p_1)}e^{-p_2(t-T)}\right)u(t-T)\end{array}\right] \tag{4.4.3}$$

The undershoot present on termination of the pulse when t = T is then given as:

$$V_{in}(t=T) = \frac{V_m}{(p_2-p_1)}\left[\frac{(z_1-p_1)(z_2-p_1)}{p_1}\left(e^{-p_1t}-1\right) - \frac{(z_1-p_2)(z_2-p_2)}{p_2}\left(e^{-p_2t}-1\right)\right] \tag{4.4.4}$$

During the recovery phase, following termination of the pulse, the slope of the amplifier input voltage, Vin, at t = T is given as:

$$\frac{dV_{in}(t)}{dt}|_{t=T} = \frac{V_m}{(p_1 - p_2)}\left[(z_1 - p_2)(z_2 - p_2)\left(e^{-p_2 T} - 1\right) - (z_1 - p_1)(z_2 - p_1)\left(e^{-p_1 T} - 1\right)\right] \tag{4.4.5}$$

A number of double time-constant models of electrodes were found in the literature [104, 133–135, 155–157] where component values were given by the researchers as listed in Table 4.10. These models are a selection which include an adhesive electrode, conductive rubber electrodes and polymer-based electrodes with details as listed in Table 4.10.

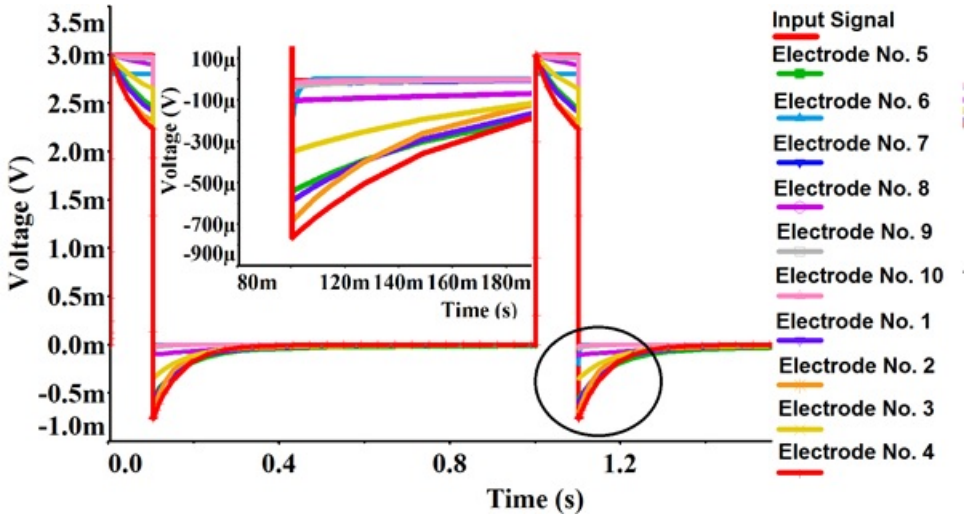

Figure 4.13: Rectangular Pulse Response DC Coupled of Two Time-Constant Skin-Electrode-Amplifier Interface.

In the first instance, these models were used to carry out simulations in Matlab to obtain the response of the interface structure of Fig. 4.12 to the 3 mV-100 ms pulse while the input impedance of the amplifier was maintained at the minimum of 10 MΩ recommended by IEC 60601. The results of simulations are presented in Table 4.11 for both undershoot and recovery slope. Waveforms of the responses in time are presented in Fig. 4.13. It can be observed that for seven of the models examined the undershoot limit of 100 μV is violated and in all cases the recovery slope limit is exceeded considerably, in some instances by more than an order of magnitude.

Next, a synthetic ECG signal was created in Matlab based on previous work on ECG signal

Table 4.10: Values of Electrical Elements of the Electrode Models Examined

Electrode No.	R_{P1} (kΩ)	C_{P1} (μF)	τ_1 (ms)	R_{P2} (kΩ)	C_{P2} (kΩ)	τ_2 (ms)	Electrode Type & Material
1	1274	0.06	76.4	852	0.44	375	WANDY WA-45, 6.5 cm Diameter Silicone Rubber
2	1462	0.04	58.5	819	0.5	410	WANDY WA-45, 4.5 cm Diameter Silicone Rubber
3	990	0.1	99	990	1	1000	WANDY Q04, $5cm \times 9cm$ Rectangular Silicone Rubber
4	1101	0.08	88.1	1271	0.08	102	Can-Med C5005PF, 2.5 cm Diameter Carbonized Rubber
5	1380	0.07	10.4	1380	0.72	994	Can-Med C5005PF, 2.5 cm Diameter Carbonized Rubber
6	328	6E-04	2.1	31	0.004	0.11	Polymer, Polyurethane-A (no further details available)
7	35.2	0.9	31.7	29.5	5.8	171	Adhesive, Wandy, E50mm hydrogel
8	220	6.6	1450	440	0.5	220	Conductive Rubber (no further details available)
9	8	0.8	6.6	56	0.54	30.4	Polymer, Polyurethane-A (no further details available)
10	10	0.62	162	21	1.57	32.2	Polymer, Polyurethane-B (no further details available)

Table 4.11: Values of Undershoot & Recovery Slope for the Electrodes Simulated with R_{in} =10 MΩ

Electrode No.	Undershoot (μV)	Recovery Slope (μV/sec)
1	587	8816
2	685	14108
3	350	4227
4	764	11812
5	541	6641
6	201	241970
7	28	692
8	104	481
9	37	1817
10	18	1341

Table 4.12: Values of Undershoot & Recovery Slope Obtained in Response to the Synthetic ECG Signal, having No S- Wave, at a H.R. of 120 b.p.m.

Electrode No.	Undershoot (μV)	Recovery Slope (μV/sec)
1	218	2267
2	260	162
3	127	4010
4	283	1140
5	198	3115
6	2.9	1779
7	10.4	3019
8	36	2874
9	12.6	3060
10	4.7	3312

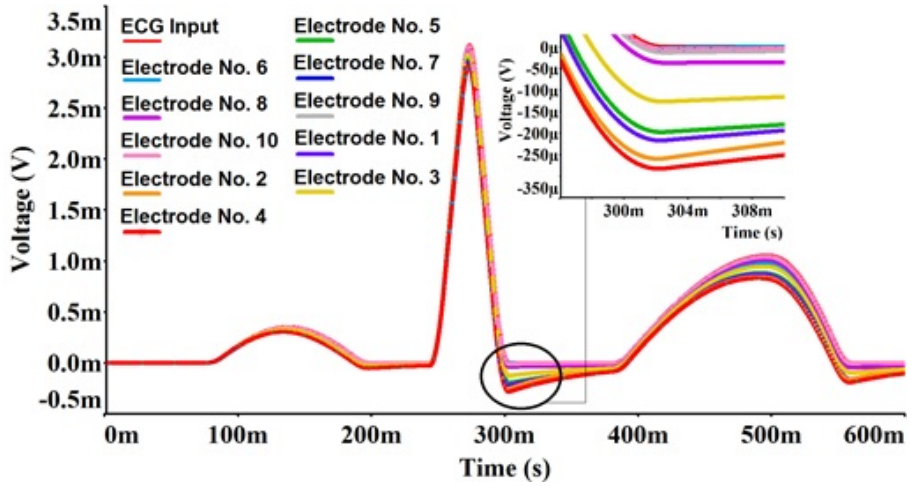

Figure 4.14: Synthetic ECG Wave Response of Two Time-Constant Skin-Electrode-Amplifier Interface, having No S-Wave and a H.R. of 120 bpm for Electrode Models Listed in Table 4.10

characterisation and synthesis [152, 153]. A test signal at a heart-rate 120 bpm, having a horizontal isoelectric line and no negative excursion following the QRS complex was synthesized. This allows the undershoot created in the waveforms by the model under investigation to be readily observed.

Simulations were run using the test ECG signal as the source for the models of Table 4.10, which were dc coupled to an amplifier resistance of 10 MΩ as before. The values of undershoot and recovery slope at the end of the QRS complex downslope are listed in Table 4.12. Waveforms of the time domain response for each model are shown in Fig. 4.14. Simulations of all electrode models show the production of a virtual S-wave with an accompanying recovery profile in time following the downslope of the QRS complex. This is a direct result of distortion of the input signal waveform when the input resistance is maintained at 10 MΩ. The results presented in Table 4.12 indicate that 60% of the undershoot values measured and 100% of recovery slope values infringe the limits of the IEC 60601 performance specification. Closer examination of the waveforms of Fig. 4.14 shows a depression of the S-T segment beneath the isoelectric line immediately after the QRS complex in a number of cases. This has been generated by the skin-electrode-amplifier interface entirely and is attributed to the insufficiently high resistance of 10 MΩ present at the input of the amplifier, this being much too low compared with the impedance of the electrodes considered.

Finally, a set of bench tests were undertaken on a physically constructed circuit in order to establish the practical performance of the dc coupled amplifier of Fig. 4.12. An instrumentation amplifier having unity gain was constructed using three OPA602BP operational amplifiers (Texas Instruments Inc.) having very high input impedance (10^{13} Ω ||1 pF). A previously recorded ECG signal containing an S-wave was downloaded from the MIT-PhysioNet online archive. This signal was installed on an arbitrary signal generator (Le Croy 2012) and the time-base set to provide a heart rate of 120 bpm. A signal amplitude of 300mV applied differentially as ±150 mV on either side of the amplifier, was used in the bench tests to overcome the inherent noise created by the signal generator. The output signal of the amplifier was subsequently attenuated by a scale of 100 to correct the relative levels. All signals provided by the amplifier were measured using a digital oscilloscope (Keysight DSOX3024A) which facilitated storage on a memory stick. The physical test ECG signal was applied to the amplifier through circuit-based electrode models using commercially available components having values as close as possible to those given in Table 4.10. The amplifier input resistance was fixed at 10 MΩ.

Table 4.13: Values of Undershoot & Recovery Slope for the Electrodes Simulated with R_{in} =10 MΩ

Electrode No.	Undershoot (μV)	Recovery Slope (μV/sec)
1	22	40.6
2	78	14.53
3	105	22.30
4	3	20.85
5	28	12.30
6	35	23.73
7	49	2.82
8	2	25.81
9	5	16.57
10	32	2.86

Table 4.13 shows the differences between the magnitudes of the S-wave in the PhysioNet database waveform applied to the electrode models and those recorded in the signal at the

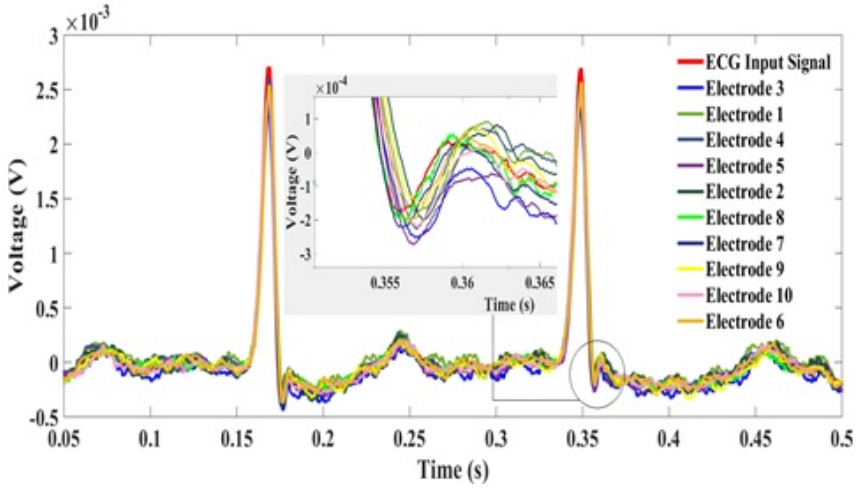

Figure 4.15: Real ECG Wave Response of Two Time-Constant Skin-Electrode-Amplifier Interface, having an S-Wave and a H.R. of 120 bpm for Electrode Models Listed in Table 4.10

amplifier input, given as increased values of undershoot in each case. It also lists the increase in the recovery slope values measured at the input of the amplifier compared to those associated with the PhysioNet test signal. The waveforms shown in Fig. 4.15 are those of the amplifier input voltage and allow the degree of alteration of the ECG signal profile that takes place at the skin-electrode amplifier interface to be seen. The depth of each S-wave has been exaggerated and the time profile of the signal immediately after the S-wave on its return to the isoelectric line has been prolonged and its slope at the onset of the recovery phase increased. The distortion is entirely due to insufficiently high resistance at the input of the amplifier compared to the impedance of the electrodes used. This resistance needs to be much greater than the 10 MΩ suggested in the IEC 60601 performance standard when ungelled, and even some modern pre-gelled, adhesive electrodes are used in the ECG recording environment. It is therefore clear that the required input resistance of the amplifier must be established based on the electrical properties of the electrodes. When the IEC 60601 limit of 100 μV undershoot is applied to the voltage at the amplifier input given by (4.4.4) and normalized with respect to the input pulse amplitude, V_m, this gives the constraint:

$$\frac{V_{in}(t=T)}{V_m} = \frac{1}{(p_2-p_1)}\left[\begin{array}{l}\frac{(z_1-p_1)(z_2-p_1)}{p_1}\left(e^{-p_1 t}-1\right)- \\ \frac{(z_1-p_2)(z_2-p_2)}{p_2}\left(e^{-p_2 t}-1\right)\end{array}\right] \leq 0.033 \qquad (4.4.6)$$

If the poles and zeros as defined in (4.4.1) are substituted this gives a requirement for the minimum amplifier input resistance as:

$$R_{in} \geq 60.60 \left[R_{p1} \left(1 - e^{-p_1 T} \right) + R_{p2} \left(1 - e^{-p_2 T} \right) \right] \tag{4.4.7}$$

When the limit of $300\,\mu Vs^{-1}$ stipulated for the recovery slope is applied to the derivative of the voltage at the amplifier input as given by (4.4.5) and normalized with regard to the input pulse amplitude, V_m, a second constraint is established as:

$$\frac{1}{V_m} \frac{dV_{in}(t)}{dt}\Big|_{t=T} = \frac{1}{(p_1 - p_2)} \left[\begin{array}{l} (z_1 - p_2)(z_2 - p_2)\left(e^{-p_2 T} - 1\right) - \\ (z_1 - p_1)(z_2 - p_1)\left(e^{-p_1 T} - 1\right) \end{array} \right] \leq 0.1 \tag{4.4.8}$$

Table 4.14: Input Resistance Required as Given by (4.4.7) and (4.4.9)

Electrode No.	Undershoot $R_{in}(M\Omega)\|$	Recovery Slope $R_{in}(M\Omega)$
1	68	254
2	83	418
3	44	129
4	94	326
5	62	187
6	22	8550
7	2.8	23
8	11	15
9	3.8	61
10	1.8	45

If, as is necessarily the case, $Rin >> R_{P1}, R_{P2}$ so that attenuation of the input signal can be avoided, then the values of the poles approach those of the zeros and can be closely approximated as $p_1 \approx 1/C_{P1}R_{P1}$ and $p_2 \approx 1/C_{P2}R_{P2}$. When the poles and zeros are substituted into (4.4.8) this gives a second requirement for the minimum input resistance of the amplifier

as:

$$R_{in} \geq 20 \left[\frac{\left(1 - e^{-\frac{T}{C_{P1}R_{P1}}}\right)}{C_{P1}} + \frac{\left(1 - e^{-\frac{T}{C_{P2}R_{P2}}}\right)}{C_{P2}} \right] \tag{4.4.9}$$

No universal assumptions can be made regarding the exponential terms so that no approximating series can be substituted for these. In this case (4.4.7) and (4.4.9) above may be used to give design criteria for the input resistance, R_{in}.

The value used is determined by whichever constraint imposes the greater requirement. The limiting values of resistance R_{in} given by (4.4.7) and (4.4.9) were established for all electrode models used in the previous simulations and are listed in Table 4.14 with values for undershoot and recovery slope shown separately.

Table 4.15: Input Resistance Required as Determined by Simulation

Electrode No.	Undershoot R_{in}(MΩ)	Recovery Slope R_{in}(MΩ)
1	67	256
2	81	422
3	43	131
4	91	330
5	60	189
6	21	8160
7	2.8	23
8	10	15
9	3.6	50
10	1.8	45

Simulations were re-run with the narrow pulse defined by (4.1.2) as input for all of the electrode models of Table 4.10, dc coupled to the recording amplifier of Fig. 4.12. For each model the minimum value of R_{in} required to satisfy the IEC 60601 standard was established for both the undershoot and the recovery slope. The results presented in Table 4.15 indicate that a value of resistance R_{in} significantly higher than 10 MΩ is required in almost all instances to satisfy the undershoot criterion with higher values in excess of 8 GΩ needed to meet the recovery slope

criterion. The corresponding calculated values in Table 4.14 and simulation derived values of Table 4.15 are in close agreement and validate the design constraints presented in (4.4.7) and (4.4.9) as accurate. The use of these constraints requires a knowledge of the component values of an accurate double time-constant model of the electrodes. This information is not always available in a clinical environment and may need to be measured using an engineering approach.

4.5 AC Coupled Double Time-Constant Electrode Model

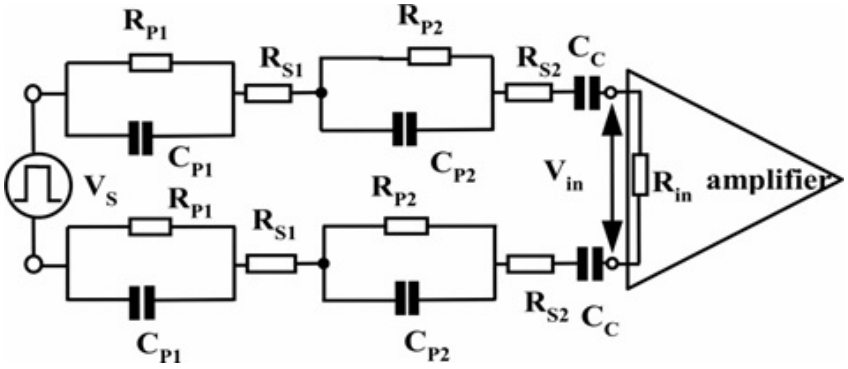

Figure 4.16: AC Coupling of a Two Time-Constant Electrode Equivalent Circuit

Finally, the electrodes are ac coupled to the amplifier as illustrated in Fig. 4.16. A dc blocking capacitor, C_C, is included at each terminal of the amplifier to give a high-pass frequency response. The transfer function of the ac coupled skin-electrode-amplifier model with $R_{in} >> R_{S1}, R_{S2}$ is given in the Laplace domain as:

$$\frac{V_{in}(s)}{V_s(s)} = \frac{(s+z_1)(s+z_2)}{(s+p_1)(s+p_2)(s+p_3)} \tag{4.5.1}$$

This transfer function contains zeros at z_1 and z_2 given as:

$$z_1 = \frac{1}{C_{P1}R_{P1}},\ z_2 = \frac{1}{C_{P2}R_{P2}} \tag{4.5.2}$$

The poles of the transfer function with $R_{in} >> R_{S1}, R_{S2}$ can be approximated as:

$$p_1 = \frac{1}{C_c\frac{R_{in}}{2}},\ p_2 = \frac{\left(\frac{R_{in}}{2}+R_{P1}\right)}{C_{P1}R_{P1}\frac{R_{in}}{2}},\ p_3 = \frac{\left(\frac{R_{in}}{2}+R_{P2}\right)}{C_{P2}R_{P2}\frac{R_{in}}{2}} \tag{4.5.3}$$

On applying the narrow pulse defined by (4.1.2) to the transfer function of (4.5.1), the signal appearing at the amplifier input is given in the time domain as:

$$V_{in}(t) = V_m \left[\begin{array}{l} \left(K_1 e^{-p_1 t} + K_2 e^{-p_2 t} + K_3 e^{-p_3 t}\right) u(t) - \\ \left(K_1 e^{-p_1 (t-T)} + K_2 e^{-p_2 (t-T)} + K_3 e^{-p_2 (t-T)}\right) u(t-T) \end{array} \right] \tag{4.5.4}$$

where the coefficients K_1, K_2, and K_3 are expressed as:

$$K_1 = \frac{(z_1 - p_3)(z_2 - p_3)}{(p_1 - p_3)(p_2 - p_3)},\ K_2 = \frac{(z_1 - p_2)(z_2 - p_2)}{(p_1 - p_2)(p_3 - p_2)},\ K_3 = \frac{(z_1 - p_3)(z_2 - p_3)}{(p_1 - p_3)(p_2 - p_3)} \tag{4.5.5}$$

On the terminating edge of the pulse at t = T, the undershoot from the isoelectric line is:

$$V_{in}(t) = -V_m \left[K_1 \left(e^{-p_1 T} - 1\right) + K_2 \left(e^{-p_2 T} - 1\right) + K_3 \left(e^{-p_3 T} - 1\right)\right] \tag{4.5.6}$$

At the start of the recovery phase the slope of the input voltage is described at time t = T as:

$$\frac{dV_{in}(t)}{dt}|_{t=T} = -V_m \left[K_1 p_1 \left(e^{-p_1 T} - 1\right) + K_2 p_2 \left(e^{-p_2 T} - 1\right) + K_3 p_3 \left(e^{-p_3 T} - 1\right)\right] \tag{4.5.7}$$

Equations (4.5.6) and (4.5.7) do not provide expressions for the undershoot and recovery slope that can be easily manipulated to give symbolic constraints for either the resistance, R_{in}, or the low cut-off frequency, f_c, of the amplifier. Therefore, constraints must be established by alternative means as in the case of the previous ac coupled single time-constant electrode model.

Simulations were carried out in Matlab for the electrode models of Table 4.10 with ac coupling. The value of the dc blocking capacitor, C_c, was increased in appropriate increments from 0.01 nF to 100 μF. For every value of capacitor, C_c simulated, R_{in} was incremented from 0.001 GΩ to 100 GΩ. The associated values of undershoot and recovery slope measured in the signal at the amplifier input were recorded at each step across the range of component values for each model. Fig. 4.17 shows plots of (a) undershoot and (b) recovery slope values obtained

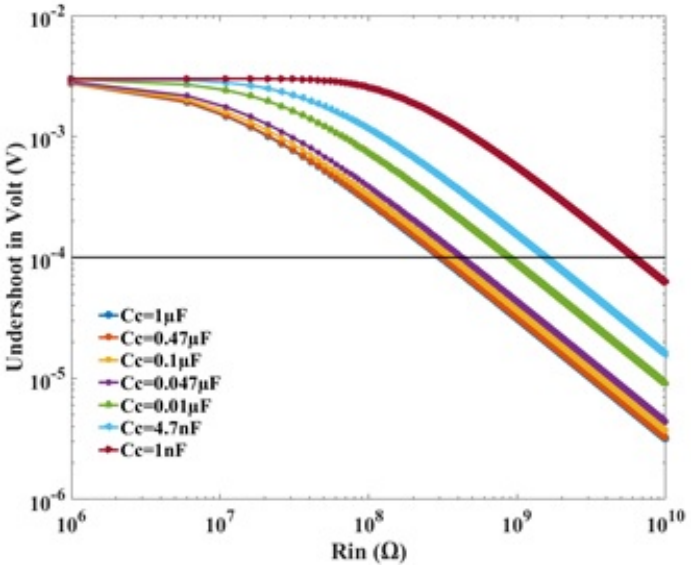

(a) Undershoot

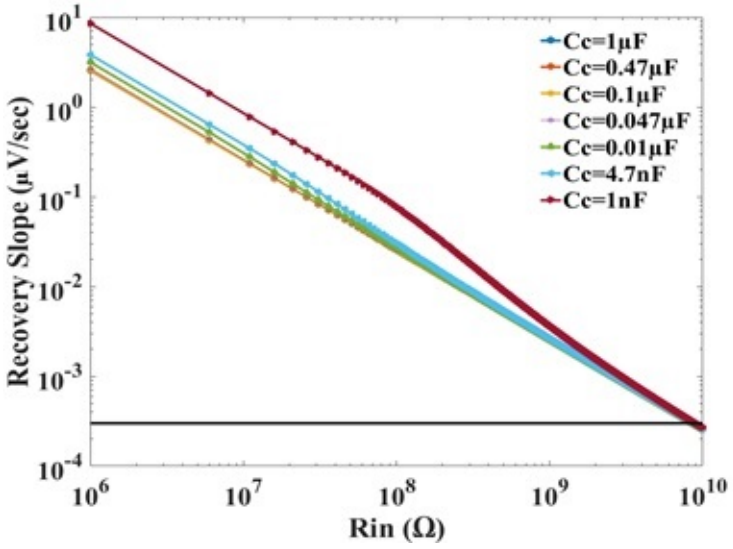

(b) Recovery Slope

Figure 4.17: Undershoot and Recovery Slope Plots for AC Coupling of Electrode No. 6.

for model no. 6 with R_{P1}= 328 kΩ, C_{P1}= 6.4 nF, R_{P2}= 31.3 kΩ and C_{P2}= 3.7 nF. Both ordinate and abscissa axes in these graphs have log scales. Curves were also acquired for all other electrode models listed in Table 4.10. From the curves of Fig. 4.17(a), it can be observed that the undershoot appears to level out at low values of input resistance, R_{in}. At low values of dc blocking capacitor, the reactance of C_C becomes the dominant part of the series impedance of the electrode and the dc blocking capacitor combined and is the determining element of the extent of undershoot. The recovery slope plots of Fig. 4.17(b) converge to a straight line asymptote on the logarithmic scale at high values of R_{in}. This

asymptote represents a constant product of the time-constant $C_C R_{in}$. At very high values of R_{in} the impedance of the electrode is small compared with the amplifier input resistance and the recovery slope becomes determined by the time-constant $C_C R_{in}$.

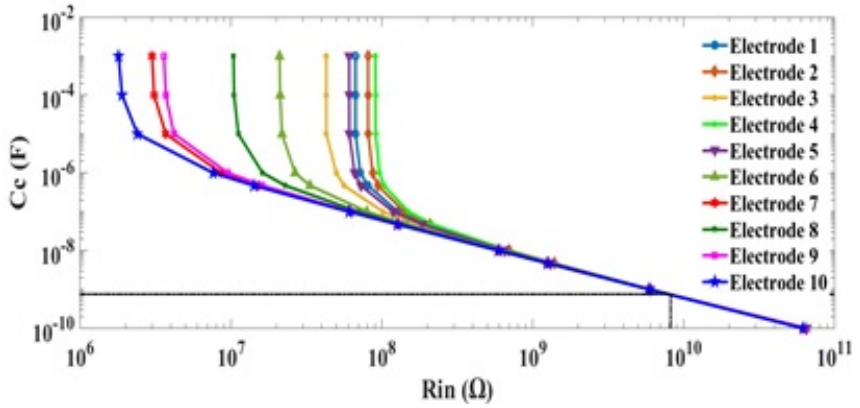

(a) Undershoot

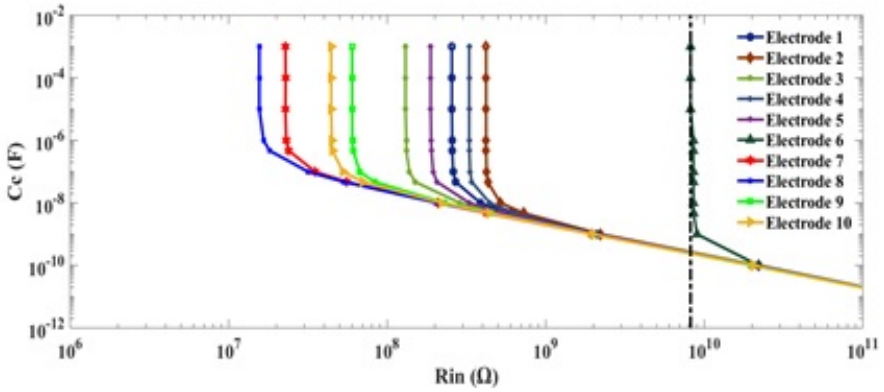

(b) Recovery Slope

Figure 4.18: Undershoot and Recovery Slope $C_C R_{in}$ Coordinates for the Electrode Models.

On each figure a horizontal line represents the IEC 60601 limiting criterion, 100 μV undershoot in figure 8(a) and 300 μVs^{-1} recovery slope in figure 8(b). This enables determination of the minimum value of R_{in} required with each value of C_C to meet the IEC 60601 performance standard. The points of crossover of each curve of the horizontal thresholds gives the coordinates of $C_C R_{in}$ that just meet the IEC 60601 criteria. A set of crossover points was established for each electrode model. The set of points for a particular model was plotted on a plane having C_C as the ordinate axis and R_{in} as the abscissa axis as seen in Fig. 4.18. These plots show the loci of the time constant $C_C R_{in}$ coordinates for (a) undershoot limit and (b) recovery slope limit for each of the models.

It is evident from the curves of Fig. 4.18(a) for the undershoot limit, that for values of $C_C > 1\mu$F, the value of R_{in} required to satisfy IEC 60601 is independent of C_C. There is, in fact, a minimum value of R_{in} that is directly associated with the resistive elements of the model. For higher values of resistance R_{in}, of greater than 1 GΩ, the plots for all models converge to a straight line associated with a constant value of $C_C R_{in}$ that does not depend of the properties of the electrodes. This vertical asymptote has a value close to 6 s, and corresponds to a low -3dB break frequency $f_C = 0.05$ Hz.

Inspecting the plots of Fig. 4.18(b) for the recovery slope, similar trends are seen for higher values of capacitance and input resistance. However, when $C_C > 1\mu$F, the values of the capacitive elements of the electrodes dictate the limiting condition. In this scenario the resistance R_{in} required to meet the performance specification ranges from 10 MΩ to slightly more than 5 GΩ. At higher values of R_{in} the curves converge to an asymptotic value of $C_C R_{in}$ = 2 s which corresponds to a cut-off frequency of $f_C = 0.08$ Hz.

The plots of Fig. 4.18 must be considered jointly when attempting to establish design constraints for the input resistance of the amplifier. The minimum value of R_{in} is determined by the recovery slope criterion and is given by the vertical asymptote value of R_{in} for values of $C_C > 1\mu$F. For electrode model no. 6 this is given by the most right-hand graph of Fig. 4.18(b) and is marked as the vertical dashed line on this figure. This has a value of $R_{in} = 8.2$ GΩ. The plots of Fig. 4.18(a) for the undershoot criterion determine the limiting value of time constant, $C_C R_{in}$. This is evaluated by projecting the dashed line of Fig. 4.18(b) upwards to the corresponding curve in Fig. 4.18(a) for Electrode No. 6 which is then reflected onto the ordinate axis, to give $C_C = 753$ pF. This procedure can then be repeated for individual electrode models to give the minimum values of R_{in} and C_C in each case. These values are listed in Table 4.16 for the range of electrode models considered, with corresponding values of $\tau = C_C R_{in}$ and high-pass cut-off frequency f_C.

Further analysis was undertaken in an effort to establish circuit design criteria for the ac coupled configuration of Fig. 4.16. When $R_{in} >> R_{P1}, R_{P2}$ the poles of the transfer function of this configuration are as given in (4.5.3) above. One of these poles is associated with

Table 4.16: Values of R_{in} and C_C as Determined from the Curves of Fig. 4.18 for the Range of Electrodes

Electrode No.	R_{in} (MΩ)	C_c (nF)	τ (s)	f_c (Hz)
1	255	37.9	9.7	0.033
2	421	18.5	7.8	0.041
3	131	69.8	9.1	0.035
4	329	26.5	8.7	0.036
5	189	45	8.5	0.037
6	8200	0.7	6.1	0.051
7	22.8	294	6.7	0.047
8	1.56	1210	1.9	0.16
9	60.3	104	6.3	0.05
10	44.3	139	6.2	0.051

the ac coupling of the amplifier while the others characterize the skin-electrode interface. The undershoot voltage described by (4.5.6) when normalized with reference to the pulse amplitude, V_m, and associated with the limit of 100 μV of the IEC60601 specification gives the constraint:

$$\left[K_1\left(e^{-p_1 T}-1\right)+K_2\left(e^{-p_2 T}-1\right)+K_3\left(e^{-p_3 T}-1\right)\right] \leq 0.033 \tag{4.5.8}$$

When the values of K_1, K_2 and K_3 as given by (4.5.5) are substituted, then for sufficiently high values of C_C with $p_1 \to 0$ and the constraint becomes:

$$\frac{1}{(p_3-p_2)}\left[\frac{(z_1-p_2)(z_2-p_2)\left(e^{-p_2 T}-1\right)}{p_2}-\frac{(z_1-p_3)(z_2-p_3)\left(e^{-p_3 T}-1\right)}{p_3}\right] \leq 0.033 \tag{4.5.9}$$

When the values of the poles p_1 and p_2 given by (4.5.3) are substituted the limiting value of R_{in} is obtained as:

$$R_{in} \geq 60.60\left[R_{p1}\left(1-e^{-\frac{T}{C_{P1}R_{P1}}}\right)+R_{p2}\left(1-e^{-\frac{T}{C_{P2}R_{P2}}}\right)\right] \tag{4.5.10}$$

This is effectively the value of the vertical asymptotic line in Fig. 4.18(a) when the value of C_C is very large. The recovery slope defined by (4.5.7) when normalised with regard to V_m and associated with the limit of $300\,\mu Vs^{-1}$, with $p_1 \to 0$ for large C_C gives the constraint:

$$\frac{1}{(p_3 - p_2)}\left[(z_1 - p_3)(z_2 - p_3)\left(e^{-p_3 T} - 1\right) - (z_1 - p_2)(z_2 - p_2)\left(e^{-p_2 T} - 1\right)\right] \leq 0.1 \tag{4.5.11}$$

If it is assumed that for large values $C_C >> C_{P1}, C_{P2}$ and the values of the poles p_1 and p_2 given by (4.5.3) are substituted a second limiting value of R_{in} is obtained as:

$$R_{in} \geq 20\left[\frac{\left(1 - e^{-\frac{T}{C_{P1}R_{P1}}}\right)}{C_{P1}} + \frac{\left(1 - e^{-\frac{T}{C_{P2}R_{P2}}}\right)}{C_{P2}}\right] \tag{4.5.12}$$

This, in fact, corresponds to the right hand sloped asymptote of Fig. 4.18(b). The right hand sloped asymptotes of Fig. 4.18 can also be found for $R_{in} >> R_{P1}, R_{P2}$. Under this condition the poles p_2 and p_3 merge with the zeros z_1 and z_2 respectively so that these cancel each other out. The undershoot and recovery slope expressions of (4.5.6) and (4.5.7) when normalised then simplify to:

$$\frac{V_{in}(t)}{V_m} = -K_1\left(e^{-p_1 T} - 1\right) \tag{4.5.13}$$

and

$$\frac{1}{V_m}\frac{dV_{in}(t)}{dt}|_{t=T} = -K_1 p_1\left(e^{-p_1 T} - 1\right) \tag{4.5.14}$$

When the performance criteria of IEC 60601 standard are imposed, limiting values of the time constant $C_C R_{in}$ as determined by the undershoot and recovery slope constraints are obtained as:

Undershoot requirement:

$$C_c R_{in} = 6.37s \tag{4.5.15}$$

Recovery slope requirement:

$$C_c R_{in} = 2s \tag{4.5.16}$$

These values are the right-hand convergence asymptotes of Figs. 4.18 (a) and (b) respectively and the asymptotic values are the same as those of the single-pole-high-pass-filter.

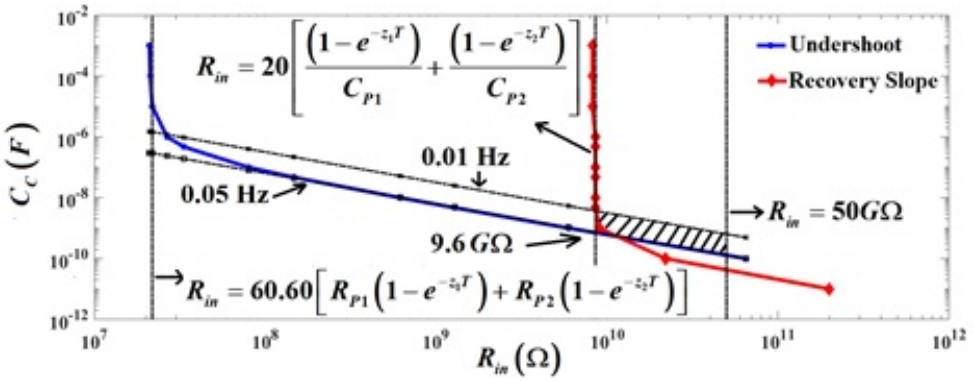

Figure 4.19: Solution Space for Time Constant $C_C R_{in}$.

The undershoot and the recovery slope curves have been extracted from Figs. 4.18(a) and 4.18(b) for Electrode No. 6 that has the highest asymptotic value of input resistance and are shown together in Fig. 4.19. The values of R_{in} and C_C used must be associated with a coordinate located above and to the right-hand side of both plots in Fig. 4.19 in order to satisfy the IEC 60601 standard. There is a maximum value of resistance that can be implemented in a practical circuit and a minimum tolerable cut-off frequency, f_C. These are illustrated arbitrarily as dashed lines $R_{inMAX} = 50$ GΩ and $f_{CMIN} = 0.01$ Hz in Fig. 4.19. This essentially generates a solution space within the hatched area of this figure. From a design point of view, the most desirable outcome is to locate the $C_C R_{in}$ coordinate in the lower left-hand portion of the hatched area so that values of both R_{in} and C_C are a minimum. Therefore the point at which the two plots cross in Fig. 4.19 is of interest. This corresponds to values of R_{in} and C_C that satisfy both undershoot and recovery slope criteria simultaneously. If (4.5.6) and (4.5.7) are normalized with respect to V_m then equated to the limits of IEC 60601, and if (4.5.6) is multiplied by the pole p_1 in order to match the equations dimensionally, this yields

the simultaneous equations:

$$\left[K_1 p_1 \left(1 - e^{-p_1 T}\right) + K_2 p_1 \left(1 - e^{-p_2 T}\right) + K_3 p_1 \left(1 - e^{-p_3 T}\right)\right] = 0.033 p_1 \tag{4.5.17}$$

$$\left[K_1 p_1 \left(1 - e^{-p_1 T}\right) + K_2 p_2 \left(1 - e^{-p_2 T}\right) + K_3 p_3 \left(1 - e^{-p_3 T}\right)\right] = -0.1 \tag{4.5.18}$$

Subtracting (4.5.17) from (4.5.18) with the K coefficients as in (4.5.5) substituted gives:

$$(z_1 - p_2)\left(1 - e^{-p_2 T}\right) + (z_2 - p_3)\left(1 - e^{-p_3 T}\right) = 0.1 - 0.033 p_1 \tag{4.5.19}$$

Fig. 4.19 shows that the plot for undershoot has converged to its asymptote prior to cross-over of the two curves. The value of $p_1 = 1/C_C R_{in} = 0.314 s^{-1}$ corresponding to $f_C = 0.05$ Hz can be substituted into (4.5.19) to give:

$$(z_1 - p_1)\left(1 - e^{-p_2 T}\right) + (z_2 - p_3)\left(1 - e^{-p_3 T}\right) = -0.089 \tag{4.5.20}$$

When the zeros and poles as defined by (4.5.2) and (4.5.3) respectively, with $p_1 = 0.314 s^{-1}$, are substituted into (4.5.20) this gives finally:

$$R_{in} = 22.47 \left[\frac{\left(1 - e^{-\frac{T}{C_{P1} R_{P1}}}\right)}{C_{P1}} + \frac{\left(1 - e^{-\frac{T}{C_{P2} R_{P2}}}\right)}{C_{P2}}\right] \tag{4.5.21}$$

For Electrode Model No. 6 represented by the plots in Fig. 4.19, this is a value of $R_{in} =$ 9.6 GΩ which is somewhat greater than the asymptotic value of 8.2 GΩ. Table 4.17 lists the values of R_{in} and C_C for all electrode models as evaluated from (4.5.15) and (4.5.21) in addition to the closest values that can be made up by combining commercially obtainable components.

To verify the findings of simulations for all of the electrodes investigated, bench tests were again undertaken. The same test set-up was used as in the case of dc coupling in the previous section. The narrow pulse of Fig. 2.13 was used as input signal to the circuit of Fig. 4.16 using the highest values of input resistance, $R_{in,near} = 10$ GΩ and $C_{C,near} = 680$ pF present in Table 4.17. The undershoot and recovery slopes were determined for all models from the

Table 4.17: Values of R_{in} and C_C from (4.5.15) and (4.5.21) and Nearest Commercially Available Values

Electrode No.	R_{in} (MΩ)	C_c (nF)	$R_{in,near}$ (MΩ)	$C_{C,near}$ (nF)
1	285	22	300	24
2	470	14	500	12
3	145	44	200	47
4	366	17	400	20
5	210	30	250	32
6	9600	0.66	10000	0.68
7	25.6	248	30	260
8	17	383	20	380
9	68	94	100	100
10	50	127	50	120

Table 4.18: Undershoot and Recovery Slope Values Measured for all Electrodes in the Constructed Circuit

Electrode No.	Undershoot (μV)	Recovery Slope (μV/sec)
1	70	27
2	60	15
3	40	21
4	83	26
5	50	31
6	37	27
7	88	25
8	36	42
9	96	30
10	83	25

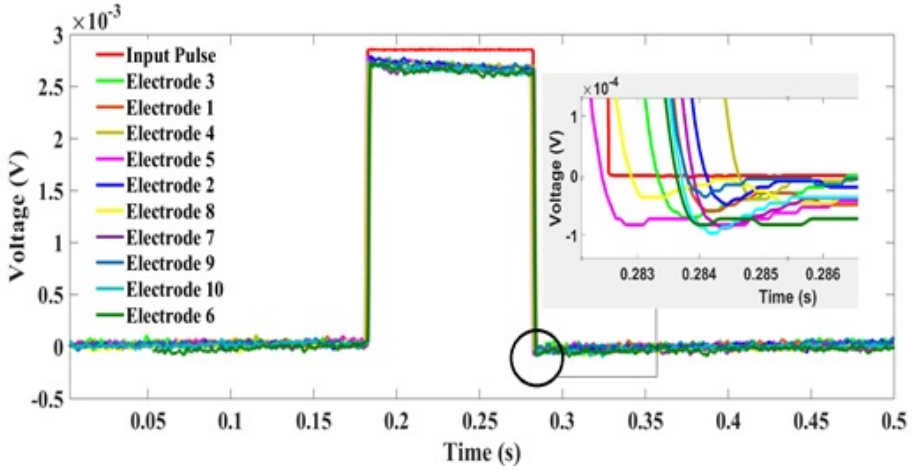

Figure 4.20: Bench Measured Pulse Response for AC Coupled Double C-R Electrode Models.

recorded waveforms and are listed in Table 4.18. All of these values lie within the limits demanded by the IEC 60601 specification. Waveforms of the signal voltages recorded at the amplifier input are shown in Fig. 4.20 and confirm that there are no violations of the IEC 60601 performance criteria. Waveforms obtained in response to the real PhysioNet ECG signal for the same values of $R_{in,near}$ = 10 GΩ and $C_{C,near}$ = 680 pF for each electrode model are shown in Fig. 4.21. These waveforms show no identifiable distortion that would interfere in any way with clinical assessment. This provides practical circuit-based validation of the results of simulation. Previous research [8, 134] suggests that double time-constant model is much more accurate and therefore equations (4.5.10) and (4.5.12) will be used to determine the amplifier input impedance.

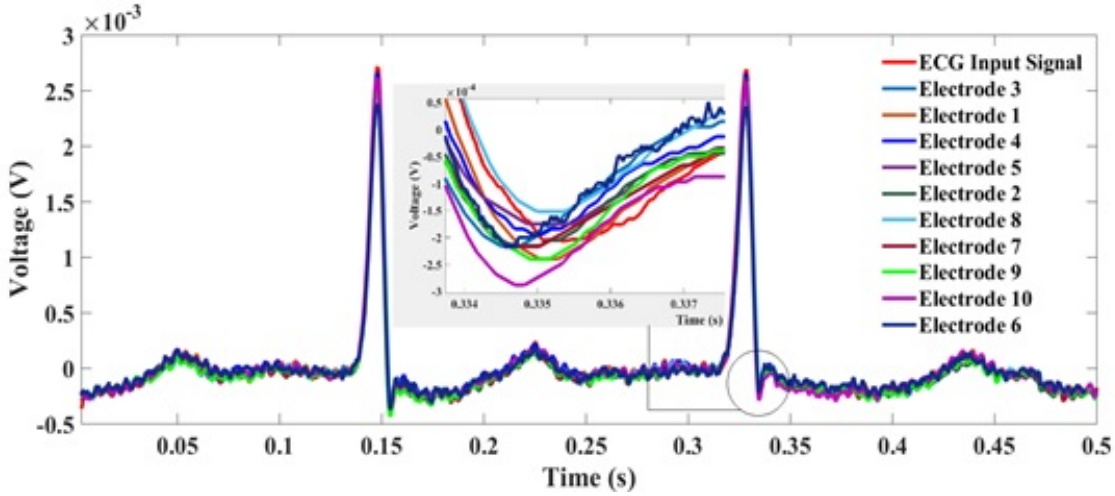

Figure 4.21: Bench Test Responses to PhysioNet ECG Signal of 120 bpm of all Electrode Models with Component Value of C_c = 680 pF and R_{in}= 10GΩ.

4.6 The Common-Mode Rejection Ratio (CMRR)

The other major factor which influences the input impedance required in the ECG amplifier is the ability of the amplifier to suppress common-mode interfering signals in favour of the wanted differential mode signal. This is shown in Fig. 4.22 for an instrumentation amplifier having two input signals V_1 and V_2. Both of these input signals have a differential and a common-mode component. The common-mode signal is generally unwanted interference often generated by the mains power supply or mains operated equipment in the vicinity of the measurement environment. The wanted signal is the differential signal which appears as the difference between the potentials at each terminal. The common-mode and the differential mode may have dc and ac components associated with them.

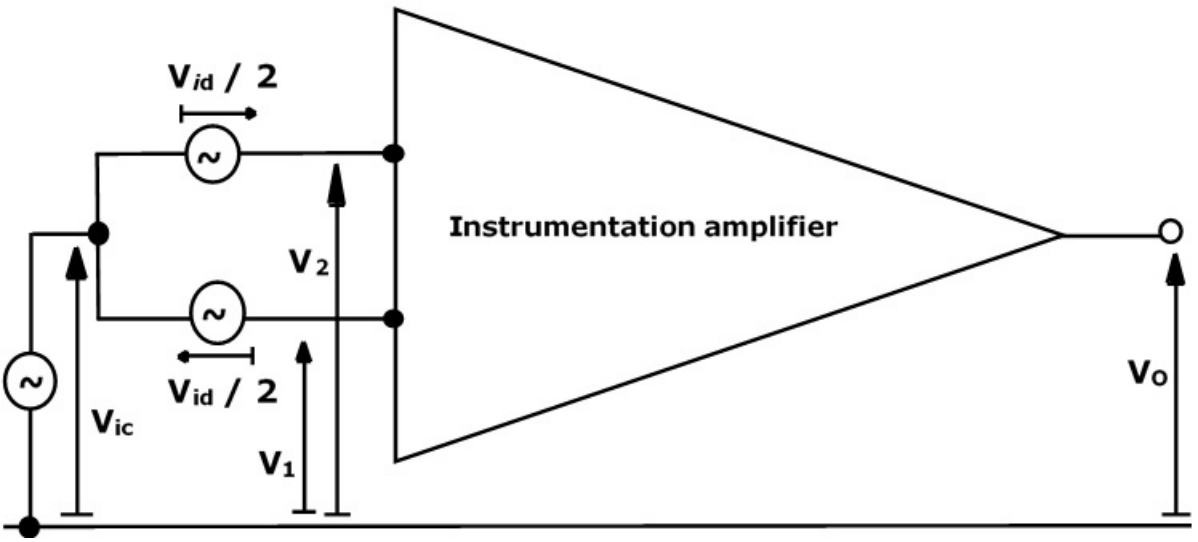

Figure 4.22: CMRR Measurement of Instrumentation Amplifier.

From Fig. 4.22, we have by definition:

$$V_{ic} = \frac{V_1 + V_2}{2} \quad ; \quad V_{id} = V_2 - V_1 \tag{4.6.1}$$

so that:

$$V_2 = V_{ic} + \frac{V_{id}}{2} \quad ; \quad V_1 = V_{ic} - \frac{V_{id}}{2} \tag{4.6.2}$$

In an ideal instrumentation amplifier the common-mode interfering signal would be suppressed completely and the differential signal would be amplified by the designated gain of the amplifier. In practice, however, the common-mode signal is not completely suppressed and receives some gain in passing through the amplifier so that it contributes to the output signal present.

The output voltage of the first stage of a instrumentation amplifier can be described as:

$$V_o = A_d V_{id} + A_c V_{ic} \tag{4.6.3}$$

where A_d represents the differential gain and A_c denotes the common-mode gain of the amplifier.

The CMRR is a measure to quantify the ability of the amplifier to suppress the common-mode interfering signal and is defined as:

$$CMRR = \frac{A_d}{A_c} \tag{4.6.4}$$

There are a number of factors which influence the overall CMRR attained in a instrumentation amplifier. Among the most important are: mismatch of source and input impedance at the input of the amplifier; manufacturing tolerances in gain determining resistors; and the CMRR of the op-amp used in the instrumentation amplifier. These factors have been well documented and have been comprehensively analysed in the literature [4, 8]. The first factor is discussed in this chapter as it directly affects the input impedance required in the ECG amplifier.

4.6.1 Impedance Mismatch

The input stage of the ECG amplifier can be modelled as shown in Fig. 4.23. The source impedances designated as Z_S and Z_S are associated with each electrode at an input terminal of the amplifier. Dry ECG electrodes exhibiting higher impedance will demonstrate significant variation from one electrode to another, hence generating a significant mismatch. The common-mode input impedance between each input terminal of the amplifier and ground is

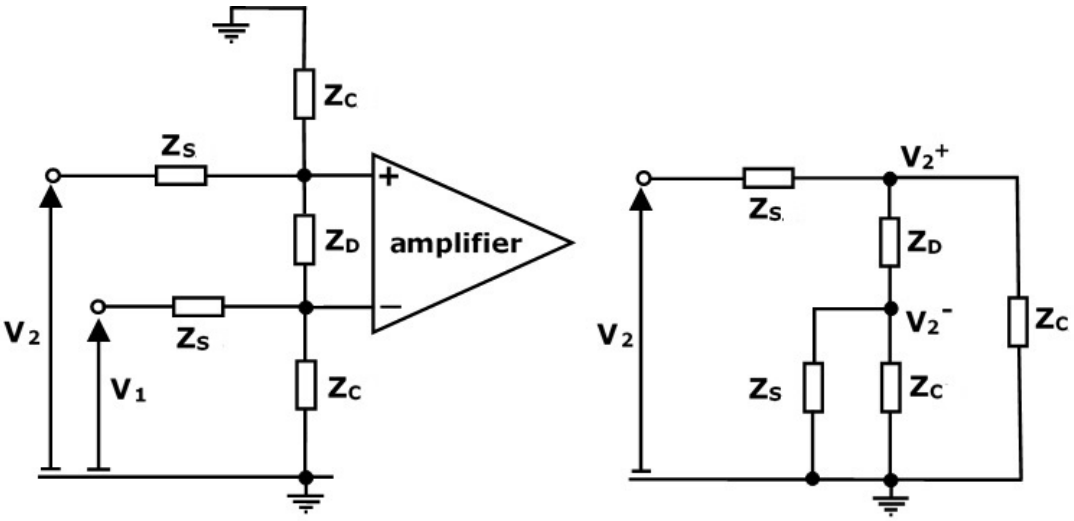

Figure 4.23: Equivalent Input Impedance Circuit of an ECG Amplifier.

represented by Z_C and Z_C. This input impedance can also be slightly different on each side. The differential input impedance will consist of a fixed impedance between the input terminals of the amplifier and is designated as Z_D. A mismatch in the electrode and common-mode impedances leads to the applied common-mode input signal being effectively converted into a differential component at the input to the amplifier. This differential component will subsequently be given the full differential gain in passing through the amplifier and will give rise to an error in the overall output signal of the ECG amplifier.

The CMRR due to the input impedance mismatch can be defined as the ratio of the magnitudes of the differential and and common-mode gains [4, 8] so that:

$$CMRR_{\Delta Z} = \left|\frac{A_{dZ}}{A_{cZ}}\right| = \frac{Z_c + Z_s}{2Z_s\left(\Delta_c + \Delta_s\right)} \tag{4.6.5}$$

The common-mode input impedance should be made much higher than the source impedance in order to prevent unnecessary attenuation of the input signal. Therefore, $CMRR_{\Delta Z}$ with $Z_c, Z_D >> Z_s$ can be closely approximated as:

$$CMRR_{\Delta Z} = \left|\frac{A_{dZ}}{A_{cZ}}\right| = \frac{Z_c}{2Z_s\left(\Delta_c + \Delta_s\right)} \tag{4.6.6}$$

and in decibels as:

$$CMRR_{\Delta Z}|_{dB} = 20log_{10}\frac{|Z_C|}{|Z_S|} + 20log_{10}\frac{1}{2\left(\Delta_C + \Delta_S\right)} \tag{4.6.7}$$

Examining (4.6.7), it is apparent that the ratio of the common-mode impedance to source impedance must be as high as possible in order to boost the overall CMRR performance of the amplifier. (4.6.7) can be modified to give the required common-mode impedance in order to realise a desired CMRR expressed in absolute terms:

$$Z_c = 2\left(\Delta_c + \Delta_s\right) CMRR_{\Delta Z} Z_s \tag{4.6.8}$$

If the input common-mode impedance is taken as purely resistive and Z_D is very high then the input resistance of the instrumentation amplifier is essentially $R_{in} = 2R_c$.

Then a constraint for the required input resistance in terms of the component mismatch at the input of the amplifier and the desired $CMRR_{\Delta Z}$ due to this limitation can be given as:

$$R_{IN} \geq 4\left(\Delta_c + \Delta_s\right) CMRR_{\Delta Z} Z_s \tag{4.6.9}$$

4.7 Conclusion

The input impedance requirements of ECG amplifiers have been investigated in the light of the transient response specification in the IEC 60601 performance standard. Several electrode models reveal that violations of this standard occur when the minimum input impedance of 10 MΩ recommended in it is used. Signal distortions take the form of S-wave exaggeration and depression of the S-T segment which could be misinterpreted clinically as signs of myocardial ischemia or the onset of myocardial infarction.

Simulations carried out on a number of electrode models indicate that an input impedance in excess of 3 GΩ, with a high-pass cut-off frequency of no greater than 0.05 Hz is necessary to avoid distortion. The conditions given by (4.3.9), (4.3.11) and (4.3.20) can be rounded

to allow a safety margin and to give convenient figures to act as constraints to determine the amplifier input resistance required with any particular electrode. This gives for the single time-constant electrode model:

$$R_{in} \geq \frac{25\,\text{sec}}{C_P} \qquad or \qquad R_{in} \geq 60R_P \tag{4.7.1}$$

whichever is the greater, and

$$C_c R_{in} > 6s \tag{4.7.2}$$

In case of double time-constant electrode model, the constraints are:

$$R_{in} \geq 60\left[R_{p1}\left(1 - e^{-\frac{T}{C_{P1}R_{P1}}}\right) + R_{p2}\left(1 - e^{-\frac{T}{C_{P2}R_{P2}}}\right)\right] \tag{4.7.3}$$

or,

$$R_{in} \geq 25\left[\frac{\left(1 - e^{-\frac{T}{C_{P1}R_{P1}}}\right)}{C_{P1}} + \frac{\left(1 - e^{-\frac{T}{C_{P2}R_{P2}}}\right)}{C_{P2}}\right] \tag{4.7.4}$$

whichever is the greater, and

$$C_c > \frac{6s}{R_{in}} \tag{4.7.5}$$

It is, of course, essential that the designer of the amplifier knows the electrical properties of the electrode to be used to measure the ECG in order to apply the constraints. These properties must either be provided by the manufacturer or be measured as outlined in the relevant literature [104, 133–135, 155–157]. This is essential if distortion of the signal and its clinical ramifications are to be avoided.

A few points should be noted in closing. Firstly, the above constraints for single time-constant models have been derived assuming that the undershoot and recovery slope curves of Fig. 4.11

overlap. The vertical asymptotes of these curves then require that:

$$R_{in} \geq \frac{20\,\text{sec}}{C_P} \qquad or \qquad C_P R_P < 0.33s \tag{4.7.6}$$

No property of the electrodes has so far been identified that can universally guarantee that this condition will be satisfied.

Similarly, for double time-constant models, the constraints presented have been derived, having assumed that the graphs of Fig. 4.19 intersect at a point where the curve for the recovery slope has reached its asymptote. This requires that the equations are such that (4.5.12) > (4.5.10) which implies:

$$20\left[\frac{\left(1-e^{-\frac{T}{C_{P1}R_{P1}}}\right)}{C_{P1}}+\frac{\left(1-e^{-\frac{T}{C_{P2}R_{P2}}}\right)}{C_{P2}}\right] > 60\left[R_{p1}\left(1-e^{-\frac{T}{C_{P1}R_{P1}}}\right)+R_{p2}\left(1-e^{-\frac{T}{C_{P1}R_{P1}}}\right)\right] \tag{4.7.7}$$

No electrical or physiological characteristics of the electrodes have thus far been identified that will guarantee that this condition is universally satisfied, but it has consistently proven to be the case in the dozens of electrodes examined.

The model parameters for the textile based electrodes examined show resistance values ranging from 260 kΩ to 28 MΩ and capacitance values ranging from 3.5 pF to 10 μF when considered in isolation. The range of time-constants for paired values of R_P and C_P spans from 5 ms to 2.65 s. The resulting skin-electrode contact impedance at the lower end of the ECG frequency spectrum for the electrodes studied reaches a maximum of 28 MΩ. The textile based electrodes studied all have varying properties for both single and double time-constant models. It is these properties that dictate the input impedance required in the recording amplifier as determined the constraints of equations (4.3.10), (4.3.12), (4.5.10), (4.5.12) and (4.6.9) Table 4.19 presents the values of the input resistance required in the case of each electrode of Table 4.1 evaluated by these constraints for both single and double time-constant models. The values of amplifier input resistance from the electrodes examined in Chapter 3 are also presented in 4.20. Table 4.19 and 4.20 also presents the input resistance required

Table 4.19: Amplifier Input Impedance Requirements, R_{in} (MΩ)

Single Time-Constant				Double Time-Constant		
Elec. No.	Undershoot	Recovery Slope	CMRR	Undershoot	Recovery Slope	CMRR
1	3	426	673.2	68	254	28063
2	58	1266	13028.4	83	418	30109
3	59	426	1320	44	129	26136
4	21	800	1923.43	94	326	31310
5	38	556	8580	62	187	36432
6	3.3	476	739.2	22	8550	4738.8
7	55	1000	12262.8	3	23	858
8	58	1400	12936	11	15	8712
9	82	1000	18480	4	61	844.8
10	235	2857	52800	2	45	409.2

Table 4.20: Amplifier Input Impedance Requirements from Electrodes examined in Chapter 3, R_{in} (MΩ)

Single Time-Constant			Double Time-Constant		
Elec. No.	Undershoot	Recovery Slope	Undershoot	Recovery Slope	CMRR
1	102	147	35	72	22440
2	660	5102	363	1750	145200
3	1680	10869	115	146	369600
4	1380	54	892	5140	303600
5	504	4237	111	118	110880
6	505	2631	378	14700	110880

to fulfill CMRR requirements as determined by constraints (4.6.9). This is done for a CMRR requirement of 80dB as outlined in IEC60601 standard. It can be seen that values of R_{in} as high as 370GΩ are listed here which are unlikely to be obtainable. However, by including a driven right leg electrode mechanism the CMRR requirements of the amplifier can be lowered and this will also be discussed in Chapter 6. Therefore, a second column is shown with values of R_{in} required for an amplifier CMRR of 80dB.

Finally, it has been assumed in the analyses that the amplifier input impedance is purely resistive. This may not always be the case and if a significant amount of capacitance is present it may affect the transient response and consequently the input impedance requirements. Moreover, no frequency response, other than ac coupling of the electrode at the input, has been attributed to the recording amplifier. An internal pole in the amplifier will also influence the transient response and the preservation of the ECG signal profile.

5 Design Overview

Previous chapters have examined the performance characteristics of ECG amplifiers intended for use with dry or un-gelled textile based electrodes in the light of meeting the IEC 60601 standard requirements. In particular input impedance and CMRR demands have been established. It has been seen that at face value an input impedance as high as 370GΩ would be required in order to meet transient response and CMRR specifications with the full range of electrodes.

This chapter will present a design overview of the ECG recording amplifier and outline a proposed multi-stage architecture. The nature of the textile electrodes and the elasticated vest to be used with them is discussed in advance of circuit design proposals. The orginal target performance specification for the amplifier is given in Table 2.6.

5.1 Elasticated Vest

5.1.1 Choice of Electrode Material and Fitting

The electrodes will form an intrinsic part of the vest so that it can be removed and put back on at will with the electrodes maintaining the correct positioning on the body. This will allow the user to remove the vest to take a shower and to put it on again. It must also be comfortable to allow it to be worn during sleep. Electrical characterisation of the textile electrodes as discussed in Chapter 3 leads to the conclusion that the self-constructed silver-woven fabric electrode (Electrode No.2) shows the most promising results in terms of having lower skin-electrode impedance and noise voltage as shown in Table 3.1. Therefore,

four of these electrodes were constructed as shown in Fig. 5.1(b).

5.1.2 Nature of the Vest

(a) Nike Pro Vest for men (b) Electrodes stitched on the vest

Figure 5.1: Self constructed round shaped textile-based electrodes mounted the Nike vest.

The proposed vest is to be constructed using a highly elasticated material so that it will be a snug body-tight fit and correctly shaped to provide sufficient tension to hold the electrodes in place and give adequate skin contact. This will take a form similar to the body-fit vest worn by rugby players as manufactured by the Nike or Cambridge sportswear companies. The Nike Pro Vent vest for men was selected as suitable for investigative prototype purposes, as shown in Fig. 5.1(a). It was modified to incorporate the fabric-based electrodes as an integral part of the vest. These were stitched into the vest at the correct positions for obtaining the ECG lead signals needed for clinical diagnostic and evaluation purposes. Fig. 5.1(b) shows a photo of the vest with electrodes mounted.

5.1.3 Optimal Placement and Location of Electrodes

Optimal placement of electrodes is essential in minimising motion artefacts and preserving the amplitude of the ECG signal. The American Heart Association (AHA) recommends that the wrists and ankle electrodes are moved to the arm and leg with the subject in supine position. The standard suggests to placing the arm electrodes closer to the shoulders and

the leg electrodes below the umbilicus [158]. Thackor and Webster in 1985 [159] studied 15 thoracic locations to identify the electrode pairs that would generate the best signal to noise ratio. The study concluded with the findings that the placement of the upper electrodes on the sternum produces the lowest movement artefacts. In addition, the highest level of QRS amplitude occurs for the thoracic equivalent of a lead II configuration. Different studies were also conducted examining the relative signal strength of closely spaced electrodes [160–162]. It was shown that both electrode orientation and distance significantly influence the ECG signal. Takuma et.al [163] used a similar approach where the electrodes were placed on the anterior acromial region and anterior superior iliac spine to reduce motion artefacts. The experiment carried out on 30 subjects showed no significant difference in the profiles of P, QRS complex, ST and T waves between the proposed lead system and standard suppine electrocardiography.

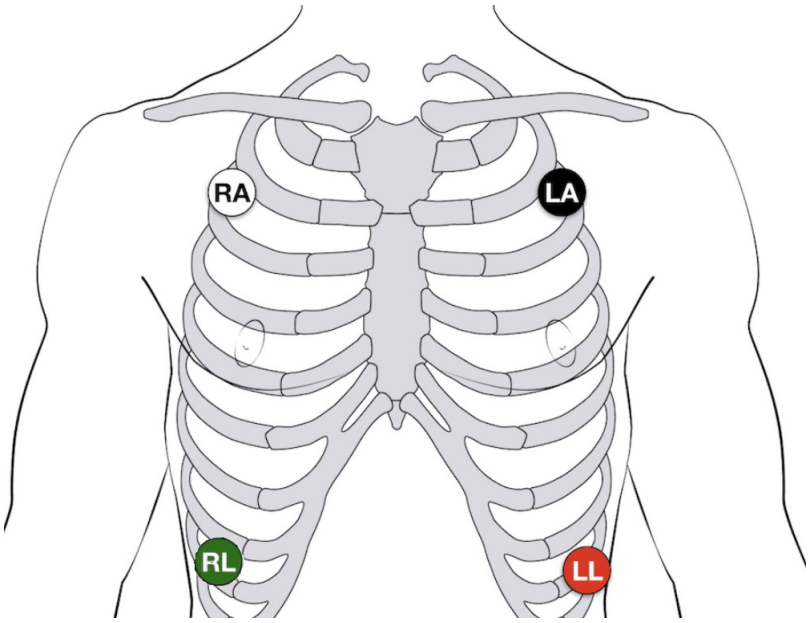

Figure 5.2: Placement of the electrodes in standard Holter Monitoring System (modified from [23]).

A study carried out by Drew et al [164] recommends the placement of the right arm (RA) electrode in the infraclavicular fossa close to the right shoulder, the left arm (LA) electrode in the infraclavicular fossa close to the left shoulder, and the left leg (LL) electrode below the rib cage on the left side of the abdomen. The ground or reference electrode (RL) can be placed anywhere, but it is usually placed on the right side of the abdomen. These positions

shown in Fig. 5.2 have been used for years in Holter monitor recordings. They were modified for the elasticated vest by moving the shoulder electrodes inwards slightly to maintain better skin contact. This can be seen in Fig. 5.2.

In our design, we intend to use a bipolar lead setup approach to record potential difference between two electrodes. A third electrode at the abdominal equivalent of the right leg position acting essentially as a ground lead will be connected to an external circuit known as the right-leg-drive to suppress the common mode interference.

5.2 Previous ECG Amplifiers for Dry ECG Electrode Recording

The first generation of a low-power ECG amplifier for use with dry electrodes was developed by Burke [24] in the department of Electronic & Electrical Engineering, Trinity College Dublin. The portable amplifier powered by a 5V single source supply was designed and tested to record heart-rate using dry-electrodes. A schematic diagram of the ECG amplifier is shown in Fig. 5.3 . It was used with dry, un-gelled electrodes made of a conductive rubber material in a tight fitting belt worn around the chest. It must be stressed that all the measurements from henceforth were performed using battery negative as ground.

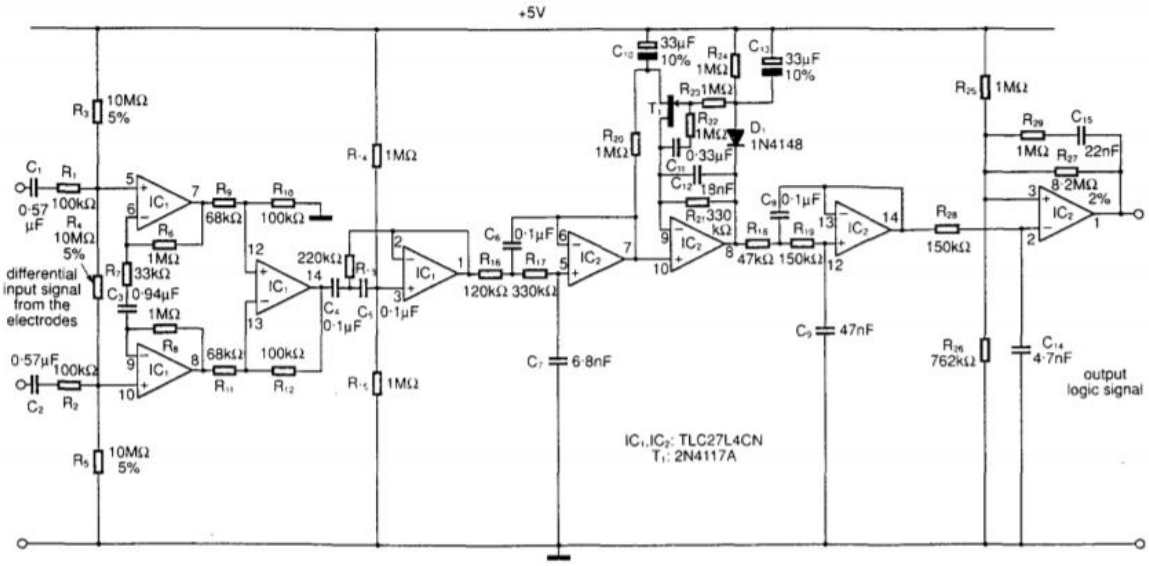

Figure 5.3: Schematic Diagram of the preamplfier by Burke [24]

The amplifier provided a 3 dB bandwidth of 7-30Hz as the signal profile did not need to be preserved to measure only heart rate. This helped to reduce motion artefact. The rejection ratio for 50 Hz power line interference was measured at 90 dB at a signal heart-rate of 100 beats/min. The amplifier also incorporated an automatic gain control stage to reduce output signal variation. The amplifier current consumption was 120μA from a 5V supply giving a power consumption of 600μW. The input impedance was measured at 18MΩ but pulse response and noise level were not measured as the current IEC60601 performance standards were not applicable. Nevertheless, the amplifier provided strong foundation for dry electrode ECG recording with low power technology.

Burke & Gleeson [20] developed the circuit shown in Fig. 5.4 which used a resistive boot-strapped amplifier operating from a single supply rail of 3.3V to boost the input impedance of the amplifier. The input impedance on each side of the amplifier is governed by resistors R_3 and R_4 and the feedback provided by R_8-R_{11} in combination with the dc biasing network. The positive feedback to the bottom of resistors R_3 and R_4 makes the magnitude of these resistors appear much higher at the input terminals of the amplifier.

The nominal input impedance at each terminal of the circuit structure can be closely approximated as:

$$R_{in} = R_3 \left[R_8 + \frac{R_5 // (R_6 // R_8)}{R_8} \right] \left[1 + \frac{R_6 + R_8}{R_5} \right] \tag{5.2.1}$$

The main advantage of this architecture is the facility to assign the dc bias using the biasing resistors R_5, R_6 and R_7. The authors report to have boosted the input impedance to 75$M\Omega$ with standard off-the-shelf $\pm$1% tolerance resistors. However, the boosted impedance value is far too low to have any clinical use with textile-based electrodes, where a value greater than 10GΩ is needed as determined in Chapter 4. The proposed circuit also does not meet the IEC 60601 transient response requirements [3, 22] which were not in operation at that time.

The common-mode output signal from the first stage of the amplifier is sensed by resistors R_{12} and R_{13}. This common-mode signal is inverted and amplified by op-amp A_6 and then fed back to the right leg electrode via resistor R_{21} and capacitor C_s. This arrangement subtracts the

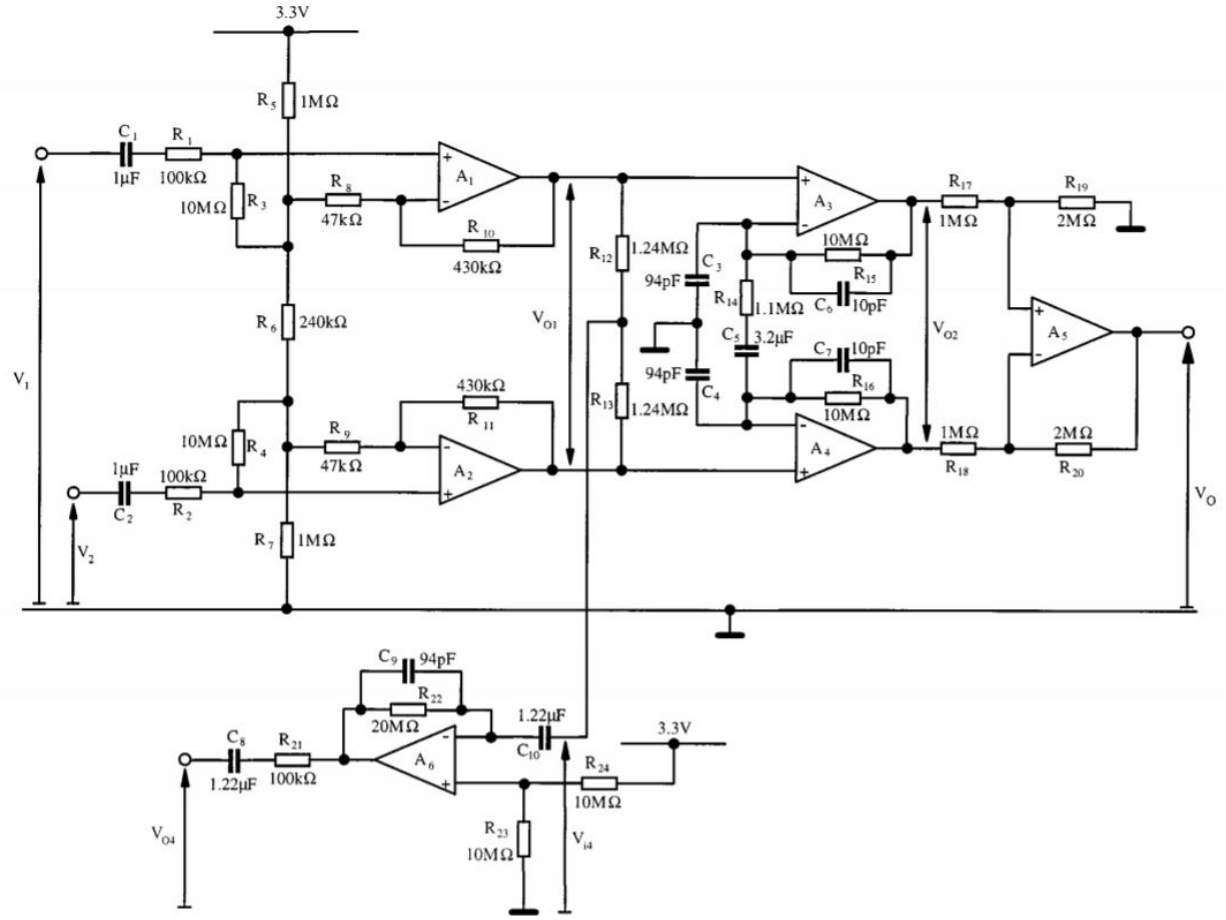

Figure 5.4: Schematic Diagram of the preamplfier by Burke & Gleeson [20]

sensed common-mode interfering signal from that present at the amplifier input and effectively increases the overall CMRR by a factor equal to the gain of the inverting amplifier stage which was set to 30dB. However, implementation of high gain in right leg drive can introduce instability [165] in the amplifier in the case of low-power op-amps. Considering a source impedance imbalance of $\pm 33\%$ at the skin-electrode interface with a worst case skin-electrode impedance Z_s=10MΩ yields $CMRR_{\Delta Z}$=32dB. Consequently, the overall CMRR performance of the amplifier is below 65dB even with the addition of the right leg drive. The amplifier CMRR without the right leg drive circuit was measured at 55dB throughout its bandwidth, with an skin-electrode impedance of less than 1.5MΩ. The CMRR of the amplifier with the inclusion of the active right leg drive was measured at 88dB. An input referred peak-to-peak noise level of 50μV ptp was measured which falls outside the IEC60601 acceptable limit of 30μV ptp.

Later, Assambo & Burke [8, 25] designed an ultra low-power ECG preamplfier that provides adequate signal quality in the light of the transient system IEC60601 performance requirements introduced in 2011 [3] as shown in Fig. 5.6. The main difference between this design and the

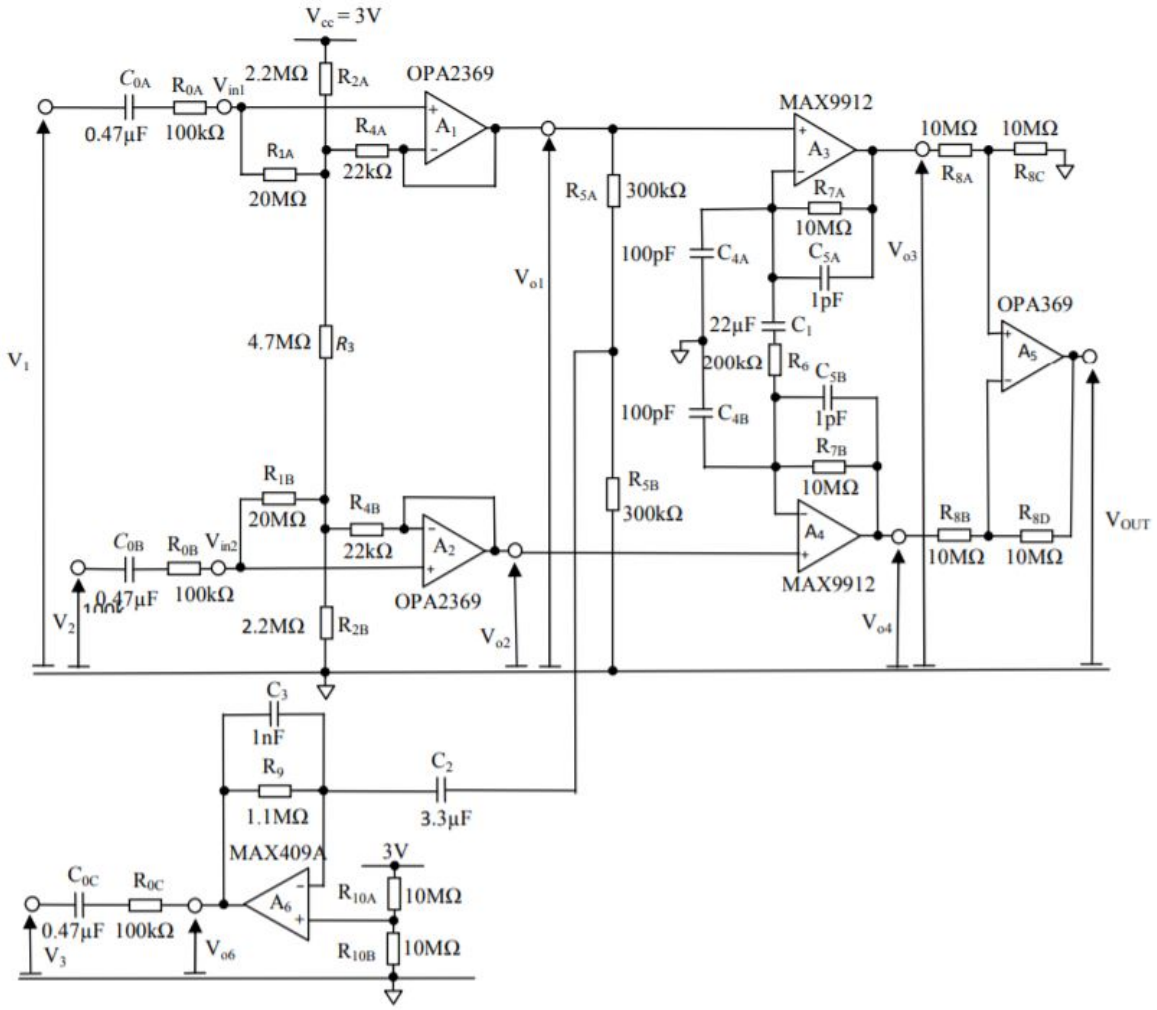

Figure 5.5: Improved amplifier front-end implementing input impedance boosting [25]

design of Burke & Gleeson resides in the allocation of the differential gain. The differential gain in this stage has been placed entirely in the second stage. The first stage of this design acts as an impedance defining unity gain differential buffer. The use of unity gain buffers eliminated the errors from the mismatched gain determining resistors used in the previous version [20, 24] and thereby increased the CMRR.

This bootstrapping mechanism receives positive feedback from op-amps A_1 and A_2 via resistors R_{2A} and R_{2B}. The magnitude of the potential drop across resistors R_{1A} and R_{2B} is very small, making their resistance appear much higher at the amplifier inputs. The authors report to have

boosted the input impedance to 2 GΩ. However, there are few limitations with this front-end design solution. The magnitude of the input impedance with a dc blocking capacitance of 0.47 μF yields a time-constant value of 940 s. Therefore, there a large initialisation time delay before an ECG signal can be recorded. The op-amps (OPA369) used in the first stage have white noise levels of 290 nV/$\sqrt{Hz}$ as quoted by the manufacturer. Noisy op-amps coupled with unity gain buffers at the front-end of the amplifier produced high levels of noise voltage at the amplifier output measured at 200μV ptp. The design therefore fails to meet the IEC 60601 input referred peak to peak noise specification and does not satisfy the requirements for a clinical quality ECG signal. Therefore, it is a more appropriate design strategy to allocate significant portion of the overall differential gain to the first stage of the amplifier. This will help to preserve the signal-to-noise ratio from input to output.

5.3 Proposed 4th generation architecture

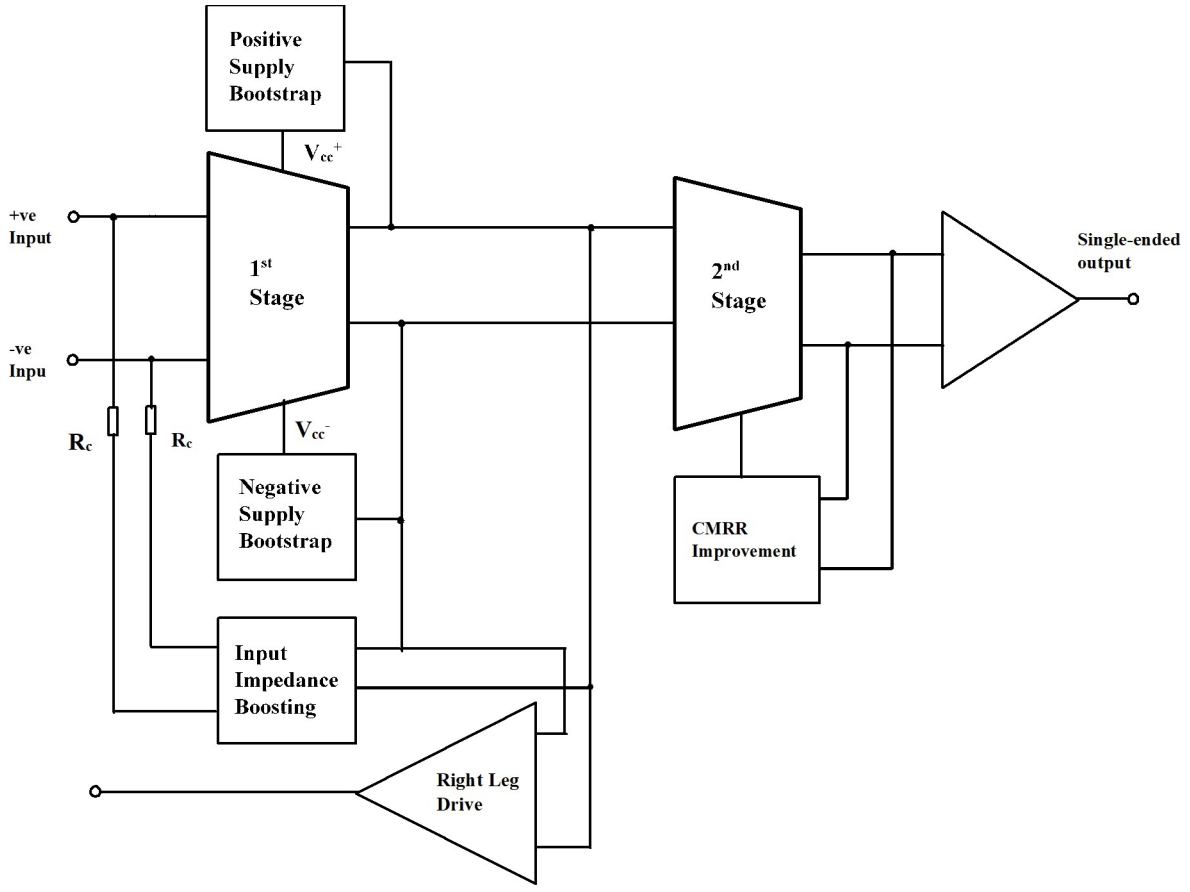

Figure 5.6: Block Diagram of the proposed ECG Amplifier

Fig, 5.6 shows a block diagram of the proposed version of the ECG amplifier. The front end of the preamplfier will have high input impedance obtained by bootstrapping the output signal back to the input resistors. Bootstrapping of the power supply will also be used to minimise the effects of the input capacitance of the op-amps. The design of the circuitry implementing the bootstrapping will be discussed in detail in Chapter 6. Unlike the amplifier used by Assambo & Burke, this version will see a distribution of gain between the first and second stages of the amplifier. Boosting the input impedance at the front end stage of the amplifier is crucial in obtaining high CMRR. The overall CMRR of the pre-amplfier is limited by the magnitude of the source impedance associated with the dry electrodes previously characterised. An active right leg drive with a gain of 20dB will be used to provide high immunity to common-mode interference in the presence of high skin-electrode impedance [165]. In addition, it is also intended to use 0.1% tolerance resistors to significantly reduce any errors from gain determining resistors. The CMRR performance of the amplifier will be discussed in detail in Chapter 7. The final stage provides a differential to single-ended signal conversion with unity gain.

5.4 Selection of low-power Op-amps

The circuit design is intended to use of ultra-low power op-amps to ensure that the total current consumption of the pre-amplifier is below 500μA. A summary of the essential electrical characteristics considered in the selection of suitable commercially available op-amps for implementing a single-supply instrumentation amplifier is presented in Table 5.1. The selection of op-amps for the proposed design was then dictated by the performance considerations outlined below.

Input Impedance and CMRR performance

The ability of the amplifier to suppress common-mode interfering signals can be achieved by selecting op-amps quoting high input impedance and CMRR values in the datasheets. The proposed amplifier front-end should have large input impedance and open loop gain characteristics so as to avoid unnecessary signal attenuation and allow the use of high values

Table 5.1: Electrical Characteristics of micro powered op-amps

Parameter		unit	target	OPA379	LT6003	OPA347	OPA369	MAX409	MAX406
CMRR	min	dB	80	90	88	70	100	71	60
	typ		90	100	115	80	114	90	80
Input impedance	min	GΩ	1						
(Differential)	typ		100	10000	10	1000	10000	-	-
Input Impedance	min	GΩ	10						
(Common Mode)	typ		1000	10000	2000	1000	10000	-	-
GBP	min	kHz	20						20
	typ		50-100	90	2	350	15	500	40
white noise	min	$nV/\sqrt{Hz}$							
	typ	@ 1 kHz	<20	80	325	60	290	12	150
current noise	min	$fA/\sqrt{Hz}$							
	typ	@ 1 kHz	<20	1	12	0.7	1	1500	-
Input offset voltage	typ	mV	1	0.4	0.175	2	0.25	0.03	0.75
(Vos)	max		20	1.5	0.5	6	0.75	1.4	2
Bias current	typ	pA	<10	±5	40	0.5	10	20000	0.1
(I_B)	max		500	±50	140	10	50	180000	10
Quiescent current	min								
(I_Q)	typ	μA	<5	2.9	1	20	0.8	115	1.2
Capacitive load drive	min								
C_{Load}	typ	pF	>100	20	500	100	100	2000	-

of external resistors at the input. It is noteworthy to mention that the input impedance requirement at the second stage, which is dc-coupled to the front-end stage, is less stringent. The low-powered op-amps that have been shortlisted in Table 5.1 have a differential input impedance of over 1GΩ and common-mode input impedance of over 1000GΩ and thereby meet the input impedance target requirements. The OPA347 and the MAX 400 series have got significantly lower CMRR performance values over the OPA379 and LT6003. Therefore, the ECG amplifier design presented in this thesis uses OPA379 and LT6003.

Gain and Bandwidth (GBW) considerations

The design presented in this thesis is intended to provide a differential mid-band gain of 40dB within the ECG signal bandwidth. The first stage will provide a mid-band gain of approximately 17dB and the second stage of 23dB. It is important to select op-amps in both stages of the amplifier that can guarantee sufficiently large gain bandwidth product without amplitude or phase distortion within the ECG bandwidth. The LT6003 is used for the first stage since the GBP=2kHz is sufficient to provide a gain of 7.8 over the ECG bandwidth. The GBW of LT6003 is not sufficient to provide the higher gain needed in the second stage. Therefore, the OPA379 is chosen here owing to its higher GBW product.

Noise considerations

The MAX409 has considerably higher current noise levels of up-to 150fA/$\sqrt{Hz}$. This high level of current present at the input terminals of the instrumentation amplifier, coupled with high values of source resistance and amplifier gain, may produce significant output noise voltage that would be detrimental to maintaining high signal-to-noise ratio. The MAX406 does not provide any value of current noise in the data-sheet and therefore is not used in this design. The OPA379 has lower values of current noise and voltage noise over other OPA series op-amps shown in Table 5.1. Hence, the OPA379 is used in the second and third stages of the proposed amplifier design.

Capacitive load driving ability

It is crucial that the amplifier has the ability to drive at least 100pF load capacitance without

becoming unstable. The cables and the leads connecting the electrodes to the amplifier will produce such values of capacitive load. Therefore, braided screened leads with low capacitance values (52pF/m) are used in the design. The percentage overshoot for the OPA379 in an unity gain configuration reaches almost 40% when the driving load capacitance value reaches 100pF. Similarly, the OPA369 in unity gain configuration produces almost 12% overshoot on driving a load capacitance of 100pF. The LT6003 can handle capacitive loads of up to 500pF with less than 5% overshoot. Therefore, the LT6003 is used in the front-end stage of the amplifier design to reduce risk of overshoot or instability.

6 Design of High Impedance Input Stage

6.1 Introduction

This chapter examines techniques that have been used over the years to boost the input impedance of several bio-amplifiers. However, most of these techniques are associated with high power consumption and the bandwidth over which this impedance can be maintained is also limited. A novel method using low power op-amps to extend the bandwidth over which very high amplifier input impedance can be maintained by reducing amplifier input capacitance via power supply bootstrapping is presented.

The overall input impedance of the amplifier usually has both resistive and capacitive components. The resistive component is usually determined by the nature of dc biasing structure used at amplifier input, particularly when a single rail power supply rail is involved. The capacitive component is present on account of finite input capacitance of the op-amps used to implement the front-end stage of the amplifier as well as any extraneous parasitic capacitance which may be present. The magnitude of the resistive component is ultimately limited by the dc bias currents at the input of the operational amplifiers. The common-mode input impedance cannot be boosted by merely increasing the resistor values at the input terminals of the amplifier. This is mainly due to the fact that even though the amplifier is boosted from a dc perspective, a bias current in the region of 100s of pico-amps (pA) will introduce a large offset voltage at the amplifier input. Therefore, the common-mode input impedance has to be

boosted from an AC point of view while maintaining the target bandwidth of 0.05 - 250 Hz. In order to keep offsets and dc drift to a minimum, the resistance of the input biasing network can rarely exceed 100MΩ, which is much lower than the 10GΩ input impedance required as seen by the signal source. The input capacitance of op-amps has stayed substantially constant over the past decades and tends to be in the region of 3-10pF, and is due to the capacitance between the bond pads of the op-amps and their supply rails. This capacitance is relatively small but, when combined with the high source impedance of un-gelled electrodes, it can seriously limit the signal bandwidth of a bioelectric amplifier. Both of these effects must be overcome in order to provide adequate input impedance of the amplifier over the bandwidth concerned. A basic diagram showing these issues is shown in Fig. 6.1 where R_c is the effective resistance of the input boosting network.

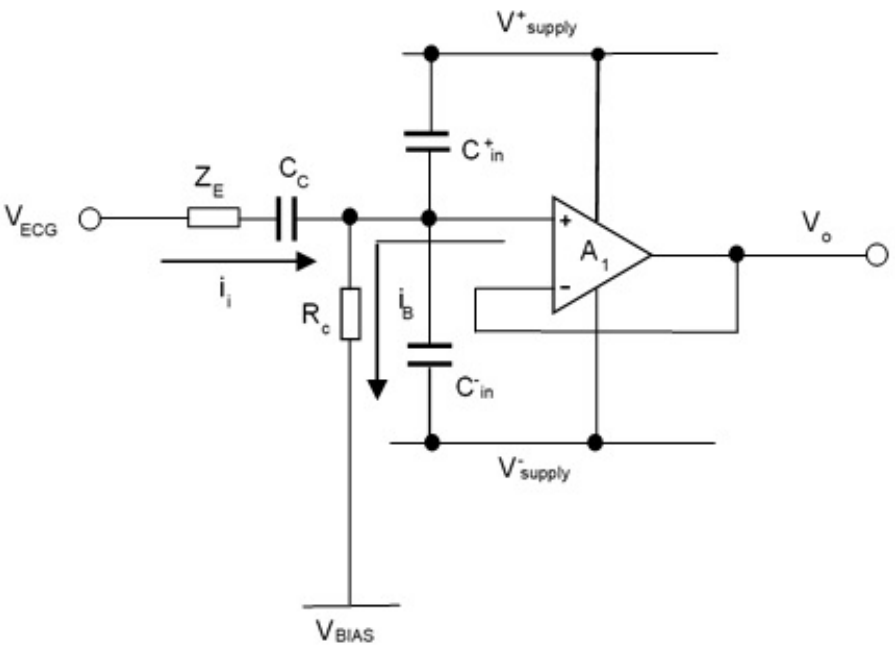

Figure 6.1: Schematic Diagram showing the issues to boost the op-amp input impedance.

6.2 Impedance Boosting Mechanism

A schematic diagram describing a basic impedance boosting technique is shown in Fig. 6.2. The amplifier has unity non-inverting gain. A fraction α of the output signal is fed back to the bottom of the input resistor R_i. The input current i_i flowing through the input resistance

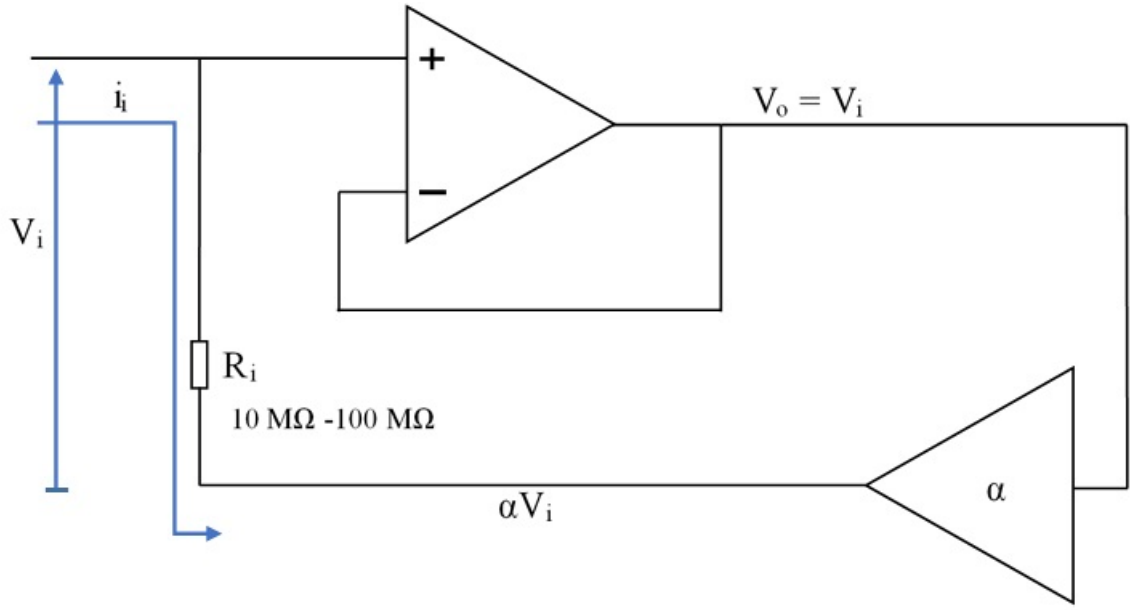

Figure 6.2: Schematic Diagram of Basic Input Impedance Boosting Mechanism.

R_i is given:

$$i_i = \frac{V_i\,(1-\alpha)}{R_i} \tag{6.2.1}$$

The boosted input impedance is:

$$Z_{in} = \frac{V_i}{i_i} = \frac{R_i}{(1-\alpha)} \tag{6.2.2}$$

The value of α should be close to unity in order to achieve a high value of boosted impedance. The target input impedance can be achieved by making $\alpha = 0.99$ and $R_i = 100M\Omega$. Therefore, a boosting ratio of 100:1 is obtained by making a 100MΩ resistor appear as 10GΩ resistance. This boosted input impedance can be maintained over the signal bandwidth using capacitance neutralisation and power supply bootstrapping.

The value of α should be chosen carefully as any value greater than unity will result in negative impedance causing instability and oscillation. Therefore, 0.1% tolerance resistors are used to ensure the magnitude of the loop gain is less than unity. The electrodes are intended to be ac-coupled to the inputs of the recording amplifier to negate the effects of large polarisation potential produced at the skin-electrode interface.

6.3 Capacitance Neutralisation

Capacitance neutralisation is an old technique used to eliminate the effect of input capacitance of op-amps as shown in Fig. 6.3. The input voltage of the amplifier as shown in 6.3 is

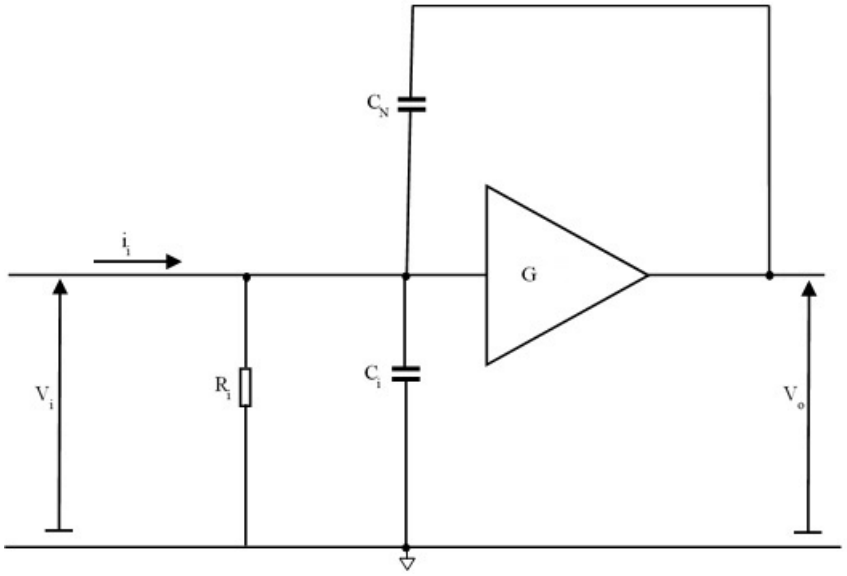

Figure 6.3: Schematic Diagram of Basic Op-amp Input Capacitance Neutralisation Mechanism.

represented as V_i and the voltage sensed at the output of the amplifier is denoted as V_o. The input capacitance is modelled as C_i and the feedback capacitance C_N is used to reduce the effect of parasitic capacitance of the op-amp. The gain of the non-inverting amplifier is set at G. The current i_i flowing into the the input impedance can be described as:

$$i_i = \frac{V_i}{R_i} + \frac{V_i}{1/j\omega C_i} + \frac{V_i - V_o}{1/j\omega C_N} \tag{6.3.1}$$

Substituting $V_o = GV_i$ in (6.3.1), the input current i_i can be further described as:

$$i_i = \frac{V_i}{R_i} + j\omega C_i V_i + j\omega C_N (V_i - GV_i) \tag{6.3.2}$$

Finally, the input impedance Z_i as a function of frequency can be expressed as:

$$Z_i = R_i + \frac{1}{1 + j\frac{\omega}{\omega_p}} \tag{6.3.3}$$

where $\omega_p = 1/[C_i - C_N(G-1)]R_i$. The magnitude of op-amp input capacitance, C_i should equal to the magnitude of $C_N(G-1)$ in order to get $\omega_p \to \infty$.

Therefore, bandwidth can be extended as the neutralising capacitance C_N cancels out the effect of the input capacitance C_i. However, it needs a close match between (G-1)C_N and C_i to be effective in extending the bandwidth. On the other hand if a mismatch in the capacitance results in (G-1)$C_N > C_i$, then the effective input impedance becomes negative and the circuit will become unstable. Hence, this method is not feasible in circuits with low values of C_i due to the difficulty in obtaining commercially available accurate small values of neutralising capacitance.

6.4 Bootstrapping Techniques

The amplifier input impedance can be significantly increased by reducing the magnitude of the input current via positive feedback. This can be achieved by using ac or dc feedback and the technique is popularly known as bootstrapping [26, 28–30]. Some of the popular bootstrapping techniques that have been used are considered below.

6.4.1 DC Bootstrapped amplifier

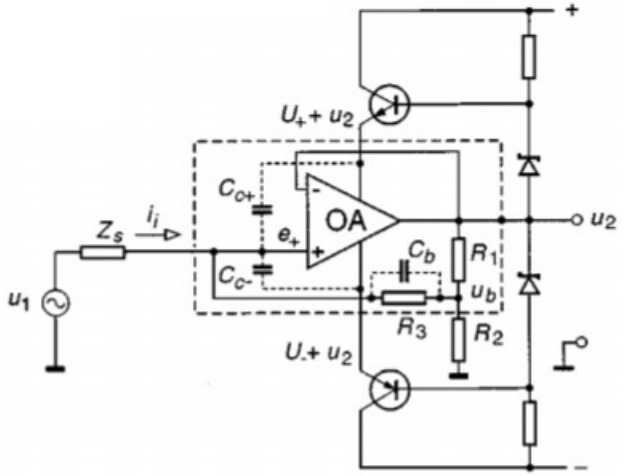

Figure 6.4: DC Bootstraped buffers with biasing resistors [26]

Lányi & Pisani [26] presented a high input impedance buffer with a bootstrapped biasing circuit as shown in Fig. 6.4 and the power supply nodes were also bootstrapped using emitter

followers. A voltage divider network formed by R_1 and R_2 is used to avoid instability of the buffer by maintaining the feedback factor less than unity. The zener diodes D_1 and D_2 provide the necessary bias voltages for the emitter followers connected to the supply pins of the op-amp OA. The input impedance of the the amplifier as shown in Fig. 6.4 can be written as:

$$Z_i = \frac{1 + A_{ol}(s)}{A_{ol}(s)} \left[\frac{1}{\frac{1}{R_3'} + \frac{1}{A_{ol}(s)} \left(\frac{1}{R_3} + \frac{1}{X_i} \right)} \right] \tag{6.4.1}$$

where A_{ol} is the open loop gain of the op-amps, X_i is the input reactance and R_3' is the boosted resistance given by:

$$R_3' = R_3 \left(1 + \frac{R_2}{R_1} \right) \tag{6.4.2}$$

The authors report to have measured an input impedance as high as 350GΩ with this structure [26]. This ultra high input impedance has been achieved by making $R_3 \gg R_1, R_2$. In order to further improve the performance of the design, a capacitor can be placed in parallel with R_1. This would have created an additional pole that could have increased the high frequency bootstrapping of R_3. Nevertheless, this circuit configuration requires a large supply current to turn on the emitter followers and the zener diodes at both supply rails of the op-amp. This does not come as surprise as the supply current of the op-amp used OPA655 in Fig. 6.4 is 29 mA as quoted by the manufacturer. This circuit can not be considered applicable to the intended low-power aims of this thesis.

6.4.2 Negative Impedance Conversion

Negative Impedance Conversion commonly known as NIC is a popular technique used to boost the input impedance of an amplifier within the bandwidth of the signal of interest. Parente et.al [27] boosted the differential input impedance of the amplifier using NIC as shown in Fig. 6.5.

The input impedance of the second stage for a single NIC resistance [27] can be described

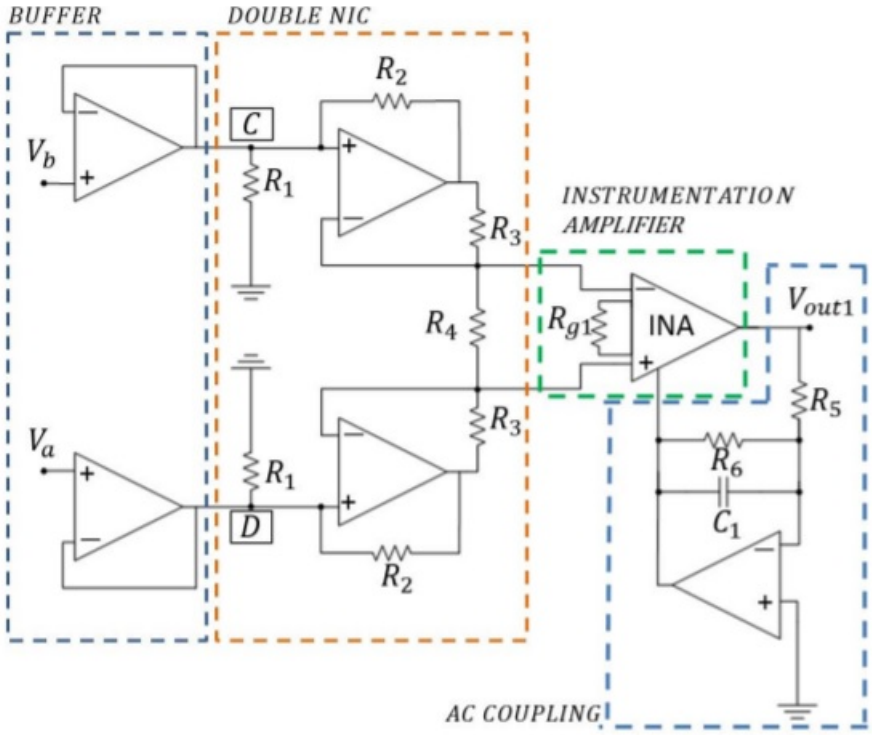

Figure 6.5: AC-Coupled Bootstraped amplfier employing Negative Impedance Conversion [27]

as:

$$R_{NIC} = -\frac{R_2 R_4}{2R_3} \tag{6.4.3}$$

Similarly, the differential input resistance at low frequency can be given as:

$$R_d = \frac{R_1}{1 + \frac{R_1}{R_{NIC}}} \tag{6.4.4}$$

Therefore, the differential input resistance from (6.4.4) can approach infinity by making $R_1 R_3 = \frac{R_2 R_4}{2}$. However, it is a good practice to keep the value of R_{NIC} less than unity to avoid instability. The authors report to have boosted the differential input impedance to 500 MΩ. However, the measured common-mode impedance value is as low as 135kΩ which is far too low for any clinical use with the dry electrodes [86, 87]. Moreover, low values of common-mode input impedance can distort an ECG signal leading to clinical misrepresentation as discussed in Chapter 4. There are several other problems associated with this design. The implemented bootstrapping has been used after the op-amp buffers, where its effectiveness

is of no value [166]. A gain value of 201 in a single stage instrumentation amplifier is too high to handle any realistic skin-electrode offset voltage of 300mV. Therefore, it is sensible to distribute the gain in two different ac coupled stages of the amplifier. The implemented bandwidth reported in the paper is from 0.2-36Hz and is not as claimed by the authors [166]. The bandwidth must be extended from 0.05-250Hz to preserve the signal morphology.

6.4.3 Bootstrapped Amplifier with Capacitance Cancellation

Hajime & Ueno [28] used a stray capacitance canceller in conjunction with a bootstrapped non-inverting amplifier (NIA) as shown in Fig.6.6 to boost the input impedance of an amplifier.

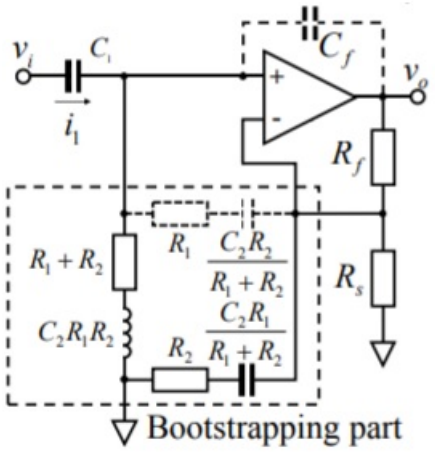

Figure 6.6: Non Inverting Bootstraped amplfier with capacitance canceller [28]

In Fig. 6.6, the capacitance C_1 represents the electrode capacitance coupled to the body surface. The feedback capacitance C_f has been used mainly to cancel the effects of the input capacitance of the amplifier. The analog front end (AFE) of the non inverting amplifier is bootstrapped by the combined resistances of R_1 and R_2. The bootstrapped circuit behaves differently for dc and ac measurements. The input impedance of the circuit is (R_1+R_2) dc wise as the capacitor C_2 will block any dc currents flowing from the output node voltage v_o. On the contrary, ac wise, the voltages seen at the two nodes located on both sides of R_1 are identical and equal to $v_oR_s/(R_f + R_s) = v_i$. This is because the voltage drop across C_2 is very small when the frequency is $f >> 1/(2C_2R_2)$. Consequently, the differential impedance

between the nodes appears to be boosted to an extremely high value. The authors report to have measured input impedance values as high as 6.4GΩ at 10 Hz. However, the magnitude of impedance drops to about 60MΩ at 250 Hz.

6.4.4 Two electrode bootstrapped amplifier

Dobrev et.al [29] presented a biopotential amplifier that bootstraps the differential input impedance via positive feedback as demonstrated in Fig. 6.7. The op-amps with ideal gain blocks have a gain coefficient of -G where G=R_2/R_1. The resistors R_{3a} and R_{3b} are connected in a crossover network from the output voltage nodes to the input pins of the differential amplifier. The differential input seen at each input terminal of the amplifier can then be expressed as $R_d = \frac{V_d/2}{I_d}$, where I_d=$I_{R1} - I_{R3}$ and $\frac{1}{R_d}$=$\frac{1}{R_1}$+$\frac{1-G}{R_3}$.

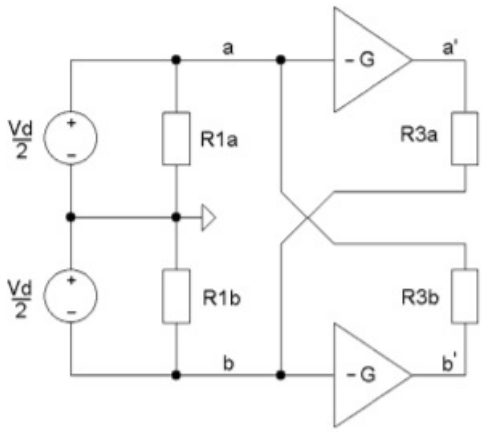

Figure 6.7: Differential mode input impedance boosting amplifier structure [29]

The differential input resistance can be further simplified as:

$$R_d = \frac{R_1 R_3}{(R_1 + R_3) - R_2} \tag{6.4.5}$$

The differential input impedance can approach infinity when $R_1 + R_3 = R_2$. The authors report to have boosted the differential input impedance to 60 MΩ using op-amps MCP607.

6.4.5 Two-Wired High Input Impedance Amplifier

Guerrero & Spinelli [30] proposed a two-wired active electrode that produces high amplifier input impedance using power supply bootstrapping. The circuit shown in Fig. 6.8 reduces the op-amp parasitic capacitance to 71fF and boosts the input impedance bandwidth to 1kHz.

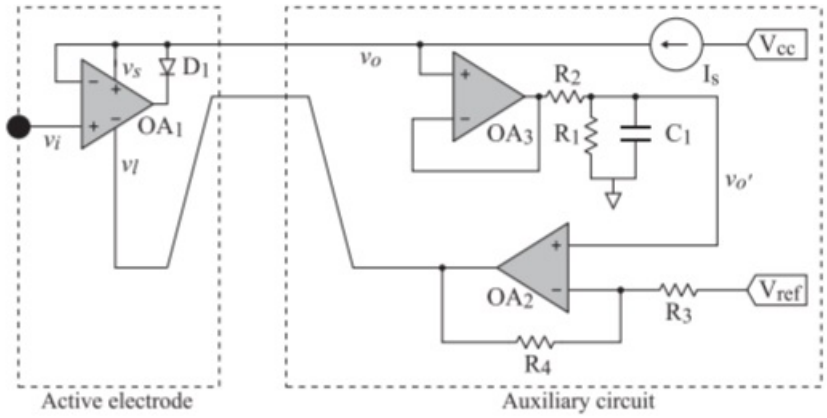

Figure 6.8: Two wired high input impedance active electrode [30]

The work relies on the subject of two-wire active electrodes for bio-potential measurements which introduces the method of biasing an active electrode with a current source. The design included a single diode D_1 and a pair of op-amps to cater for the negative power rail of the op-amp buffer OA_1. The AC signal has been superimposed on top of the positive supply rail of the buffer, OA_3. However, a difference amplifier is used to create the negative supply instead of using another current source. OA_3 is used as a buffer to prevent power-line loading and OA_2 serves as a difference amplifier that allows the input signal to be superimposed on a negative DC voltage, V_{ref}.

By this mechanism power supply bootstrapping is achieved and the input capacitance reduced, increasing the high impedance bandwidth. However, the power consumption was measured at 25mW and is one of the main limitations of this design. Therefore, any potential in this design lies in whether or not it can be adapted for low power applications.

6.5 Low-power Input Impedance Boosting

6.5.1 Bootstrapping Principle

A bootstrapping circuit with a non-inverting gain as shown in Fig. 6.9 is initially investigated to boost the amplifier input impedance. The resistors R_3 and R_4 are included to ensure the fraction α of the output voltage V_o fedback as voltage V_B is less than unity. These resistors must also be chosen to counteract the gain of stage $(1 + \frac{R_2}{R_1})$.

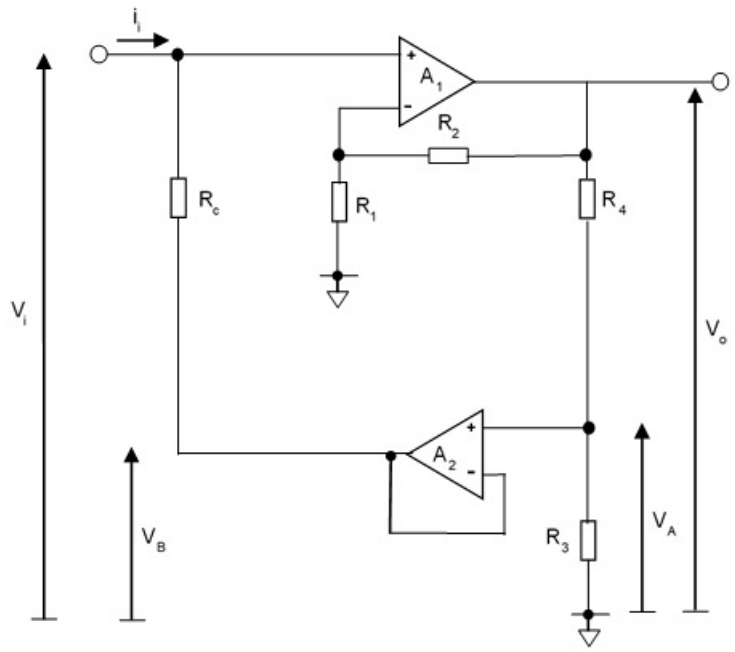

Figure 6.9: Bootstrapping Input Impedance with DC Gain.

The current i_i flowing into the non-inverting amplifier with a gain of $\frac{(R_1+R_2)}{R_1}$ can be described as:

$$i_i = \frac{V_i - V_B}{R_i} \tag{6.5.1}$$

The input resistance of the amplifier can be expressed as:

$$R_{in} = \frac{V_i}{i_i} = \frac{1}{1 - \frac{V_B}{V_i}} R_c = \frac{1}{1 - \alpha} R_c = M R_c \tag{6.5.2}$$

where M is the effective impedance multiplying factor. and,

$$\alpha = \frac{V_B}{V_i} = \frac{R_3}{R_3 + R_4} \times \frac{R_1 + R_2}{R_1} \tag{6.5.3}$$

and,

$$M = \frac{1}{1 - \alpha} \tag{6.5.4}$$

The input resistance R_{in} will approach infinity by making $\alpha \rightarrow 1$. This is possible when:

$$\frac{R_3 + R_4}{R_3} = \frac{R_1 + R_2}{R_1} \tag{6.5.5}$$

If all resistors have a manufacturing tolerance of Δ_R then (6.5.3) can be rewritten as:

$$\alpha = \frac{R_3 (1 \pm \Delta_R)}{R_3 (1 \pm \Delta_R) + R_4 (1 \pm \Delta_R)} \times \frac{R_1 (1 \pm \Delta_R) + R_2 (1 \pm \Delta_R)}{R_1 (1 \pm \Delta_R)} \tag{6.5.6}$$

A worst case condition exists when R_2/R_1 is high and R_3/R_4 is also high. Considering:

$$\begin{aligned} &R_1 = R_1 (1 - \Delta_R) \quad ; \quad R_2 = R_2 (1 + \Delta_R) \quad ; \quad R_3 = R_3 (1 + \Delta_R) \\ &R_4 = R_4 (1 - \Delta_R) \quad ; \end{aligned} \tag{6.5.7}$$

which in effect gives the highest value of α as:

$$\alpha_{MAX} = \frac{R_3 (R_1 + R_2)}{R_1 (R_3 + R_4)} \frac{(1 + \Delta_R)}{(1 - \Delta_R)} \left[\frac{1 + \left(\frac{R_2 - R_1}{R_2 + R_1} \right) \Delta_R}{1 + \left(\frac{R_3 - R_4}{R_3 + R_4} \right) \Delta_R} \right] \tag{6.5.8}$$

The value of α with $R_2 >> R_1$ and $R_4 >> R_3$ can be approximated by neglecting higher order terms as:

$$\alpha_{MAX} \approx \frac{R_3 (R_1 + R_2)}{R_1 (R_3 + R_4)} (1 + 4\Delta_R) \tag{6.5.9}$$

If the errors in the resistors are reversed for the alternative worst case so that:

$$\begin{aligned} &R_1 = R_1(1+\Delta_R) \quad ; \quad R_2 = R_2(1-\Delta_R) \quad ; \quad R_3 = R_3(1-\Delta_R) \\ &R_4 = R_4(1+\Delta_R) \end{aligned} \tag{6.5.10}$$

The value of α_{MIN} using this alternative worst case can be described as:

$$\alpha_{MIN} = \frac{R_3(R_1+R_2)}{R_1(R_3+R_4)}(1-4\Delta_R) \tag{6.5.11}$$

The value of α in (6.5.8) should be less than unity to prevent instability which implies:

$$\begin{aligned} &\alpha(1 \pm 4\Delta_R) < 1 \\ &\alpha < \tfrac{1}{(1\pm 4\Delta_R)} \end{aligned} \tag{6.5.12}$$

Table 6.1: Variation of boosted resistance for a range of Δ_R= 0.1% to 1%.

$\Delta_R(\%)$	α_{MAX}	$\alpha(1-4\Delta_R)$	$\alpha(1+4\Delta_R)$	M_{MIN}	M_{MAX}	M_{MAX}/M_{MIN}
0.1	0.995	0.991	0.99898	111	980	8.82
0.25	0.99	0.98	0.9999	50	10000	200
0.5	0.98	0.96	0.9996	25	2500	100
0.75	0.97	0.941	0.9991	16.95	1100	64.9
1	0.96	0.922	0.9984	12.82	625	48.75

The variation in the values of α and M for a range of Δ_R from 0.1% to 1% are shown in Table 6.1. Examining Table 6.1, it is apparent that the input resistance boosted factor, M ranges from 50:1 with $\Delta_R = 1\%$ to just under 9:1 when $\Delta_R = 0.1\%$. It is desirable to keep the input impedance as closely defined as possible and therefore, it is sensible to chose a value of $\alpha = 0.995$ and $\Delta_R = 0.1\%$ for the first stage of the ECG amplifier design. This is feasible as with surface mount technology 0.1% resistors are not prohibitively expensive nowadays.

The ac gain introduced at the first stage of the amplifier is set to 7.6 as discussed in Chapter 5. Initially, the gain at the first stage of the amplifier was kept to 14.6 but was later lowered owing to reduction in the input impedance bandwidth coverage. The gain value of 7.6 can be ensured by selecting R_1=1MΩ and R_2=3.3MΩ. Substituting values of R_1, R_2 and $\alpha = 0.995$ in (6.4.3) gives:

$$4.3 \times \frac{R_3}{R_3 + R_4} = 0.995 \tag{6.5.13}$$

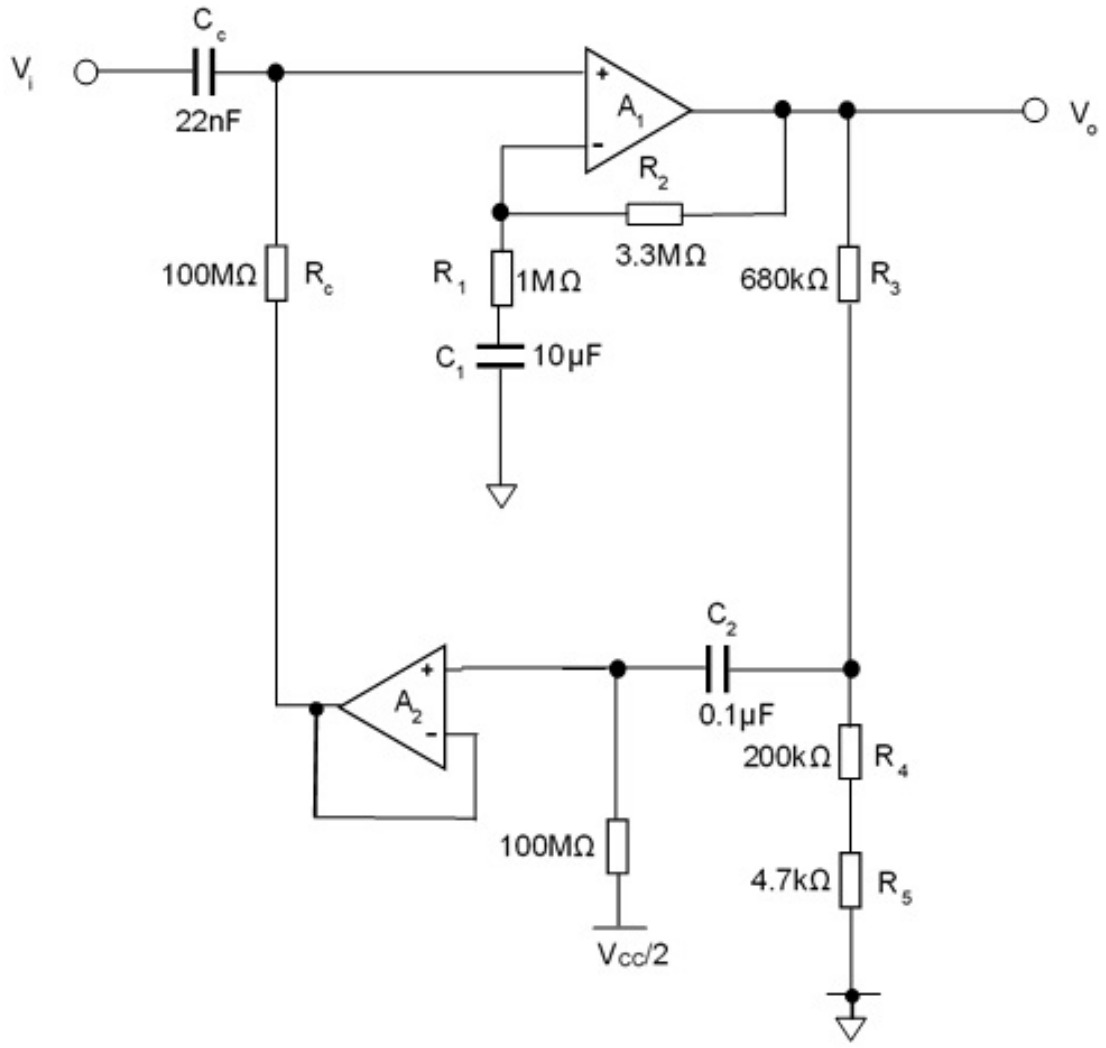

Figure 6.10: AC Coupled Single Sided Input Impedance Boosting.

Equation (6.4.13) yields R_3=0.3R_4. This gives R_3=204.7kΩ, with R_4=680kΩ. Two resistors connected in series with values of 200kΩ and 4.7kΩ can be used to account for R_3 which equals to 204.7kΩ.

6.5.2 Single sided AC Coupled Boosting

A single sided ac-coupled input impedance boosting circuit with the introduction of the bias voltage at the input is shown in Fig. 6.10. This ac-coupled non-inverting amplifier produces

an ac mid-band gain of $1 + (R_2/R_1)$ and the output voltage V_o swings around a bias voltage of $V_{cc}/2$. The potential divider network formed by resistors R_3, R_4 and R_5 counteracts the gain and gives α=0.995. The capacitor C_2 blocks the dc voltage from the potential divider network and ensures the non-inverting input terminal of op-amp A_1 is biased to mid-rail value via op-amp A_2. Capacitor C_1 ensures a low cut-off frequency of <0.5Hz.

6.5.3 Capacitance neutralisation using power supply bootstrapping

Power supply bootstrapping has been employed as an important technique to reduce op-amp input capacitance for decades and help maintain high input impedance over a large signal bandwidth. The technique is implemented in an op-amp by driving its power supply rails to ac potential levels equal to the input signal voltage as shown in Fig.6.11.

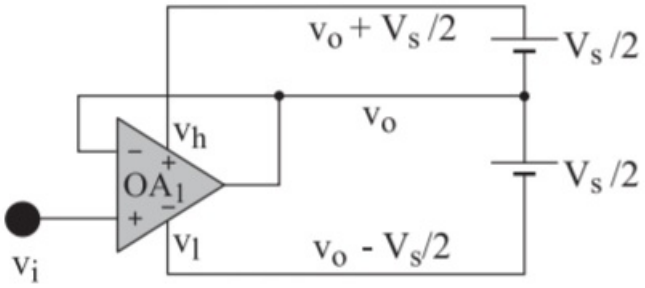

Figure 6.11: Ideal Power Supply Bootstrapping [30]

Fig. 6.11 shows an idealised circuit for a unity-gain buffer active electrode with power supply bootstrapping. The power rails of the op-amp OA_1 are driven by an ac voltage equal to the input and are also shifted by the dc bias voltage $V_s/2$. Therefore, the ac signal voltage applied across the input impedance is zero and no current flows through it. This is equivalent to an input impedance of infinite magnitude. Guerrero & Spinelli [30] as shown in Fig.6.11 improved upon this idea further by proposing two-wire active electrodes for bio-potential measurements which introduces the method of biasing an active electrode with a current source. However, there are couple of limitations in this design. The first is the use of unity gain in the first stage of the bootstrapped amplifier design. The use of unity gain buffers coupled with gain in

subsequent stage can produce high levels of noise voltage at the amplifier output and degrade the signal-to-noise ratio. The authors quote an output noise level voltage of 71μVptp when measured from 0.1-100Hz for unity gain. The design therefore fails to meet the IEC60601 input referred peak to peak noise specification recommended for a clinical quality ECG signal. The second drawback of the design is the power consumption which is in the mA range due to the polarization of the diode D_1 and the high quiescent current consumption of the op-amp OPA2320. Therefore, the potential for adopting this design is the inclusion of gain in the first stage and the use of for low power op-amps.

A single-sided, ac-coupled bootstrapping amplifier employing a non-inverting gain of 4.3 is shown in Fig. 6.12. The resistive chains formed by R_3-R_8 are used to counteract the gain in the first stage, with the 4.7kΩ resistor giving the appropriate value of α=0.995. The dc nature of the bootstrapping chains allows nominal dc voltages to be established from the nominal output dc voltage of the first stage op-amps. This in turn is determined by the inclusion of the $V_{CC}/2$ dc bias on the input impedance boosting stage.

The effect of this bootstrapping is to reduce the op-amp input pin capacitance from 3pF by the M factor of 200 to a value in the region of 15-25fF. The testing and validation of the capacitance neutralisation will be discussed in Chapter 8.

Initial simulations of the design shown in Fig. 6.12, using the OPA379 by Texas Instruments, proved unsuccessful due to the modelling of the OPA379 in the Multisim library. There were issues of the convergence of the DC operating point. This has been mainly due to the fact that Multisim reports a dc convergence error if no operating point has been found after a number of iterations. Increasing the error tolerances will finally get the circuit converge to a dc operating point but will ultimately limit confidence in the results obtained from the simulations. In short Multisim doesnot simulate effectively with anything other than a dc voltage source connected to the power-supply rails of the op-amp.

A full schematic diagram combining both the input impedance boosting and the power supply bootstrapping in a two sided differential structure is shown in Fig. 6.13. The design allows for the AC input signal to be superimposed on top of the positive and negative supply rails of

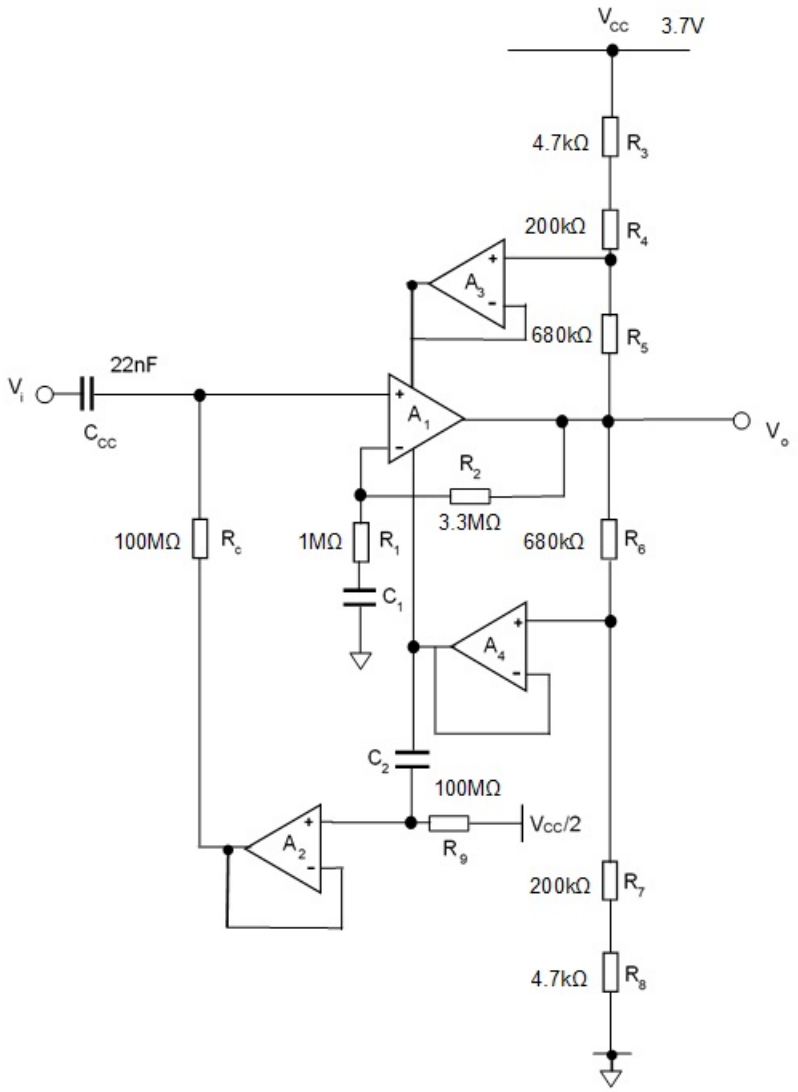

Figure 6.12: AC Coupled Single Side Bootstrapping.

op-amps A_1 and A_2. Op-amps A_3, A_4, A_6 and A_7 are used as buffers to prevent loading effects. By this mechanism power supply bootstrapping is achieved and input capacitance reduced, increasing the high impedance bandwidth. Unlike the single-sided gain of the circuit of 4.3 shown in Fig.6.10, the differential gain will now be 7.6. Therefore, the resistor values R_3, R_4, R_7 and R_8 needs to be adjusted accordingly to ensure the value of α remains at 0.995. This in turn causes R_6=R_4=100kΩ and R_3=R_8=2.7kΩ. The chain of resistive divider networks formed by resistors R_3-R_8 are used to provide for the power supply voltages of differential op-amps A_1 and A_2. These lower resistor values reduce the effect of input capacitance of the buffers and also limits the level of dc current flowing through the resistive divider chain to 2μA. In the case of a 3.7V supply, the positive power rail drive superimposes the buffered

ac signal on top of a dc level of 3.4V. Similarly, the negative power rail drive superimposes the buffered ac signal on top of dc level of 0.2V. This gives a nominal dc supply voltage of 3.2V to op-amps A_1 and A_2. The inclusion of 68pF capacitors in this design is to increase the bootstrapping at higher frequencies where the gain bandwidth of the op-amps falls off. This design symmetry allows the output voltage of op-amps A_1 and A_2 to swing around a dc voltage level of $V_{cc}/2$. The construction and testing of the prototype stripboard and a professional PCB will be discussed in Chapter 8.

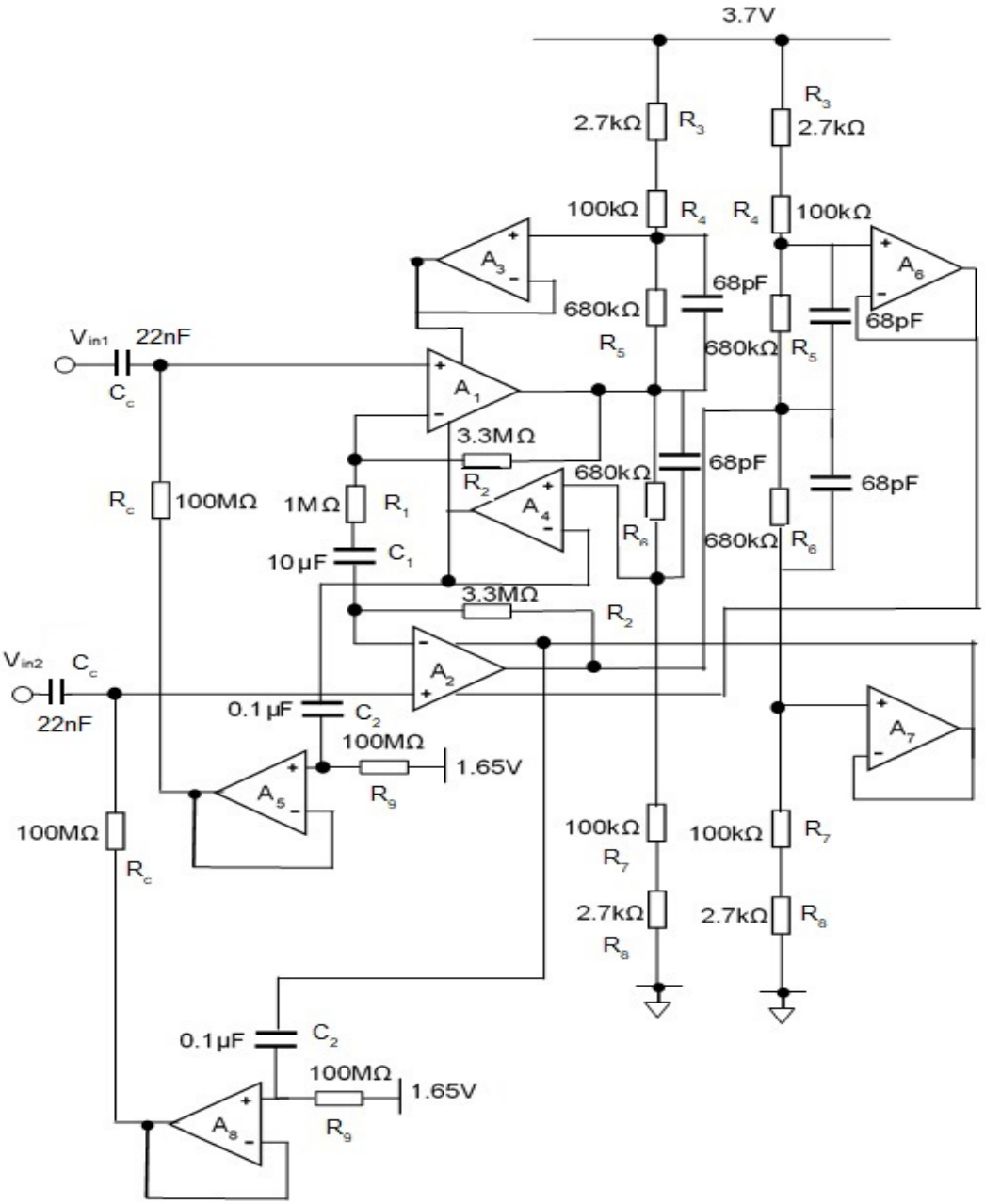

Figure 6.13: Differential Input Impedance Boosting via power supply boot-strapping.

7 Boosting Amplifier Common-Mode Rejection Ratio

7.1 Introduction

The previous chapter implemented a means of boosting the common-mode input impedance if the ECG amplifier. This was essentially to meet the transient response requirements of the IEC60601 performance specification. The high input impedance will also help to provide a high common-mode rejection ratio (CMRR) but this is not the only factor that determines the overall CMRR of the amplifier. There are three principal factors that limit the overall CMRR of the ECG recording amplifier:

- Input impedance mismatch $CMRR_{\Delta Z}$
- Resistor tolerances in the amplifier $CMRR_{\Delta R}$
- Finite CMRR of the op-amps used for the amplifier design $CMRR_{op}$

The CMRR due to the input impedance mismatch will be relatively high as the common-mode input impedance of the amplifier is boosted to at-least 10GΩ within the target bandwidth. This was discussed in Chapter 4. The $CMRR_{op}$ factor will be high as the op-amp OPA379 used in the design has a guaranteed CMRR performance of 90dB as quoted in the datasheet. Therefore, it is likely that the resistance tolerance mismatch may dominate the overall amplifier CMRR performance.

This chapter presents different designs that have been used over the years to boost the CMRR

performance of ECG recording amplifiers. However, most of these designs are associated with high power consumption or limited CMRR bandwidth. Some novel methods that have been explored to boost the CMRR performance of the recording amplifier using low-power op-amps are presented.

7.1.1 Effect of Manufacturing Resistor Tolerance on CMRR

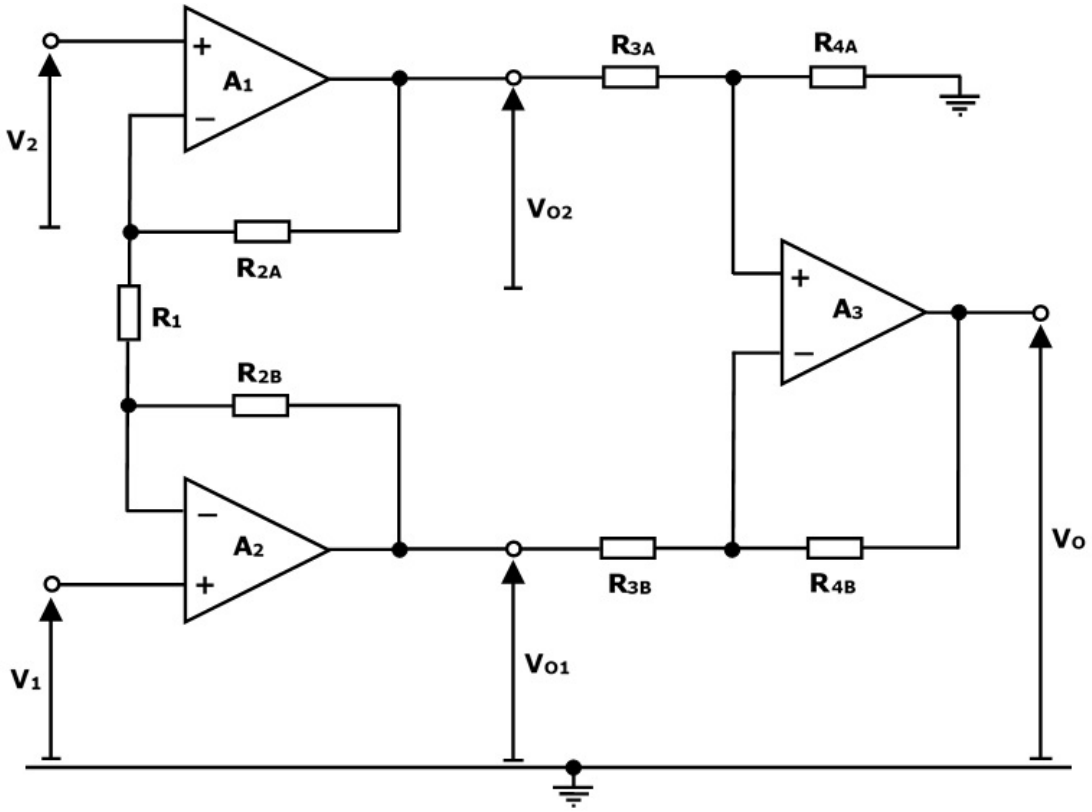

Figure 7.1: Schematic Diagram of the Standard Instrumentation Amplifier.

A classical three op-amp instrumentation amplifier configuration as commonly presented in the literature [4] is shown in Fig. 7.1. Assuming ideal op-amps, the current flowing through resistors R_{2A}, R_1 and R_{2B} can be expressed as:

$$i = \frac{V_{O2} - \mathrm{V}_2}{R_{2A}} = \frac{V_2 - V_1}{R_1} = \frac{V_1 - V_{O1}}{R_{2B}} \tag{7.1.1}$$

so that the first stage output voltages are given as:

$$V_{O2} = \left(1 + \frac{R_{2A}}{R_1}\right) V_2 - \frac{R_{2A}}{R_1} V_1 \tag{7.1.2}$$

$$V_{O1} = \left(1 + \frac{R_{2B}}{R_1}\right) V_1 - \frac{R_{2B}}{R_1} V_2 \tag{7.1.3}$$

Resistor mismatch results in a conversion of the common-mode input voltage to a differential component at the output of the single-ended stage. The worst case mismatch occurs with the following arrangement of resistor tolerances:

$$R_{2A} = R_2 (1 + \Delta_R), \qquad R_{2B} = R_2 (1 - \Delta_R) \tag{7.1.4}$$

$$R_{3A} = R_3 (1 - \Delta_R), \qquad R_{3B} = R_3 (1 + \Delta_R) \tag{7.1.5}$$

$$R_{4A} = R_4 (1 + \Delta_R), \qquad R_{4B} = R_4 (1 - \Delta_R) \tag{7.1.6}$$

When substituted in (7.1.2) and (7.1.3), the output voltages of the first stage are given as:

$$V_{O2} = V_{ic} + \left(1 + 2\frac{R_2 (1 + \Delta_R)}{R_1}\right) \frac{V_{id}}{2} \tag{7.1.7}$$

$$V_{O1} = V_{ic} - \left(1 + 2\frac{R_2 (1 + \Delta_R)}{R_1}\right) \frac{V_{id}}{2} \tag{7.1.8}$$

The output voltage of the second stage of the instrumentation amplifier with mismatches in the gain determining resistors can be described as:

$$V_O = \left[\frac{R_3 (1 + \Delta_R) + R_4 (1 - \Delta_R)}{R_3 (1 + \Delta_R)}\right] \left[\frac{R_4 (1 + \Delta_R)}{R_3 (1 - \Delta_R) + R_4 (1 + \Delta_R)}\right] V_{O2} - \left[\frac{R_4 (1 - \Delta_R)}{R_3 (1 + \Delta_R)}\right] V_{O1} \tag{7.1.9}$$

Neglecting the small contribution from the differential input signal to the common-mode output signal of the first stage, the output voltage from the second stage can be further

simplified to:

$$V_O = \left(\frac{R_4}{R_3}\right)\left[1 - 2\Delta_R\left(\frac{R_4}{R_3+R_4}\right)\right]\left(1 + 2\frac{R_2}{R_1}\right)V_{id} + 4\Delta_R\left(\frac{R_4}{R_3+R_4}\right)V_{ic} \qquad (7.1.10)$$

This is the form $V_o = A_{dR}V_{id} + A_{cR}V_{id}$. Neglecting the small error component $2\Delta_R\frac{R_4}{R_3+R_4}$ in the differential gain, the CMRR of the instrumentation amplifier due to the resistor tolerances is then given as:

$$CMRR_{\Delta_R} = \frac{A_{dR}}{A_{cR}} = \frac{\left(1 + 2\frac{R_2}{R_1}\right)\left(\frac{R_4}{R_3}\right)}{4\Delta_R\left(\frac{R_4}{R_3+R_4}\right)} \qquad (7.1.11)$$

where A_{dR} is the overall gain which is applied to the differential input signal and A_{cR} is the overall gain applied to the unwanted common-mode signal. This suggests that the attenuation factor $R_4/(R_3 + R_4)$ in (7.1.10) should be minimised by considering $R_4 << R_3$. Therefore, the minimum feasible gain should be allocated to the second differential-to-single ended stage of the ECG amplifier. An appropriate ECG amplifier design strategy is therefore to assign the required differential gain to the first stage of the amplifier and make the gain of the second stage to equal to unity.

7.1.2 Finite CMRR of op-amps

The front-end stage of a typical instrumentation amplifier [4, 8] as shown in Fig. 7.2 is designed to provide high differential gain and maintain unity common-mode gain. However, the finite CMRRs of the op-amps also create a differential component of the common-mode input signal at the outputs. The finite CMRRs of the op-amps is modelled by including a differential signal of V_{ic}/CMRR at the input of each op-amp.

The output voltage of the first stage of the amplifier with ideal resistors can be described

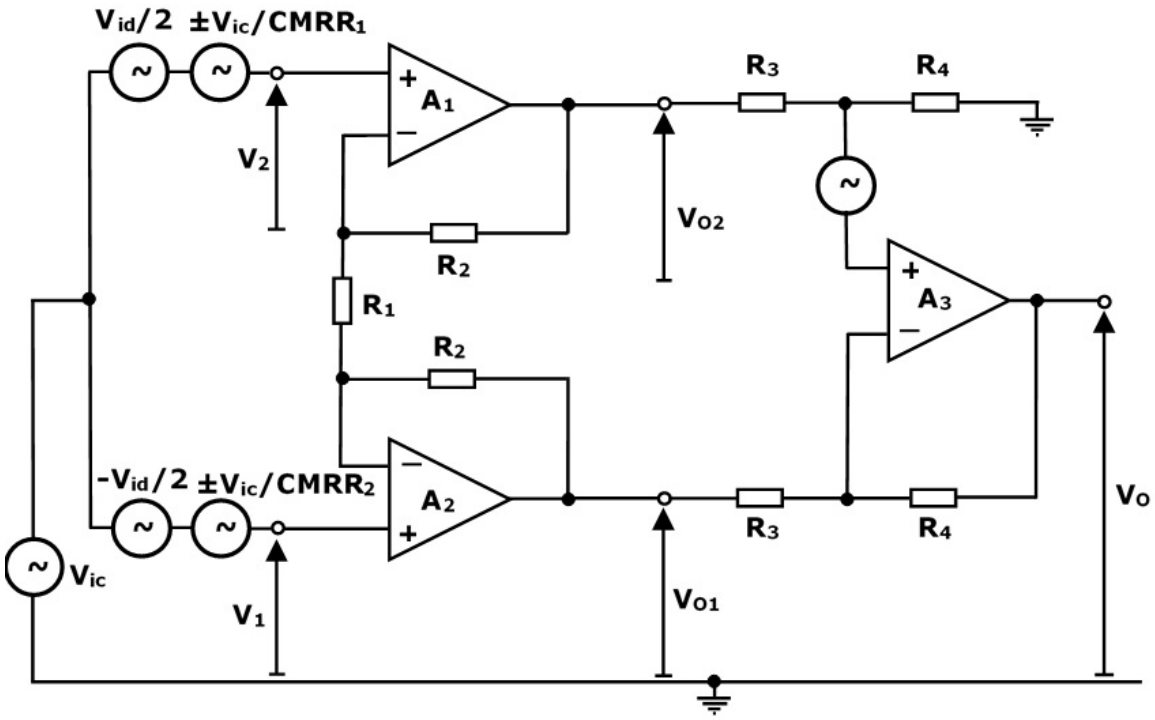

Figure 7.2: Circuit Diagram of the standard Instrumentation Amplifier modelling the effect of the finite CMRR in op-amps.

as:

$$V_{O2} = \left(1 + \frac{R_2}{R_1}\right)\left(V_{ic} + \frac{V_{id}}{2} \pm \frac{V_{ic}}{CMRR_1}\right) - \left(\frac{R_2}{R_1}\right)\left(V_{ic} - \frac{V_{id}}{2} \pm \frac{V_{ic}}{CMRR_2}\right) \quad (7.1.12)$$

$$V_{O1} = \left(1 + \frac{R_2}{R_1}\right)\left(V_{ic} - \frac{V_{id}}{2} \pm \frac{V_{ic}}{CMRR_2}\right) - \left(\frac{R_2}{R_1}\right)\left(V_{ic} + \frac{V_{id}}{2} \pm \frac{V_{ic}}{CMRR_1}\right) \quad (7.1.13)$$

The overall output voltage of the instrumentation amplifier can be expressed after some algebraic manipulation and taking all CMRR components to be additive as:

$$V_O = \left(\frac{R_4}{R_3}\right)\left(1 + 2\frac{R_2}{R_1}\right)V_{id} + \left(\frac{R_4}{R_3}\right)\left\{\left(1 + 2\frac{R_2}{R_1}\right)\left(\frac{1}{CMRR_1} + \frac{1}{CMRR_2}\right) + \frac{1}{CMRR_3}\right\}V_{ic} \quad (7.1.14)$$

The overall CMRR of the amplifier due to finite CMRRs in the op-amps from (4.6.25) can be obtained as:

$$CMRR_{OP} = \frac{A_{dop}}{A_{cop}} = \frac{\frac{R_4}{R_3}\left(1 + 2\frac{R_2}{R_1}\right)}{\frac{R_4}{R_3}\left[\left(1 + 2\frac{R_2}{R_1}\right)\left(\frac{1}{CMRR_1} + \frac{1}{CMRR_2}\right) + \frac{1}{CMRR_3}\right]} \quad (7.1.15)$$

so that finally:

$$CMRR_{OP} = \frac{1}{\frac{1}{CMRR_1} + \frac{1}{CMRR_2} + \frac{1}{\left(1+2\frac{R_2}{R_1}\right)CMRR_3}} \tag{7.1.16}$$

This analysis demonstrates that the CMRR of the input stage op-amps are more influential, while the effect of the CMRR of the second stage op-amp is reduced by a factor equal to the differential gain of the first stage.

7.2 Literature Review of CMRR Boosting Techniques

Several designs have been put forward in the literature for enhancing the CMRR performance of the recording amplifier. Some designs have counteracted the source impedance imbalance by enhancing the amplifier input impedance, others have worked on eliminating errors due to resistor tolerance mismatch. This section presents a selection of CMRR boosting designs that have been closely associated with dry ECG recording.

7.2.1 Resistor trimming techniques

The resistor value trimming technique is one of the oldest methods of counteracting the imbalances caused by mismatched op-amps and resistor tolerance values. Pallas Areny & Webster [31] reported a CMRR performance value greater than 100dB using an active trimming technique, without needing high precision resistors or op-amps with high CMRR values. A schematic diagram with a potentiometer R_{4B2} in the non inverting side of a difference amplifier is shown in Fig. 7.3.

The value of the resistor potentiometer is adjusted to eliminate the effects of common-mode interference at the recording amplifier output stage. The CMRR performance can be optimised by introducing a deliberate mismatch between the resistor ratios $\frac{R_{3B}}{R_{4B}}$ and $\frac{R_{3A}}{R_{4A}}$ such that:

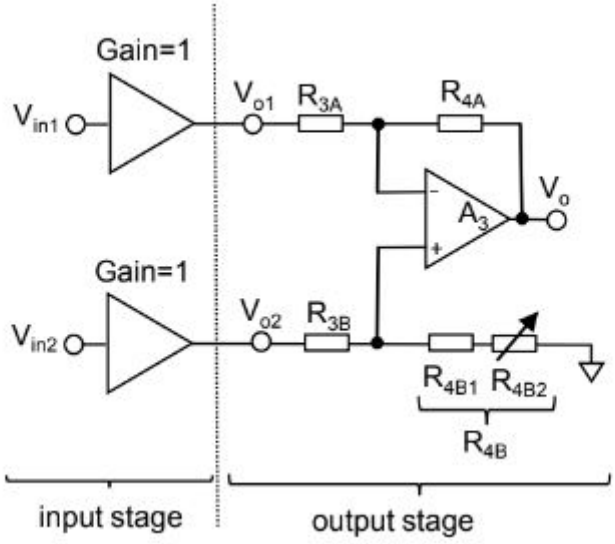

Figure 7.3: Schematic Diagram to show the effect of potentiometer on the common-mode interference output voltage [8, 31].

$$\frac{R_{3B}}{R_{4B}} - \frac{R_{3A}}{R_{4A}} = \frac{1}{CMRR_{op}|_{\omega=0}} \tag{7.2.1}$$

The overall CMRR after considering optimisation of the resistor ratios in (7.2.1) can be described as:

$$CMRR_{overall} = \frac{1}{\frac{1}{CMRR_{op}} - \frac{1}{CMRR_{op}|_{\omega=0}}} \tag{7.2.2}$$

And (7.2.2) suggests that the overall CMRR at the output stage of the amplifier will go to infinity when the opamp $CMRR_{op}$ shows zero phase shift in the signal bandwidth. However, trimming techniques are time consuming and require a lot of resources when implemented in large scale production. Automation in trimming mechanisms will also increase circuit complexity, cost and power [118, 167].

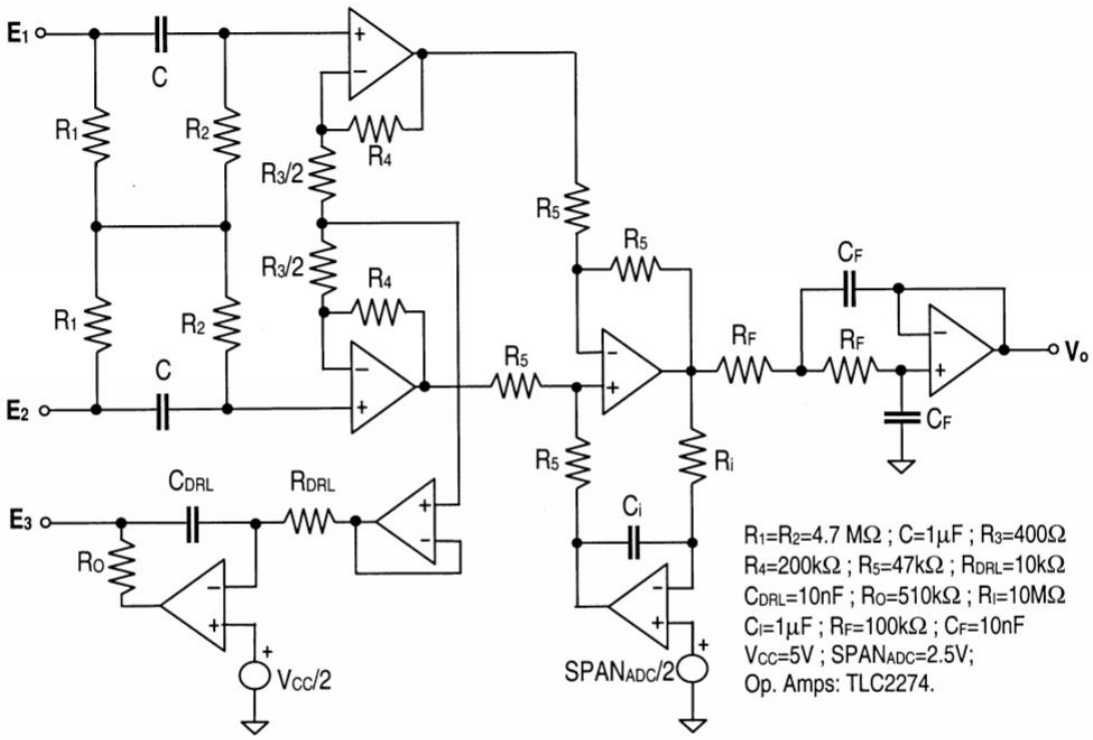

Figure 7.4: Circuit Diagram to show two ac coupled input stage, and an active dc suppression technique [32] .

7.2.2 An ac coupled front end differential amplifier

Spinelli et.al [32] as shown in 7.4, proposed an active ac coupled front end stage for a bio-potential amplifier that produces a large CMRR value of 123dB at 50Hz without requiring grounded resistors. The dc offset voltages produced by the source impedance at the inputs are blocked by the input coupling capacitor C. This balanced ac coupling network at the input of the amplifier provides a dc path for the amplifier bias current to flow through subject's body to ground via the third electrode, E_3. However, all the nodes of the circuit will have same potential when a common-mode signal is applied at the input terminals of E_1 and E_2. Therefore, the overall CMRR of the amplifier is extremely high and independent of the component tolerances. The integrator network formed by the time constant R_i-C_i around the feedback loop of the difference amplifier is used to eliminate any active dc offset voltage at the amplifier output. A second order low-pass filter with a cut-off frequency of 156Hz was included at the final output stage of the amplifier.

One of the main drawbacks of this approach is the limited application of the technique to two-

electrode amplifier configurations. There also may be associated high in-band noise when large values of source impedance values are used. The dc bias current in the region of pA to several nA for some low-power op-amps, can charge the electrode capacitance producing unwanted in-band artefacts associated with motion and changes in the skin-electrode interface [8]. Therefore, instrumentation amplifiers based on this technique would be difficult to implement with dry electrodes, considering the high values of the electrical properties of the electrodes previously measured.

7.2.3 Two Electrode ECG Amplifier

Dobrev [33] proposed a two electrode low-power instrumentation amplifier capable of producing a differential gain of 40-60dB and a CMRR greater than 60 dB from 0.05 Hz to 100 Hz using 1% resistors. A schematic diagram to illustrate the two electrode configuration is shown in Fig. 7.5.

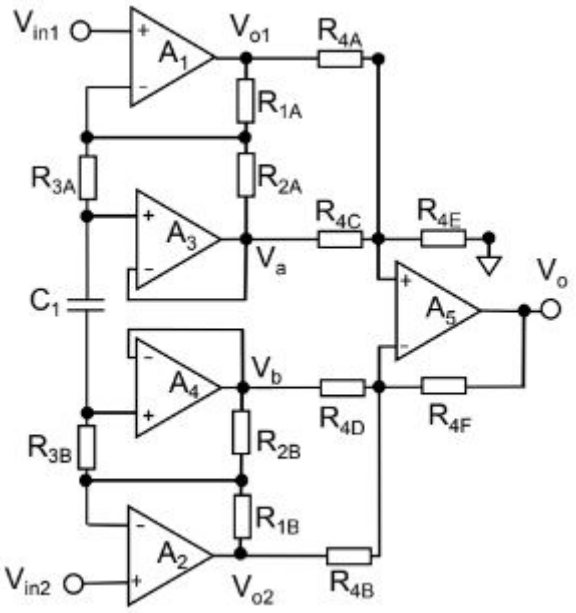

Figure 7.5: Schematic Diagram of two electrode ECG amplifier [8, 33]

The amplifier lower cut-off frequency is governed by resistor R_3 and capacitor C_1 and is set to 0.05Hz. The ac mid-band differential gain is determined by the ratio of $\frac{R_1}{R_2//R_3}$ as shown in

(7.2.3).

$$A_d = \left(1 + \frac{R_1}{R_2//R_3}\right) \frac{2R_3C_1}{1 + 2R_3C_1} \tag{7.2.3}$$

The differential gain in (7.2.3) can be approximated as $A_{d1} = \left(1 + \frac{R_1}{R_2}\right)$ with $R_3 >> R_2$. The ac input signal is decoupled using capacitor C_1 and resistor R_3. The op-amps A_1 and A_2 form the gain stage of the amplifier and contribute one-half of the amplified differential input signals. The half differential signals from each side are converted to a single-ended signal using op-amp A_5 in a difference amplifier configuration. The common mode gain in the first stage of this design is unity, which is the same as that of the standard instrumentation amplifier. Considering the tolerances in the gain determining resistors, the magnitude of the minimum CMRR performance is given as:

$$CMRR_{\text{min}} = 1.5 \left(\frac{A_{d1}}{4\Delta_{\text{max}}}\right) \tag{7.2.4}$$

(7.2.4) suggests that the amplifier proposed by Dobrev can improve the CMRR performance by a factor of 1.5 when compared with the classic three op-amp instrumentation amplifier. The CMRR performance of the constructed circuit was measured at 66dB for a mid-band differential gain of 46dB.

This design has a couple of limitations, the first being that it allows a dc bias current to flow through the subject's body. A mismatch of bias currents at the two input terminals of the op-amps can create imbalance in the node voltages of the circuit network when a common-mode signal is applied. Dry electrodes exhibiting high values of source impedance will produce greater imbalance in common-mode node voltages and thereby can degrade the performance of the amplifier. The second drawback is the small reduction of common-mode interference, at the expense of two additional op-amps at the input and the associated increase in semiconductor noise.

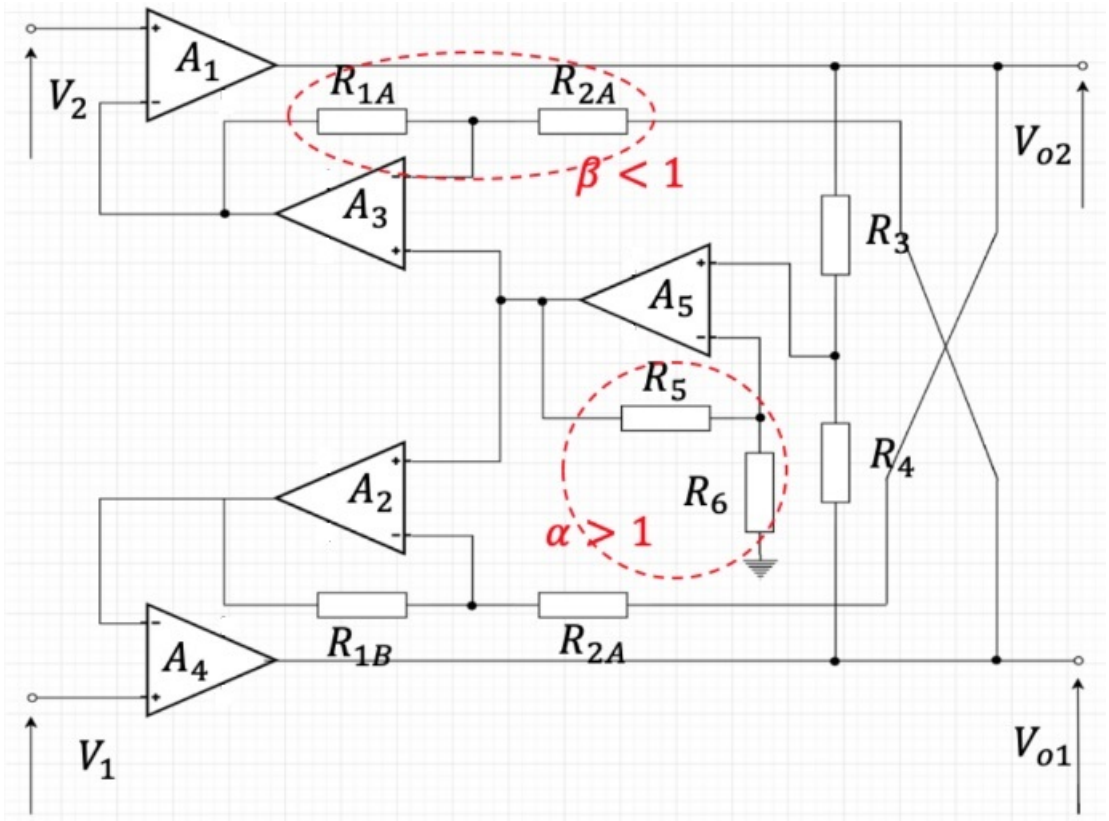

Figure 7.6: Circuit Diagram of proposed CMRR boosting mechanism [34]

7.2.4 Common-mode boosting feedback Amplifier

Grennan [34] used a cross coupling mechanism as shown Fig.7.6 in an effort to suppress the common-mode gain introduced by resistor mismatches in R_{1A} and R_{1B}, R_{2A} and R_{2B}. The common-mode component present at the input of the amplifier is boosted by a gain of $1+\frac{R_4}{R_3}$. It is then combined with the β feedback network formed by resistors R_{1A}, R_{1B}, R_{2A} and R_{2B} and then fed back into the negative terminals of the input op-amps A_1 and A_4.

The cross coupling mechanism is implemented by connecting one side of the β feedback loop to V_{o2} and the other side to V_{o1}. Therefore, the input will consist of both differential and common-mode components. The common-mode components that are boosted by the β feedback loop will be suppressed by the α feedback gain.

However, the overall CMRR of this cross coupling design fails to eliminate error due to resistor mismatch. Infact, the loss of cross coupling and a single R_1 resistor in a three op-amp instrumentation amplifier appears to have degrading effect. The CMRR was measured at

75dB with a differential gain of 100. Therefore, this design does not reach the goal of 80dB required for diagnostic quality of ECG monitoring.

7.3 Alternative novel method to enhance CMRR performance

A novel method as shown in Fig. 7.7 was explored by the author in an attempt to boost the overall CMRR performance of the ECG amplifier.

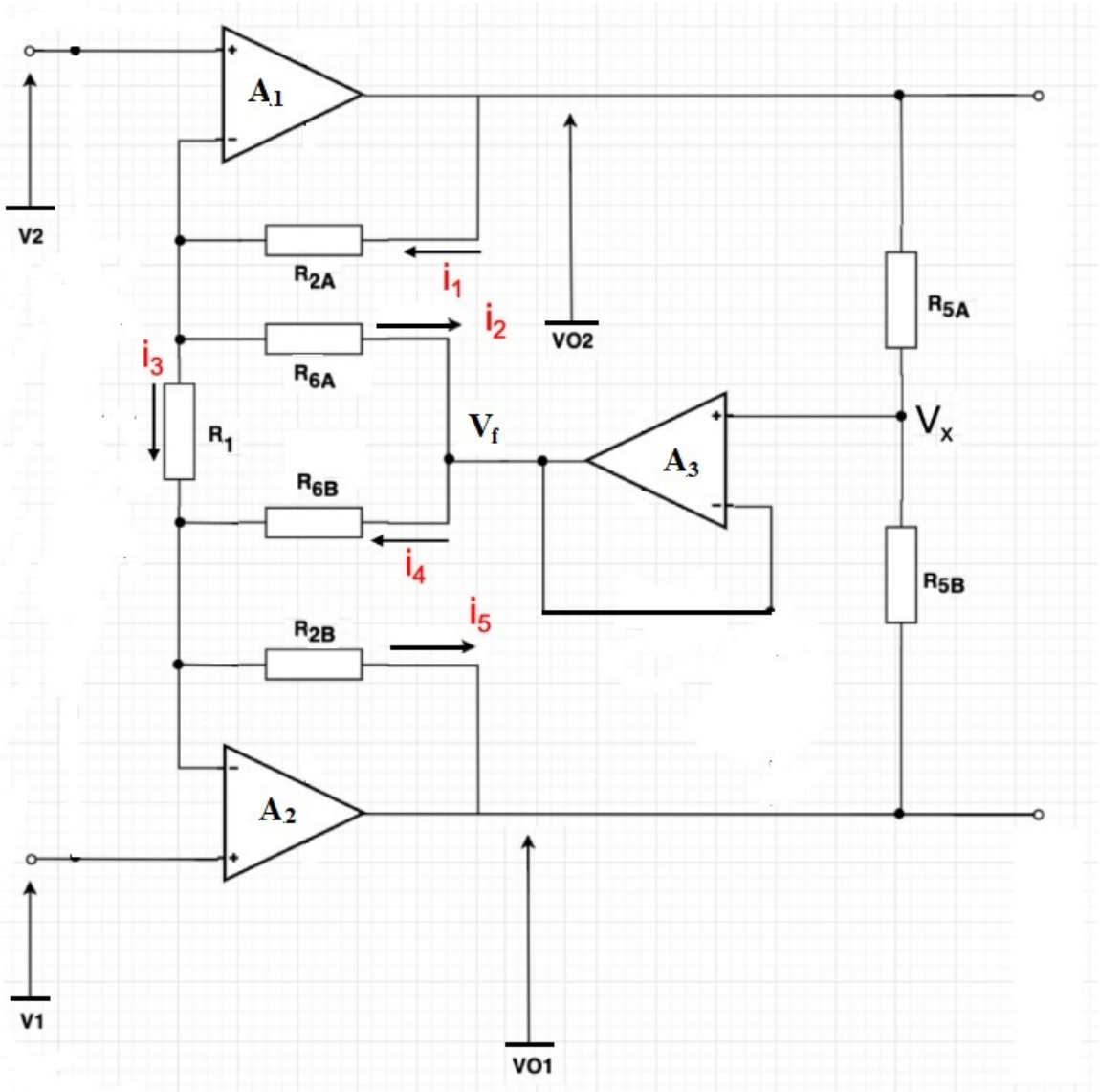

Figure 7.7: Circuit Diagram of proposed CMRR boosting mechanism

Applying Kirchhoff's Current Law at the inverting terminal of op-amp A_1, we have

$$i_1 = i_2 + i_3 \tag{7.3.1}$$

(7.3.1) can be further rewritten as:

$$\frac{V_{02} - V_2}{R_{2A}} = \frac{V_2 - V_f}{R_{6A}} + \frac{V_2 - V_1}{R_1} \tag{7.3.2}$$

The output voltage of op-amp A_1 after rearranging (7.3.2) is given by:

$$V_{02} = V_2 \left(1 + \frac{R_{2A}}{R_{6A}} + \frac{R_{2A}}{R_1}\right) - \frac{R_{2A}}{R_1} V_1 - \frac{R_{2A}}{R_{6A}} V_f \tag{7.3.3}$$

Similarly, the output voltage of op-amp A_2 can be described as:

$$V_{01} = V_1 \left(1 + \frac{R_{2B}}{R_{6B}} + \frac{R_{2B}}{R_1}\right) - \frac{R_{2B}}{R_1} V_2 - \frac{R_{2B}}{R_{6B}} V_f \tag{7.3.4}$$

Considering no resistor tolerances with R_{2A}=R_{2B}=R_2 and R_{6A}=R_{6B}=R_6, the output voltages of op-amps A_1 and A_2 can be expressed as:

$$V_{02} = V_2 \left(1 + \frac{R_2}{R_6} + \frac{R_2}{R_1}\right) - \frac{R_2}{R_1} V_1 - \frac{R_2}{R_6} V_f \tag{7.3.5}$$

$$V_{01} = V_1 \left(1 + \frac{R_2}{R_6} + \frac{R_2}{R_1}\right) - \frac{R_2}{R_1} V_2 - \frac{R_2}{R_6} V_f \tag{7.3.6}$$

The voltage at node V_f with zero resistor tolerance such that R_{5B}=R_{5A}=R_5, can be described as:

$$V_f = \frac{(V_{02} + V_{01})}{2} \tag{7.3.7}$$

The common-mode output voltage of the amplifier can be described as $\frac{V_{o1}+V_{o2}}{2} = \frac{V_1+V_2}{2} = V_{ic}$. This result suggests that the common-mode output voltage of this design configuration is not

attenuated and is equal to the input common-mode voltage. Therefore, this design setup is not useful in reducing the common-mode interference. This is because of the use of unity gain in amplifier A_3. The differential output voltage is given as:

$$V_{oid} = \left(1 + \frac{R_2}{R_6} + 2\frac{R_2}{R_1}\right) V_{id} \tag{7.3.8}$$

where V_{oid} is the differential output voltage and V_{id} is the differential input voltage of the amplifier. Therefore, the CMRR of the amplifier can be described as:

$$CMRR = \frac{A_d}{A_c} = \left(1 + \frac{R_2}{R_6} + 2\frac{R_2}{R_1}\right) \tag{7.3.9}$$

which is simply the differential gain.

The circuit shown in Fig.7.7 is modified to include a gain stage in the common-mode feedback. This is shown in Fig. 7.8. Considering no resistor tolerances with R_{2A}=R_{2B}=R_2 and R_{6A}=R_{6B}=R_6, the output voltages of op-amps A_1 and A_2 can be expressed as:

$$V_{02} = V_2\left(1 + \frac{R_2}{R_6} + \frac{R_2}{R_1}\right) - \frac{R_2}{R_1}V_1 - \frac{R_2}{R_6}\left(1 + \frac{R_8}{R_7}\right)(V_{o1} + V_{o2}) \tag{7.3.10}$$

$$V_{01} = V_1\left(1 + \frac{R_2}{R_6} + \frac{R_2}{R_1}\right) - \frac{R_2}{R_1}V_2 - \frac{R_2}{R_6}\left(1 + \frac{R_8}{R_7}\right)(V_{o1} + V_{o2}) \tag{7.3.11}$$

The differential output signal remains the same is described in (7.3.8). The common-mode output voltage V_{oic} using (7.3.9) and (7.3.10) can be described as:

$$V_{oic} = V_{ic}\frac{\left(1 + \frac{R_2}{R_6}\right)}{\left[1 + \frac{R_2}{R_6}\left(1 + \frac{R_8}{R_7}\right)\right]} \tag{7.3.12}$$

(7.3.11) suggests that the gain of the differential stage to the common-mode input voltage is reduced by including the gain in the feedback path. However, a mismatch in the R_6 resistors will produce a common-mode to differential signal conversion and will subsequently get the gain of the differential stage to counteract the improvement obtained with the feedback

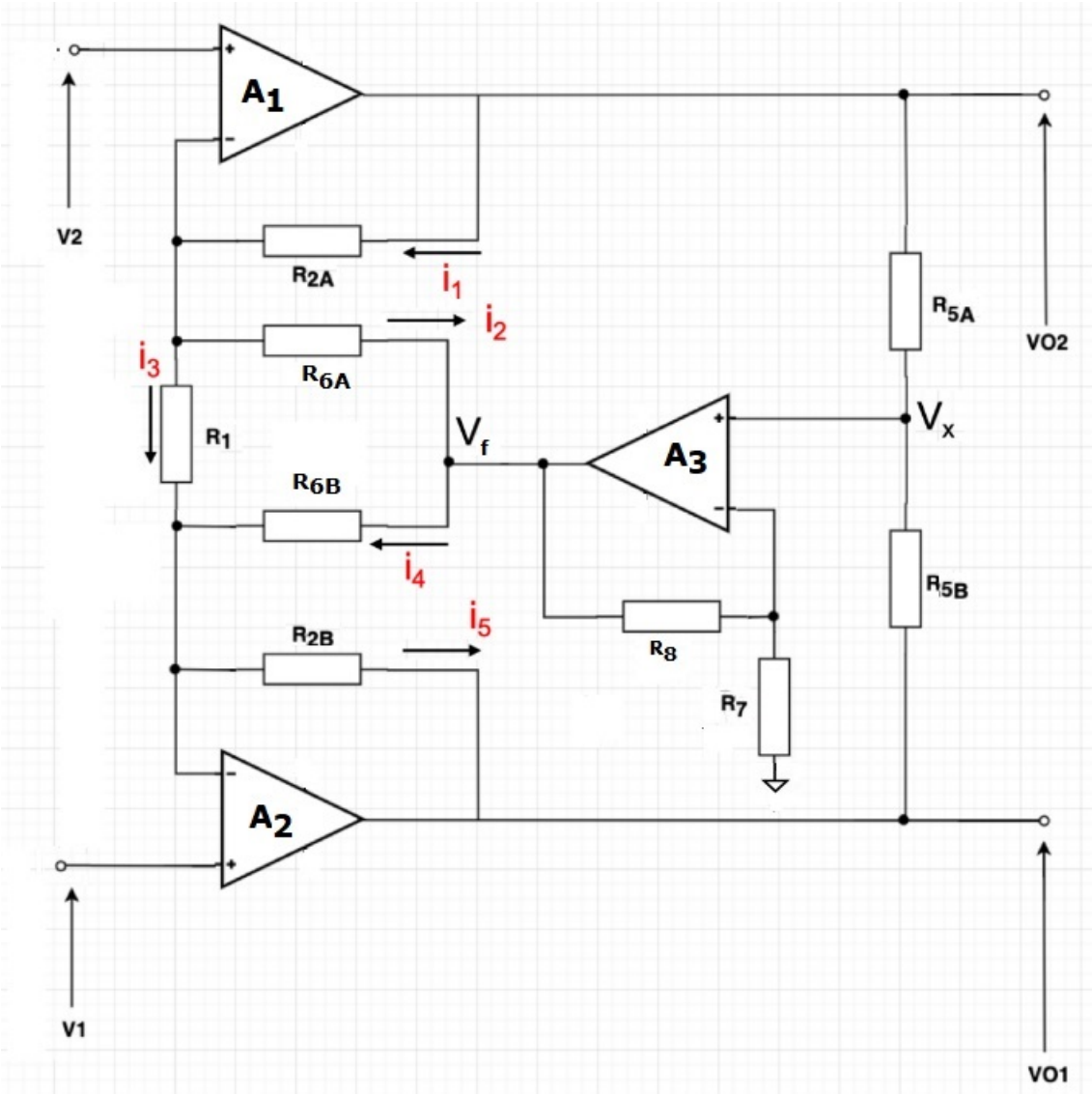

Figure 7.8: Common-mode feedback with gain stage

and degrade the CMRR. The circuit shown in Fig. 7.8 is simulated for Monte Carlo CMRR analysis due to the resistor tolerance mismatch in Multisim. The Monte Carlo simulation shown in Fig. 7.9 suggests that the worst case CMRR is 65dB for 0.1% resistors tolerance mismatch and is 60dB with 1% resistor tolerance errors. This verifies that the CMRR performance of the amplifier is further degraded when compared with the standard instrumentation amplifier.

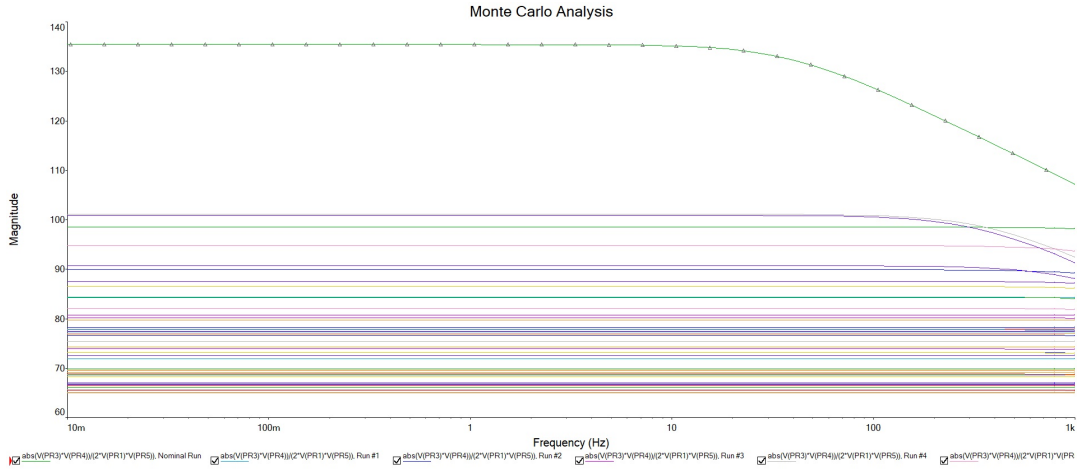

(a) CMRR due 0.1% resistor tolerance mismatch

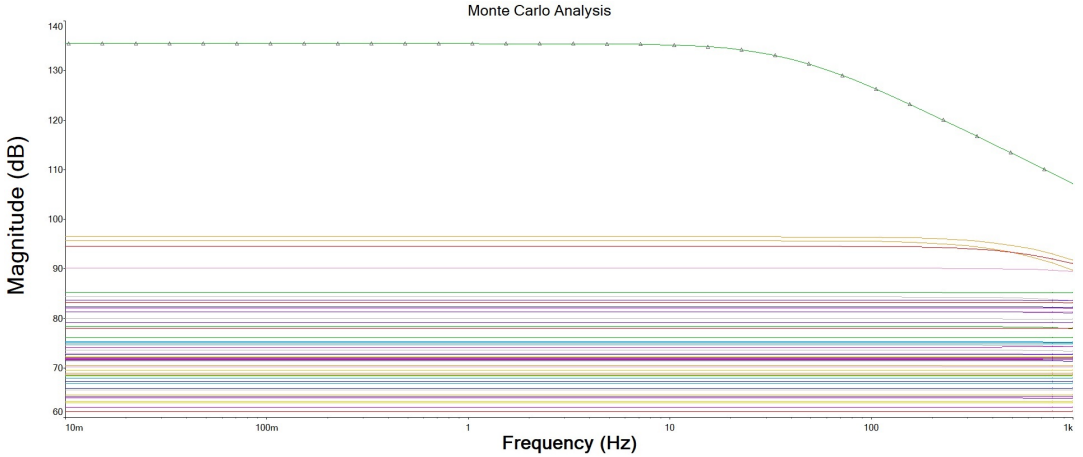

(b) CMRR due 1% resistor tolerance mismatch

Figure 7.9: Monte Carlo simulation for the degradation of the CMRR performance due to errors in resistor tolerance mismatch

7.4 Analysis of CMRR due to resistor tolerances in a Multistage amplifier setup

A schematic diagram shown in Fig. 7.10 is used to analyse the effects of resistor tolerance mismatch in the CMRR performance of our proposed ECG multistage amplifier.

For the highest degree of mismatch the errors in the resistors are chosen in a way such that the gain is made highest in one channel and lowest in the other. Then, the worst case mismatch occurs with the following resistor errors:

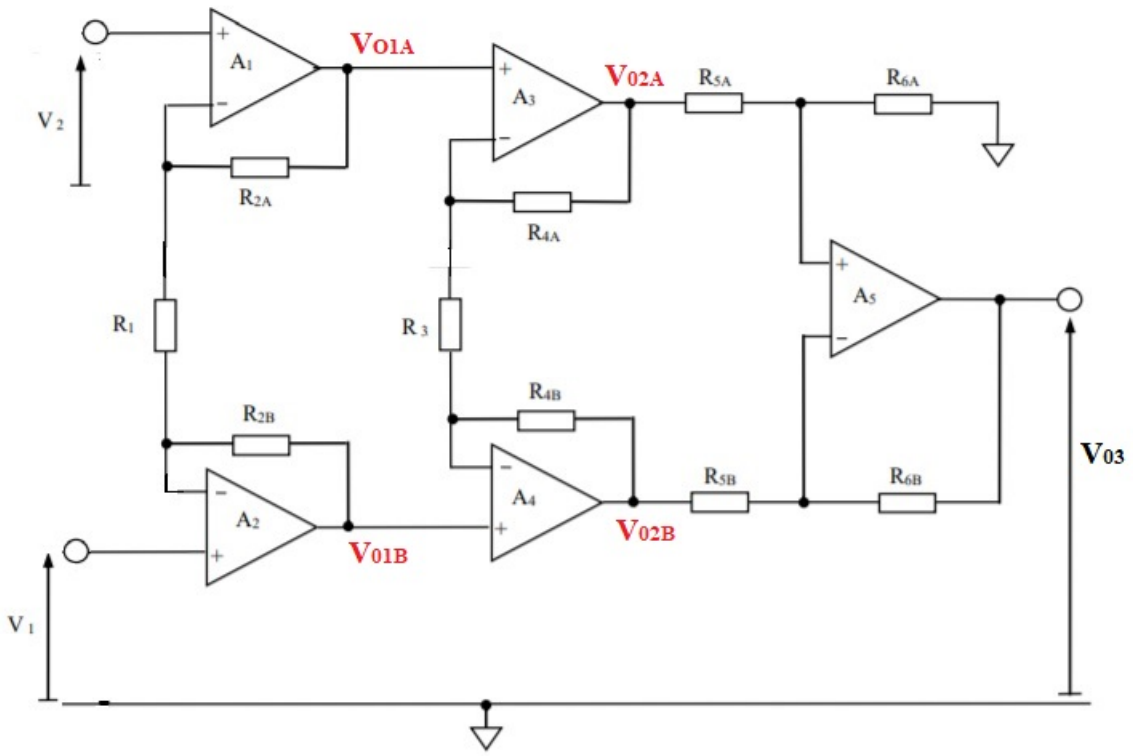

Figure 7.10: CMRR analysis of our proposed Multistage ECG Amplifier

$$
\begin{aligned}
&R_{2A} = R_2\,(1+\Delta_{2A})\,;\, R_{4A} = R_4\,(1+\Delta_{4A})\,;\, R_{5A} = R_5\,(1-\Delta_{5A}) \\
&R_{6A} = R_6\,(1+\Delta_{6A})\,;\, R_{2B} = R_2\,(1-\Delta_{2B})\,;\, R_{4B} = R_4\,(1-\Delta_{4B}) \\
&R_{5B} = R_5\,(1+\Delta_{5B})\,;\, R_{6B} = R_6\,(1-\Delta_{6B})
\end{aligned}
\tag{7.4.1}
$$

The output voltages of the first stage when differential and common-mode input voltages are included are given as:

$$V_{01A} = V_{ic} + \frac{V_{id}}{2}\left[1 + 2\frac{R_2}{R_1}\,(1+\Delta_{2A})\right] \tag{7.4.2}$$

$$V_{01B} = V_{ic} - \frac{V_{id}}{2}\left[1 + 2\frac{R_2}{R_1}\,(1-\Delta_{2B})\right] \tag{7.4.3}$$

Then the output differential V_{oid} and common-mode V_{oic} components of the first stage can

be established as:

$$V_{01d} = V_{O1A} - V_{O1B} = V_{id}\left[1 + 2\frac{R_2}{R_1}\left(1 + \frac{\Delta_{2A} - \Delta_{2B}}{2}\right)\right] \tag{7.4.4}$$

$$V_{01c} = \frac{V_{O1A} + V_{O1B}}{2} = V_{ic} + \frac{R_2}{R_1}\left(\Delta_{2A} + \Delta_{2B}\right)V_{id} \tag{7.4.5}$$

It can be seen that the common mode signal at the input V_{ic} gets unity gain and the errors in the resistors do not alter this. There is however a component of conversion of the differential input signal V_{id} to a common-mode signal in the first stage as well as a small error in the gain given to the differential signal which depends on the different values of Δ. It can also be seen that the common-mode input signal receives only unity gain in both stages and there is no conversion of the common-mode signal to a differential component.

A similar approach to analysis of the second stage gives:

$$V_{02A} = \left[1 + \frac{R_4}{R_3}\left(1 + \Delta_{4A}\right)\right]V_{01A} - \frac{R_4}{R_3}\left(1 + \Delta_{4A}\right)V_{01B} \tag{7.4.6}$$

$$V_{02B} = \left[1 + \frac{R_4}{R_3}\left(1 - \Delta_{4B}\right)\right]V_{01B} - \frac{R_4}{R_3}\left(1 - \Delta_{4B}\right)V_{01A} \tag{7.4.7}$$

Substituting the values of V_{01A} and V_{01B} into (7.4.6) and (7.4.7):

$$\begin{aligned} V_{02A} = V_{ic} &+ \tfrac{V_{id}}{2}\left[1 + \tfrac{R_4}{R_3}\left(1 + \Delta_{4A}\right) + 2\tfrac{R_2}{R_1}\left(1 + \Delta_{2A}\right) + 2\tfrac{R_4R_2}{R_3R_1}\left(1 + \Delta_{4A}\right)\left(1 + \Delta_{2A}\right)\right] \\ &+ \tfrac{V_{id}}{2}\left[\tfrac{R_4}{R_3}\left(1 + \Delta_{4A}\right) + 2\tfrac{R_4R_2}{R_3R_1}\left(1 + \Delta_{4A}\right)\left(1 - \Delta_{2B}\right)\right] \end{aligned} \tag{7.4.8}$$

$$V_{02B} = V_{ic} - \frac{V_{id}}{2}\left[1 + \frac{R_4}{R_3}(1-\Delta_{4B}) + 2\frac{R_2}{R_1}(1-\Delta_{2B}) + 2\frac{R_4R_2}{R_3R_1}(1-\Delta_{4B})(1-\Delta_{2B})\right] - \frac{V_{id}}{2}\left[\frac{R_4}{R_3}(1-\Delta_{4B}) + 2\frac{R_4R_2}{R_3R_1}(1-\Delta_{4B})(1+\Delta_{2A})\right] \tag{7.4.9}$$

Neglecting the second order Δ terms in (7.4.8) and (7.4.9), the second stage output voltages can be simplified as:

$$V_{02A} = V_{ic} + \frac{V_{id}}{2}\left[\left(1+2\frac{R_4}{R_3}\right)\left(1+2\frac{R_2}{R_1}\right)\right] + \frac{V_{id}}{2}\left[\begin{array}{l} 2\frac{R_4}{R_3}\left(1+2\frac{R_2}{R_1}\right)\Delta_{4A} \\ +2\frac{R_2}{R_1}\left(1+\frac{R_4}{R_3}\right)\Delta_{2A} - 2\frac{R_4R_2}{R_3R_1}\Delta_{2B} \end{array}\right] \tag{7.4.10}$$

$$V_{02B} = V_{ic} - \frac{V_{id}}{2}\left[\left(1+2\frac{R_4}{R_3}\right)\left(1+2\frac{R_2}{R_1}\right)\right] + \frac{V_{id}}{2}\left[\begin{array}{l} 2\frac{R_4}{R_3}\left(1+2\frac{R_2}{R_1}\right)\Delta_{4B} \\ +2\frac{R_2}{R_1}\left(1+\frac{R_4}{R_3}\right)\Delta_{2B} - 2\frac{R_4R_2}{R_3R_1}\Delta_{2A} \end{array}\right] \tag{7.4.11}$$

The common mode signal with Δ_{2A}=Δ_{2B}=Δ_2 and Δ_{4A}=Δ_{4B}=Δ_4 can then be established at the output of the second stages as:

$$V_{02c} = V_{ic} + V_{id}\left[\frac{R_4}{R_3}\left(1+2\frac{R_2}{R_1}\right)\Delta_4 + \frac{R_2}{R_1}\Delta_2\right] \tag{7.4.12}$$

This again shows that the input common-mode signal obtains unity gain while there is also a component due to the conversion of the differential input signal into a common-mode output component. This converted component is maximum when the magnitude of the Δs are considered equal. It should also be stressed that there is no conversion of common-mode signal to a differential component.

The errors will have maximum effect on the output differential signal when the magnitude of the errors on each side are most mismatched. Therefore, the differential output voltage with Δ_{2A}=Δ_2, Δ_{2B}=0 and Δ_{4A}=Δ_4, Δ_{4B}=0 can be expressed as:

$$V_{02d} = V_{id}\left[\left(1+2\frac{R_4}{R_3}\right)\left(1+2\frac{R_2}{R_1}\right)\right] + V_{id}\left[\frac{R_4}{R_3}\left(1+2\frac{R_2}{R_1}\right)\Delta_4 + \frac{R_2}{R_1}\left(1+2\frac{R_4}{R_3}\right)\Delta_2\right] \tag{7.4.13}$$

The degree of mismatch between the errors in the resistor values determines the extent of the error component of the input differential signal that appears in both differential and common mode signals at the output of the second stage. The common input signal receives only unity gain in both stages and there is no conversion of this signal into a differential component. In the third and final stage, all the components of the signals at the output of the second stage will be converted into a single-ended output. Consequently, at the output of the final stage all components will be present due to either the input differential signal or the input common mode signal and can be grouped accordingly when determining the CMRR from A_d and A_c overall.

The output voltage at the third stage can be described with worst-case resistor tolerance imbalance between channels as:

$$V_{03} = \frac{R_6}{R_5}\left[\left(1-\frac{R_6-R_5}{R_6+R_5}2\Delta\right)V_{02A}\right] - \frac{R_6}{R_5}\left[(1-2\Delta)\,V_{02B}\right] \tag{7.4.14}$$

Substituting the values of V_{02A} and V_{02B} in (7.4.14), the third stage output voltage can be rewritten as:

$$V_{03} = \frac{R_6}{R_5}\left\{\begin{array}{l}\left[V_{id}\left(1+2\frac{R_4}{R_3}\right)\left(1+2\frac{R_2}{R_1}\right)\right] + 4V_{ic}\frac{R_5}{R_5+R_6}\Delta \\ -V_{id}\left[1+\frac{R_4}{R_3}+\frac{R_2}{R_1}+\left(1+2\frac{R_4}{R_3}\right)\left(1+2\frac{R_2}{R_1}\right)\left(\frac{R_6-R_5}{R_6+R_5}\right)\right]\Delta\end{array}\right\} \tag{7.4.15}$$

The overall output of the 3-stage amplifier is of the form:

$$V_o = A_d V_{id} + A_c V_{ic} \tag{7.4.16}$$

where,

$$A_c = 4\frac{R_6}{R_5}\left(\frac{R_5}{R_5+R_6}\right)\Delta$$

and

$$A_d = \frac{R_6}{R_5}\left\{\begin{array}{l}\left[\left(1+2\frac{R_4}{R_3}\right)\left(1+2\frac{R_2}{R_1}\right)\right] \\ +\left[1+\frac{R_4}{R_3}+\frac{R_2}{R_1}+\left(1+2\frac{R_4}{R_3}\right)\left(1+2\frac{R_2}{R_1}\right)\left(\frac{R_6-R_5}{R_6+R_5}\right)\right]\Delta\end{array}\right\}$$

Therefore, the CMRR can be described as:

$$CMRR = \frac{\left\{A_{d1}A_{d2}+\left[1+\frac{R_4}{R_3}+\frac{R_2}{R_1}+A_{d1}A_{d2}\left(\frac{R_6-R_5}{R_6+R_5}\right)\right]\Delta\right\}}{4\left(\frac{R_5}{R_6+R_5}\right)\Delta} \tag{7.4.17}$$

where $A_{d1} = 1+2\frac{R_2}{R_1}$, $A_{d2} = 1+2\frac{R_4}{R_3}$.

If the Δ factor in the numerator of (7.4.17) is considered as a small error in the differential gain of only a few percent, then this would have only a fractional effect on the CMRR of the order of less than 1dB. In this case the CMRR can be approximated as:

$$CMRR = \frac{A_{d1}A_{d2}}{4\left(\frac{1}{1+A_{d3}}\right)\Delta} \tag{7.4.18}$$

The CMRR given in (7.4.18) can be further expressed in dB as:

$$CMRR(dB) = 20\log_{10}A_d + 20\log_{10}\frac{1}{\Delta} - 20\log_{10}2 \tag{7.4.19}$$

The variation in CMRR values for different values of Δ and a differential gain of 41dB is shown in 7.1 using (7.4.19).

Table 7.1: Variation of CMRR performance for different values ofΔ, A_d=41dB

Δ%	1	0.5	0.25	0.1
CMRR (dB)	75	81	87	95

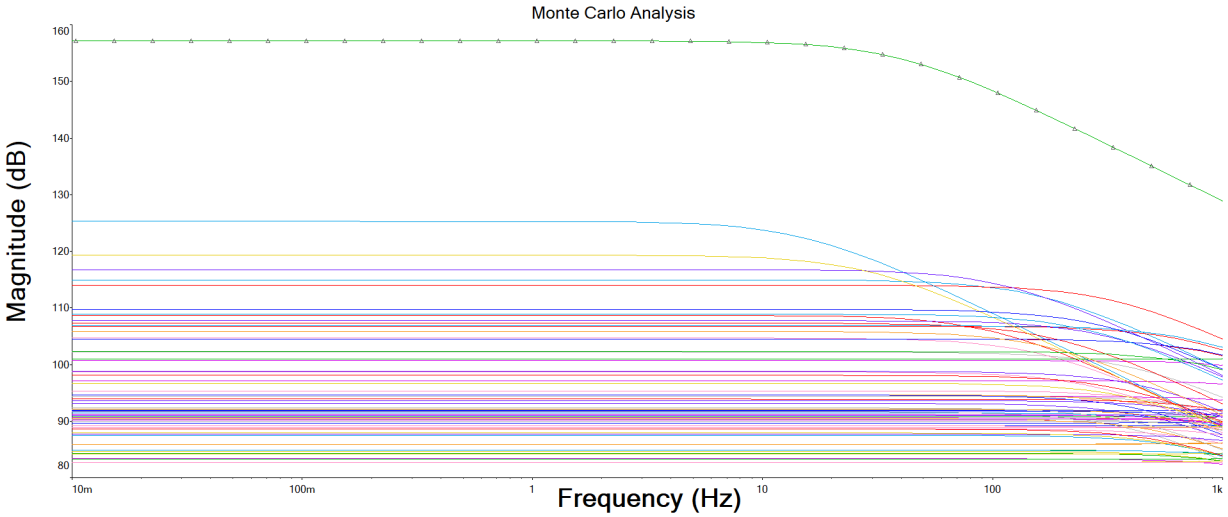

(a) CMRR due 1% resistor tolerance mismatch

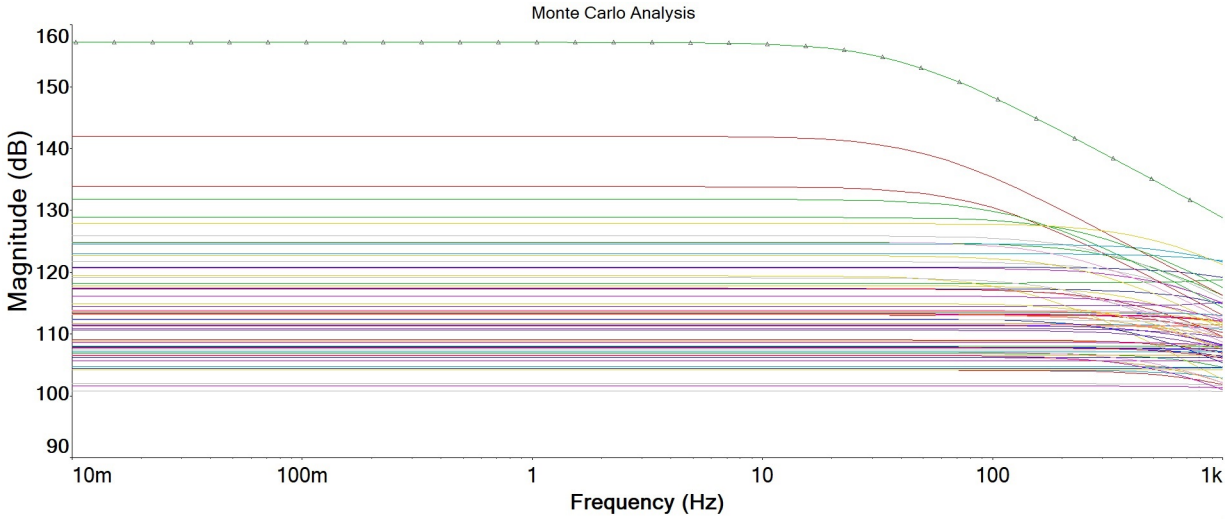

(b) CMRR due 0.1% resistor tolerance mismatch

Figure 7.11: Monte Carlo simulation for a multistage amplifier to assess the CMRR performance due to errors in resistor tolerance mismatch

The results presented in Table 7.1 suggests the use of resistor tolerance of 0.1% to guarantee a CMRR value of greater than 90dB. The 0.1% resistors are already used in the first stage and it is a simple matter to extend this to the second and third stages as only another six resistors are needed with this low tolerance. The circuit shown in Fig. 7.10 is simulated in Multisim to assess the CMRR performance due to the mismatch in resistor tolerance errors. The Monte Carlo Analysis using Multisim for a multistage amplifier is shown in Fig. 7.11. Examining Fig. 7.11 suggest that the worst case CMRR for a multistage amplifier due to 1% tolerance resistor is 80dB and is about 100dB for a resistor tolerance error of 0.1%. Therefore, the simulation results validate the theoretical findings. The 5dB difference could be attributed to

not running Monte Carlo long enough.

7.5 Finite CMRR in a Multistage Amplifier

The effect on CMRR performance due to finite op-amp CMRR limitation in a multistage amplifier configuration is illustrated in Fig. 7.12. Taking the resistors as ideal on both A and B sides of the amplifier but treating $CMRR_A$ and $CMRR_B$ values as separate gives:

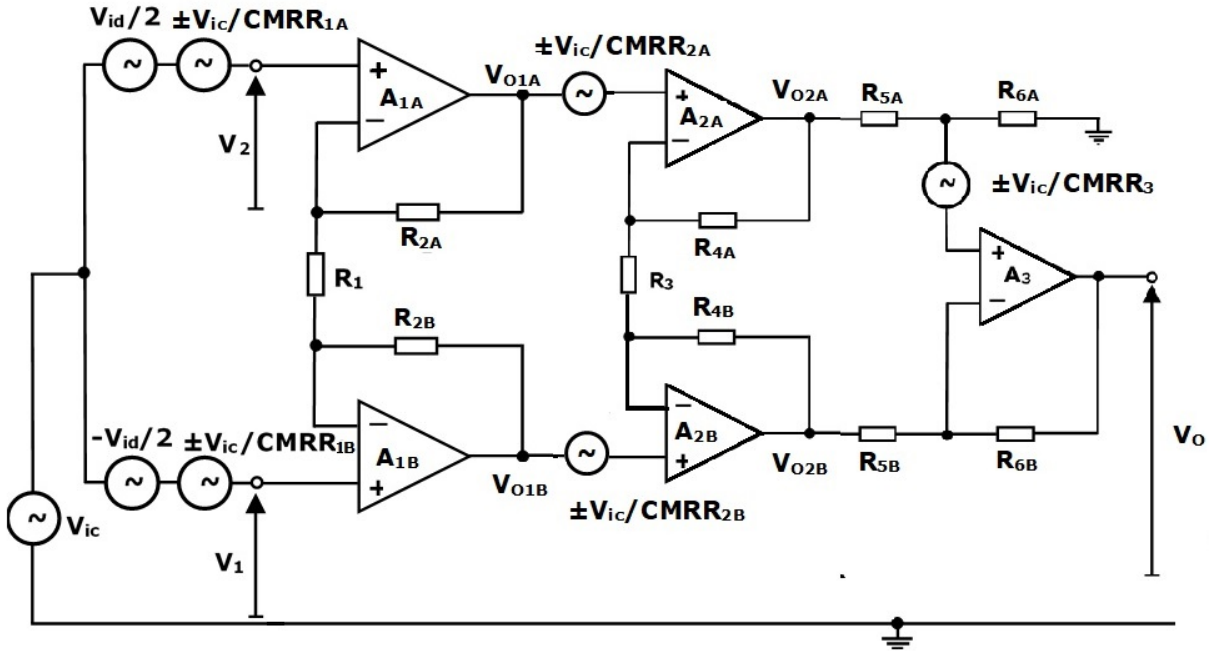

Figure 7.12: Finite op-amp CMRR analysis of our proposed Multistage ECG Amplifier

$$V_{01A} = V_{ic} + \left(1 + 2\frac{R_2}{R_1}\right)\frac{V_{id}}{2} \pm \left(1 + \frac{R_2}{R_1}\right)\frac{V_{ic}}{CMRR_{1A}} \mp \frac{R_2}{R_1}\frac{V_{ic}}{CMRR_{1B}} \tag{7.5.1}$$

$$V_{01B} = V_{ic} - \left(1 + 2\frac{R_2}{R_1}\right)\frac{V_{id}}{2} \pm \left(1 + \frac{R_2}{R_1}\right)\frac{V_{ic}}{CMRR_{1B}} \mp \frac{R_2}{R_1}\frac{V_{ic}}{CMRR_{1A}} \tag{7.5.2}$$

For the second stage we have:

$$V_{02A} = V_{01A} \pm \frac{V_{ic}}{CMRR_{2A}} + \frac{R_4}{R_3}\left(V_{01A} - V_{01B}\right) \pm \frac{R_4}{R_3}\left(\frac{V_{ic}}{CMRR_{2A}} - \frac{V_{ic}}{CMRR_{2B}}\right) \tag{7.5.3}$$

$$V_{02B} = V_{01B} \pm \frac{V_{ic}}{CMRR_{2B}} - \frac{R_4}{R_3}(V_{01A} - V_{01B}) \pm \frac{R_4}{R_3}\left(\frac{V_{ic}}{CMRR_{2B}} - \frac{V_{ic}}{CMRR_{2A}}\right) \quad (7.5.4)$$

For the third stage with matched resistors:

$$V_0 = \left[\frac{R_6}{R_5}(V_{02A} - V_{02B}) \pm \frac{V_{ic}}{CMRR_3}\right] \quad (7.5.5)$$

where,

$$V_{02A} - V_{02B} = \left(1 + 2\frac{R_4}{R_3}\right)(V_{01A} - V_{01B}) \pm \frac{V_{ic}}{CMRR_{2A}} \mp \frac{V_{ic}}{CMRR_{2B}} \pm 2\frac{R_4}{R_3}\left[\frac{V_{ic}}{CMRR_{2A}} - \frac{V_{ic}}{CMRR_{2B}}\right] \quad (7.5.6)$$

If $CMRR_{2B} = -CMRR_{2A}$, then the worst case maximum output will occur from the CMRR terms. These can then be taken as $CMRR_2$ implying the CMRR of the op-amps used in the second stage. In this case:

$$V_{02A} - V_{02B} = \left(1 + 2\frac{R_4}{R_3}\right)\left[(V_{01A} - V_{01B}) \pm 2\frac{V_{ic}}{CMRR_2}\right] \quad (7.5.7)$$

Similarly, CMRR values for the worst case mismatch using (7.5.1) and (7.5.2) gives:

$$V_{01A} - V_{01B} = \left(1 + 2\frac{R_2}{R_1}\right)\left[\left(V_{id} \pm \frac{V_{ic}}{CMRR_1}\right) \pm 2\frac{V_{ic}}{CMRR_2}\right] \quad (7.5.8)$$

Substituting (7.5.6) in (7.5.5) gives:

$$V_o = \frac{R_6}{R_5}\left\{\left(1 + 2\frac{R_4}{R_3}\right)\left[(V_{01A} - V_{01B}) \pm 2\frac{V_{ic}}{CMRR_2}\right] \pm \frac{V_{ic}}{CMRR_3}\right\} \quad (7.5.9)$$

Substituting (7.5.7) in (7.5.5) gives:

$$V_o = \frac{R_6}{R_5}\left\{\left(1 + 2\frac{R_4}{R_3}\right)\left[\left(1 + 2\frac{R_2}{R_1}\right)\left(V_{id} \pm 2\frac{V_{ic}}{CMRR_1}\right) \pm 2\frac{V_{ic}}{CMRR_2}\right] \pm \frac{V_{ic}}{CMRR_3}\right\} \quad (7.5.10)$$

If A_{d1}=$1 + 2\frac{R_2}{R_1}$, A_{d1}=$1 + 2\frac{R_4}{R_3}$ and A_{d3}=$1 + 2\frac{R_6}{R_5}$, then the output voltage in the third stage

can be described as:

$$V_o = A_{d3}\left\{A_{d2}\left[A_{d1}\left(V_{id} \pm 2\frac{V_{ic}}{CMRR_1}\right) \pm 2\frac{V_{ic}}{CMRR_2}\right] \pm \frac{V_{ic}}{CMRR_3}\right\} \tag{7.5.11}$$

This third stage output voltage V_o can be expressed in terms of differential and common-mode components of the input V_{id} and V_{ic} as:

$$V_o = A_{d3}A_{d2}A_{d1}V_{id} \pm 2A_{d3}A_{d2}A_{d1}\frac{V_{ic}}{CMRR_1} \pm 2A_{d2}A_{d3}\frac{V_{ic}}{CMRR_1} \pm A_{d3}\frac{V_{ic}}{CMRR_1} \tag{7.5.12}$$

This can be further rewritten as:

$$V_o = A_d V_{id} \pm \left[\frac{2A_d}{CMRR_1} \pm \frac{2A_d}{A_{d1}CMRR_2} \pm \frac{A_d}{A_{d1}A_{d2}CMRR_3}\right] V_{ic} \tag{7.5.13}$$

If the output due to the CMRR factors are all combined and taken as positive, then (7.4.13) becomes:

$$V_o = A_d V_{id} + A_d\left[\frac{2}{CMRR_1} + \frac{2}{A_{d1}CMRR_2} + \frac{1}{A_{d1}A_{d2}CMRR_3}\right] V_{ic} \tag{7.5.14}$$

where,

$$A_c = A_d\left[\frac{2}{CMRR_1} + \frac{2}{A_{d1}CMRR_2} + \frac{1}{A_{d1}A_{d2}CMRR_3}\right]$$

Then the overall CMRR of the amplifier due to finite op-amp CMRR's is given as:

$$\frac{1}{CMRR_{op}} = \frac{1}{\frac{1}{2}CMRR_1} + \frac{1}{\frac{1}{2}A_{d1}CMRR_2} + \frac{1}{A_{d1}A_{d2}CMRR_3} \tag{7.5.15}$$

This will depend on the distribution of the overall gain A_d between the three stages and the CMRR of the op-amps used in each stage which need not to be identical. Considering the typical op-amp CMRR values of LT6003 and OPA379 as 100dB, the overall CMRR of the amplifier due to finite op-amp CMRR is calculated using (7.5.15) to be 93dB.

7.6 Active Right Leg Drive

The right leg driven (RLD) circuit is one of the most commonly used techniques to eliminate common-mode interference signals from the wanted signal in ECG recording [165]. The common-mode signal is first sensed and then fed-back to the subject's body via a third electrode after inversion and amplification as illustrated in Fig. 7.13(b). The input common-mode voltage present with the active right-leg-drive incorporated into the amplifier is represented as V_{icRLD}. The output common-mode voltages at both sides of the first stage of the amplifier are amplified by the inverting op-amp structure having a gain of A_f so that the output voltage of this op-amp is designated as $-A_f V_{icRLD}$.

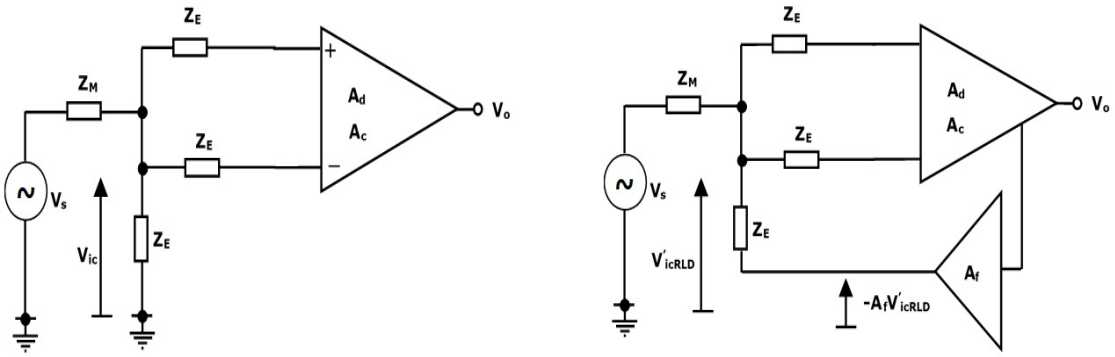

(a) No Right Leg Drive (b) Right Leg Drive Included

Figure 7.13: Schematic diagram to illustrate the benefit of active right leg drive circuit.

Considering the circuit shown in Fig. 7.13(a), the common mode input voltage can be given by:

$$V_{ic} = \frac{Z_E}{Z_E + Z_M} V_s \tag{7.6.1}$$

The component V_{ic} appears on the body due to the mains source of interference V_s through the impedance of the coupling medium Z_M. The modified common-mode voltage with the RLD present as shown in Fig. 7.13(b) can be described as:

$$V_{icRLD} = \frac{\frac{Z_E}{Z_E+Z_M} V_s}{\left[1 + A_f \frac{Z_M}{Z_M+Z_E}\right]} = \frac{V_{ic}}{\left[1 + A_f \frac{Z_M}{Z_M+Z_E}\right]} \tag{7.6.2}$$

This clearly shows that the inclusion of the right-leg-drive mechanism reduces the common-mode signal and at the input of the amplifier by the magnitude of the gain of the right-leg-drive feedback loop A_f. Then, the CMRR of the RLD network can be given by:

$$CMRR_{RLD} = \frac{A_d}{A_c} A_f \frac{Z_M}{Z_M + Z_E} \tag{7.6.3}$$

where $CMRR_{RLD}$ is the modified CMRR of the amplifier and the complete closed loop system with RLD. Normally if $Z_M \gg Z_E$, then $CMRR_{RLD} \rightarrow A_f CMRR$.

A schematic diagram as shown in Fig. 7.14 is used to illustrate the second and third stages of the pre-amplifier design. The common-mode signal from the output of the first stage is sensed by resistors R_{5A} and R_{5B}. This common-mode signal is first inverted and ac coupled to A_4 using C_2 and then fed-back to the right leg using C_3 and skin-electrode impedance Z_E. This structure reduces the sensed common-mode interfering signal at the amplifier input and effectively increases the CMRR by a factor equal to the gain of the inverting amplifier stage which is set to 20dB by making R_{5A}=R_{5B}=1MΩ and R_6=10MΩ. The gain of the right leg drive mechanism is set to 20dB to ensure the CMRR requirement of 80dB is met as outlined in the IEC60601 standard, even with high values of skin-electrode impedance. This was discussed in Chapter 4.

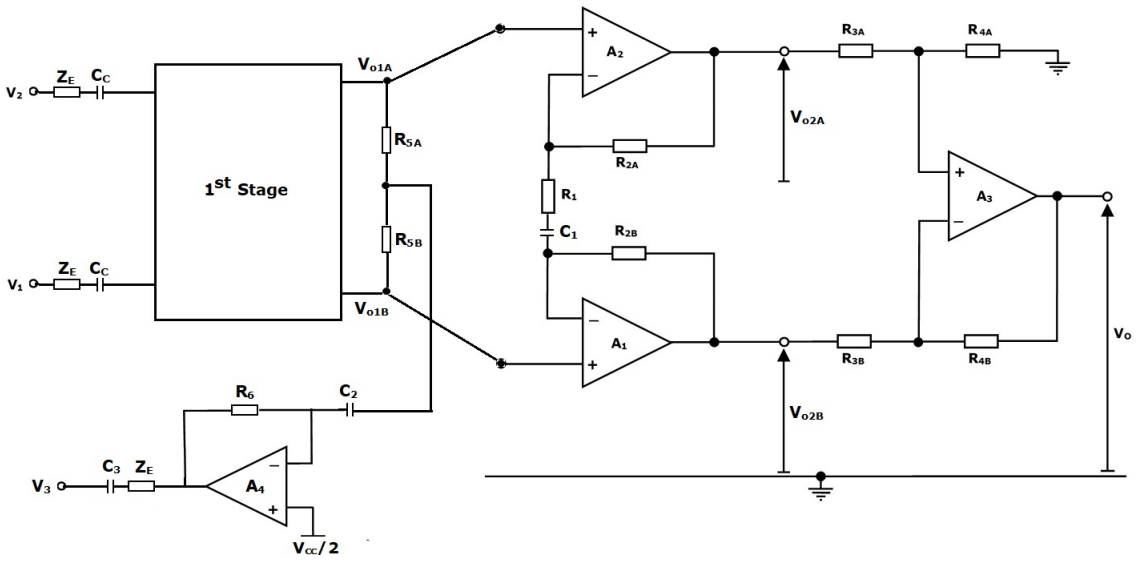

Figure 7.14: Schematic diagram of the 2^{nd} and 3^{rd} stage of the pre-amplifier design

The gain of the second stage is set to 14.6. This is implemented by making R_{2A}=R_{2B}=6.8MΩ

and R_1=1MΩ. The third stage provides a differential to single-ended conversion with unity gain. A high value of source impedance will limit the CMRR performance and the input impedance mismatch $CMRR_{\Delta Z}$ will dominate the overall CMRR of the amplifier. Considering a source impedance of 10MΩ, the boosted input impedance of 10GΩ, the input impedance mismatch $CMRR_{\Delta Z}$ is calculated using (4.6.7) as 63dB. Therefore, the overall CMRR of the recording amplifier with the finite op-amp CMRR as $CMRR_{\Delta OP}$=87dB for a single op-amp and the CMRR due to 0.1% resistor tolerance mismatch as $CMRR_{\Delta R}$=95dB can be obtained as:

$$\frac{1}{\text{CMRR}} = \frac{1}{\text{CMRR}_{\Delta \text{Z}}} + \frac{1}{\text{CMRR}_{\Delta \text{R}}} + \frac{1}{\text{CMRR}_{\text{OP}}} \tag{7.6.4}$$

Substituting the values of $CMRR_{\Delta Z}$, $CMRR_{\Delta R}$ and $CMRR_{\Delta OP}$ in (7.6.4), the overall CMRR of the pre-amplifier is calculated to be 62dB. The variation of the CMRR and the skin-electrode impedance with frequency is presented in Table 7.2. The results presented in Table 7.2 consider the worst case single-time and the double-time electrode models as discussed in Chapter 4. It can be seen that the skin-electrode impedance for a single-time CR model drops to about 676kΩ at 50Hz from 10MΩ at dc. For the double-time CR model, the highest value of resistance and the lowest value of capacitance is considered for CMRR and impedance analysis. The corresponding CMRR for both single C-R and double C-R is then well over 80dB at 50Hz and meets the IEC60601 specification. In addition, the RLD with a gain of 20dB is included in the design to guarantee the CMRR target requirements of 80dB as outlined in the IEC60601 specification.

Table 7.2: Variation of skin-electrode impedance and CMRR with frequency

Frequency (Hz)	Single C-R Impedance (MΩ)	Double C-R Impedance (MΩ)	CMRR for Single C-R (dB)	CMRR for Double C-R (dB)	$CMRR_{RLD}$ for Single C-R (dB)	$CMRR_{RLD}$ for Double C-R (dB)
0.05	9.999	7.98	62.5	63.96	82.5	83.96
0.1	9.996	7.93	62.5	64.01	82.5	84.01
0.5	9.893	6.62	62.9	63.58	82.9	83.58
1	9.591	4.75	63.36	66.47	83.36	86.47
10	3.209	0.59	69.87	84.58	89.87	104.58
30	1.122	0.2	79	93.98	99	113.98
50	0.676	0.12	83.4	98.42	103.4	118.42
100	0.339	0.06	89.4	104.44	109.4	124.44
150	0.226	0.04	92.92	107.96	112.92	127.96
250	0.136	0.02	97.33	113.98	117.33	133.98
500	0.068	0.01	103.35	120	123.35	140
1000	0.034	0.01	109.37	120	129.37	140

8 Construction and Testing of Prototype ECG Amplifiers

8.1 Introduction

This chapter outlines the construction and testing of a low-power low-noise, battery-operated amplifier to be used with dry electrodes. The schematic diagram of the complete multistage amplifier is shown in Fig. 8.1. The recording amplifier is driven by a single-rail supply consisting of a lithium-thionyl chloride battery (AA battery, RS Pro Inc.) with a nominal voltage of 3.7V. The battery life can be increased by minimising the supply current of the op-amps used in the circuit. The amplifier uses thirteen op-amps in total as shown in Fig. 8.1. These op-amps draw a total quiescent current of 31.5μA and therefore consume a total power of 125μW, which is well below the maximum target value of 1mW specified in Table 2.6. Current limiting resistors R_p of 100kΩ are placed in series with the dc blocking capacitors C_c at the input terminals of the amplifier to limit the continuous flow of dc current through the patient's body in the event of a fault. The performance requirements related to transient response, noise considerations, input impedance boosting, common-mode signal reduction strategies have been discussed in previous chapters. This chapter will present comprehensive bench tests to assess these performance parameters of two prototype recording amplifiers. The design was first implemented on a stripboard and subsequently on professional PCB. The bench tests results from measurements on both boards are presented together and contrasted in this chapter. Due to the Covid-19 pandemic worldwide and nationally, only two subjects

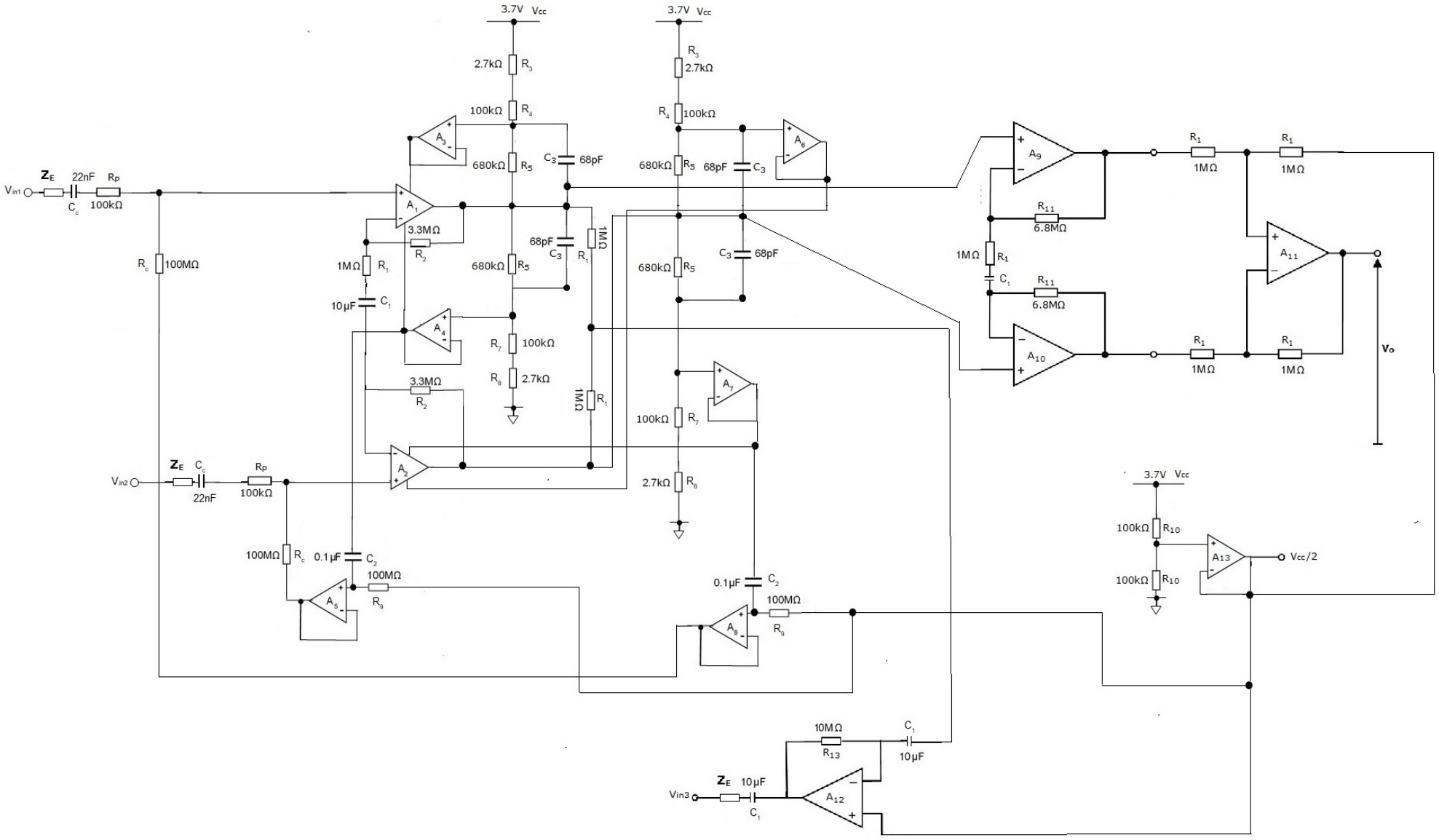

Figure 8.1: The Multistage ECG amplifier with active right leg drive.

could be included in the practical in-vivo tests. Applications to the School ethics committee to include more subjects in studies were rejected. Actual in-vivo ECG recordings on two male subjects using dry and wet electrodes are presented.

8.2 Differential Signal Generator

A prototype circuit as shown in Fig. 8.2 was constructed on stripboard to generate a differential signal having a dc voltage bias of $V_{cc}/2$. A dual op-amp OPA379 operating from a single supply voltage of 3.7V is used to generate a differential signal. This test circuit is used to measure the amplifier performance parameters such as: CMRR, input impedance and frequency response. The op-amp A_1 forms the unity gain buffer to generate the positive half of the differential signal $V_{cc}/2 + V_{id}/2$. Similarly, the unity gain inverting op-amp formed by A_2 is used to generate the negative half of the differential signal $V_{cc}/2 - V_{id}/2$. The 3.3μF capacitor serves to ac couple the source and block any dc offset in it.

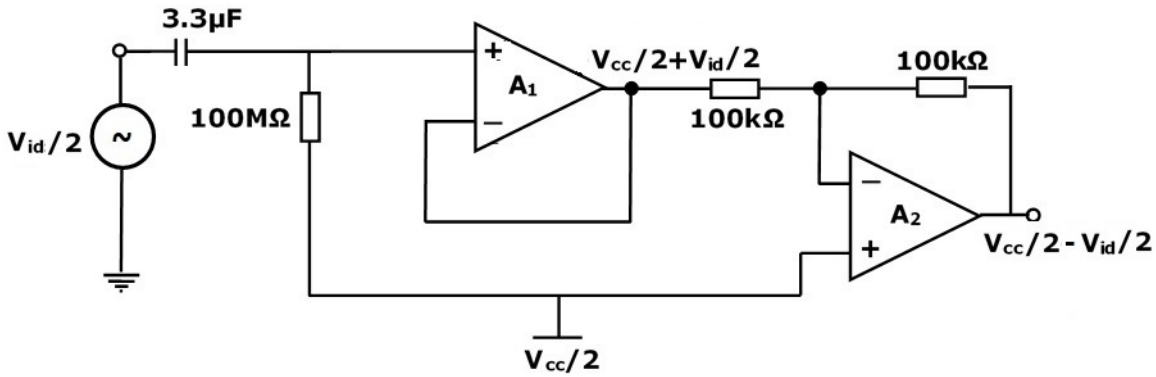

Figure 8.2: Differential signal generator circuit.

8.3 Layout of the Amplifier Prototype

8.3.1 Stripboard Layout

The circuit shown in Fig. 8.1 was built and tested on a stripboard. A photo illustrating a finished strip-board is shown in Fig. 8.3. It should be pointed out that the differential signal generator circuit shown above is included on the strip-board. It is noteworthy to mention that

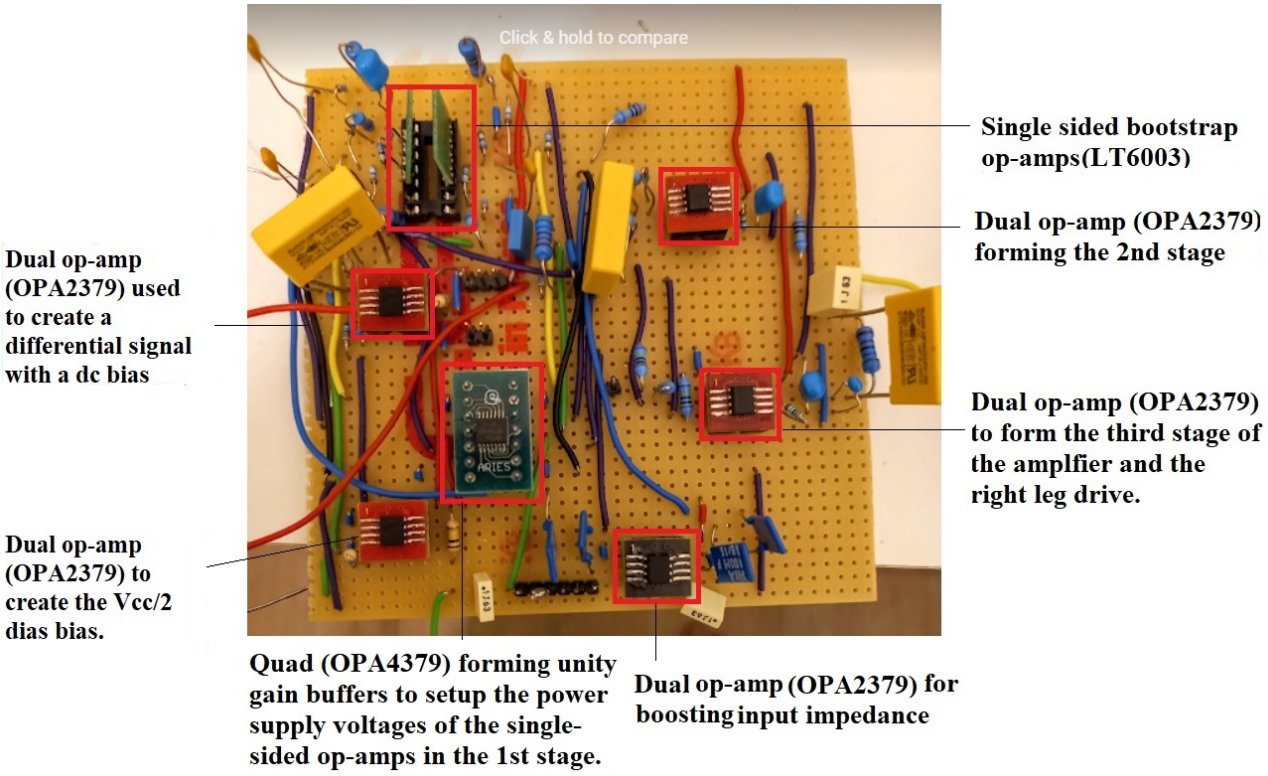

Figure 8.3: Stripboard prototype Layout.

all the resistors used in this design are of 1% tolerance. Initially on strip-board, it was decided to have the amplifier built with OPA379 op-amps. However, instabilities were experienced at the output of the first stage owing to lower capacitive load drive ability of OPA379. The LT6003 can handle capacitive loads of up to 500pF and was finally used in the first stage of the amplifier design. The reduction of gain bandwidth product (GBW) from 90kHz in OPA379 to 2kHz in LT6003 compelled us to lower the gain in the first stage of the amplifier. Consequently, the first stage gain was dropped from 14.6 down to 7.6 and the 6.8MΩ resistors in this stage were changed to 3.3MΩ.

8.3.2 PCB Layout

The PCB design did not include the signal generator test circuit shown in Fig. 8.2. This test circuit was built separately when testing with the PCB. This was intended to mimic an actual ECG recording scenario and was also intended to reflect the effects of cable capacitance on amplifier performance. A photo of the PCB prototype board with the track layout and its corresponding placement of the surface mounted components are shown in Fig. 8.4(a)

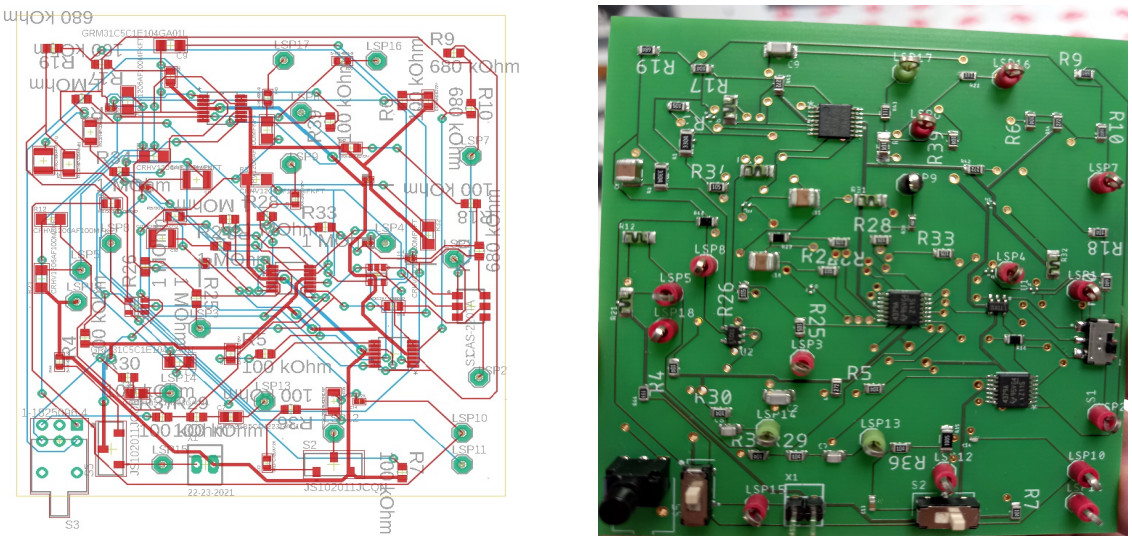

(a) Layout (b) Finished Look of the PCB

Figure 8.4: Professional PCB prototype Layout.

and 8.4(b) respectively. Multiple test points on this board denoted as 'LSP' are used to give probe points and allow intermediate access. All the surface mounted resistors are of 0.1% tolerance, except for the gain determining resistors of 3.3$M\Omega$ and 6.8$M\Omega$ which are of 0.5% tolerance.

There are three different switches that are incorporated in the PCB design:

- One miniaturised single pole double throw slide switch (SPDT) from CK Inc. is used to power the amplifier on and off. This switch on/off mechanism is demonstrated in Fig. 8.5. A 100Ω resistor R_1 is connected across a capacitor C_1 of 68pF in the switch off position to allow fast discharge of the polarised charges and ground the supply rail via the resistor.

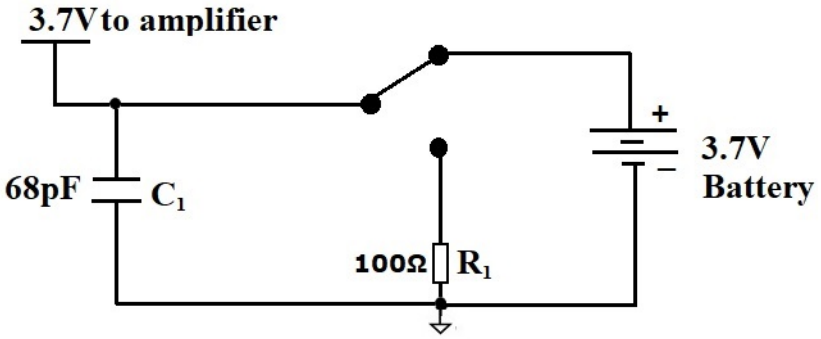

Figure 8.5: Circuit diagram illustrating battery switch on/off mechanism.

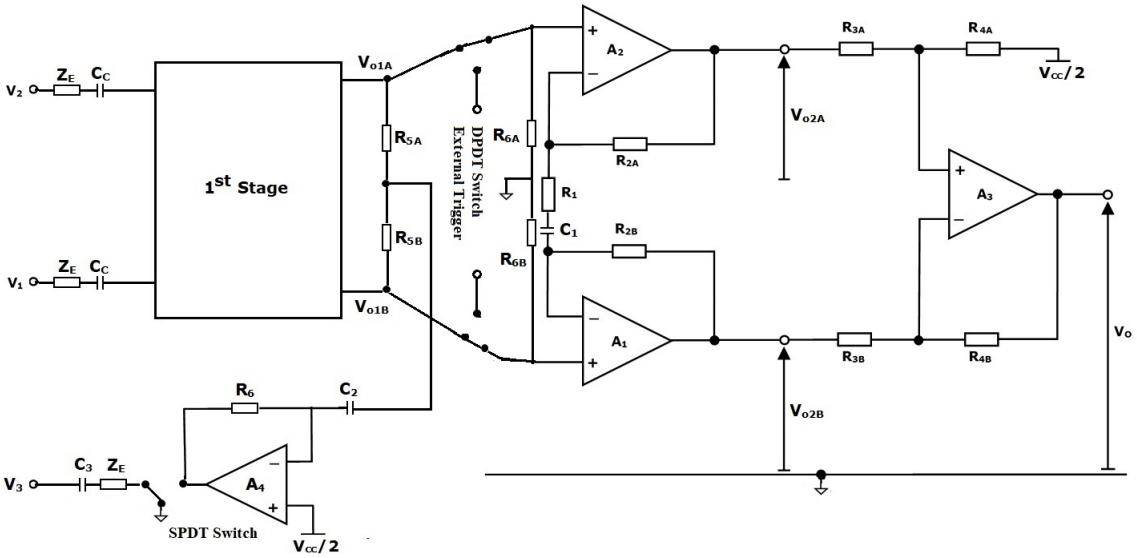

Figure 8.6: Circuit diagram illustrating usuage of DPDT and SPDT switches in the amplifier design.

Another SPDT switch from the same manufacturer as shown in Fig.8.6 is used to activate/deactivate the right-leg drive circuit (RLD) by connecting the third electrode either to ground or to the output of op-amp A_4.

- One miniaturised double pole double throw switch (CAS220TA, DPDT) is used in the design to isolate the first stage from the second as demonstrated in Fig. 8.6. This is implemented mainly to troubleshoot the design and to allow intermediate access to the second stage of the amplifier.

- One double pole single throw (DPST) push button tactile on/off switch is used to mitigate against the large power up time of the recording amplifier. This switch allows a fast charge up or initialisation by connecting a smaller resistor R_2 of 100kΩ across the 100MΩ resistor at the inputs of the amplifier. This is shown in Fig. 8.7.

The PCB layout was completed using EAGLE 9.6.2 Student version. The board design in EAGLE is a two-step process. First the schematic as shown in Fig. 8.1 was drawn and then the layout board based on that schematic was generated. The relevant libraries of the components used in the schematic were imported from Ultra Librarian website to ensure a correct footprint was used in the layout. An auto routing feature in EAGLE was used coupled with optimal component placement to ensure the tool is able to route it 91% automatically.

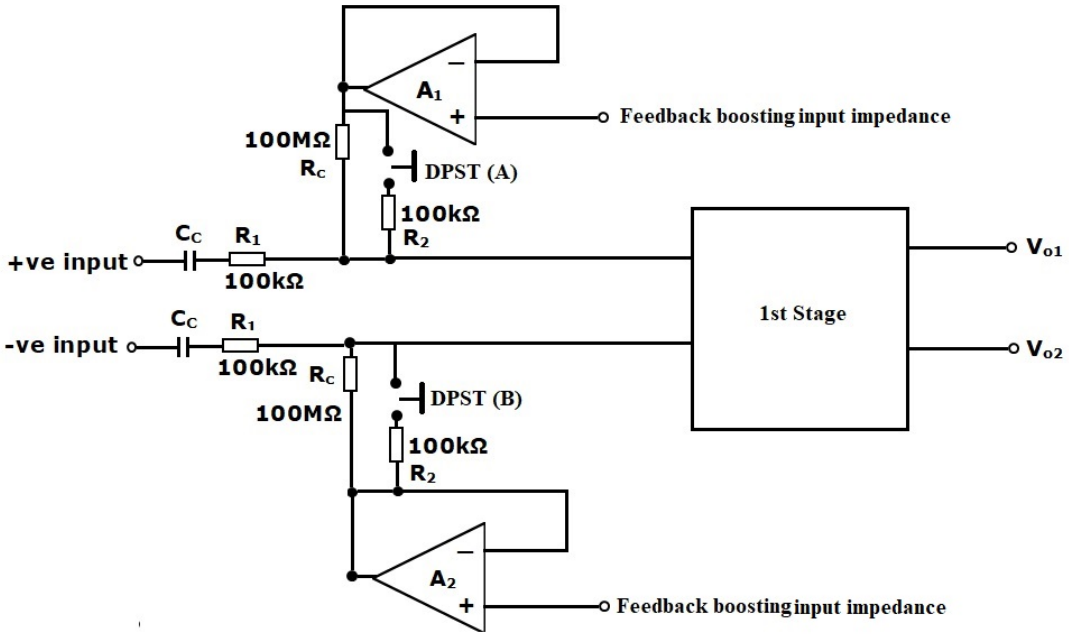

Figure 8.7: Schematic diagram describing usuage of push button DPST switches at the amplifier inputs.

The rest of the routing was completed manually.

There were several problems that were encountered during this prototype debug. A 100MΩ resistor R_c was mistakenly substituted with a 100kΩ resistor in the first stage of the amplifier. This resulted in an incorrect behaviour of the differential and common-mode gains. The mistake was swiftly identified by isolating the first stage from the second and third stage with the help of the DPDT switch. The library defining the footprinted power supply pins for the two single sided bootstrap op-amps didn't match the actual data-sheet. This problem was also identified when the amplifier didn't operate correctly. It was corrected by manual rewiring on the board. The DSPDT access switch wiring also had to be modified.

8.4 Worst Case Electrode Models

The worst-case equivalent single C-R and double C-R electrode models obtained from Electrode No. 2 as discussed in Chapter 3 are shown in Fig. 8.8. The self-constructed silven woven textile-based electrodes have been used for the final in-vivo ECG recordings. The electrical properties of these models needed highest values of input resistance R_{in} to meet the

IEC60601 transient requirements. This is discussed in Chapter 3 and Chapter 4. These worst case electrode models are then considered as the internal impedance of the signal source to the ECG amplifier as shown in Fig. 8.1. The performance of the amplifier with these worst case electrode models is outlined in the following sections.

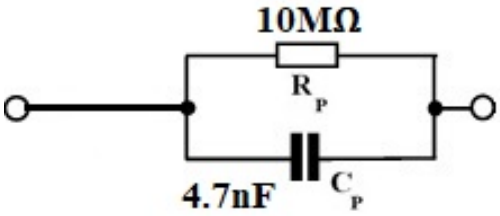

(a) Worst-case single C-R skin-electrode model

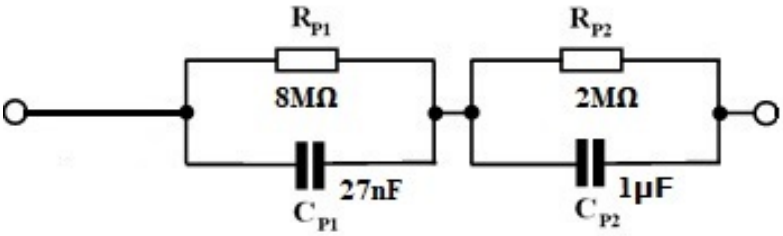

(b) Worst-case double C-R skin-electrode model

Figure 8.8: Circuit equivalent of worst-case skin-electrode models.

8.5 Frequency Response

Table 8.1: -3dB bandwidth from differential gain measurements

	Stripboard		PCB	
	Lower cut-off Frequency (Hz)	Upper cut-off Frequency (Hz)	Lower cut-off Frequency (Hz)	Upper cut-off Frequency (Hz)
Amplifier	0.03	450	0.02	450
Single C-R Model	0.04	400	0.03	450
Double C-R Model	0.03	450	0.03	450

A differential signal having an amplitude of 5mVptp is applied between both inputs of the recording amplifier as shown in Fig. 8.1. The magnitude of the frequency response at different spot frequencies is shown in Fig. 8.9. The bench measurements that were undertaken on

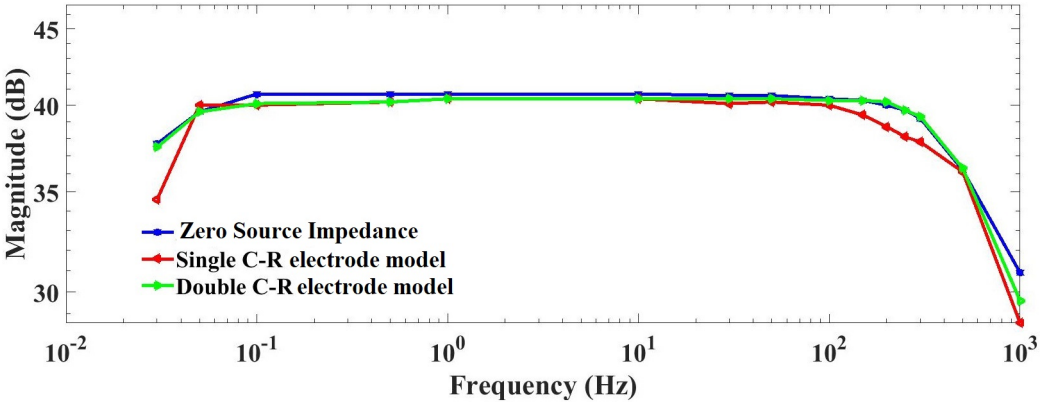

(a) Magnitude response on stripboard

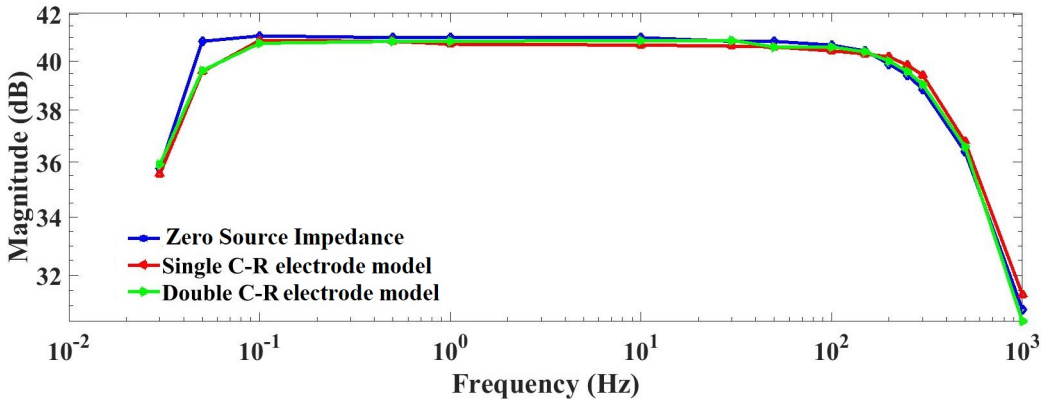

(b) [Magnitude response on PCB

Figure 8.9: Magnitude Response at different spot frequencies.

the prototype strip-board are contrasted with those made on professional PCB in Fig. 8.9(b). Examining Fig. 8.9(a) and (b), it is evident that there is hardly any noticeable difference in the magnitude response between the strip-board and that of the PCB within the target ECG bandwidth. It must be stressed here that the strip-board was built and tested with 1% tolerance through hole resistors, whereas the PCB was built with 0.1% tolerance surface mount resistors. The graphs in Fig. 8.9 suggest that the recording amplifier when considered with worst case electrode models maintains a minimum differential gain of about 40dB within the ECG bandwidth. The variation in the magnitude of the frequency response is kept within $\pm 0.5dB$ (6 %) of the mid-band gain down to a low cut-off frequency of 0.1 Hz and a high cut-off of 30Hz. Therefore, the measurements from the practical bench test meets the frequency response design requirements as indicated in Table 2.6. The upper and lower 3dB cut-off frequencies presented for the amplifier and for the electrode models are given in Table 8.1 and meet the frequency response requirements as outlined in Table 2.6.

8.6 Input Impedance Measurement

The circuit was tested for input impedance over a wide range of frequency values. Ideally, input impedance is measured by simultaneously measuring AC current through the input impedance and also measuring the AC voltage drop across it to calculate input impedance as a function of frequency. However, measuring current values in the region of pico-amps was not feasible with the equipment available and therefore an alternative measurement method was undertaken. By placing a known value of source impedance Z_E in series with the input impedance R_{in} between the source and the input to the amplifier, the attenuation relative to the source as a function of frequency can be measured using a signal analyser. A diagram outlining the test set-up is shown in Fig. 8.10. The transfer function of the circuit shown in Fig. 8.10 can be

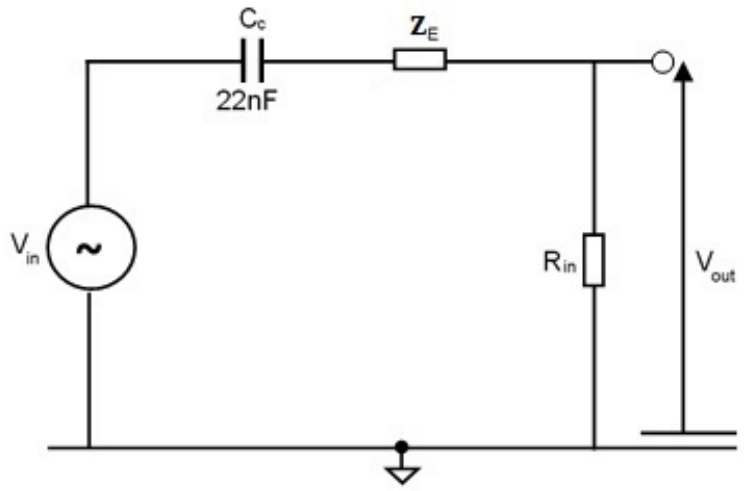

Figure 8.10: Input attenuation measurement setup.

described in the Laplace domain as:

$$\frac{V_{out}(s)}{V_{in}(s)} = \frac{R_{in}}{R_{in} + Z_E + \frac{1}{sC_c}} \tag{8.6.1}$$

The magnitude of the input resistance as a function of frequency from (8.6.1) can be further expressed as:

$$R_{in} = |Z_E| \frac{V_{out}}{(V_{out} - V_{in})} \left[\sqrt{1 + \left(\frac{1}{\omega C_c |Z_E|} \right)^2} \right] \tag{8.6.2}$$

A differential input signal of 20mVptp is injected between the input terminals of the op-amps A_1 and A_2 as shown in Fig. 8.1. A typical attenuation level of 0.01mV accuracy as shown in Fig.8.11 is measured with the help of battery operated 16 bit resolution oscilloscope, Picoscope. The precise measurement values recorded from both channels of the oscilloscope can be clearly seen by zooming on to Fig. 8.11 of the electronic version of this thesis. The variation of the voltage drop at different frequencies seen at the input terminals of the amplifier is presented in Table 8.2 and Table 8.3. The practical bench results on the prototype strip-board are presented in Table 8.2. Similarly, the measurement results on the professional PCB are given in Table 8.3. The measured values of the input resistance using (8.6.1) are also listed in these Tables. The results in Table 8.2 show that the common-mode input resistance at each amplifier input irrespective of the presence of any electrode models as indicated in Fig. 8.8 is boosted to at-least 10GΩ from 0.1Hz - 250Hz. The mid-band boosted input impedance was measured at 20GΩ and is in agreement with the design and analysis of Chapter 6. It is possible to further lower the cut-off frequency down to 0.05Hz but that would require a higher value of ac-gain feedback network capacitor greater than 10μF. This would ultimately increase the time-constant associated with power up and initialisation of the amplifier. The boosted mid-band input resistance of 10GΩ in the PCB as shown in Table 8.3 is maintained in the frequency bandwidth of 0.1Hz-150Hz. The drop of upper cut-off frequency from 250Hz down to 150Hz is mainly attributed to the cables used to couple the differential signal test circuit to the amplifier input as discussed in section 8.3.

In an effort to validate further the magnitude of the boosted impedance value, the input source signal shown in Fig. 8.1 is fed with a 3mV-100ms rectangular pulse for the two worst case electrode models as outlined in Fig. 8.8. The output of the amplifier A_{11} as shown in Fig. 8.1 was then attenuated by a factor of 110 to restore it to a relative input level. The waveforms obtained from the responses of each of these worst-case electrode models on the PCB are shown in Fig. 8.12.

The undershoot and recovery slope values obtained from these bench tests are presented in Table 8.4 for the two different boards and electrode models. The results suggest that the undershoot and the recovery slope values meet the IEC 60601 transient performance

Table 8.2: Variation of Input Impedance with frequency on prototype stripboard

Single C-R Model					Double C-R Model				
Frequency (Hz)	Op-amp A_1 o/p (mV)	R_{in1} (GΩ)	Op-amp A_2 o/p (mV)	R_{in2} (GΩ)	Frequency (Hz)	Op-amp A_1 o/p (mV)	R_{in1} (GΩ)	Op-amp A_2 o/p (mV)	R_{in2} (GΩ)
0.03	19	4.588	19	4.588	0.03	19	4.588	14.5	4.588
0.05	19.3	4.001	19.5	5.659	0.05	19.3	7.11	19.5	7.11
0.1	19.84	9.06	19.9	14.54	0.1	19.86	10.36	19.9	14.54
0.5	19.97	11.712	19.98	17.577	0.5	19.98	17.577	19.98	17.577
1	19.98	12.332	19.98	18.979	1	19.99	18.979	19.99	24.677
10	19.99	20.042	19.99	20.042	10	19.99	20.042	19.99	20.042
30	19.99	19.996	19.99	19.996	30	19.99	19.996	19.99	19.996
50	19.99	19.992	19.99	19.992	50	19.99	19.992	19.99	19.992
100	19.99	19.991	19.99	19.991	100	19.99	19.991	19.99	19.991
150	19.99	19.99	19.99	19.99	150	19.99	19.99	19.99	19.99
200	19.99	19.99	19.99	19.99	200	19.99	19.99	19.99	19.99
250	19.98	9.99	19.99	19.99	250	19.98	19.99	19.99	19.99
300	19.9	1.99	19.84	1.24	300	19.9	6.657	19.84	6.657
500	15.26	0.032	14.65	0.027	500	15.26	0.038	14.65	0.038
1000	4.7	0.003	4.12	0.003	1000	4.7	0.01	4.12	0.01

Table 8.3: Variation of Input Impedance with frequency on PCB

Single C-R Model					Double C-R Model				
Frequency (Hz)	Op-amp A_1 o/p (mV)	R_{in1} (GΩ)	Op-amp A_2 o/p (mV)	R_{in2} (GΩ)	Frequency (Hz)	Op-amp A_1 o/p (mV)	R_{in1} (GΩ)	Op-amp A_2 o/p (mV)	R_{in2} (GΩ)
0.03	18.2	2.442	19	2.3	0.03	17.8	1.954	17.8	1.954
0.05	19.68	8.924	19.5	8.924	0.05	19.6	7.11	19.6	7.11
0.1	19.82	8.046	19.9	9.06	0.1	19.9	14.54	19.9	14.54
0.5	19.97	11.712	19.98	8.779	0.5	19.98	17.577	19.98	17.577
1	19.98	12.332	19.98	12.332	1	19.99	24.677	19.99	24.677
10	19.99	20.042	19.99	20.042	10	19.99	20.042	19.99	20.042
30	19.99	19.996	19.99	19.996	30	19.99	19.996	19.99	19.996
50	19.99	19.992	19.99	19.992	50	19.99	19.992	19.99	19.992
100	19.99	19.991	19.99	19.991	100	19.99	19.991	19.99	19.991
150	19.98	9.99	19.99	9.99	150	19.98	9.99	19.98	9.99
200	19.9	1.99	19.99	1.99	200	19.92	2.49	19.92	2.49
250	19.84	1.24	19.99	1.24	250	18.9	0.172	18.9	0.172
300	19.67	0.596	19.84	0.596	300	18.8	0.157	18.8	0.157
500	13.3	0.02	14.65	0.02	500	13.6	0.021	13.6	0.021
1000	10.1	0.01	4.12	0.01	1000	10.4	0.011	10.4	0.011

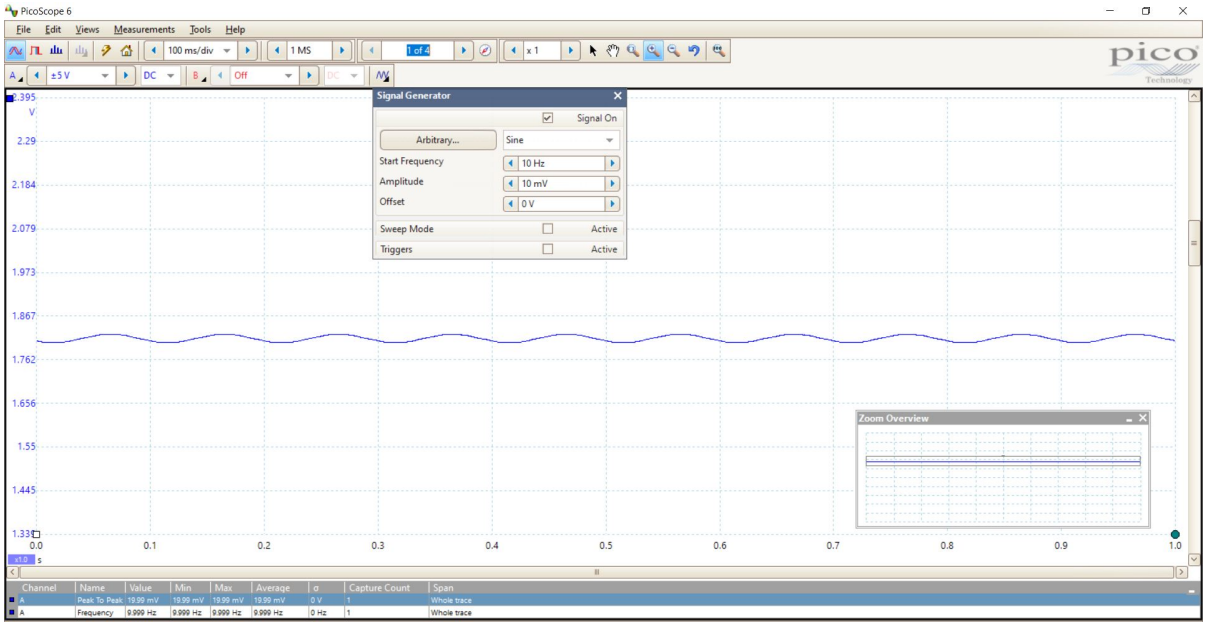

(a) Output voltage attenuation of op-amp A_1, Channel A oscilloscope

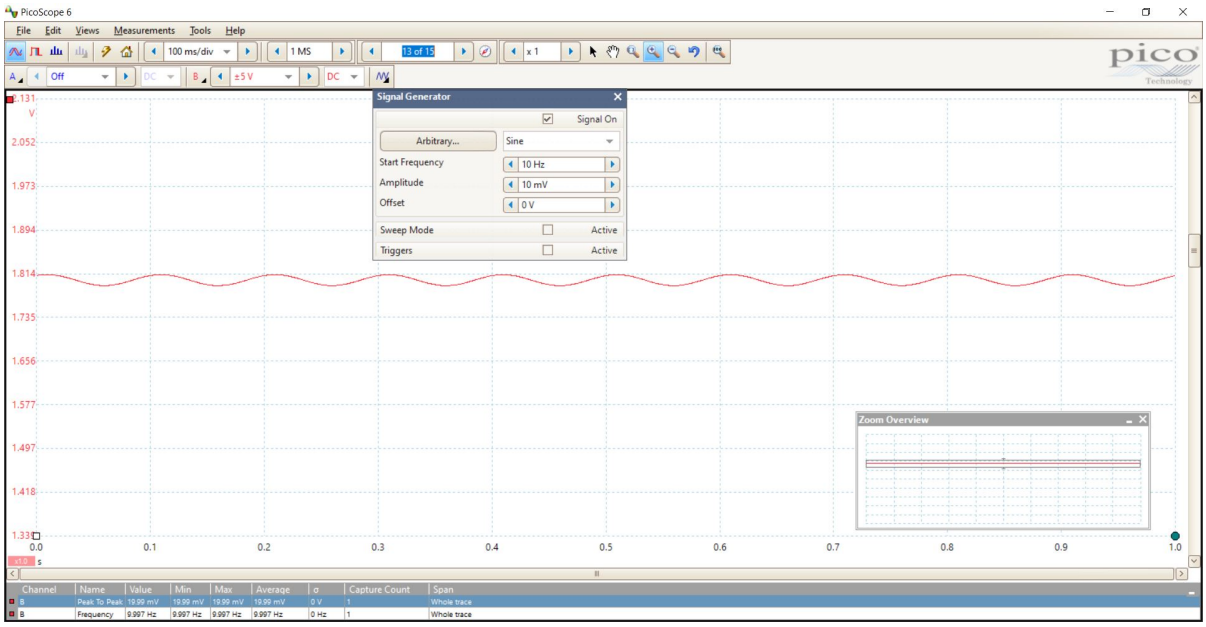

(b) Output voltage attenuation of op-amp A_2, Channel B oscilloscope

Figure 8.11: Output voltage attenuation measured at the input of bootstrap op-amps A_1 and A_2 in response to an input differential voltage amplitude of 20mVptp at 10Hz.

Table 8.4: Undershoot and Recovery Slope Values for the worst case Electrode Models in Response to 3mV-100ms Rectangular Pulse

Board Type	Performance parameters	Single C-R model	Double C-R model
Strip-board	Undershoot (μV)	10	5
	Recovery Slope (μV/sec)	173	123
PCB	Undershoot (μV)	14	8
	Recovery Slope (μV/sec)	216	169

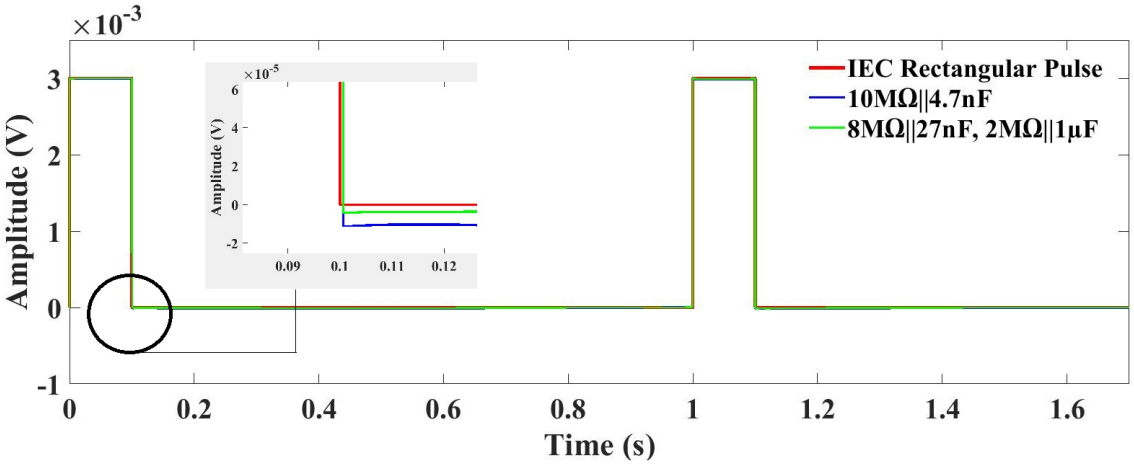

Figure 8.12: Transient Response to the 3 mV- 100 ms Narrow Pulse for two worst case electrode models.

specification of 100μV and 300μV/sec respectively.

8.7 CMRR Measurement

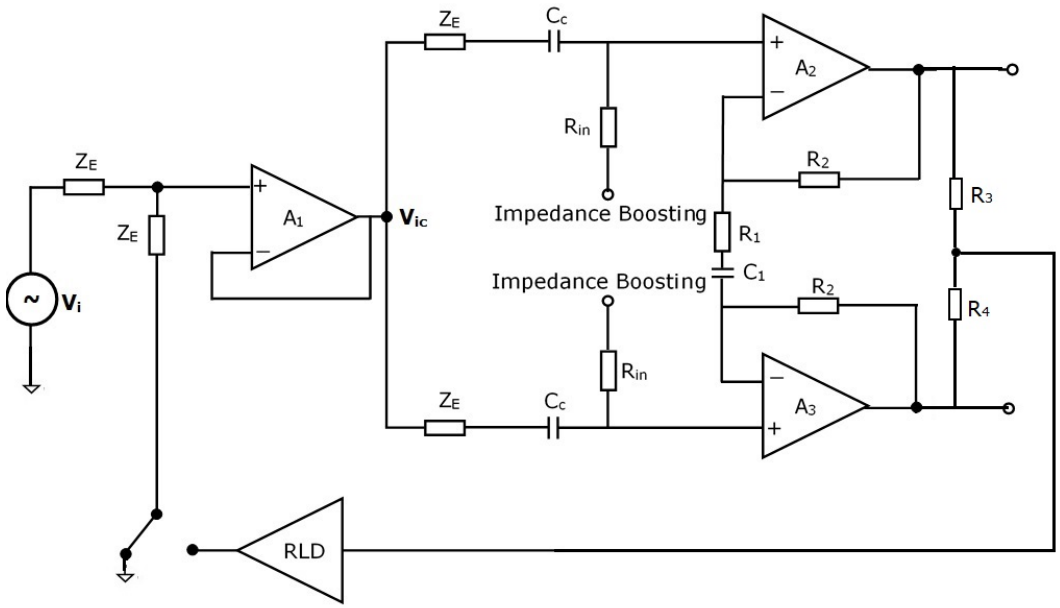

Figure 8.13: Schematic diagram of Right Leg Drive (RLD) measurement circuitry.

The CMRR performance of the ECG recording amplifier as shown in Fig.8.1 as a function of frequency is presented in Table 8.5. The use of the active right-leg drive (RLD) mechanism as shown in 8.13 on two worst case electrode models boosts the CMRR performance of the pre-amplfier as indicated in Table 8.5. The common-mode input voltage V_{ic} without the inclusion

Table 8.5: Variation of CMRR measurements with frequency using two worst case electrode models

	Stripboard				PCB			
	Single C-R Model		Double C-R Model		Single C-R Model		Double C-R Model	
Frequency (Hz)	CMRR (dB)	$CMRR_{RLD}$ (dB)	CMRR (dB)	$CMRR_{RLD}$ (dB)	CMRR (dB)	$CMRR_{RLD}$ (dB)	CMRR (dB)	$CMRR_{RLD}$ (dB)
0.03	49.868	60.868	51.33	63.33	50.818	60.413	48.772	66.66
0.05	53.147	66.147	53.678	68.078	59.766	71.264	55.437	73.572
0.1	61.743	78.743	62.12	77.12	61.976	75.697	63.331	79.457
0.5	63.024	81.024	66.778	81.578	65.943	81.156	66.728	82.984
1	63.82	80.52	70.138	84.238	66.102	83.156	69.749	86.156
10	67.198	84.598	85.673	98.873	73.082	91.943	88.441	100.963
30	78.168	95.168	86	99.1	81.766	92.848	91.285	100.807
50	74.772	91.572	81.332	93.202	80.827	89.925	86.848	97.285
100	71.379	89.379	74.6	87.48	75.563	88.606	78.389	97.126
150	68.453	84.853	71.1	85.7	69.794	86.778	73.189	90.86
200	65.192	81.892	66.98	80.65	66.243	83.589	70.326	87.806
250	64.386	76.386	59.7	71.3	64.147	82.01	64.298	78.971
300	60.475	71.775	48.07	60.157	61.11	77.757	51.308	63.933
500	44.209	53.209	39.89	52.49	43.741	57.629	43.561	59.593
1000	33.8	41.7	35.289	48.489	34.908	45.277	37.439	50.561

of the RLD is $V_{ic}/2$. The reduction of this common-mode voltage with the inclusion of RLD from $V_{ic}/2$ to a lower value is measured to determine the gain of the RLD. It can be seen that the CMRR values without the right leg drive are as low as 60dB at lower frequencies. This is mainly attributed to the source input and impedance mismatch, as discussed in Chapter 7. The CMRR values shown in Table 8.5 are in line with the calculated CMRR values due to this mismatch indicated in Table 7.2. It must be stressed here that the CMRR performance specification as outlined in Table 2.3 only applies at a mains frequency of 50Hz. The CMRR attains an approximate minimum value of 80dB when the two worse-case skin-electrode models are considered. The CMRR with the inclusion of the RLD is over 100dB when the worst-case double C-R model is considered. It has been established in the literature [8, 134, 135] that the double C-R model is a more accurate representation of the skin-electrode impedance. Therefore, the proposed amplifier design meets the CMRR performance specification for both ambulatory and clinical ECG requirements as outlined by the IEC and ANSI. It should be also pointed here that the measured CMRR values from the strip-board and the PCB are in close agreement, even though the strip-board uses 1% tolerance resistors and the PCB is built with 0.1% tolerance resistors. Therefore, it reinforces the findings that the the input impedance mismatch is the dominant factor in determining the overall amplifier CMRR performance as opposed to mismatch in gain determining resistors or finite CMRR values of the op-amps used in the design.

8.8 Noise Measurements

The semiconductor noise at the output of the amplifier is measured by grounding the input terminals, V_{in1} and V_{in2} of the recording amplifier through source impedances. This noise measurement has been carried out inside a Faraday cage coupled with a battery operated amplifier to ensure an extremely low level of 50Hz pick-up. This guaranteed that the measured noise levels at the amplifier output were a true representation of the semiconductor noise. The peak-to-peak input-referred noise produced with the electrode models outlined in Fig. 8.8 is presented in Table 8.6 and Table 8.7. Examining these Tables, it is evident that the

input referred peak-to-peak noise levels in a 250Hz bandwidth is slightly outside the $30\mu V_{ptp}$ IEC60601 noise specification limit. It must be re-iterated that most of the noise measurements in the literature are conducted in a bandwidth of 100Hz [8, 25, 30] and without considering a source impedance value as high as 10MΩ. The input referred peak-to-peak noise values obtained from the strip-board are in close agreement with the measured values from the PCB. Fig. 8.14 presents the recording amplifier peak-to-peak noise output voltage when the two electrode models are used in a 250Hz bandwidth.

Table 8.6: Peak to peak input referred noise of prototype strip-board

Frequency (Hz)	Amplifier only (μV_{ptp})	Single C-R Model (μV_{ptp})	Double C-R Model (μV_{ptp})
250	32.7	38	36.7
150	17.2	23	19
100	2.3	18.5	10.6

Table 8.7: Peak to peak input referred noise of PCB

Frequency (Hz)	Amplifier only (μV_{ptp})	Single C-R Model (μV_{ptp})	Double C-R Model (μV_{ptp})
250	31.8	35	34.6
150	21	18	21.2
100	14.7	15.4	8.8

8.9 ECG Recordings

8.9.1 Recording scenarios

Practical ECG recordings were carried out on two subjects using dry and wet electrodes under the following conditions:

• Sitting ECG : the subject was sitting comfortably on a chair and breathing normally.

• Waving ECG : the subject had to raise their arms up and down while sitting on a chair. One arm was raised and lowered again and the other arm raised and lowered with about 4s cycle.

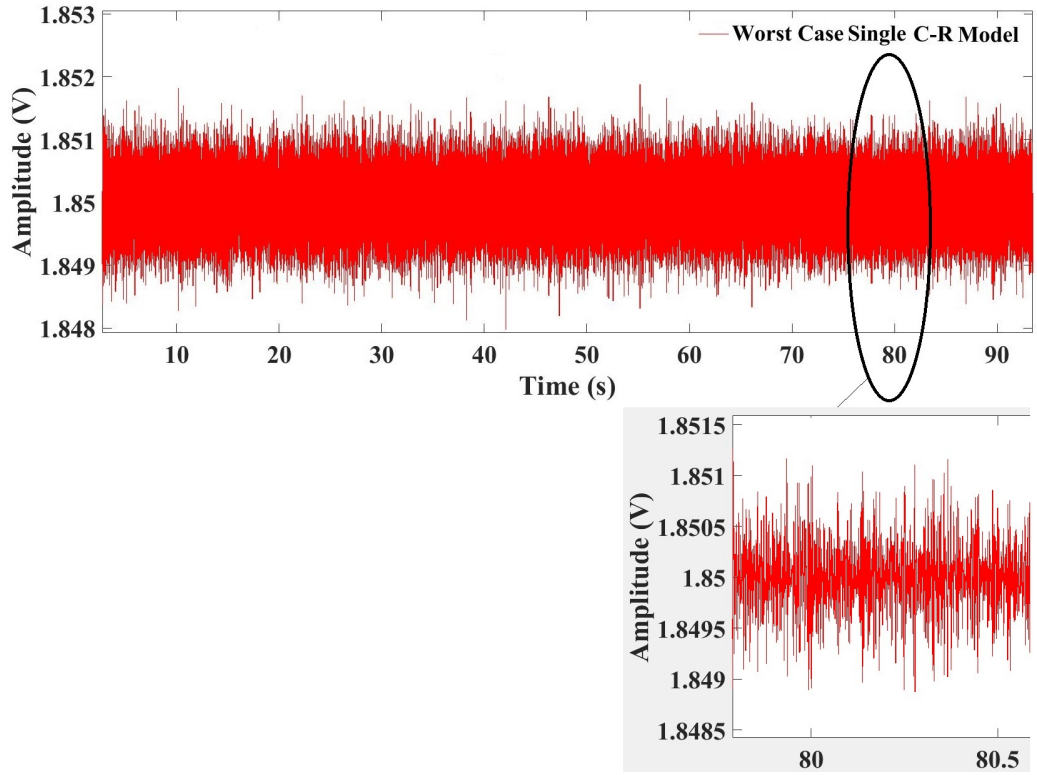

(a) Peak-to-Peak Output Noise Voltage Recorded using Worst-Case Single C-R Electrode Model

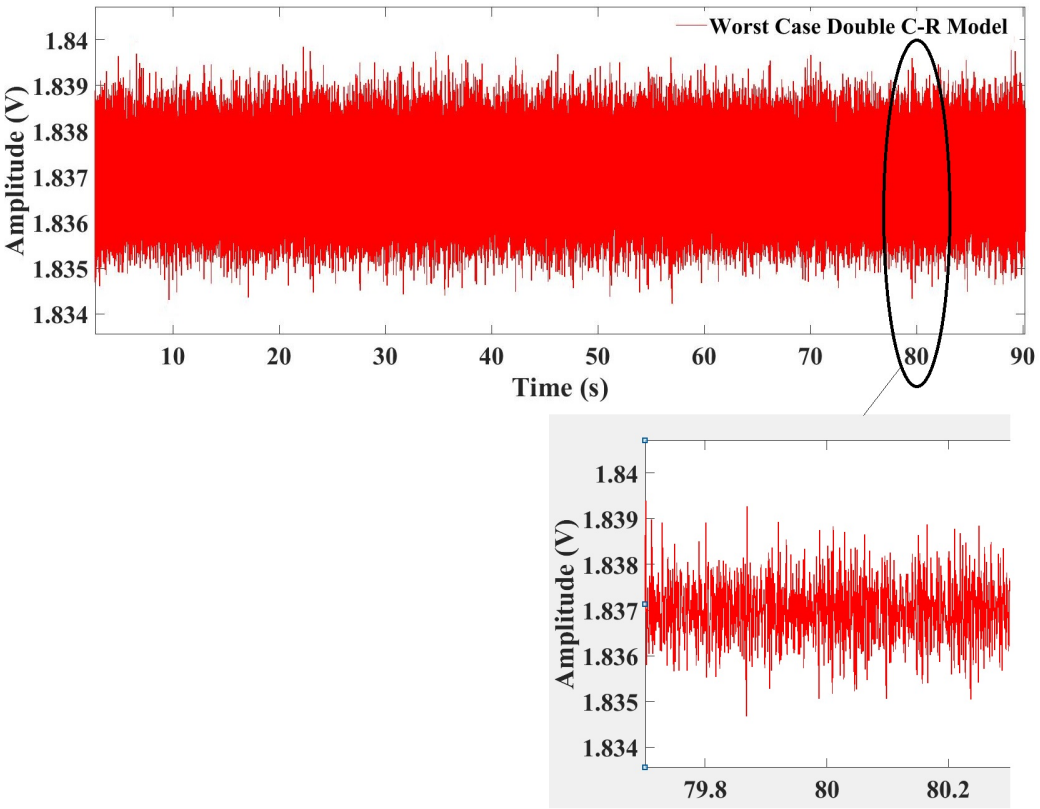

(b) Peak-to-Peak Output Noise Voltage Recorded using Worst-Case Double C-R Electrode Model

Figure 8.14: Peak-to-Peak Output Noise Voltage measured on PCB at a frequency bandwidth of 250Hz.

• Harvard step test: the subject was required to step up and down from a rectangular platform of height 200m. The subject stepped up with one foot, then followed by the other foot, then the first foot was taken down followed by the second foot in about 4s cycle.

8.9.2 ECG Signal Pre-processing

In modern times, several signal processing methods are employed to pre-process a bio-signal. Different digital processing algorithms have been used in the literature to ensure recording a bio-potential signal of diagnostic quality. This work first uses a low-pass filter in Picoscope having a cut-off frequency of 400Hz to record the ECG traces in .mat file format. Then, a zero-phase digital notch filter is used in MATLAB 2019b to remove any 50Hz power line interference from the wanted ECG signal.

8.9.3 Recordings with self adhesive gelled electrodes

Actual ECG recordings with a sampling rate of 1Ms/s using Picoscope were made on two subjects using wet electrodes under all the recording scenarios. The ECG recordings using the adhesive electrodes were conducted to compare the signal quality with the dry electrodes. The ECG traces for subject 1 using gelled electrodes under sitting condition are presented in Fig. 8.15. It is evident from these ECG traces that there is a drift in signal recording when the battery is not connected to real ground. This is mainly due to the presence of body isolation capacitance that makes this effect much more pronounced when the body of the subject is not connected to ground. The body isolation capacitance and the signal drift decreases significantly on connecting the battery to real ground, which is shown in Fig. 8.15.

8.9.4 Vest recordings with dry electrodes

Dry electrode ECG recordings were first performed using the Nike Pro vest setup as discussed in Chapter 5. In-vivo recordings on the two subjects using textile based electrodes under sitting ECG condition is shown in Fig. 8.16.

There were several problems with the vest setup that were encountered during arm waving

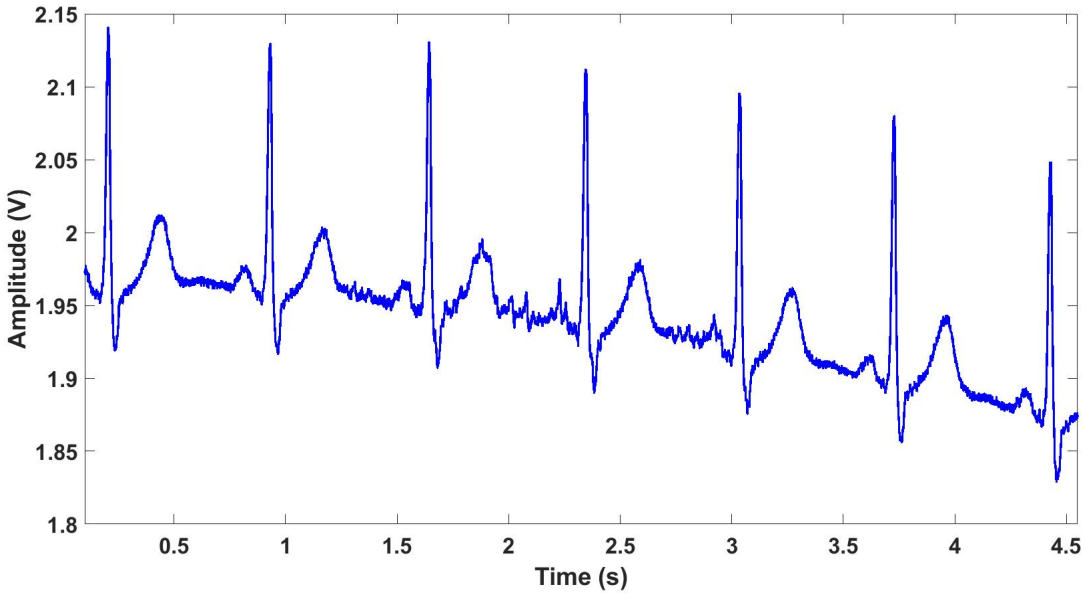

(a) Wet Electrode and Battery Floating

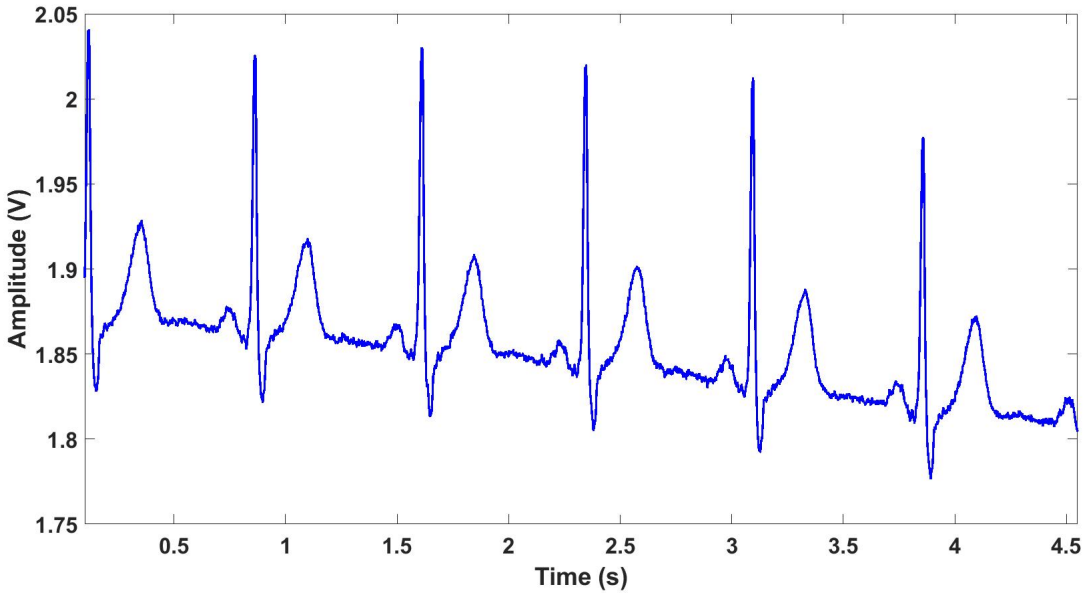

(b) Wet Electrode and Battery Real Ground

Figure 8.15: ECG Recordings of Subject 1 with Wet Electrodes under sitting condition. Subject 1 is 66 years old having a hairy chest.

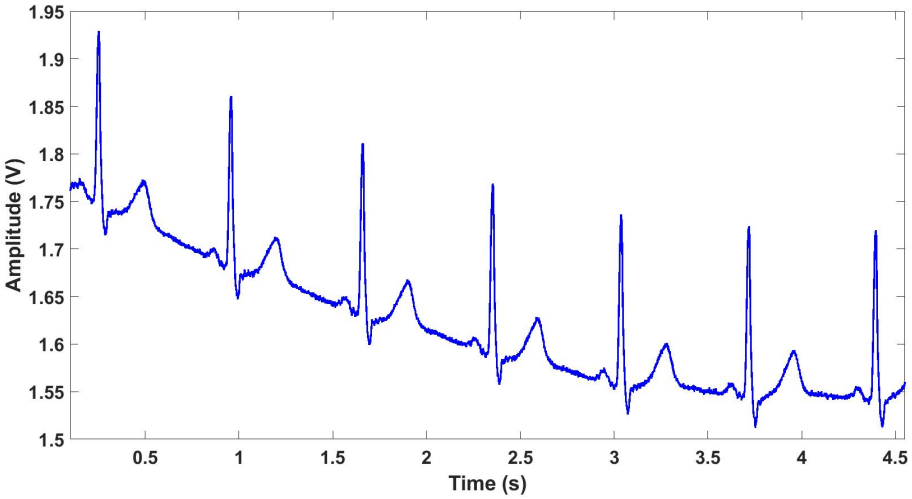

(a) Dry Electrode and Battery Floating

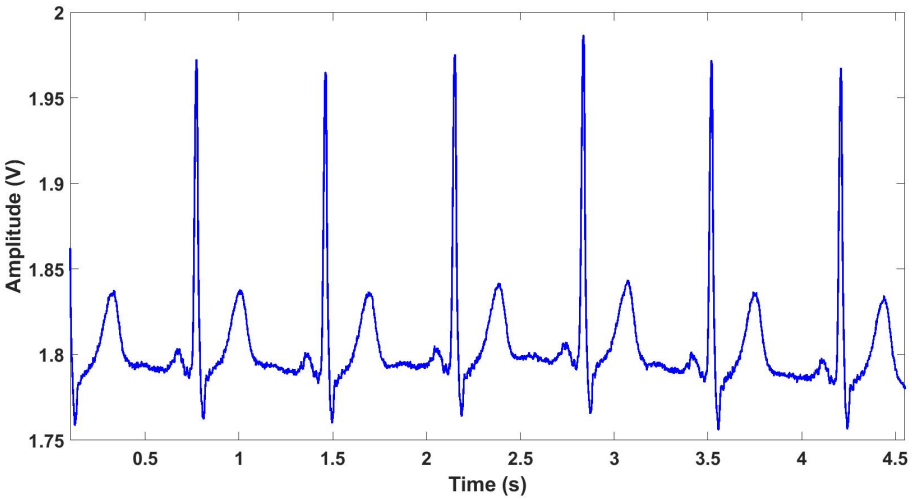

(b) Dry Electrode and Battery Real Ground

Figure 8.16: Vest ECG Recordings of Subject 1 with Dry Electrodes under sitting condition.

and the step test. The vest did not provide adequate skin-electrode contact as was hoped for. This was further exaggerated by a heavy breathing artefact being superimposed on the wanted ECG signal during exercise. Unfortunately, it became impossible to do any vest recordings with the dry electrodes under these exercise conditions. It is felt that a suitable vest would have to be specially designed for use with textile based electrodes.

8.9.5 Dry ECG recording using adhesive tape

A simple alternative solution was then exploited where the dry electrodes were cut out of the vest and connecting leads were held in contact with the skin using surgical adhesive tape, as

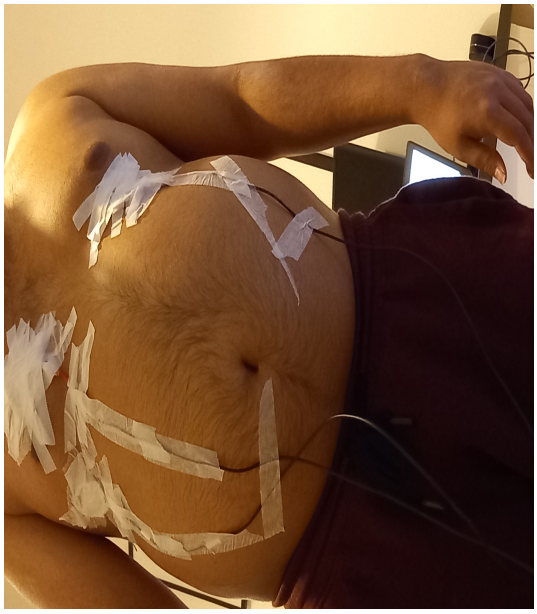

Figure 8.17: Subject 2, Male, with dry electrodes held onto the skin with the aid of a surgical adhesive tape.

shown in Fig. 8.17 on Subject 2. It must be stressed that the skin was not cleaned, rubbed or prepared in any way so as to uphold the credibility of textile based dry electrodes. ECG traces for Subject 2 using dry electrodes under all conditions are presented in Fig. 8.18.

8.9.6 Concluding remarks

The presented ECG traces on a limited study of two subjects show that the morphology of the ECG signal for both wet and dry electrodes contain no significant distortion, apart from the interference present in the recordings. In addition, baseline wandering and motion artefacts have been observed in waveforms where the subjects underwent physical exercise. This further confirms the necessity to have an integrated recording system in a customised body-fit vest to secure good contact between skin and electrodes. The quality of the signals recorded will be further improved by the use of advanced signal processing.

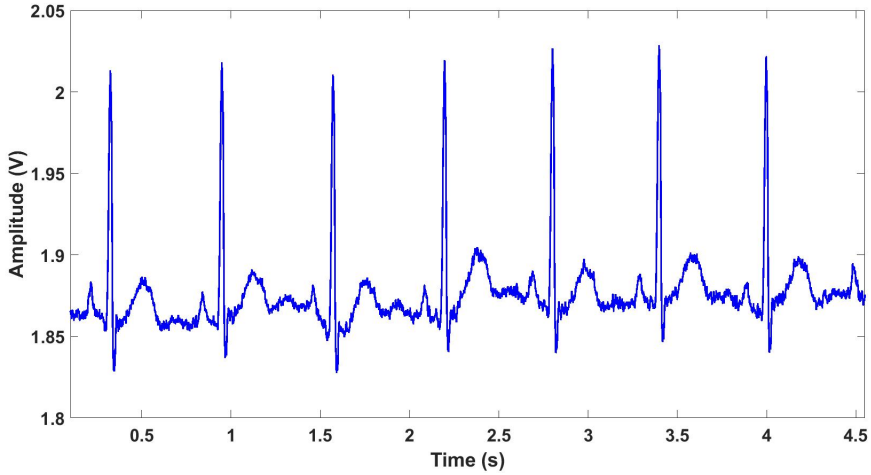

(a) Sitting

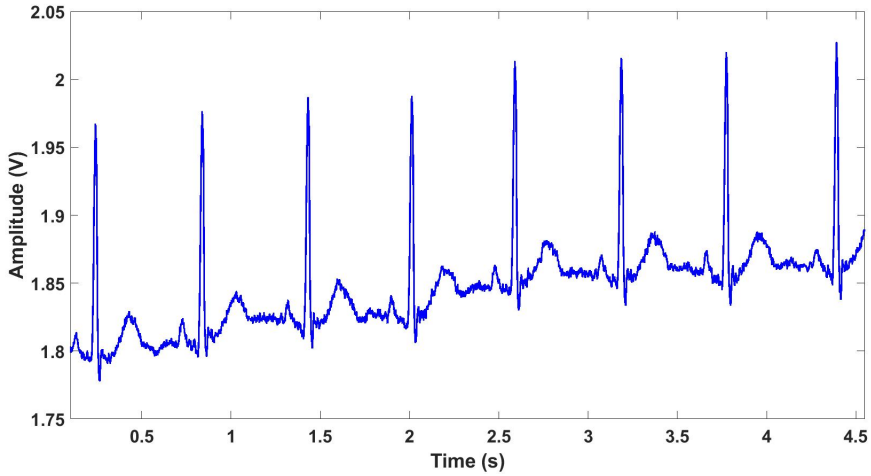

(b) Arm Waving

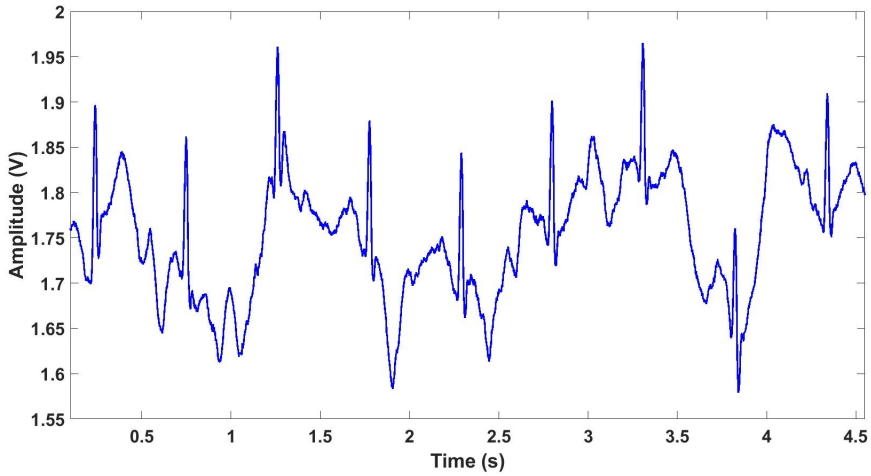

(c) Step Test

Figure 8.18: Comparison of ECG Recording of Subject 2 with Dry Electrodes under all scenarios.

9 Conclusion & Future Work

9.1 Analytical Work

This thesis presents a novel low-power, low-noise single supply ECG amplifier that can be interfaced with textile-based ungelled electrodes for ambulatory monitoring of the human electrocardiogram. The work emphasises the need to include the effect of skin-electrode impedance to evaluate amplifier performance parameters such as - Frequency Response, Transient Response, Input Impedance, Noise and CMRR. The variation of these parameters at different input frequencies have been comprehensively studied in this work. A substantial amount of analytical and experimental work on modelling the skin-electrode-amplifier interface and its electrical behaviour was carried out. This was done in the light of the current international performance standards IEC 60601 pertaining to electrocardiographic equipment and has led to the identification of shortcomings in this standard. The work completed has allowed design criteria for the amplifier input impedance needed for recording diagnostic quality of ECG signals with dry un-gelled electrodes to be established and suggestions to be made for revision of the IEC60601 standards. This work identifies that ECG amplifiers adhering to the IEC 60601 standard with respect to input impedance requirements can introduce undershoot distortion of over 100μV, false S-wave creation, recovery slope exceeding 300μV/s and alterations in the ST segment of the ECG signal. Rigorous analytical work supplemented with practical bench tests has identified that the single-time constant electrode model imposes more stringent amplifier performance requirements when compared with the more accurate double-time constant electrode model. The work also characterises the noise voltage generated by the electrodes to be lower than that introduced by the amplifier. Some of the novel contributions

of this work are listed below:

- skin-electrode impedance characterisation of dry textile based ECG electrodes.
- skin-electrode noise measurement of un-gelled textile based electrodes.
- recommendation to revise the IEC 60601 input impedance requirements in context of the transient performance specification.
- design of a low-power, low-noise ECG recording amplifier that can be interfaced with textile-based electrodes.

Using equation (4.7.1) and considering R_{in}=10GΩ, it is evident that the amplifier presented in this work can handle a maximum single C-R skin-electrode impedance value of 166MΩ//2.5nF to meet the IEC60601 transient response requirements. This impedance value is much higher than the worst case single C-R model as indicated in section 8.4. The maximum limiting skin-electrode impedance value to meet the transient response for a double C-R model can only be derived graphically or numerically as no analytical solutions can be found from equations (4.7.3) and (4.7.4). It must be stressed that the transient response requirements for a single C-R model has proven to be stringent when compared with a double C-R model. This is based on twenty different skin-electrode impedance models that were studied in Chapter 4. The performance of the ECG recording amplifier when compared with target requirements are summarised in Table 9.1. The amplifier has met all performance parameters except the semiconductor noise, which is measured slightly outside the IEC 60601 noise margin. The noise levels can be further improved at the expense of power consumption [25].

9.2 Amplifier Design and Verification

An amplifier for use with textile electrodes was designed with some novel features to ensure that the performance requirements of IEC60601 are met. This includes the common-mode impedance boosting mechanism and the neutralisation of op-amp input capacitance by power supply bootstrapping. The PCB design has shown that the input impedance has been boosted to a minimum value of 10GΩ within a frequency range of 0.1-150Hz. The design offers a linear,

Table 9.1: Amplifier Performance Evaluation

	Measured Value	Target Value
Supply voltage	3.7 V	3-5 V
Power	112 μW	1 mW (max)
Gain	41 dB	40-46 dB
3dB Bandwidth	0.03 – 350 Hz	0.05 – 1000 Hz
$\pm$0.5 dB Bandwidth	0.1 – 42 Hz	0.1 – 30 Hz
CMRR at 50 Hz	90 dB	80 dB (min)
Max. undershoot	14 μV	100 μV (max)
Max. recovery slope	216 μV/s	300 μV/s (max)
Noise referred to input	32 μV	30 μV (max)

low complexity, novel method of achieving power supply bootstrapping using low-power, low-noise op-amps. Tolerance of 0.1% resistors are used in all the stages of the amplifier design to reduce CMRR degradation due to resistor errors. The electrode and input impedance mismatch proved to be the dominant factor in determining the overall CMRR of the recording amplifier when an skin-electrode impedance as high as 10MΩ is considered.

Therefore, an active right-leg-drive (RLD) with a gain of 20dB is used in the design to guarantee a CMRR of over 80dB, which is the current medical standard for ambulatory ECG monitoring. In bench tests, the CMRR with the inclusion of the RLD was measured at over 90 dB at 50 Hz, and 80 dB at 200 Hz for the worst case electrode models, meeting the IEC60601 requirements. Unfortunately, when used with electrodes placed on a subjects chest, the right leg drive amplifier became unstable. This is mainly attributed to the low capacitive load drive ability of OPA379 as it has a limit of 100pF as outlined in Chapter 5. The redesigning of this stage using LT6001 op-amps used in the first stage which can drive a capacitive load of 500pF would be likely to solve the problem. This would further require redesigning a new PCB as the footprints of LT6003 is different than that of OPA379. Designing a new board was not undertaken as the manufacturing cost was significantly high.

Due to the COVID 19 pandemic word-wide and nationally, only 2 subjects could be recruited for in-vivo actual ECG recordings. Measurements were recorded for the subjects at rest and also

when exercising. The recorded ECG waveforms showed signs of semiconductor noise but it did not distort the signal as there was hardly any noticeable difference observed in ECG recordings made using wet and dry electrodes. Table 9.2 presents some essential overall performance of the pre-amplfier and contrasts it with the design solutions provided by Burke & Gleeson in 2000 and Assambo & Burke in 2011. The thesis presented uses a lot of analytical and practical bench tests to evaluate the performance of the amplifier. Most of these parameters using worst case electrode models have met the target design standards.

Table 9.2: Comparison of ECG Recording Amplifiers Performance Characteristics

	diff. gain	-3dB bandwidth	input imped.	CMRR @50Hz	inp. ptp. noise	power diss.	approx. cost
spec. limits	N.A	$\leq$0.05-$\geq$250Hz	$\geq$10MΩ	$\geq$80dB	$\leq$30μV	N.A	N.A
Burke [20]	43dB	0.04-2.2kHz	66MΩ	84dB	50μV	27μW	20 Euros
Assambo [8]	40dB	0.04-1.25kHz	2GΩ	97dB	200μV	45μW	10 Euros
This work	**41dB**	**0.03-350Hz**	**10GΩ**	**90dB**	**32μV**	**112μW**	**20 Euros**

9.3 The Vest and the Connecting Leads

The use of the Nike Pro Vent body-fit sports vest proved to be infeasible solution as difficulties in recording ECG arose when the subjects had to undergo physical exercise. Good skin-electrode contact is essential to record a high quality ECG signals. Therefore, electrodes stitching inside the vest needs to be customised to ensure a good contact between the skin and the electrode. The vest would probably have to include additional elastication at the location of the electrodes and be shaped specially to maintain good contact between electrodes and skin during exercise. The movement of the leads during exercise contributed to motion artefacts within the signal bandwidth. Some special purpose channel could be woven into the vest to hold the leads in place and prevent their relative movement. Proper vest design would require a separate future interdisciplinary project with the involvement of mechanical engineers, people from art&design and a manufacturing company.

The past decade has seen a significant rise in the use ECG monitors in professional athletic

training and evaluation programmes. There is now more than 100 sudden and unexplained deaths annually in Ireland on the sports-field of young healthy athletes under 35 years of age. This has led to calls for more adequate screening programmes for these athletes when undergoing rigorous training so that these risks can be identified in advance. Therefore, the interdisciplinary project has a good prospect of getting a manufacturer involved as the market demands to record a diagnostic ECG are substantial. The use of leads can be eliminated by recording the ECG signal wirelessly using Bluetooth Low Energy (BLE) [168–170] but it will come at the expense of power consumption. Accelerometers [171–173] used at the electrode site can also be potentially used to monitor the nature of movement artefacts and provide a means of eliminating or minimising their effects.

9.4 Signal Processing

There are several digital signal processing techniques that have been introduced in the literature to mitigate the effects of motion artefacts [174] causing baseline drifts. Traditional signal processing algorithms have used finite/infinite impulse response (FIR/IIR) high pass filters, average filters [175, 176], wavelet transforms [177, 178] to suppress motion artefacts. The use of FIR/IIR high-pass filtering with a lower cut-off frequency of 0.5Hz or 0.67Hz is one of the most common practice in modern times [179, 180]. However, a low cut-off frequency higher than 0.05Hz can introduce distortion in the ST segment of the ECG waveform [6, 181, 182]. The performance of a median filter and a moving average filter on removing motion artefact is highly susceptible to the chosen length of the window [174]. Suitable selection of the wavelet function, including choosing correct threshold levels is essential to reduce in-band noise[174]. Various adaptive filtering techniques [183, 184] have been used in recent years to remove any low frequency baseline wandering. These sophisticated digital filtering algorithms can be used in conjunction with the recorded signals from the amplifier to obtain a diagnostic ECG waveform during movements or exercise.

Bibliography

[1] "UpToDate." [Online]. Available: https://www.uptodate.com/contents/image?imageKey=PI%2F71235&topicKey=PI%2F3448&source=outline_link

[2] "Electrocardiogram (ECG)." [Online]. Available: https://acuclinic.com.au/pocit/ECG.htm

[3] International Electrotechnical Commission, *Medical electrical equipment, Part 2-25*. International Electrotechnical Commission, 2011.

[4] M. J. Burke, "A microcontroller based athletic cardiotachometer," PhD dissertation, Trinity College Dublin, 1990.

[5] J. G. Webster, *Medical instrumentation: application and design*. John Wiley & Sons, 2009.

[6] A. S. Berson and H. V. Pipberger, "The low-frequency response of electrocardiographs, a frequent source of recording errors," *American Heart Journal*, vol. 71, no. 6, pp. 779–789, Jun. 1966.

[7] L. T. Sheffield, A. Berson, D. Bragg-Remschel, P. C. Gillette, R. E. Hermes, L. Hinkle, H. Kennedy, D. M. Mirvis, and C. Oliver, "AHA special report. Recommendations for standards of instrumentation and practice in the use of ambulatory electrocardiography. The Task Force of the Committee on Electrocardiography and Cardiac Electrophysiology of the Council on Clinical Cardiology," *Circulation*, vol. 71, no. 3, pp. 626A–636A, Mar. 1985.

[8] C. Assambo, "Amplifier front-end design in dry-electrode electrocardiography," PhD dissertation, Trinity College Dublin, 2011.

[9] D. Gleeson, "Low-power ecg amplifier and detector," Master's dissertation, Trinity College Dublin, 1996.

[10] D. Swanson and J. G. Webster, "A model for skinelectrode impedance," in *A model for skinelectrode impedance*, 1st ed. Biomedical Electrode Technology-Theory and Practice, 1974, pp. 117–128.

[11] M. R. Neuman *et al.*, "Biopotential electrodes," *Medical instrumentation: application and design*, vol. 4, pp. 189–240, 1998.

[12] S. Maji, J. Dookhy, and M. J. Burke, "Electrical characterization of conductive textile based ECG recording electrodes," vol. 15, p. 100044, 2021-06. [Online]. Available: https://linkinghub.elsevier.com/retrieve/pii/S2665917421000064

[13] B. Taji, S. Shirmohammadi, V. Groza, and I. Batkin, "Impact of skin–electrode interface on electrocardiogram measurements using conductive textile electrodes," vol. 63, no. 6, pp. 1412–1422, 2014. [Online]. Available: http://ieeexplore.ieee.org/document/6670113/

[14] C. C. Oliveira, J. M. da Silva, I. G. Trindade, and F. Martins, "Characterization of the electrode-skin impedance of textile electrodes," in *Design of Circuits and Integrated Systems*. IEEE, 2014, pp. 1–6.

[15] Y. M. Chi, T.-P. Jung, and G. Cauwenberghs, "Dry-contact and noncontact biopotential electrodes: Methodological review," vol. 3, pp. 106–119, 2010. [Online]. Available: http://ieeexplore.ieee.org/document/5598518/

[16] N. Gandhi, C. Khe, D. Chung, Y. M. Chi, and G. Cauwenberghs, "Properties of dry and non-contact electrodes for wearable physiological sensors," in *2011 international conference on body sensor networks*. IEEE, 2011, pp. 107–112.

[17] L. Casal and G. La Mura, "Skin-electrode impedance measurement during ecg acquisition: method's validation," in *Journal of Physics: Conference Series*, vol. 705, no. 1. IOP Publishing, 2016, p. 012006.

[18] H. Saadi and M. Attari, "Electrode-gel-skin interface characterization and modeling for surface biopotential recording: Impedance measurements and noise," in *2013 2nd International Conference on Advances in Biomedical Engineering*. IEEE, 2013-09, pp. 49–52. [Online]. Available: https://ieeexplore.ieee.org/document/6648844/

[19] K.-H. Lee, J.-W. Lee, W.-C. Jung, K.-S. Kim, J.-H. Jun, and D.-J. Kim, "Asymmetric skin-to-electrode impedance characteristics of concentric circular ring electrode for monitoring of electrical activity of the heart," in *2006 SICE-ICASE International Joint Conference*. IEEE, 2006, pp. 1135–1136.

[20] M. Burke and D. Gleeson, "A micropower dry-electrode ECG preamplifier," vol. 47, no. 2, pp. 155–162, 2000-02. [Online]. Available: http://ieeexplore.ieee.org/document/821734/

[21] A. Ankhili, X. Tao, C. Cochrane, D. Coulon, and V. Koncar, "Study on the measurement method of skin textile electrodes contact impedance," *J. Fashion Technol. Textile Eng.*, vol. 5, p. 4, 2018.

[22] International Electrotechnical Commission, *Medical electrical equipment. Part 2-47*. International Electrotechnical Commission, 2012.

[23] J. E. Atwood, J. Myers, S. Forbes, P. Hall, R. Friis, G. Marcondes, D. Mortara, and V. F. Froelicher, "High-frequency electrocardiography: An evaluation of lead placement and measurements," *American heart journal*, vol. 116, no. 3, pp. 733–739, 1988.

[24] M. J. Burke, "Low-power ECG amplifier/detector for dry-electrode heart rate monitoring," *Medical & Biological Engineering & Computing*, vol. 32, no. 6, pp. 678–683, Nov. 1994. [Online]. Available: http://link.springer.com/10.1007/BF02524247

[25] C. Assambo and M. J. Burke, "An optimised high-impedance amplifier for dry-electrode ecg recording," *International Journal of Circuits, Systems Signal Processing*, vol. 6, no. 5, pp. 332–341, 2012.

[26] S. Lanyi and M. Pisani, "A high-input-impedance buffer," vol. 49, no. 8, pp. 1209–1211, 2002. [Online]. Available: http://ieeexplore.ieee.org/document/1023024/

[27] F. R. Parente, S. Di Giovanni, G. Ferri, V. Stornelli, G. Pennazza, and M. Santonico, "An analog bootstrapped biosignal read-out circuit with common-mode impedance two-electrode compensation," vol. 18, no. 7, pp. 2861–2869, 2018. [Online]. Available: https://ieeexplore.ieee.org/document/8274956/

[28] H. Nakamura and A. Ueno, "Bootstrapped non-inverting front-end amplifier for capacitive electrocardiogram measurement *," in *2018 IEEE Biomedical Circuits and Systems Conference (BioCAS)*. IEEE, 2018, pp. 1–4. [Online]. Available: https://ieeexplore.ieee.org/document/8584676/

[29] D. P. Dobrev, T. Neycheva, and N. Mudrov, "Bootstrapped two-electrode biosignal amplifier," vol. 46, no. 6, pp. 613–619, 2008. [Online]. Available: http://link.springer.com/10.1007/s11517-008-0312-4

[30] F. N. Guerrero and E. M. Spinelli, "A two-wired ultra-high input impedance active electrode," vol. 12, no. 2, pp. 437–445, 2018. [Online]. Available: https://ieeexplore.ieee.org/document/8305528/

[31] R. Pallas-Areny and J. Webster, "Common mode rejection ratio in differential amplifiers," vol. 40, no. 4, pp. 669–676, 1991. [Online]. Available: http://ieeexplore.ieee.org/document/85332/

[32] E. M. Spinelli, R. Pallàs-Areny, and M. A. Mayosky, "Ac-coupled front-end for biopotential measurements," *IEEE transactions on biomedical engineering*, vol. 50, no. 3, pp. 391–395, 2003.

[33] D. Dobrev, "Two-electrode low supply voltage electrocardiogram signal amplifier," *Medical and Biological Engineering and Computing*, vol. 42, no. 2, pp. 272–276, 2004.

[34] A. Grennan, "Boosting cmrr of instrumentation amplifiers," Master's dissertation, Trinity College Dublin, 2019.

[35] C. Cajavilca and J. Varon, "Willem Einthoven: The development of the human electrocardiogram," *Resuscitation*, vol. 76, no. 3, pp. 325–328, Mar. 2008.

[36] W. C. Roberts and M. A. Silver, "Norman Jefferis Holter and ambulatory ECG monitoring," *The American Journal of Cardiology*, vol. 52, no. 7, pp. 903–906, Oct. 1983.

[37] H. A. Serebro, A. E. Cocco, and B. Tabatznik, "Continuous electrocardiographic monitoring employing the electrocardiocorder during gastrointestinal endoscopy," *Gastrointestinal Endoscopy*, vol. 14, no. 1, pp. 28–30, Aug. 1967.

[38] H. L. Kennedy, "Ambulatory (Holter) electrocardiography technology," *Cardiology Clinics*, vol. 10, no. 3, pp. 341–359, Aug. 1992.

[39] R. L. Verrier and B. D. Nearing, "Ambulatory ECG monitoring of T-wave alternans for arrhythmia risk assessment," *Journal of Electrocardiology*, vol. 36 Suppl, pp. 193–197, 2003.

[40] D. Sanders, L. Ungar, M. A. Eskander, and A. H. Seto, "Ambulatory ECG monitoring in the age of smartphones," *Cleveland Clinic Journal of Medicine*, vol. 86, no. 7, pp. 483–493, Jul. 2019. [Online]. Available: https://www.ccjm.org//lookup/doi/10.3949/ccjm.86a.18123

[41] I.Romero, "Ambulatory electrocardiology," *Cardiology in Review*, vol. 21, no. 5, pp. 239–248, Oct. 2013.

[42] F. Chiarugi, M. Spanakis, P. J. Lees, C. E. Chronaki, M. Tsiknakis, and S. C. Orphanoudakis, "Ecg in your hands: a multi-vendor ecg viewer for personal digital assistants," in *Computers in Cardiology, 2003*, 2003, pp. 359–362.

[43] P. Santos, P. Pessanha, M. Viana, M. Campelo, J. Nunes, A. Hespanhol, F. Macedo, and L. Couto, "Accuracy of general practitioners' readings of ECG in primary care," *Open Medicine*, vol. 9, no. 3, pp. 431–436, Jun. 2014.

[44] S. A. M. Compiet, R. T. A. Willemsen, K. T. S. Konings, and H. E. J. H. Stoffers, "Competence of general practitioners in requesting and interpreting ECGs - a case vignette study," *Netherlands Heart Journal*, vol. 26, no. 7-8, pp. 377–384, Aug. 2018.

[45] Y. Sun, X. Yu, and J. Berilla, "An innovative non-invasive ecg sensor and comparison study with clinic system," in *2013 39th Annual Northeast Bioengineering Conference*, 2013, pp. 163–164.

[46] M. Mitra, J. N. Bera, and R. Gupta, "Electrocardiogram compression technique for global system of mobile-based offline telecardiology application for rural clinics in india," *IET Science, Measurement Technology*, vol. 6, no. 6, pp. 412–419, 2012.

[47] G. Gargiulo, P. Bifulco, A. McEwan, J. Nasehi Tehrani, R. A. Calvo, M. Romano, M. Ruffo, R. Shephard, M. Cesarelli, C. Jin, A. Mohamed, and A. van Schaik, "Dry electrode bio-potential recordings," *Conference proceedings: ... Annual International Conference of the IEEE Engineering in Medicine and Biology Society. IEEE Engineering in Medicine and Biology Society. Annual Conference*, vol. 2010, pp. 6493–6496, 2010.

[48] A. Galli, G. Frigo, D. Chindamo, A. Depari, M. Gadola, and G. Giorgi, "Denoising ecg signal by cstfm algorithm: Monitoring during motorbike and car races," *IEEE Transactions on Instrumentation and Measurement*, vol. 68, no. 7, pp. 2433–2441, 2019.

[49] M. J. Alberts and J. D. Easton, "Stroke Best Practices: a team approach to evidence-based care," *Journal of the National Medical Association*, vol. 96, no. 4 Suppl, pp. 5S–20S, Apr. 2004.

[50] J. Hoogsteen, J. H. Bennekers, E. E. van der Wall, N. M. van Hemel, A. a. M. Wilde, H. J. G. M. Crijns, A. P. M. Gorgels, J. L. R. M. Smeets, R. N. W. Hauer, J. L. M. Jordaens, and M. J. Schalij, "Recommendations and cardiological evaluation of athletes with arrhythmias: Part 2," *Netherlands Heart Journal: Monthly Journal of the Netherlands Society of Cardiology and the Netherlands Heart Foundation*, vol. 12, no. 5, pp. 214–222, May 2004.

[51] D. S. Reid, "The electrocardiogram in the assessment of the effect of drugs on cardiac arrhythmias," *British Journal of Clinical Pharmacology*, vol. 6, no. 6, pp. 473–485, Dec. 1978.

[52] J. Coosemans, B. Hermans, and R. Puers, "Integrating wireless ECG monitoring in textiles," in *The 13th International Conference on Solid-State Sensors, Actuators and Microsystems, 2005. Digest of Technical Papers. TRANSDUCERS '05.*, vol. 1. Seoul, Korea: IEEE, 2005, pp. 228–232. [Online]. Available: http://ieeexplore.ieee.org/document/1496399/

[53] W. Galjan, D. Naydenova, J. M. Tomasik, D. Schroeder, and W. H. Krautschneider, "A portable soc-based ecg-system for 24h x 7d operating time," in *2008 IEEE Biomedical Circuits and Systems Conference*, 2008, pp. 85–88.

[54] S. Lee, J. Hong, C. Hsieh, M. Liang, S. Chang Chien, and K. Lin, "Low-power wireless ecg acquisition and classification system for body sensor networks," *IEEE Journal of Biomedical and Health Informatics*, vol. 19, no. 1, pp. 236–246, 2015.

[55] M. Pandiyan, G. Mani, J. Jerome, and Natarajan S, "Integrating wearable low power cmos ecg acquisition soc with decision making system for wsbn applications," in *2015 IFIP/IEEE International Conference on Very Large Scale Integration (VLSI-SoC)*, 2015, pp. 154–158.

[56] M.J. Burke and D.T. Gleeson, "A micropower dry-electrode ecg preamplifier," *IEEE Transactions on Biomedical Engineering*, vol. 47, no. 2, pp. 155–162, 2000.

[57] G. Gargiulo, P. Bifulco, M. Cesarelli, M. Ruffo, M. Romano, R. A. Calvo, C. Jin, and A. van Schaik, "An ultra-high input impedance ECG amplifier for long-term monitoring of athletes," *Medical Devices (Auckland, N.Z.)*, vol. 3, pp. 1–9, 2010.

[58] C.-L. Chang, C.-W. Chang, H.-Y. Huang, C.-M. Hsu, C.-H. Huang, J.-C. Chiou, and C.-H. Luo, "A power-efficient bio-potential acquisition device with DS-MDE sensors for long-term healthcare monitoring applications," *Sensors (Basel, Switzerland)*, vol. 10, no. 5, pp. 4777–4793, 2010.

[59] D. Pani, A. Dessi, J. F. Saenz-Cogollo, G. Barabino, B. Fraboni, and A. Bonfiglio, "Fully Textile, PEDOT:PSS Based Electrodes for Wearable ECG Monitoring Systems," *IEEE Transactions on Biomedical Engineering*, vol. 63, no. 3, pp. 540–549, Mar. 2016. [Online]. Available: http://ieeexplore.ieee.org/document/7182320/

[60] Tong InOh, Sun Yoon, Tae Eui Kim, Hun Wi, Kap Jin Kim, Eung Je Woo, and R. J. Sadleir, "Nanofiber Web Textile Dry Electrodes for Long-Term Biopotential Recording," *IEEE Transactions on Biomedical Circuits and Systems*, vol. 7, no. 2, pp. 204–211, Apr. 2013. [Online]. Available: http://ieeexplore.ieee.org/document/6237554/

[61] H. Ozkan, O. Ozhan, Y. Karadana, M. Gulcu, S. Macit, and F. Husain, "A Portable Wearable Tele-ECG Monitoring System," *IEEE Transactions on Instrumentation and Measurement*, vol. 69, no. 1, pp. 173–182, Jan. 2020. [Online]. Available: https://ieeexplore.ieee.org/document/8672078/

[62] N. Meziane, J. G. Webster, M. Attari, and A. J. Nimunkar, "Dry electrodes for electrocardiography," *Physiological Measurement*, vol. 34, no. 9, pp. R47–R69, Sep. 2013. [Online]. Available: https://iopscience.iop.org/article/10.1088/0967-3334/34/9/R47

[63] A. A. Chlaihawi, B. B. Narakathu, S. Emamian, B. J. Bazuin, and M. Z. Atashbar, "Development of printed and flexible dry ECG electrodes," *Sensing and Bio-Sensing Research*, vol. 20, pp. 9–15, Sep. 2018. [Online]. Available: https://linkinghub.elsevier.com/retrieve/pii/S2214180418300254

[64] A. Searle and L. Kirkup, "A direct comparison of wet, dry and insulating bioelectric recording electrodes," *Physiological Measurement*, vol. 21, no. 2, pp. 271–283, May 2000. [Online]. Available: https://iopscience.iop.org/article/10.1088/0967-3334/21/2/307

[65] J. Yoo, L. Yan, S. Lee, H. Kim, B. Kim, and H.-J. Yoo, "An Attachable ECG Sensor Bandage with Planar-Fashionable Circuit Board," in *2009 International Symposium*

on Wearable Computers. Linz, Austria: IEEE, Sep. 2009, pp. 145–146. [Online]. Available: http://ieeexplore.ieee.org/document/5254662/

[66] L. M. Yu, F. E. H. Tay, D. G. Guo, L. Xu, M. N. Nyan, F. W. Chong, K. L. Yap, and B. Xu, "A mems-based bioelectrode for ecg measurement," in *SENSORS, 2008 IEEE*, 2008, pp. 1068–1071.

[67] J. Muhlsteff and O. Such, "Dry electrodes for monitoring of vital signs in functional textiles," in *The 26th Annual International Conference of the IEEE Engineering in Medicine and Biology Society*, vol. 1, 2004, pp. 2212–2215.

[68] J. Muhlsteff, O. Such, R. Schmidt, M. Perkuhn, H. Reiter, J. Lauter, J. Thijs, G. Musch, and M. Harris, "Wearable approach for continuous ecg - and activity patient-monitoring," in *The 26th Annual International Conference of the IEEE Engineering in Medicine and Biology Society*, vol. 1, 2004, pp. 2184–2187.

[69] M. G. Srinivasa and P. S. Pandian, "Dry electrodes for bio-potential measurement in wearable systems," in *2017 2nd IEEE International Conference on Recent Trends in Electronics, Information Communication Technology (RTEICT)*, 2017, pp. 270–276.

[70] D. Tayler and R. Vincent, "Signal Distortion in the Electrocardiogram Due to Inadequate Phase Response," *IEEE Transactions on Biomedical Engineering*, vol. BME-30, no. 6, pp. 352–356, Jun. 1983. [Online]. Available: http://ieeexplore.ieee.org/document/4121647/

[71] D. Noble, *The initiation of the heartbeat*, 2nd ed. Clarendon Press ; Oxford University Press, 1979.

[72] R. Plonsey, "Bioelectric phenomena," in *Wiley Encyclopedia of Electrical and Electronics Engineering*, J. G. Webster, Ed. John Wiley & Sons, Inc., 1999-12, p. W1403. [Online]. Available: https://onlinelibrary.wiley.com/doi/10.1002/047134608X.W1403

[73] R. Plonsey and R. C. Barr, *Bioelectricity: a quantitative approach*, 2nd ed. New York: Kluwer Academic/Plenum Publishers, 2000.

[74] E. E. van der Wall, M.-J. de Boer, P. A. Doevendans, A. A. Wilde, and F. Zijlstra, "Major achievements in cardiology in the past century: influence on dutch cardiovascular medicine," vol. 17, no. 4, pp. 136–139, 2009-04. [Online]. Available: http://link.springer.com/10.1007/BF03086235

[75] B. F. Hoffman and P. F. Cranefield, *Electrophysiology of the Heart*. McGraw-Hill, Blakiston Division, 1960, google-Books-ID: UdRqAAAAMAAJ.

[76] V. Nesterenko and C. Antzelevitch, "Simulation of the electrocardiographic U wave in heterogeneous myocardium: effect of local junctional resistance," in *Proceedings Computers in Cardiology*. Durham, NC, USA: IEEE Comput. Soc. Press, 1992, pp. 43–46. [Online]. Available: http://ieeexplore.ieee.org/document/269451/

[77] B. Surawicz, "U Wave: Facts, Hypotheses, Misconceptions, and Misnomers," *Journal of Cardiovascular Electrophysiology*, vol. 9, no. 10, pp. 1117–1128, Oct. 1998. [Online]. Available: https://onlinelibrary.wiley.com/doi/10.1111/j.1540-8167.1998.tb00890.x

[78] J. Wu, J. Wu, and D. P. Zipes, "Early afterdepolarizations, u waves, and torsades de pointes," vol. 105, no. 6, pp. 675–676, 2002. [Online]. Available: https://www.ahajournals.org/doi/10.1161/circ.105.6.675

[79] J. Kors, H. Ritsema van Eck, and G. van Herpen, "The u wave explained as an intrinsic part of repolarization," in *Computers in Cardiology, 2005*. IEEE, 2005, pp. 101–104. [Online]. Available: https://ieeexplore.ieee.org/document/1588044

[80] D. Geselowitz, "On the theory of the electrocardiogram," vol. 77, no. 6, pp. 857–876, 1989-06. [Online]. Available: http://ieeexplore.ieee.org/document/29327/

[81] J. D. Symanski and L. S. Gettes, "Drug effects on the electrocardiogram: A review of their clinical importance," vol. 46, no. 2, pp. 219–248, 1993-08. [Online]. Available: http://link.springer.com/10.2165/00003495-199346020-00002

[82] S. Maji and M. J. Burke, "Establishing the input impedance requirements of ecg recording amplifiers," vol. 69, no. 3, Mar. 2020, pp. 825–835. [Online]. Available: https://ieeexplore.ieee.org/document/8698291/

[83] Association for the Advancement of Medical Instrumentation (AAMI), *Particular requirements for the safety, in- cluding essential performance, of ambulatory electrocardiographic systems, Part 2-47*. Association for the Advancement of Medical Instrumentation, 2007.

[84] P. M. Rautaharju, B. Surawicz, and L. S. Gettes, "AHA/ACCF/HRS Recommendations for the Standardization and Interpretation of the Electrocardiogram," *Journal of the American College of Cardiology*, vol. 53, no. 11, pp. 982–991, Mar. 2009. [Online]. Available: https://linkinghub.elsevier.com/retrieve/pii/S0735109708041363

[85] M. H. Crawford, S. J. Bernstein, P. C. Deedwania, J. P. DiMarco, K. J. Ferrick, A. Garson, L. A. Green, H. L. Greene, M. J. Silka, P. H. Stone, C. M. Tracy, R. J. Gibbons, J. S. Alpert, K. A. Eagle, T. J. Gardner, A. Garson, G. Gregoratos, R. O. Russell, T. J. Ryan, and S. C. Smith, "ACC/AHA Guidelines for Ambulatory Electrocardiography: Executive Summary and Recommendations: A Report of the American College of Cardiology/American Heart Association Task Force on Practice Guidelines (Committee to Revise the Guidelines for Ambulatory Electrocardiography) *Developed in Collaboration With the North American Society for Pacing and Electrophysiology*," *Circulation*, vol. 100, no. 8, pp. 886–893, Aug. 1999. [Online]. Available: https://www.ahajournals.org/doi/10.1161/01.CIR.100.8.886

[86] S. Maji and M. J. Burke, "Effect of electrode impedance on the transient response of ECG recording amplifiers," in *2018 IEEE International Symposium on Medical Measurements and Applications (MeMeA)*. IEEE, 2018, pp. 1–6. [Online]. Available: https://ieeexplore.ieee.org/document/8438732/

[87] S.Maji and M. J. Burke, "Determining the input impedance of ecg amplifiers using accurate electrode modelling," *Biomedical Physics & Engineering Express*, vol. 6, no. 1, p. 015030, 2020.

[88] S. Maji and M. J. Burke, "Establishing the input impedance requirements of ecg recording amplifiers," *IEEE Transactions on Instrumentation and Measurement*, vol. 69, no. 3, pp. 825–835, 2020.

[89] S. Heuer, D. R. Martinez, S. Fuhrhop, and J. Ottenbacher, "Motion artefact correction for capacitive ecg measurement," in *2009 IEEE Biomedical Circuits and Systems Conference*, 2009, pp. 113–116.

[90] T. Pawar, S. Chaudhuri, and S. P. Duttagupta, "Body movement activity recognition for ambulatory cardiac monitoring," *IEEE Transactions on Biomedical Engineering*, vol. 54, no. 5, 2007.

[91] H. Tam and J. G. Webster, "Minimizing electrode motion artifact by skin abrasion," vol. BME-24, no. 2, pp. 134–139, 1977-03. [Online]. Available: http://ieeexplore.ieee.org/document/4122659/

[92] J. G. Webster, "Reducing motion artifacts and interference in biopotential recording," vol. BME-31, no. 12, pp. 823–826, 1984-12. [Online]. Available: http://ieeexplore.ieee.org/document/4121779/

[93] K. Kearney, C. Thomas, and E. McAdams, "Quantification of motion artifact in ECG electrode design," in *2007 29th Annual International Conference of the IEEE Engineering in Medicine and Biology Society*. IEEE, 2007-08, pp. 1533–1536, ISSN: 1557-170X. [Online]. Available: http://ieeexplore.ieee.org/document/4352594/

[94] K.-P. Hoffmann and R. Ruff, "Flexible dry surface-electrodes for ECG long-term monitoring," in *2007 29th Annual International Conference of the IEEE Engineering in Medicine and Biology Society*. IEEE, 2007-08, pp. 5739–5742. [Online]. Available: https://ieeexplore.ieee.org/document/4353650/

[95] W. Pei, H. Zhang, Y. Wang, X. Guo, X. Xing, Y. Huang, Y. Xie, X. Yang, and H. Chen, "Skin-Potential Variation Insensitive Dry Electrodes for ECG Recording," *IEEE Transactions on Biomedical Engineering*, vol. 64, no. 2, pp. 463–470, Feb. 2017. [Online]. Available: http://ieeexplore.ieee.org/document/7464900/

[96] Y. Ider and H. Koymen, "A new technique for line interference monitoring and reduction in biopotential amplifiers," vol. 37, no. 6, pp. 624–631, 1990-06. [Online]. Available: http://ieeexplore.ieee.org/document/55666/

[97] M. Chimene and R. Pallas-Areny, "A comprehensive model for power line interference in biopotential measurements," vol. 49, no. 3, pp. 535–540, 2000-06. [Online]. Available: http://ieeexplore.ieee.org/document/850390/

[98] Z. Nikolic, D. Popovic, R. Stein, and Z. Kenwell, "Instrumentation for ENG and EMG recordings in FES systems," vol. 41, no. 7, pp. 703–706, 1994-07. [Online]. Available: http://ieeexplore.ieee.org/document/301739/

[99] M. Burke and D. Gleeson, "An ultra-low power pre-amplifier for pasteless electrocardiography," in *ICECS'99. Proceedings of ICECS '99. 6th IEEE International Conference on Electronics, Circuits and Systems (Cat. No.99EX357)*, vol. 2. IEEE, 1999, pp. 615–619. [Online]. Available: http://ieeexplore.ieee.org/document/813183/

[100] M. J. Burke and C. Assambo, "An improved very-low power pre-amplifier for use with un-gelled electrodes in ecg recording," *International Journal of Biology Biomedical Engineering*, vol. 1, no. 1, pp. 25–35, 2007.

[101] S. Maji and M. J. Burke, "The skin-electrode interface impedance and the transient performance of ECG recording amplifiers," in *2018 IEEE SENSORS*. IEEE, 2018, pp. 1–4. [Online]. Available: https://ieeexplore.ieee.org/document/8630308/

[102] K. Kaczmarek and J. Webster, "Voltage-current characteristics of the electrotactile skin-electrode interface," in *Images of the Twenty-First Century. Proceedings of the Annual International Engineering in Medicine and Biology Society*. IEEE, 1989, pp. 1526–1527. [Online]. Available: http://ieeexplore.ieee.org/document/96322/

[103] T. Zagar and D. Krizaj, "An instrumentation amplifier as a front-end for a four-electrode bioimpedance measurement," *Physiological measurement*, vol. 28, no. 8, p. N57, 2007.

[104] A. Baba and M. Burke, "Electrical characterisation of dry electrodes for ECG recording." World Scientific and Engineering Academy and Society (WSEAS), 2008-07, pp. 76–81.

[105] ——, "Measurement of the electrical properties of ungelled ECG electrodes," vol. 2, no. 3, pp. 89–97, 2008.

[106] IEC Std., *Effects of current on human beings and livestock. Part 1, Part 1,*. IEC Std., 2005, OCLC: 946516737.

[107] M. M. Laks, R. Arzbaecher, J. J. Bailey, D. B. Geselowitz, and A. S. Berson, "Recommendations for safe current limits for electrocardiographs: A statement for healthcare professionals from the committee on electrocardiography, american heart association," vol. 93, no. 4, pp. 837–839, 1996-02. [Online]. Available: https://www.ahajournals.org/doi/10.1161/01.CIR.93.4.837

[108] N. Rai, H. Shaik, N. Veerapandi, V. S. Nagaraj, and S. Veena, "Carbon-based textile dry and flexible electrodes for ecg measurement," in *Advances in Renewable Energy and Electric Vehicles*. Springer, 2022, pp. 37–53.

[109] H. Ali, H. H. Naing, and R. Yaqub, "An iot assisted real-time high cmrr wireless ambulatory ecg monitoring system with arrhythmia detection," *Electronics*, vol. 10, no. 16, p. 1871, 2021.

[110] T. Tang, W. L. Goh, L. Yao, and Y. Gao, "A 16-channel tdm analog front-end with enhanced system cmrr for wearable dry eeg recording," in *2017 IEEE Asian Solid-State Circuits Conference (A-SSCC)*. IEEE, 2017, pp. 33–36.

[111] J. Lee, G.-H. Lee, H. Kim, and S. Cho, "An ultra-high input impedance analog front end using self-calibrated positive feedback," *IEEE Journal of Solid-State Circuits*, vol. 53, no. 8, pp. 2252–2262, 2018.

[112] W. Bai, Z. Zhu, Y. Li, and L. Liu, "A $64.8~\mu$ w > 2.2 g ω DC–AC configurable CMOS front-end IC for wearable ECG monitoring," vol. 18, no. 8, pp. 3400–3409, 2018. [Online]. Available: http://ieeexplore.ieee.org/document/8302889/

[113] X. Zhang, Z. Zhang, Y. Li, C. Liu, Y. X. Guo, and Y. Lian, "A 2.89μw dry-electrode enabled clockless wireless ecg soc for wearable applications," *IEEE journal of solid-state circuits*, vol. 51, no. 10, pp. 2287–2298, 2016.

[114] X. Pu, L. Wan, Y. Sheng, P. Chiang, Y. Qin, and Z. Hong, "A wireless 8-channel ecg biopotential acquisition system for dry electrodes," in *2012 IEEE International Symposium on Radio-Frequency Integration Technology (RFIT)*. IEEE, 2012, pp. 140–142.

[115] S. Maji and M. J. Burke, "Noise performance of textile-based dry ECG recording electrodes," vol. 57, no. 2, pp. 45–48, 2021-01. [Online]. Available: https://onlinelibrary.wiley.com/doi/10.1049/ell2.12063

[116] E. Huigen, A. Peper, and C. Grimbergen, "Investigation into the origin of the noise of surface electrodes," *Medical and biological engineering and computing*, vol. 40, no. 3, pp. 332–338, 2002.

[117] M. Fernandez and R. Pallas-Areny, "Electrode contact noise in surface biopotential measurements," in *Proceedings of the Annual International Conference of the IEEE Engineering in Medicine and Biology Society*. IEEE, 1992, pp. 123–124. [Online]. Available: http://ieeexplore.ieee.org/document/5760887/

[118] T. Degen and H. Jackel, "Enhancing interference rejection of preamplified electrodes by automated gain adaption," *IEEE transactions on biomedical engineering*, vol. 51, no. 11, pp. 2031–2039, 2004.

[119] T. Degen and H. JÄckel, "Continuous monitoring of electrode–skin impedance mismatch during bioelectric recordings," vol. 55, no. 6, pp. 1711–1715, 2008. [Online]. Available: https://ieeexplore.ieee.org/document/4457865/

[120] P. Hamilton, M. Curley, R. Aimi, and C. Sae-Hau, "Comparison of methods for adaptive removal of motion artifact," in *Computers in Cardiology 2000. Vol.27 (Cat. 00CH37163)*. IEEE, 2000, pp. 383–386. [Online]. Available: http://ieeexplore.ieee.org/document/898537/

[121] E. Spinelli, M. Mayosky, and R. Pallas-Areny, "A practical approach to electrode-skin impedance unbalance measurement," vol. 53, no. 7, pp. 1451–1453, 2006. [Online]. Available: http://ieeexplore.ieee.org/document/1643419/

[122] E. Richard and A. D. C. Chan, "Design of a gel-less two-electrode ECG monitor," in *2010 IEEE International Workshop on Medical Measurements and Applications*. IEEE, 2006, pp. 92–96. [Online]. Available: http://ieeexplore.ieee.org/document/5480198/

[123] A. Pourahmad and R. Dehghani, "Two-Wired Current Modulator Active Electrode for Ambulatory Biosignal Recording," *IEEE Transactions on Biomedical Circuits and Systems*, pp. 1–1, 2018. [Online]. Available: https://ieeexplore.ieee.org/document/8584126/

[124] R. Pallás-Areny and J. G. Webster, *Analog signal processing*. John Wiley & Sons, 1999.

[125] Y. M. Chi, C. Maier, and G. Cauwenberghs, "Integrated ultra-high impedance front-end for non-contact biopotential sensing," in *2011 IEEE Biomedical Circuits and Systems Conference (BioCAS)*. IEEE, 2011, pp. 456–459. [Online]. Available: http://ieeexplore.ieee.org/document/6107826/

[126] Z. Zhou and P. A. Warr, "A high input impedance low noise integrated front-end amplifier for neural monitoring," vol. 10, no. 6, pp. 1079–1086, 2016. [Online]. Available: http://ieeexplore.ieee.org/document/7476826/

[127] J. M. Kootsey and E. A. Johnson, "Buffer amplifier with femtofarad input capacity using operational amplifiers," vol. BME-20, no. 5, pp. 389–391, 1973. [Online]. Available: http://ieeexplore.ieee.org/document/4120681/

[128] J. Hribik, S. Lanyi, and M. Hruskovic, "A high-input-impedance buffer," in *2008 18th International Conference Radioelektronika*. IEEE, 2008, pp. 1–4. [Online]. Available: https://ieeexplore.ieee.org/document/4542707/

[129] P. Wilson, "Printed circuits," in *The Circuit Designer's Companion*. Elsevier, 2017, pp. 49–91. [Online]. Available: https://linkinghub.elsevier.com/retrieve/pii/B9780081017647000025

[130] V. Stornelli and G. Ferri, "A single current conveyor-based low voltage low power bootstrap circuit for ElectroCardioGraphy and ElectroEncephaloGraphy

acquisition systems," vol. 79, no. 1, pp. 171–175, 2014. [Online]. Available: http://link.springer.com/10.1007/s10470-013-0252-2

[131] Y. Chi and G. Cauwenberghs, "Micropower non-contact EEG electrode with active common-mode noise suppression and input capacitance cancellation," in *2009 Annual International Conference of the IEEE Engineering in Medicine and Biology Society*. IEEE, 2009, pp. 4218–4221. [Online]. Available: http://ieeexplore.ieee.org/document/5333527/

[132] E. Spinelli, M. Haberman, P. García, and F. Guerrero, "A capacitive electrode with fast recovery feature," vol. 33, no. 8, pp. 1277–1288, 2012. [Online]. Available: https://iopscience.iop.org/article/10.1088/0967-3334/33/8/1277

[133] A. Bosnjak, A. Kennedy, P. Linares, M. Borges, J. McLaughlin, and O. J. Escalona, "Performance assessment of dry electrodes for wearable long term cardiac rhythm monitoring: Skin-electrode impedance spectroscopy," in *2017 39th Annual International Conference of the IEEE Engineering in Medicine and Biology Society (EMBC)*. IEEE, 2017, pp. 1861–1864. [Online]. Available: https://ieeexplore.ieee.org/document/8037209/

[134] C. Assambo, A. Baba, and M. Burke, "Determination of the parameters of the skin-electrode impedance model for ECG measurement." World Scientific and Engineering Academy and Society (WSEAS)Stevens PointWisconsinUnited States, 2007-02, pp. 90–95.

[135] R. Dozio, A. Baba, C. Assambo, and M. J. Burke, "Time based measurement of the impedance of the skin-electrode interface for dry electrode ECG recording," in *2007 29th Annual International Conference of the IEEE Engineering in Medicine and Biology Society*. IEEE, 2007-08, pp. 5001–5004, ISSN: 1557-170X. [Online]. Available: http://ieeexplore.ieee.org/document/4353463/

[136] A. Achilli, A. Bonfiglio, and D. Pani, "Design and characterization of screen-printed

textile electrodes for ECG monitoring," vol. 18, no. 10, pp. 4097–4107, 2018. [Online]. Available: https://ieeexplore.ieee.org/document/8325296/

[137] R. Kusche, S. Kaufmann, and M. Ryschka, "Dry electrodes for bioimpedance measurements—design, characterization and comparison," vol. 5, no. 1, p. 015001, 2018-11. [Online]. Available: https://iopscience.iop.org/article/10.1088/2057-1976/aaea59

[138] B. Taji, A. D. C. Chan, and S. Shirmohammadi, "Effect of pressure on skin-electrode impedance in wearable biomedical measurement devices," vol. 67, no. 8, pp. 1900–1912, 2018. [Online]. Available: https://ieeexplore.ieee.org/document/8320545/

[139] K. Tomczyk, "Procedure for correction of the ECG signal error introduced by skin-electrode interface," vol. 18, no. 3, 2011-01. [Online]. Available: http://journals.pan.pl/dlibra/publication/103802/edition/89807/content

[140] S. Del Bino, C. Duval, and F. Bernerd, "Clinical and biological characterization of skin pigmentation diversity and its consequences on UV impact," vol. 19, no. 9, p. 2668, 2018. [Online]. Available: http://www.mdpi.com/1422-0067/19/9/2668

[141] D. Buxi, Sunyoung Kim, N. van Helleputte, M. Altini, J. Wijsman, R. F. Yazicioglu, J. Penders, and C. van Hoof, "Correlation between electrode-tissue impedance and motion artifact in biopotential recordings," vol. 12, no. 12, pp. 3373–3383, 2012-12. [Online]. Available: http://ieeexplore.ieee.org/document/6316054/

[142] L. A. Geddes, *Electrodes and the measurement of bioelectric events*. Wiley-Interscience, 1972.

[143] L. A. Geddes and L. E. Baker, *Principles of applied biomedical instrumentation*, 3rd ed. Wiley, 1989.

[144] M. M. Puurtinen, S. M. Komulainen, P. K. Kauppinen, J. A. V. Malmivuo, and J. A. K. Hyttinen, "Measurement of noise and impedance of dry and wet textile electrodes, and textile electrodes with hydrogel," in *2006 International Conference*

of the IEEE Engineering in Medicine and Biology Society. IEEE, 2006-08, pp. 6012–6015. [Online]. Available: http://ieeexplore.ieee.org/document/4463178/

[145] E. Huigen, A. Peper, and C. A. Grimbergen, "Investigation into the origin of the noise of surface electrodes," vol. 40, no. 3, pp. 332–338, 2002. [Online]. Available: http://link.springer.com/10.1007/BF02344216

[146] E. Novakov, "Evaluation of the electrode-amplifier noise in high resolution biological signal acquisition," in *Proceedings of the 19th Annual International Conference of the IEEE Engineering in Medicine and Biology Society. 'Magnificent Milestones and Emerging Opportunities in Medical Engineering' (Cat. No.97CH36136)*, vol. 4. IEEE, 1997, pp. 1452–1454. [Online]. Available: http://ieeexplore.ieee.org/document/756979/

[147] S. Yacoub, E. Novakov, P.-Y. Gumery, C. Gondran, and E. Siebert, "Noise analysis of NASICON ceramic dry electrodes," in *Proceedings of 17th International Conference of the Engineering in Medicine and Biology Society*, vol. 2. IEEE, 1995, pp. 1553–1554. [Online]. Available: http://ieeexplore.ieee.org/document/579823/

[148] M. Fernández and R. Pallás-Areny, "Ag-AgCl electrode noise in high-resolution ECG measurements," vol. 34, no. 2, pp. 125–130, 2000.

[149] X. Liu, A. Demosthenous, and N. Donaldson, "On the noise performance of pt electrodes," in *2007 29th Annual International Conference of the IEEE Engineering in Medicine and Biology Society*. IEEE, 2007-08, pp. 434–436, ISSN: 1557-170X. [Online]. Available: http://ieeexplore.ieee.org/document/4352316/

[150] B. Taji, S. Shirmohammadi, V. Groza, and I. Batkin, "Impact of skin–electrode interface on electrocardiogram measurements using conductive textile electrodes," vol. 63, no. 6, pp. 1412–1422, 2014. [Online]. Available: http://ieeexplore.ieee.org/document/6670113/

[151] Y. M. Chi, T.-P. Jung, and G. Cauwenberghs, "Dry-contact and noncontact

biopotential electrodes: Methodological review," vol. 3, pp. 106–119, 2010. [Online]. Available: http://ieeexplore.ieee.org/document/5598518/

[152] G. P. Shorten and M. J. Burke, "A precision ecg signal generator providing full lead ii qrs amplitude variability and an accurate timing profile," in *2009 Annual International Conference of the IEEE Engineering in Medicine and Biology Society*. IEEE, 2009, pp. 3008–3011.

[153] G. P. Shorten, "Accurate modelling and synthesis of the lead 11 ecg signal," Ph.D. dissertation, Trinity College Dublin, 2012.

[154] "PhysioNet Databases." [Online]. Available: https://physionet.org/about/database/

[155] A. Baba and M. Burke, "Measurement of the electrical properties of ungelled ECG electrodes," vol. 2, no. 3, pp. 89–97, 2008.

[156] M. Młyńczak, K. Pariaszewska, W. Niewiadomski, and G. Cybulski, "Design and construction of the artificial patient module for testing bioimpedance measuring devices," in *Photonics Applications in Astronomy, Communications, Industry, and High-Energy Physics Experiments 2013*, vol. 8903. International Society for Optics and Photonics, 2013, p. 890314.

[157] A. Bosnjak, P. Linares, J. McLaughlin, and O. J. Escalona, "Characterizing dry electrodes impedance by parametric modeling for arm wearable long-term cardiac rhythm monitoring," in *2017 Computing in Cardiology (CinC)*. IEEE, 2017, pp. 1–4.

[158] R. E. Mason and I. Likar, "A new system of multiple-lead exercise electrocardiography," *American heart journal*, vol. 71, no. 2, pp. 196–205, 1966.

[159] N. Thakor and J. Webster, "Electrode studies for the long-term ambulatory ecg," *Medical and Biological Engineering and Computing*, vol. 23, no. 2, pp. 116–121, 1985.

[160] I. Turner, W. Wang, M. English, and R. Vincent, "Noise coherence in closely-spaced electrodes: The implications for spatial averaged egg recordings," *Journal of medical engineering & technology*, vol. 19, no. 5, pp. 158–161, 1995.

[161] J. Welch, F. Guilak, and S. D. Baker, "A wireless ecg smart sensor for broad application in life threatening event detection," in *The 26th Annual International Conference of the IEEE Engineering in Medicine and Biology Society*, vol. 2. IEEE, 2004, pp. 3447–3449.

[162] M. C. Burke, J. Jenkins, M. Garrett, J. Moss, J. Beshai, and R. Arzbaecher, "Is a cardioalarm using ambulatory subcutaneous electrocardiography from closely spaced electrodes feasible?" 2010.

[163] K. Takuma, S. Hori, J. Sasaki, Y. Shinozawa, T. Yoshikawa, S. Handa, M. Horikawa, and N. Aikawa, "An alternative limb lead system for electrocardiographs in emergency patients," *The American journal of emergency medicine*, vol. 13, no. 5, pp. 514–517, 1995.

[164] B. J. Drew, R. M. Califf, M. Funk, E. S. Kaufman, M. W. Krucoff, M. M. Laks, P. W. Macfarlane, C. Sommargren, S. Swiryn, and G. F. Van Hare, "Practice standards for electrocardiographic monitoring in hospital settings: an american heart association scientific statement from the councils on cardiovascular nursing, clinical cardiology, and cardiovascular disease in the young: endorsed by the international society of computerized electrocardiology and the american association of critical-care nurses," *Circulation*, vol. 110, no. 17, pp. 2721–2746, 2004.

[165] B. B. Winter and J. G. Webster, "Driven-right-leg circuit design," *IEEE Transactions on Biomedical Engineering*, vol. BME-30, no. 1, pp. 62–66, Jan. 1983. [Online]. Available: http://ieeexplore.ieee.org/document/4121504/

[166] D. P. Dobrev and T. D. Neycheva, "Comments on:"an analog bootstrapped biosignal read-out circuit with common-mode impedance two-electrode compensation"," *IEEE Sensors Journal*, 2021.

[167] I.-D. Hwang and J. G. Webster, "Direct interference canceling for two-electrode biopotential amplifier," *IEEE Transactions on Biomedical Engineering*, vol. 55, no. 11, pp. 2620–2627, 2008.

[168] Y.-j. Park and H.-s. Cho, "Transmission of ecg data with the patch-type ecg sensor system using bluetooth low energy," in *2013 International Conference on ICT Convergence (ICTC)*. IEEE, 2013, pp. 289–294.

[169] S. Sivanathan and A. Oleon, "Real-time bluetooth low energy (ble) electrocardiogram monitoring device," in *2021 IEEE International Instrumentation and Measurement Technology Conference (I2MTC)*. IEEE, 2021, pp. 1–5.

[170] Q. Dong, R. S. Downen, B. Li, N. Tran, and Z. Li, "A cloud-connected multi-lead electrocardio-gram (ecg) sensor ring," *IEEE Sensors Journal*, 2021.

[171] J. Martinez-Quijada and S. Chowdhury, "Body-motion driven mems generator for implantable biomedical devices," in *2007 Canadian Conference on Electrical and Computer Engineering*. IEEE, 2007, pp. 164–167.

[172] E. Romero, R. O. Warrington, and M. R. Neuman, "Body motion for powering biomedical devices," in *2009 Annual International Conference of the IEEE Engineering in Medicine and Biology Society*. IEEE, 2009, pp. 2752–2755.

[173] E. Romero et. al., "Powering biomedical devices with body motion," in *2010 Annual International Conference of the IEEE Engineering in Medicine and Biology*. IEEE, 2010, pp. 3747–3750.

[174] X. An and G. K Stylios, "Comparison of motion artefact reduction methods and the implementation of adaptive motion artefact reduction in wearable electrocardiogram monitoring," *Sensors*, vol. 20, no. 5, p. 1468, 2020.

[175] M. Sun and J. Hill, "A method for measuring mechanical work and work efficiency during human activities," *Journal of biomechanics*, vol. 26, no. 3, pp. 229–241, 1993.

[176] J. M. Łęski and N. Henzel, "Ecg baseline wander and powerline interference reduction using nonlinear filter bank," *Signal processing*, vol. 85, no. 4, pp. 781–793, 2005.

[177] E.-S. A. El-Dahshan, "Genetic algorithm and wavelet hybrid scheme for ecg signal denoising," *Telecommunication Systems*, vol. 46, no. 3, pp. 209–215, 2011.

[178] P. Karthikeyan, M. Murugappan, and S. Yaacob, "Ecg signal denoising using wavelet thresholding techniques in human stress assessment," *International Journal on Electrical Engineering and Informatics*, vol. 4, no. 2, p. 306, 2012.

[179] M. S. Chavan, R. Agarwala, and M. Uplane, "Suppression of noise in the ecg signal using digital iir filter," in *WSEAS International Conference. Proceedings. Mathematics and Computers in Science and Engineering*, no. 8. World Scientific and Engineering Academy and Society, 2008.

[180] J. A. Van Alste and T. Schilder, "Removal of base-line wander and power-line interference from the ecg by an efficient fir filter with a reduced number of taps," *IEEE transactions on biomedical engineering*, no. 12, pp. 1052–1060, 1985.

[181] P. Kligfield, L. S. Gettes, J. J. Bailey, R. Childers, B. J. Deal, E. W. Hancock, G. Van Herpen, J. A. Kors, P. Macfarlane, D. M. Mirvis *et al.*, "Recommendations for the standardization and interpretation of the electrocardiogram: part i: the electrocardiogram and its technology a scientific statement from the american heart association electrocardiography and arrhythmias committee, council on clinical cardiology; the american college of cardiology foundation; and the heart rhythm society endorsed by the international society for computerized electrocardiology," *Journal of the American College of Cardiology*, vol. 49, no. 10, pp. 1109–1127, 2007.

[182] D. A. Bragg-Remschel, C. M. Anderson, and R. A. Winkle, "Frequency response characteristics of ambulatory ecg monitoring systems and their implications for st segment analysis," *American Heart Journal*, vol. 103, no. 1, pp. 20–31, 1982.

[183] M. N. Salman, P. T. Rao, and M. Z. U. Rahman, "Novel logarithmic reference free adaptive signal enhancers for ecg analysis of wireless cardiac care monitoring systems," *IEEE Access*, vol. 6, pp. 46 382–46 395, 2018.

[184] N. V. Thakor and Y.-S. Zhu, "Applications of adaptive filtering to ecg analysis: noise cancellation and arrhythmia detection," *IEEE transactions on biomedical engineering*, vol. 38, no. 8, pp. 785–794, 1991.